Dipl.-Ing. Tomas Kamencek, BSc BSc

Methodological Benchmark and Structure-to-Property Relations for Phonon Derived Properties of Organic Semiconductor Crystals

MASTER'S THESIS

to achieve the university degree of
Diplom-Ingenieur

Master's degree programme:
Advanced Materials Science

submitted to
Graz University of Technology

Supervisor

Ao.Univ.-Prof. Dipl.-Ing. Dr.techn. Egbert Zojer

Institute of Solid State Physics

Graz, February 2021

AFFIDAVIT

I declare that I have authored this thesis independently, that I have not used other than the declared sources/resources, and that I have explicitly indicated all material which has been quoted either literally or by content from the sources used. The text document uploaded to TUGRAZonline is identical to the present master's thesis.

Date, Signature

Abstract

Organic semiconductors (OSCs) are a technologically important materials class, which can be used for numerous (opto-)electronic devices such as transistors, light-emitting diodes or solar cells. Today, OSCs are found in many devices such as televisions, cell phones or laptops. Despite the usage of OSCs on an industrial scale, most of the thermal properties determined by lattice vibrations (phonons) are still not well understood. These include heat transport, thermal expansion, or thermodynamic quantities like heat capacities and free energies determining the relative stability of possible polymorphs. Even charge transport processes are affected due to strong electron-phonon coupling. Here, a precise knowledge of the phonon band structures is necessary. While the experimental measurement of those faces many difficulties, the alternative computational approach is often hampered by the large numbers of atoms per unit-cell using methods such as (dispersion-corrected) density functional theory (DFT). Therefore, one often needs to resort to lower levels of theory. Thus, the evaluation of the performance of such methodologies of (supposedly) lower accuracy comprising density functional tight binding (DFTB) and a few classical force fields (FF) is at the very heart of this thesis. To this end, not only differences in band structures but also their impact on the derived properties are analysed. Comparisons and benchmarks are carried out for deuterated naphthalene - the only OSC for which experimental phonon bands are available. The methodology most accurately reproducing experimental Raman spectra, band structures, and lattice constants is dispersion-corrected DFT using the PBE functional and the D3-BJ van der Waals correction. The approximate methodology showing the best overall performance among the tested ones is the system-specifically parametrised second-generation force field MOF-FF. In the very low frequency regime dominated by dispersion interactions, also less sophisticated FFs fare relatively well. Surprisingly, the - supposedly more sophisticated - tested DFTB approach performs worse than the FFs, which can be mostly ascribed to a significant underestimation of the unit-cell volume leading to overestimated intermolecular phonon frequencies. Also using the DFT-optimised unit-cells in the DFTB calculations does not yield a large improvement of the frequencies. Here, using isotropically shrunk DFT-calculated lattice vectors for DFTB simulations leads to much better agreement. This trick, in spite of being physically not well justified, has been found to improve the results for further OSCs as well. Although all tested approximate methodologies have their strengths and weaknesses, none of them yields a fully satisfying agreement with the PBE/D3-BJ results. Thus, this approach is then applied to a number of crystalline OSCs to find structure-to-property relations for their phonon-related properties. One finds that the effective force constants of rigid intermolecular vibrations for displacements along the long molecular axes in oligoacenes approximately stay constant as a function of the number of rings per molecule. In contrast, for vibrations perpendicular to the long molecular axis, they increase approximately linearly with the number of rings. In combination with the larger unit-cells, the phonon group velocities are found to be largest for long oligoacenes, while they are suppressed by low-lying intramolecular modes in pyrene and fluorene. For the studied polymorphs of quinacridone and benzene, the obtained relative thermodynamic stability is in agreement with the

experimental observation. In contrast to the free energies, which differ significantly among the systems mostly due to differences in zero-point energies, the heat capacity normalised by the number of bands is found to be nearly identical for all the studied systems. As a result, a straightforward way to estimate molar heat capacities is established.

Zusammenfassung

Organische Halbleiter (OHL) bilden eine relevante Materialklasse, die für viele (opto-)elektronische Bauteile wie Transistoren, Leuchtdioden und Solarzellen verwendet werden kann. Heutzutage findet man OHL in einigen Geräten wie Fernsehern, Mobiltelefonen oder Laptops. Trotz der Anwendung in industriellem Maß ist das Verständnis der thermischen Eigenschaften, die hier von Gitterschwingungen (Phononen) dominiert sind, immer noch nicht sehr umfassend. Das beinhaltet den Wärmetransport, die Wärmeausdehnung und thermodynamische Größen wie Wärmekapazitäten und freie Energien, die die thermodynamische Stabilität von Polymorphen bestimmen. Sogar der Ladungstransport ist wegen der starken Elektron-Phonon-Kopplung betroffen. Hier ist das Wissen um die zugrundeliegende Phononenbandstruktur erforderlich. Während deren experimentelle Bestimmung einige Probleme mit sich bringt, stößt die Simulation mit Methoden wie (dispersionskorrigierter) Dichtefunktionalstheorie (engl. density functional theory, DFT) durch die große Zahl an Atomen pro Einheitszelle oft an ihre Grenzen. Daher muss man auf einfachere Methoden zurückgreifen, welche hier density functional tight binding (DFTB) und klassische Kraftfelder (KF) umfassen. Die Evaluierung hinsichtlich deren Leistung und ihrer (vermeintlich) geringeren Genauigkeit bildet das Herzstück dieser Arbeit. Dabei werden nicht nur die Unterschiede in den Bandstrukturen, sondern auch deren Auswirkung auf abgeleitete Größen analysiert. Dies wird anhand von deuteriertem Naphthalin diskutiert - dem einzigen OHL, für den gemessene Phononenbänder verfügbar sind. Die geeignetste Methode, um experimentelle Raman-Spektren, Bandstrukturmessungen und Gitterparameter zu reproduzieren, ist DFT mit dem PBE-Funktional und der D3-BJ van-der-Waals-Korrektur. Ein systemspezifisches KF der zweiten Generation hat sich als die beste der getesteten einfacheren Methoden herausgestellt. Für sehr geringe Frequenzen liefern auch simplere KF zufriedenstellende Genauigkeit. Überraschenderweise zeigen die DFTB-Resultate viel geringere Qualität. Dies kann dem deutlich unterschätzten Einheitszellenvolumen zugeschrieben werden, was zu erhöhten intermolekularen Frequenzen führt. Auch das Verwenden der mit DFT optimierten Einheitszelle in der DFTB-Simulation liefert keine große Verbesserung dieser Frequenzen. Eine DFT-optimierte Einheitszelle mit isotrop verkürzten Gittervektoren als Input für die DFTB-Simulation erzielt deutlich bessere Ergebnisse. Dieser physikalisch nicht gut rechtfertigbare Trick führt jedoch auch bei anderen Systemen zu verbesserten DFTB-Bandstrukturen. Obwohl alle getesteten approximativen Methoden Stärken und Schwächen aufweisen, liefert keine von ihnen eine in allen Aspekten zufriedenstellende Übereinstimmung mit den PBE/D3-BJ-Resultaten. Daher wurde diese Methode verwendet, um für weitere OHL Relationen zwischen deren Strukturen und ihren phononischen Eigenschaften zu untersuchen. Dabei wurde beobachtet, dass die effektiven Kraftkonstanten für starre intermolekulare Vibrationen entlang der langen Molekülachse in Oligacenen als Funktion der Moleküllänge etwa konstant sind, während sie für Schwingungen orthogonal dazu zunehmen. Zusammen mit den größeren Einheitszellen führt das dazu, dass die Gruppengeschwindigkeiten für lange Oligoacene am größten sind, während sie in Fluoren und Pyren durch niederfrequente intramolekulare Moden unterdrückt werden. Für die untersuchten Benzol- und Chinacridon-Polymorphe entspricht die

simulierte relative thermodynamischen Stabilität der experimentell beobachteten. Im Gegensatz zur freien Energie, in der sich die Systeme erheblich (hauptsächlich aufgrund der Nullpunktsenergie) voneinander unterscheiden, ist die mit der Zahl der Bänder normierte Wärmekapazität nahezu gleich für alle Systeme. Daraus kann ein einfacher Zusammenhang für die molare Wärmekapazität abgeleitet werden.

Contents

Preface 1

1. Introduction 3

2. Theoretical Background 8
2.1. The Born-Oppenheimer Approximation . . . 8
2.2. The Potential-Energy Surface . . . 9
2.3. Phonons and the Dynamical Matrix . . . 11
2.3.1. Anharmonicities in a nutshell . . . 19
2.4. Phonons in the (Grand) Canonical Ensemble . . . 22
2.4.1. Atom-resolved thermodynamic averages . . . 32
2.5. Relevant Frequency Ranges . . . 35
2.6. Density Functional Theory . . . 38
2.6.1. *A posteriori* van der Waals corrections . . . 41
2.7. Density Functional Tight Binding . . . 45
2.8. Classical Force Fields . . . 49

3. Methodology and Computational Details 52
3.1. Phonon Properties for the Benchmark of Approximate Methodologies . . 52
3.1.1. Density-Functional Theory Calculations . . . 52
3.1.2. Density-Functional Tight Binding Calculations . . . 59
3.1.3. Force Field Calculations . . . 61
3.1.4. Phonon Calculations . . . 63
3.1.5. Phonon Mode Assignment . . . 65
3.2. Phonon Properties of Organic Semiconductors Other Than Naphthalene . 66

4. Methodological Benchmark: The Instructive Case of Naphthalene 71
4.1. Crystalline Naphthalene . . . 71
4.2. Low-Frequency Phonons ($\leq$ 9 THz) . . . 72
4.2.1. Identifying an Accurate Reference Methodology . . . 72
4.2.2. Phonon Band Structures from Density Functional Tight Binding . 78
4.2.3. Phonon Band Structures from Classical Force Fields . . . 86
4.2.4. Quantitative Benchmark of Low-Frequency Phonon Properties . . 90
4.2.5. Assessment of the Suitability of Approximate Methods to Describe Physical Observables Based on the (Low-Frequency) Phonon Band Structure . . . 97
4.3. High-Frequency Phonons ($>$ 9 THz) . . . 103
4.3.1. Quantitative Benchmark of High-Frequency Phonon Properties . . 103
4.3.2. Assessment of the Suitability of Approximate Methods to Describe Physical Observables Based on the Entire Phonon Spectrum . . . 114
4.4. Summary and Conclusions of the Methodological Benchmark . . . 120

5. Phononic Properties in Various Organic Semiconductors **125**
5.1. Low-Frequency Band Structures . . . 133
5.1.1. Benzene . . . 133
5.1.2. Naphthalene . . . 139
5.1.3. Anthracene . . . 143
5.1.4. Tetracene . . . 146
5.1.5. Pentacene . . . 148
5.1.6. Fluorene . . . 152
5.1.7. Pyrene . . . 154
5.1.8. Quinacridone . . . 157
5.2. Properties Derived from the Phonon Spectrum . . . 162
5.2.1. Group Velocities . . . 162
5.2.2. Densities of States . . . 168
5.2.3. Thermodynamic Properties . . . 171

6. Summary **179**

A. Appendices **199**
A.1. Mathematical Details for the Derivation of the Bose-Einstein Distribution 199
A.2. Commutation Rules for Phonon Ladder Operators . . . 199
A.3. Some More Details on the One-Dimensional Phonon Model System . . . 199
A.4. Convergence of the DOSs with respect to the wave vector sampling . . . 202
A.5. Lowest-frequency Intramolecular Modes in Naphthalene . . . 205
A.6. More Views of the Crystal Structure of β-Quinacridone . . . 206
A.7. More Views of the Crystal Structure of γ-Quinacridone . . . 208
A.8. Further Thermodynamic Properties . . . 209
A.9. General relation between the heat capacities at constant pressure and at constant volume . . . 212

Preface

It shall be emphasised already at the very beginning of this thesis that large parts of Sec. 3 and nearly the entire Sec. 4 had already been published before I wrote this thesis. The article is called "Evaluating Computational Shortcuts in Supercell-Based Phonon Calculations of Molecular Crystals: The Instructive Case of Naphthalene" and has been published in the *Journal of Chemical Theory and Computation* in 2020 (see `https://pubs.acs.org/doi/full/10.1021/acs.jctc.0c00119`, Copyright © American Chemical Society) [1]. Figures and data found in this thesis, which have been taken from this paper or its Supporting Information, are specifically labelled as such.
Since the above-mentioned publication has been the joint effort of several authors, their individual contributions and especially my own role shall be briefly commented on. Below, the authors (in the order in which they appear in the publication) will be referred to as with the following abbreviations: Tomas Kamencek (TK), Sandro Wieser (SW), Hirotaka Kojima (HK), Natalia Bedoya-Martínez (NB), Johannes P. Dürholt (JD), Rochus Schmid (RS), and Egbert Zojer (EZ).

EZ and TK had the original idea that it is worthwhile to test the performance of various approaches - comprising density functional theory (DFT), density functional tight binding (DFTB), and force fields (FFs) - to obtain simulated phonon band structures, as the promised level of accuracy is often not achieved with lower levels of theory. TK carried out all the DFT calculations, including the detailed comparison with all available experimental data, Raman spectra simulations for crystalline and molecular naphthalene, as well as all DFTB calculations. HK calculated the phonon band structure with the "COMPASS"-FF with the help of SW and TK, while the band structures with the force field "GAFF" and "MOF-FF" were calculated by SW, who - with the help of JD and RS - was also mostly involved in the parametrisation process of this intransferable FF. Based on the phonon band structures, TK has evaluated all derived properties for all methodologies comprising heat capacities, free energies, group velocities, densities of states, mean-squared thermal displacements etc., followed by a detailed analysis of the origin of the observed differences. With the help of the evaluation tools developed by TK in this context (including routines for the assignment of phonon modes, the calculation of quantitative measures of errors, statistical analysis, etc.) the results were interpreted mostly by TK, NB, and EZ. Moreover, TK wrote the first version of the manuscript, prepared all figures while being in constant exchange with EZ, with whom the manuscript has prevailingly been revised in multiple iterations. In this phase, slight changes to the actual formulations were inspired by continuous discussions with all coauthors.

1. Introduction

From the beginning of their existence, human beings have increasingly made use of tools and their properties to overcome difficulties in their lives. Outsourcing task, which one does not want to do or is not capable of doing alone to a machine or a device is at the very heart of technology. Over the years, more and more types of devices have been constructed and engineered. They exploit a number of materials properties such as the mechanical, thermal, electronic, magnetic, or optical properties of a material. The more technology determines our daily lives, the more the society relies on devices which come at affordable prices. A special materials class which offers an incredible versatility in terms of its properties and yet is relative cheap, is the family of organic semiconductors. Nowadays, organic semiconductor crystals - i.e. solids formed by the crystalline arrangement of π-conjugated organic molecules or polymers - can be found in many everyday objects such as laptops, cell phones, or displays [2] (as so-called organic light-emitting diodes, OLEDs, consisting of amorphous OSCs [3], or organic thin film transistors, OTFTs [4]) or - more specific - in organic solar cells [5].
Although organic semiconductors (OSCs) differ quite significantly from conventional inorganic semiconductors in terms of their properties due to the fundamentally different atomistic architecture of those solids, and even though some of their properties are much less advantageous than in other (inorganic) materials, OSCs are still a relevant scientific topic. The number of publications listed in the online database *Web of Science* obtained when searching for "organic semiconductor" can be seen in the top panel of Fig. 1.1: except for the year 2020, the number of OSCs-related scientific articles has been increasing for several decades[1]. The ongoing scientific interest in this low-cost materials can most probably be ascribed to their huge versatility making use of the entire toolbox of organic chemistry [6].

One of the most important differences between inorganic and organic semiconductors causing the need of alternative considerations and pictures is the fundamentally different electronic structure. In general, semiconductors show band gaps and no density of electronic states at the respective Fermi level, in contrast to metallic solids [7]. In OSCs, these band gaps are typically relatively large, and, moreover, the band dispersion is often very small such that Bloch-waves usually exhibit only minor group velocities. This means that electrons are typically relatively heavy and localised in OSCs (without clever designs) and, thus, cannot effectively contribute to many materials properties.
Instead, another quasi-particle is of increasing relevance determining many properties of OSCs. This type of quasi-particle has its origin in the atomic motion: phonons are the quanta of lattice vibrations as a consequence of the Born-Oppenheimer approximation (see Sec. 2.1). Practically relevant aspects, which are dominated by the influence of phonons are, for instance, the strong electron-phonon coupling, which has been found to be one of the key obstacles in electronic transport in OSCs [8, 9, 10, 11, 12, 13], thermal transport properties [14], or the materials' suitability for thermoelectric applications

[1] The fact that the increasing trend has not been continued in 2020 can most probably ne ascribed to (i) a certain temporal delay that this database shows, or (ii) the global SARS-CoV-2 pandemic in that year.

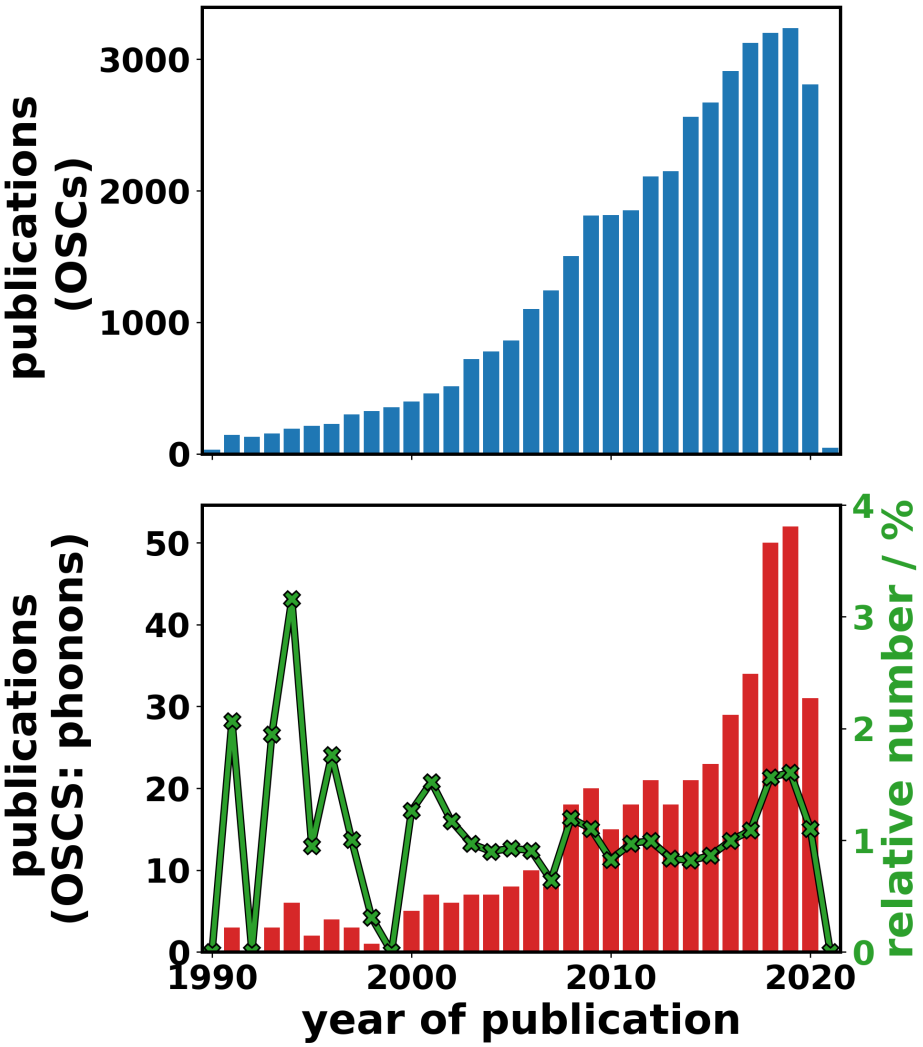

Fig. 1.1.: The top panel shows the number of publications as a function of the publication year found in *Web of Science* searching for "organic semiconductors" (accessed on 04 January 2021, 12:00). The bottom panel shows the number of publications, which can be found when additionally searching for the terms "phonons" or "vibrations". The green line indicates the number of those phonon-related relative to the total number of publications in this field.

[15, 16]. All these (transport) properties strongly depend on the given polymorphic arrangement of the molecules in the crystal: since the intramolecular bonding forces are typically much lower than the interatomic ones in inorganic semiconductors, the structural arrangement of the molecules is much more flexible leading to rich polymorphism, with the polymorphs being typically very close in energy [17, 18]. Also here, the phonon contribution to the free energy provides a useful means to consider entropy in thermodynamic stability considerations [19, 20].

It is obvious that having a profound understanding of phonons in OSCs available would lead to benefits in the engineering and designing processes of OSCs-based electronic devices such as being able to estimate the thermal conductivity of a device or getting an idea about the relevant frequency ranges of intermolecular modes, which could decrease the charge carrier mobility due to strong electron-phonon coupling. In spite of the obviously significant role that phonons play in obtaining an fundamental understanding of the physics behind the observed materials properties, comparably few publications (see bottom panel in Fig. 1.1) of the search results (searching for "organic semiconductors") additionally deal with phonons (searching for "phonons" or "vibration"). The relative share of phonon-related publications in OSCs amounts to approximately 1 % from 2010-2017 with a slightly increasing tendency in the following two years.
A possible explanation for this relatively low percentage of phonon-related publications in the field of OSCs might be the fact the complexity of OSCs poses an extreme challenge when trying to obtain the phonon band structure, which can be seen as the fundamental ingredient for all further phonon-related physical observables.
In order to experimentally measure phonon band structures, one usually relies on the method of inelastic neutron scattering, which typically require relatively large single crystals to be able to exactly know the relative orientation between the neutron source, the crystallographic axes and the detector. Single crystals of this size are, however, often difficult to grow for OSCs. Additionally, in order to decrease the incoherent neutron scattering cross section [21, 22, 23], one strives to synthesise deuterated versions of the molecules forming the OSC crystal of interest. Even if one overcame all these complications regarding sample preparation, further experimental problems persist. Typical medium-sized OSCs consist of approximately 100 atoms per (primitive) unit-cell. As a result, the entire phonon band structure will consist of approximately 300 (densely lying) bands, which exceeds the number of bands of conventional inorganic semiconductors by orders of magnitude. In addition to the experimental complexity arising from the large number of phonon bands, OSCs also tend to crystallise in low-symmetry (monoclinic, triclinic) Bravais lattices. As a consequence, one must record the phonon band structure in a large number of directions to obtain a complete picture of the entire band structure. The fact that (to the best of my knowledge) the only available experimentally obtained phonon band structure has been determined for (deuterated) naphthalene [24] can most probably be ascribed to all the mentioned experimental difficulties.
Learning about those experimental inconveniences that OSCs bring about when it comes to inelastic neutron scattering, one might immediately think, that accurate *ab initio* simulations yielding the phonon band structures render such experiments redundant.

Unfortunately, this is not fully true, since phonon calculations are also a delicate topic for which a certain amount of care must be taken. The most commonly applied approach to calculate phonon band structures is to set up the dynamical matrix of the system, which can either be done within density functional perturbation theory [25, 26] or by employing a finite-difference approach, for which the well-known *Phonopy* [27] package provides a convenient framework (more details on both approaches can be found in Sec. 2.3). Notably, the latter is also applicable for levels of theory lower in sophistication than density functional theory. This circumstance becomes important especially if one is interested in the entire phonon band structure rather than in the phonons at the centre of the first Brillouin zone, Γ. In contrast to the calculation of Γ-phonons, which are experimentally accessible from infrared or Raman spectroscopy, one needs to consider supercells for calculations of the entire phonon band structure. Supercells - i.e. integer multiples of the already large primitive unit-cells - at some point become prohibitively expensive to be considered within more sophisticated frameworks such as density functional theory (DFT).
In order to overcome the inaccessibility of phonon band structures for complex OSCs, there are two typical alternatives. First, some (negative) examples in literature neglect any phonon dispersion to calculate thermodynamic properties such as free energies and only use the Γ-phonons, which can be obtained by (computationally relatively cheap) calculations considering primitive unit-cells only [28, 29]. It will be discussed later in Sec. 2.4 (Fig. 2.1) that this approach is a very dangerous (and desperate) one, as a calculated thermodynamic property can show significant differences depending on whether one considers phonons in the entire first Brillouin zone or only the Γ-phonons.
The second possible alternative is to resort to lower levels of theory, which decrease the computational cost in exchange for a (supposed) loss of accuracy. However, there exist only few exceptional cases in literature, in which a systematic study of the influence of the simulation parameters or the used level of theory on the phonon band structure has been presented (rather than calculating band structures without knowing how the assumed approximations affect those). One of them is the paper of Brown-Altvater et al. [30], who studied the influence of various functionals and *a posteriori* van der Waals-corrections within DFT on the phonon band structure of deuterated naphthalene. In the context of this thesis, this study is extended for the same system to various levels of theory comprising DFT, density functional tight binding (DFTB) [31, 32, 33, 34], and classical force fields (FFs). Moreover, the analysis of the differences is not only limited to mere band structures but also to the observables derived from them (thermal displacements, free energies, heat capacities). This study is supposed to answer the research question of how well various methods perform in terms of their suitability for phonon calculations and which error in various derived properties one has to expect using those approximate methodologies. The majority of the presented results of this study has already been published under the title "Evaluating Computational Shortcuts in Supercell-Based Phonon Calculations of Molecular Crystals: The Instructive Case of Naphthalene" in 2020 in the Journal of Chemical Theory and Computation (`https://pubs.acs.org/doi/full/10.1021/acs.jctc.0c00119`)[1], from which most of the graphics in Sec. 4 have been taken in accordance with the American Chemical Society's

policy (`https://pubs.acs.org/pb-assets/acspubs/Migrated/dissertation.pdf`). Finally, based on the results of the above-mentioned study whether or not one can resort to lower levels of theory and still reliably calculate phonon bands, the methodology being found most suitable for this task is employed to simulate the respective band structures for a large variety of OSCs. Here, the main goal is the systematic variation of certain aspects in the atomic structures - such as the molecule length, bonding motifs, or the polymorphic arrangement of the molecules in the crystal - and to analyse potential trends in band structures and the derived properties. This study is supposed to yield first systematic insight into phonon-related structure-to-property relations in OSCs. In this context, in addition to the phonon group velocities and important thermodynamic properties such as the heat capacity and the free energy, the intermolecular (Γ-)modes are studied in more detail, as they have been found relevant for the strong electron-phonon coupling. In all cases, the differences in the derived properties can be ascribed to certain structural arguments.

Since the main interests of this thesis have been pointed out, its contents are organised as follows: in Sec. 2 the theoretical foundation is laid for understanding the details in phonon calculations. Moreover, the basic concepts of the used levels of theory (DFT, DFTB, and FFs) are briefly commented on. Next, computational details will be discussed in Sec. 3 including convergence and efficiency tests. Subsequently, in Sec. 4, an in-depth analysis of the differences in phonon band structures and phonon-derived properties for crystalline naphthalene with respect to a previously identified reference methodology is presented. The latter is found by comparison to available experimental data (lattice constants, the low-frequency phonon band structure, and the Raman spectrum). In anticipation of the detailed benchmark, one sees that the most suitable methodology to reliably produce phonon band structures is dispersion-corrected DFT because none of the tested approximate methodologies resulted in a comparable accuracy in all categories of the benchmarking part. Thus, this (relatively costly but accurate) approach is applied to a variety of organic semiconductors including oligoacenes, oligophenylenes, fluorene, pyrene, and (polymorphs of) quinacridone and rubrene. After the discussion of the similarities and differences in the calculated phonon band structures of the considered bulk OSCs, a few results concerning derived properties are presented comprising an analysis of phonon group velocities, (phonon contributions to) the free energies and the heat capacities. Finally, the most important results of this thesis are summarised in Sec. 6.

2. Theoretical Background

As the main focus of interest of this thesis lies on phonons, the quasiparticles of atomic motion, it is essential to theoretically understand where those quasiparticles come from, how they affect the thermodynamics of a crystal and by which means one can practically obtain the required ingredients from *ab-initio* simulations to calculate phonon-related properties. The here presented concise summary of the most relevant properties and formulations has been inspired by several books and articles, mostly by Refs. [7, 27, 35, 36, 37].

2.1. The Born-Oppenheimer Approximation

The following considerations and equations in this subsection are based on Ref. [35]. Before one can define a phonon, one must go one step back and - as usual in non-relativistic quantum mechanics - look at the time-independent Schrödinger equation (i.e. the eigenvalue equation of the Hamilton operator $\widehat{H}$ with eigenvalue E):

$$\widehat{H}\Psi = E\Psi \tag{2.1}$$

In this equation, Ψ is the wave function, a complex-valued object depending on as many (Cartesian) coordinates as there are particles - in general all the electrons and the bare nuclei (atomic number Z) - in the system: $\Psi = \Psi(\mathbf{r}_1, \mathbf{r}_2, \ldots, \mathbf{r}_n, \mathbf{R}_1, \mathbf{R}_2, \ldots, \mathbf{R}_m)$, with $\mathbf{r}_i$ ($\mathbf{R}_i$) being the Cartesian position vector of the i^{th} electron (nucleus). In the absence of external perturbations such as electromagnetic fields, the Hamiltonian can be written as the sum of the kinetic energy of the electrons $\widehat{T}_e$ and that of the nuclei $\widehat{T}_N$ as well as the (local) interactions among the electrons $\widehat{V}_{e-e}$, among the nuclei $\widehat{V}_{N-N}$ and between nuclei and the electrons $\widehat{V}_{e-N}$ [35]:

$$\begin{aligned}
\widehat{H} &= \widehat{T}_N + \widehat{T}_e + \hat{V}_{e-e} + \widehat{V}_{N-N} + \widehat{V}_{e-N} && (2.2)\\
&= -\frac{\hbar^2}{2}\sum_A \frac{\nabla_A^2}{m_A} - -\frac{\hbar^2}{2m_e}\sum_i \nabla_i^2 + \\
&+ \sum_{i<j} \frac{e^2}{4\pi\varepsilon_0 \left\|\mathbf{r}_i - \mathbf{r}_j\right\|} + \sum_{A<B} \frac{Z_A Z_B e^2}{4\pi\varepsilon_0 \left\|\mathbf{R}_A - \mathbf{R}_B\right\|} - \sum_{i,A} \frac{Z_A e^2}{4\pi\varepsilon_0 \left\|\mathbf{r}_i - \mathbf{R}_A\right\|} && (2.3)
\end{aligned}$$

Since, except, for the last term in the many-body Hamiltonian shown in Eq. (2.2), the differential equation for electronic and atomic coordinates are decoupled, one can arrive at a simplification of this problem by making use of the physically motivated argument that the electron mass, m_e, is much less than the mass of the nuclei. Thus, the motion of the nuclei and that of the electrons typically happens on a different time scale. As a result, the electrons can follow the atomic motion instantaneously, which makes the atomic positions parameters rather than variables for the electronic problem[2]. Thus, one can reformulate the problem as:

[2] All the potential energy terms have been condensed in the operator $\widehat{V}$.

$$\left(\widehat{T}_e + \hat{V}\right) \Phi_l \left(\{\mathbf{r}\}_n | \{\mathbf{R}\}_m\right) = W_l(\{\mathbf{R}\}_m) \Phi_l \left(\{\mathbf{r}\}_n | \{\mathbf{R}\}_m\right) \tag{2.4}$$

Here, the eigenvalue of this equation, $W_l(\{\mathbf{R}\}_m)$, is the original eigenvalue E plus terms depending on a given configuration of the atomic coordinates, which enter this equation only as parameters, but are not solved for any more. This is the basic idea of the *Born-Oppenheimer approximation*. Mathematically, one can arrive at the meaning of this approximation by making the following ansatz for the wave function:

$$\Psi \left(\{\mathbf{r}\}_n, \{\mathbf{R}\}_m\right) = \sum_l \chi_l(\{\mathbf{R}\}_m) \Phi_l \left(\{\mathbf{r}\}_n | \{\mathbf{R}\}_m\right) \tag{2.5}$$

In other words, the many-body wave function is expanded in terms of expansion coefficients, χ_l, which, however, still depend on the atomic positions. Substituting the electronic kinetic energy and the potential by the "new" eigenvalue W_l (Eq. (2.4)) for a given set of atomic coordinates as well as inserting the ansatz of Eq. (2.5) above in the original problem (Eq. (2.2)), multiplying with Φ_n^* from the left and integrating over all electronic coordinates, one finds

$$\left(\widehat{T}_N + W_l(\{\mathbf{R}\}_m) - E\right) \chi_l \left(\{\mathbf{R}\}_m\right) = \sum_{lk} \Lambda_{lk} \chi_k \left(\{\mathbf{R}\}_m\right) \tag{2.6}$$

One can show that the matrix elements Λ_{lk} are given by the following equation:

$$\Lambda_{lk} = \sum_A \frac{\hbar^2}{M_A} \int d\mathbf{r}_1 d\mathbf{r}_2 \cdots d\mathbf{r}_n \left\{ \Phi_l^* \left[\frac{\partial}{\partial \mathbf{R}_A} \Phi_k \right] \frac{\partial}{\partial \mathbf{R}_A} + \Phi_l^* \frac{\partial^2}{\partial \mathbf{R}_A^2} \Phi_k \right\} \tag{2.7}$$

It is important to note, that mathematically no approximation has been made to arrive at Eq. (2.6) since all the steps only resulted in a rewritten form of the original problem by introducing expansion coefficients χ_l and the matrix Λ_{lk}. Mathematically, the Born-Oppenheimer approximation is equivalent to neglecting this matrix and demanding that $\Lambda_{lk} = 0 \; \forall l, k$. In that way, the electronic part is described by Eq. (2.4), while the atomic part is approximated by the following equation:

$$\left(\widehat{T}_N + W_l(\{\mathbf{R}\}_m)\right) \chi_l \left(\{\mathbf{R}\}_m\right) = E \chi_l \left(\{\mathbf{R}\}_m\right) \tag{2.8}$$

2.2. The Potential-Energy Surface

It turns out that the term $W_l \left(\{\mathbf{R}\}_m\right)$) is the potential energy of the nuclei determined by the electrons in a fixed atomic configuration, typically referred to as the "potential energy surface" (PES). The PES is key to understanding the quantised atomic motion in a quantum mechanical system. This can be understood by expanding the PES in a Taylor series in terms of the atomic displacements defined by being the difference between the α^{th} Cartesian component of the position vector of atom i and the equilibrium position indicated by an additional subindex 0. The ideas presented in the following are based

on Ref. [36] with slight adaptations having been made in terms of the notation to be consistent with previous expressions.

$$u_i^\alpha = R_i^\alpha - R_{i,0}^\alpha \tag{2.9}$$

By carrying out the multi-dimensional Taylor expansion, one obtains the following expression for the PES:

$$W = W_0 + \frac{1}{2}\sum_{\alpha,\beta}\sum_{i,j}\frac{\partial^2 W}{\partial u_i^\alpha \partial u_j^\beta}u_i^\alpha u_j^\beta + \frac{1}{3!}\sum_{\alpha,\beta,\gamma}\sum_{i,j,k}\frac{\partial^3 W}{\partial u_i^\alpha \partial u_j^\beta \partial u_k^\gamma}u_i^\alpha u_j^\beta u_k^\gamma + \dots \tag{2.10}$$

As the expansion is carried out around the minimum of the PES - i.e. at the energetic equilibrium of the atomic configuration - the first-order terms vanishes due to the vanishing gradients of the hypersurface at the minimum. The second-order term is of special importance for practical vibrational calculations, as the Taylor series is typically truncated after this term. Neglecting all higher order terms is the so-called harmonic approximation, in the framework of which vibrational frequencies and phonon band dispersions are usually calculated.
The harmonic approximation is convenient for two reasons:

1. In the harmonic approximation, the vibrations are assumed to lack any interaction with each other. Thus, the problem essentially reduces to many independent one-dimensional[3] quantum-mechanical harmonic oscillators (for which detailed discussions can be found in many text books such as in Ref. [7]) of the form

$$\left(-\frac{\hbar^2}{2M}\frac{d^2}{dx^2} + \frac{C}{2}x^2\right)\psi(x) = E\psi(x) \tag{2.11}$$

   with a force constant C, the oscillator mass M, and the well-known equally-spaced eigenenergies

$$E_n = \hbar\omega\left(n + \frac{1}{2}\right) \qquad \text{with } \omega^2 = \frac{C}{M},\ n \in \mathbb{N}^0 \tag{2.12}$$

   and the eigenfunctions being related to Hermite's polynomials.

2. The second reason is more of technical nature. Since one is typically able to get hold of the second derivatives of the PES for systems with a small enough number of atoms, the higher-order terms become prohibitively difficult to obtain because of the combinatorial explosion.

For mainly those two reasons, first-principles vibrational calculations are nearly exclusively carried out in the context of the harmonic approximation, which approximates the real potential energy surface by means of its second derivative near the equilibrium:

[3] Here, the coordinate x is used for the variable of the wave function $\psi(x)$ and the harmonic potential $\propto x^2$.

$$W \approx \frac{1}{2}\sum_{\alpha,\beta}\sum_{i,j}\frac{\partial^2 W}{\partial u_i^\alpha \partial u_j^\beta}u_i^\alpha u_j^\beta = \frac{1}{2}\sum_{\alpha,\beta}\sum_{i,j}C_{ij}^{\alpha\beta}u_i^\alpha u_j^\beta \tag{2.13}$$

Note that in the last part of the equation above, the second derivatives have been replaced by the matrix of force constants ("Hessian matrix") $C_{ij}^{\alpha\beta}$.

2.3. Phonons and the Dynamical Matrix

In crystalline systems, the vibrations can be more conveniently described by making use of Bloch's theorem due to the periodic boundary conditions. For reasons of transparency, here an additional index (capital letters) is added to the atomic displacements to label the unit-cell in the crystal. Similarly, two unit-cell indices (A, B) must be added to the force-constant tensor:

$$u_i^\alpha \rightarrow u_i^\alpha(A) \tag{2.14}$$

$$C_{ij}^{\alpha\beta} \rightarrow C_{ij}^{\alpha\beta}(A,B) \tag{2.15}$$

The following derivation of the central quantity in lattice dynamics, the dynamical matrix, is based on the ideas found in Ref. [7]. Some of the mathematical steps are, however, presented more slowly to make them more comprehensible. Prior to being able to calculate the (thermally occupied) vibrations being present in the system and the thermodynamic properties resulting from those, one must obtain the knowledge of the allowed vibrational states. In analogy to the one-dimensional mass-spring system, whose eigenfrequency is given by the square root of the spring constant over the mass, one chooses a classical way to solve for the possible frequencies in the crystal by solving the Newtonian equation of motion for atom i in Cartesian direction α:

$$m_i \ddot{u}_i^\alpha(A) = -\sum_{j,\beta,B} C_{ij}^{\alpha\beta}(A,B)u_j^\beta(B) \tag{2.16}$$

These equations of motions can be solved by making a plane-wave ansatz (with angular frequency ω and wave vector $\mathbf{q}$, which is proportional to the momentum of the plane wave) according to the following equation.

$$u_i^\alpha(A) = \frac{e_i^\alpha}{\sqrt{m_i}}\exp\left\{\mathrm{i}\left(\omega t - \mathbf{q}\cdot\mathbf{R_A}\right)\right\} \tag{2.17}$$

Including the masses in the amplitudes of the plane waves turns out to be a convenient choice as it allows for a consistent way of considering them in the band structure calculations, as will be obvious very soon. Please note that there exists also an alternative ansatz differing in the argument of the exponential function. Here, the physically more motivated approach of the unit-cell vector $\mathbf{R_A}$ (pointing to unit-cell A) is chosen. The other convention is to use the absolute atomic position $\mathbf{R_{i,A}} = \mathbf{r_i} + \mathbf{R_A}$. Both conventions only differ in a phase factor that does not play a role for expectation values as long as the same convention is consistently used.

Inserting this ansatz in the Newtonian equation of motion, one can solve for the amplitudes e_i^α:

$$-\omega^2\sqrt{m_i}e_i^\alpha \exp\left\{\mathrm{i}\left(\omega t - \mathbf{q}\cdot\mathbf{R_A}\right)\right\} =$$

$$\begin{aligned}
&= -\sum_{j,\beta,B} C_{ij}^{\alpha\beta}(A,B)\frac{e_j^\beta}{\sqrt{m_j}} \exp\left\{\mathrm{i}\left(\omega t - \mathbf{q}\cdot\mathbf{R_B}\right)\right\} \\
\omega^2 e_i^\alpha &= \sum_{j,\beta}\left(\sum_B \frac{1}{\sqrt{m_i m_j}} C_{ij}^{\alpha\beta}(A,B)\exp\left\{-\mathrm{i}\mathbf{q}\cdot\left(\mathbf{R_B}-\mathbf{R_A}\right)\right\}\right) e_j^\beta \\
\omega^2 e_i^\alpha &= \sum_{j,\beta}\left(\sum_B \frac{1}{\sqrt{m_i m_j}} C_{ij}^{\alpha\beta}(0,B)\exp\left\{-\mathrm{i}\mathbf{q}\cdot\mathbf{R_B}\right\}\right) e_j^\beta \\
\omega^2 e_i^\alpha &= \sum_{j,\beta} D_{ij}^{\alpha\beta}(\mathbf{q}) e_j^\beta \qquad (2.18)
\end{aligned}$$

Where in the second last line it has been exploited that for the force constants between two atoms, only the relative distances are relevant. Thus, one can constrain one's considerations only relative to one "central" unit-cell 0 instead of arbitrary ones A. One sees that due to the homogeneity of the differential equations, the periodic boundary conditions and the harmonic potential, one arrives at an eigenvalue equation of a matrix $D_{ij}^{\alpha\beta}$, with the squared frequencies being the eigenvalues of this so-called *dynamical matrix*. The eigenvectors of the dynamical matrix, e_i^α, are related to the polarisation of a given phonon mode and have the dimension of length times square root of mass. In order to convert those vectors to real-space atomic displacements, one must make use of Eq. (2.17).

Before some properties of the dynamical matrix are discussed, it should be briefly commented on how to actually set up the dynamical matrix, from which directly the dispersion relation $\omega(\mathbf{q})$ and the polarisation of each phonon mode at each wave vector $\mathbf{q}$ follow. In principle, there are two possible approaches to construct the dynamical matrix of a system:

1. Real-space approach: One approach, which is the one that has been consistently utilised throughout this thesis, is based on the idea of calculating the real-space force constant matrices $C_{ij}^{\alpha\beta}(0,B)$. Having this object available means that one can carry out a Fourier transform of the (mass-weighted) force constant tensor to transform from real-space coordinates to the reciprocal-space quantity, $\mathbf{q}$, the wave vector. That means, if one happens to have enough force constants available to make the (infinite!) sum in the definition of the dynamical matrix converge, every wave vector is directly accessible. In other words, the information about the wave vector and, thus, the phonon dispersion, is only accessible if force constants beyond the primitive unit-cell are available. This procedure is somewhat different to typical electronic structure calculations in periodic systems, for which contributions for each (electronic) wave vector $\mathbf{k}$ must be computed separately. Here, the entire

first Brillouin zone is directly accessible if the dynamical matrix is converged. The only challenge in this approach is obtaining enough force constants $C_{ij}^{\alpha\beta}(0, B)$ - i.e. by considering enough unit-cells B in your crystal by means of a supercell containing sufficiently many unit-cells - to achieve that. This can be very difficult for systems with long-range interactions as one might end up in a situation in which the required number of unit-cells (i.e. the size of the supercell) to converge the dynamical matrix exceeds the capabilities of the (quantum mechanical) simulation program to calculate the real-space force constants.
Many available code packages such as *VASP* [38, 39, 40, 41] allow built-in calculations of the force constants in real-space. A completely code-independent framework for this approach is, however, provided by the *Phonopy* package [27]. The latter is a convenient tool to facilitate the calculation of the real-space force constants by means of finite differences. In other words, the actual gradients in the definition of the harmonic force constants are approximated via finite differences. First of all, it is necessary to understand, which quantities must really be extracted from a simulation to obtain the force constants. This can be seen by evaluating the definition of the force constants tensor:

$$C_{ij}^{\alpha\beta}(0, B) = \frac{\partial^2 W}{\partial u_i^\alpha(0) \partial u_j^\beta(B)} = -\frac{\partial F_j^\beta(B)}{\partial u_i^\alpha(0)} \tag{2.19}$$

Here it has been used that the derivative of the PES with respect to the displacement $u_j^\beta(B)$ can be interpreted as the force on atom j in unit-cell B in Cartesian direction β. What one is interested in is, thus, the change in the forces in the crystal/supercell as a result of atomic displacement. This last derivative is subsequently approximated via a finite difference scheme, typically via a central difference quotient:

$$\frac{\partial F_j^\beta(B)}{\partial u_i^\alpha(0)} = \frac{F_j^\beta(B)\{+u_i^\alpha(A)\} - F_j^\beta(B)\{-u_i^\alpha(A)\}}{2\Delta u_i^\alpha(0)} + \mathcal{O}\left((\Delta u_i^\alpha(A))^2\right) \tag{2.20}$$

Therefore, for this scheme, one needs to calculate the atomic forces in the supercell as a result of a positive and a negative displacement of one atom in the "central" unit-cell in each Cartesian direction. As a result, one must carry out $2\times3\times N = 6N$ force calculations[4] of supercells with single displaced atoms. Fortunately, except for systems with the space group $P1$, there are certain symmetries present under which the geometry is invariant. One can exploit the symmetries of the given space group to considerably decrease the number of necessary symmetry-inequivalent displacement to fully set-up the force constant tensor.

Finally, it should be noted that, while in this approach one can obtain the dynamical matrix $D(\mathbf{q})$ for all wave vectors $\mathbf{q}$ in the first Brillouin zone by means of Fourier interpolation, for certain wave vectors - so-called commensurate wave

[4] $3N$ is the number of degrees of freedom per unit-cell. The factor of 2 arises from the used finite difference scheme relying on the central difference quotient.

vectors - no Fourier interpolation is required [42]. Instead, the frequencies of those commensurate **q**-points are obtained correctly - even if the dynamical matrix is not converged yet for all wave vectors. The condition for commensurate **q**-points is the following:

$$\left(P^T\right)_{ij} q_j \in \mathbb{Z} \; \forall i \tag{2.21}$$

Here, **q** is the reduced wave vector (i.e. in units of the reciprocal lattice vectors; in the first Brillouin zone: $|q_i| \leq \frac{1}{2}$), while P refers to the matrix used to generate the supercell (lattice column vectors with subscript S) based on the (primitive) unit-cell (lattice column vectors with subscript P):

$$\begin{aligned} \left[\left(\mathbf{a_S}\right), \left(\mathbf{b_S}\right), \left(\mathbf{c_S}\right)\right] &= \left[\left(\mathbf{a_P}\right), \left(\mathbf{b_P}\right), \left(\mathbf{c_P}\right)\right] \mathbf{P} \\ A^S_{ij} &= A^P_{ik} P_{kj} \end{aligned} \tag{2.22}$$

According to Eq. (2.21), only certain **q**-points (depending on P) are commensurate and, thus, obtained *exactly* without interpolation. For example, if one considers a diagonal matrix P with $[2, 3, 4]$ on its diagonal, the following wave vectors are commensurate: $q_1 \in \left\{0, \pm\frac{1}{2}\right\} \wedge q_2 \in \left\{0, \pm\frac{1}{3}\right\} \wedge q_3 \in \left\{0, \pm\frac{1}{4}, \pm\frac{1}{2}\right\}$. This is a direct consequence of the "backfolding" of the bands at the boundaries of the first Brillouin zone, due to the larger unit-cell and the smaller first Brillouin zone, respectively [7].

2. Reciprocal-space approach: The alternative approach is not based on the calculation of the real-space force constants, but is directly capable of computing the reciprocal-space force constants (i.e. the dynamical matrix) at a given wave vector by means of perturbation theory. In the framework of density functional theory (DFT), this perturbative approach is called density functional perturbation theory (DFPT) [26]. Exploiting DFPT, there is no need for supercells at all. The dynamical matrix can be computed by a sequence of several perturbation calculations for each **q**-point separately. Although one spares oneself the large system sizes with this approach, the disadvantage is that one must consider each wave vector separately. This means, that one has absolutely no information about any **q**-point that has not been explicitly set in the perturbation calculations before. To circumvent this issue, codes like *QUANTUM ESPRESSO* [43, 44, 45] or *ABINIT* [46, 47, 48] have the following trick implemented:

$$\mathbf{D}(\mathbf{q}_i) \xrightarrow{IFT} \mathbf{C}(0, B) \xrightarrow{FT} \mathbf{D}(\mathbf{q}) \tag{2.23}$$

This means they carry out DFPT calculations for a set of discrete wave vectors $\mathbf{q}_i$ such that they can perform an inverse Fourier transform (IFT) to retrieve the real-space force constants $\mathbf{C}(0, B)$. If the original mesh of sampled wave vectors $\mathbf{q}_i$ was dense enough, the IFT yields force constants for a virtual supercell (which, however, has not really been considered during the DFT calculations), which can

now be used to calculate the dynamical matrix for every desired wave vector $\mathbf{q}$ by means of a Fourier transform (FT). This scheme is particularly efficient for highly symmetric systems, for which one must calculate only a few discrete wave vectors which can, subsequently, yield a denser mesh of symmetry-equivalent ones improving the convergence behaviour of the (I)FT.

Since the reader now understands how to construct the dynamical matrix in practice, one should notice some properties of this object. First of all, it can be shown that the dynamical matrix is hermitian [36]:

$$\begin{aligned} D_{ij}^{\alpha\beta}(\mathbf{q}) &= \sum_B \frac{1}{\sqrt{m_i m_j}} C_{ij}^{\alpha\beta}(0,B) \exp\{-\mathrm{i}\mathbf{q}\mathbf{R_B}\} = \\ &= \sum_B \frac{1}{\sqrt{m_i m_j}} C_{ji}^{\beta\alpha}(B,0) \exp\{-\mathrm{i}\mathbf{q}\mathbf{R_B}\} = \\ &= \sum_B \frac{1}{\sqrt{m_i m_j}} C_{ji}^{\beta\alpha}(0,-B) \exp\{+\mathrm{i}\mathbf{q}\mathbf{R_B}\} = \\ &= D_{ij}^{\beta\alpha\ *}(\mathbf{q}) = \left(D^\dagger\right)_{ij}^{\alpha\beta}(\mathbf{q}) \end{aligned} \tag{2.24}$$

Where in the second line it has been used that $C_{ij}^{\alpha,\beta}(0,B) = C_{ji}^{\beta\alpha}(B,0)$, which follows from the invariance of the order of differentiation of the PES (see Eq. (2.13)). The third line results from the fact that only the relative distance of atoms in a crystal is relevant, thus, one can arbitrarily exchange the position of the "central" unit-cell 0 with a cell labelled with B. As a result, the vector that points from the central unit-cell to B changes its sign so that the sign of the exponent changes. Finally, as we sum over all unit cells B, one can simply relabel them with B instead of $-B$, which yields the complex conjugate transposed dynamical matrix.
The fact that $\mathbf{D}$ is hermitian for fixed wave vector is an important result because it means that all its eigenvalues ω_λ^2 are real-valued and its eigenvectors form an orthonormal base. In bra-ket notation this can be written as follows:

$$\mathbf{D}\left|\mathbf{e}_\lambda\right\rangle = \omega_\lambda^2 \left|\mathbf{e}_\lambda\right\rangle \tag{2.25}$$

$$\left\langle\mathbf{e}_\mu\right|\mathbf{D}\left|\mathbf{e}_\lambda\right\rangle = \omega_\lambda^2 \left\langle\mathbf{e}_\mu|\mathbf{e}_\lambda\right\rangle = \omega_\lambda^2 \delta_{\mu\lambda} \tag{2.26}$$

With $\delta_{\mu\lambda}$ being the Kronecker delta. Furthermore, the dynamical matrix is positive semi-definite, which means that all eigenvalues are ≥ 0. This is an important result because it implies that all frequencies in a system at equilibrium are real-valued and greater or equal to zero (if one omits negative-valued frequencies):

$$\omega_\lambda^2 \geq 0, \omega_\lambda^2 \in \mathbb{R} \Rightarrow \omega_\lambda \geq 0, \omega_\lambda \in \mathbb{R} \tag{2.27}$$

The equality in the above inequality can be found at the centre of the first Brillouin zone, Γ ($\mathbf{q} = \mathbf{0}$). To show this mathematically, we need to physically demand that the

energy of the system does not change along the displacements of the acoustic modes at Γ - i.e. a rigid translation of the system must not affect its energy. The eigendisplacement of such a rigid translation has the same entry e.g. for each x-position of each atoms such that it corresponds to a rigid translation in e.g. x-direction. The unnormalised, $3N$-dimensional eigendisplacement vector for an acoustic mode in x-direction would, thus, look like:

$$\mathbf{u} = [1, 0, 0, 1, 0, 0, 1, 0, 0, \ldots, 1, 0, 0] \tag{2.28}$$

The corresponding eigenvector, however, must include the respective atomic masses according to its dimension:

$$\mathbf{e} = [\sqrt{m_1}, 0, 0, \sqrt{m_2}, 0, 0, \sqrt{m_3}, 0, 0, \ldots, \sqrt{m_3}, 0, 0] \tag{2.29}$$

If one multiplies such an eigenvector with the dynamical matrix at Γ, one obtains:

$$\mathbf{D}\,|\mathbf{e}\rangle = \sum_{j,B} \frac{1}{\sqrt{m_i m_j}} C_{ij}^{\alpha\beta}(0, B)\sqrt{m_j} = \sum_{j,B} \frac{1}{\sqrt{m_i}} C_{ij}^{\alpha\beta}(0, B) = \omega^2\,|\mathbf{e}\rangle \tag{2.30}$$

Since the energy of the system must not change upon this kind of displacement, the frequency ω must be zero, i.e. the right-hand side of the equation above vanishes. Thus, one can multiply the equation by $\sqrt{m_i}$ and find the so-called acoustic sum rule (ASR):

$$\sum_{j,B} C_{ij}^{\alpha\beta}(0, B) = 0 \Longleftrightarrow -\sum_{(j,B)\neq(i,0)} C_{ij}^{\alpha\beta}(0, B) = C_{ii}^{\alpha\beta}(0, 0) \tag{2.31}$$

The ASR are, therefore, a consequence of the translational invariance of the crystal and show that the sum of force constants between one atom i and all the other atom in the crystal (atom index j and unit-cell index B) must vanish. Equivalently, one can exclude the the element $C_{ii}^{\alpha\beta}(0, 0)$ from this sum and carry out the summation over all remaining terms, as it is written in the right part of the equation above. This element is the force constant (matrix $\alpha\beta$) of an atom i with itself, which is - according to the equation - equivalent to the negative sum of all force constants between atom i and every other atom (j, B) in the crystal. For that reason, in the following context, such force constants will be referred to as "self-harmonic force constants" (SHFCs) as they measure the total interaction of an atom with itself (equalling the sum of interactions with all the others).

An important property of the dynamical matrix is that it can be analytically expressed in terms of the wave vector. This fact offers a convenient way to compute the phonon group velocity - i.e. the gradients of the phonon band dispersion [7]:

$$\mathbf{v}_{\mathbf{g}\lambda} = \nabla_{\mathbf{q}}\omega_\lambda \tag{2.32}$$

The group velocity, being the **q**-derivative of the frequency, corresponds to the velocity with which a wave packet of plane waves travels inside a (dispersive) material. This quantity is especially important for phonon transport properties as it defines the time scale at which the quasiparticles of lattice vibrations are capable to transfer heat through the crystal.

The most straightforward way to compute the group velocities would, obviously, be to calculate the frequencies at very fine meshes and compute the derivatives from finite differences at each point. This strategy would, however, require relatively dense **q**-meshes to reduce the numerical error and a thorough treatment of bands near problematic regions such as avoided crossings. A much more versatile and useful alternative is provided by using the spectral theorem [49]. In case of the dynamical matrix, the spectral theorem relates a function f of the dynamical matrix to a function of its eigenvalues ω_λ^2:

$$f\left(\omega_\lambda^2\right) = \langle \mathbf{e}_\lambda | \, f\left(\mathbf{D}\right) | \mathbf{e}_\lambda \rangle \tag{2.33}$$

Using the spectral theorem, one can directly calculate the group velocity at a given wave vector with the aid of the **q**-gradient of the dynamical matrix[5]:

$$\mathbf{v}_{\mathbf{g}_\lambda} \;=\; \frac{1}{2\omega_\lambda} \langle \mathbf{e}_\lambda | \, \nabla_\mathbf{q} \mathbf{D} \, | \mathbf{e}_\lambda \rangle \tag{2.34}$$

The only problem with this definition is that the group velocity diverges for the three acoustic bands at Γ, for which the frequencies vanish. In practice, the group velocities at Γ are, however, defined to be zero for every band - also for the acoustic ones. This choice of setting the group velocities to zero for the acoustic bands has its origin in the fact that near Γ, the band dispersion is comparable to a multidimensional cone - i.e. with a linear band dispersion like $c_\mathbf{q}\|\mathbf{q}\|$, with $c_\mathbf{q}$ being an anisotropic sound velocity. Thus, this cone has a distinct cusp at $\mathbf{q} = \mathbf{0}$, where the dispersion relation cannot be continuously differentiated: depending on whether one approaches Γ from one side ($\mathbf{q} \to \mathbf{0}^+$) or the other ($\mathbf{q} \to \mathbf{0}^-$) the derivative is $\pm c_\mathbf{q}$. For this mathematical reason as well as for the fact that at Γ, the phonons do not correspond to propagating waves, but rather to oscillations, the group velocities at the centre of the first Brillouin zone are set to zero for every band.
The derivative of the dynamical matrix with respect to **q** needed for the expression of the group velocity can either be calculated numerically from small differences[6] in the wave vector $\mathbf{q} \pm \delta\mathbf{q}$ or from the analytical expression of the gradient, which is the state-of-the-art way:

$$\nabla_\mathbf{q} D_{ij}^{\alpha\beta}(\mathbf{q}) = \sum_B \frac{-\mathrm{i}\mathbf{R_B}}{\sqrt{m_i m_j}} C_{ij}^{\alpha\beta}(0, B) \exp\left\{-\mathrm{i}\mathbf{q}\mathbf{R_B}\right\} \tag{2.35}$$

Besides the group velocities and the frequencies, one can also make use of the eigenvectors of the dynamical matrix in many ways. The most obvious one is the calculation of the real-space representation of the atomic motion corresponding to one of the modes

[5] $\nabla_\mathbf{q}\omega_\lambda^2 = 2\omega_\lambda \nabla_\mathbf{q}\omega_\lambda = 2\omega_\lambda \mathbf{v}_{\mathbf{g}_\lambda} \Rightarrow \mathbf{v}_{\mathbf{g}_\lambda} = (2\omega_\lambda)^{-1} \nabla_\mathbf{q}\omega_\lambda^2$

[6] This approach was the historically earlier one implemented in *Phonopy*. Although it is more robust than the direct calculation of the gradients of the bands as it is not affected by avoided crossings, it still shows the drawback of having the need to calculate the dynamical matrix at **q**, $\mathbf{q} + \delta\mathbf{q}$, and $\mathbf{q} - \delta\mathbf{q}$ in order to compute the group velocities at **q**.

(band index n) by using Eq. (2.17) or for the static representation, i.e. the so-called eigendisplacement:

$$\eta^{\alpha}_{i,(n,\mathbf{q})}(A) = \frac{1}{H}\frac{e^{\alpha}_{i,(n,\mathbf{q})}}{\sqrt{m_i}}\exp\left\{-\mathrm{i}\mathbf{q}\cdot\mathbf{R_A}\right\} \tag{2.36}$$

By calculating $\eta^{\alpha}_{i,(n,\mathbf{q})}(A)$, one obtains (real-space) insight into the nature of a phonon mode $(n, \mathbf{q})$ and which atomic displacement from the equilibrium position it generates for atom i in unit-cell A in the Cartesian direction α. In other words, the actual real-space representation of a phonon mode is not the eigenvector, but the eigendisplacements. Typically, the normalisation constant H is chosen such that the eigendisplacements are normalised $\sum_{j,\alpha}\left|\eta^{\alpha}_{j,(n,\mathbf{q})}\right|^2 = 1$. This means that one needs H to be determined from the following equation:

$$H = \sum_{i,\alpha}\left|\frac{e^{\alpha}_{i,(n,\mathbf{q})}}{\sqrt{m_i}}\right|^2 \tag{2.37}$$

With the (properly normalised) eigendisplacements, one can define so-called normal mode coordinates, $Q_{(n,\mathbf{q})}$, which are the coefficients of an arbitrary set of atomic displacements, u^{α}_i, expressed in the basis of the eigendisplacements, $\eta^{\alpha}_{j,(n,\mathbf{q})}$:

$$u^{\alpha}_i(A) = \mathrm{Re}\sum_{n,\mathbf{q}} Q_{(n,\mathbf{q})}\eta^{\alpha}_{i,(n,\mathbf{q})} \tag{2.38}$$

In other words, the above equation represents a coordinate transformation from the $3N$-dimensional Cartesian space to the space spanned by the normal modes of the $3N$ bands (per unit-cell and $\mathbf{q}$-point, respectively). Thus, the actual amplitude (and also the time dependence) of atomic motion can conveniently be included in the normal mode coordinate Q.
The concept of normal mode coordinates is a relatively practical one, as it not only allows to express every displacement from the equilibrium in terms of phonon mode displacements, but also has some interesting mathematical consequences as pointed out in Ref. [50]. For example, one can define the entire equations of lattice dynamics in normal mode coordinates based on the finding that the equation of motion formulated not in Cartesian but in normal mode coordinates are uncoupled (if no higher order expansions of the PES are considered). This results in one mutually independent one-dimensional harmonic oscillator equation for every band n and every wave vector $\mathbf{q}$ with the following Hamiltonian [37]:

$$\widehat{H}_{n,\mathbf{q}} = \left(-\frac{\hbar^2}{2\mu_{n,\mathbf{q}}}\frac{\partial^2}{\partial Q^2_{n,\mathbf{q}}} + \frac{\Phi_{n,\mathbf{q}}}{2}Q^2_{n,\mathbf{q}}\right) \tag{2.39}$$

In this Hamiltonian, the mass is replaced by the effective mass of the mode - i.e. the measure of inertia of a given phonon - which can be calculated from the eigenvectors

according to the following equation [51]:

$$\mu_{n,\mathbf{q}} = \frac{\sum_i^N m_i \left\|\mathbf{u}^i_{n,\mathbf{q}}\right\|^2}{\sum_i^N \left\|\mathbf{u}^i_{n,\mathbf{q}}\right\|^2} = \frac{\sum_i^N \left\|\mathbf{e}^i_{n,\mathbf{q}}\right\|^2}{\sum_i^N m_i^{-1} \left\|\mathbf{e}^i_{n,\mathbf{q}}\right\|^2} \tag{2.40}$$

Here, $\|.\|$ indicates the (complex) vector norm of the three-component vector for each atom, i.e. the sqare-root of the sum of the absolute values squared.
The other parameter appearing in the Hamiltonian above is the effective mode force constant $\Phi_{n,\mathbf{q}}$, which represents the stiffness of a given phonon mode. This quantity can be replaced by using the effective mass and the corresponding frequency - equivalent to the classical case.

$$\Phi_{n,\mathbf{q}} = \omega^2_{n,\mathbf{q}} \mu_{n,\mathbf{q}} \tag{2.41}$$

Finally, a last important quantity that can be calculated from the eigenvectors of the dynamical matrix is the so-called participation ratio (PR) of a mode [52, 53, 54]. As defined in the following equation, the PR is a scalar quantity ranging between N^{-1} and 1, and measures the degree of participation of the atoms in the crystal - and, thus the localisation - in one given phonon mode.

$$\mathrm{PR}_{n,\mathbf{q}} = \frac{\left(\sum_{i=1}^N \sum_{\alpha=1}^3 \frac{\left|\mathbf{e}^\alpha_{i,(n,\mathbf{q})}\right|^2}{m_i}\right)^2}{N \left(\sum_{i=1}^N \sum_{\alpha=1}^3 \frac{\left|\mathbf{e}^\alpha_{i,(n,\mathbf{q})}\right|^4}{m_i^2}\right)} \tag{2.42}$$

One can, for example, quite easily see that for an acoustic mode in x-direction at Γ, for which every value $\left|\mathbf{e}^{\alpha=x}_{i,(n,\mathbf{q})}\right|^2 / m_i$ equals one common value ξ, the numerator equals $(N\xi)^2$. The sum in the denominator amounts to $N\xi^2$, which cancels the numerator considering the additional factor N in front of the sum. Thus, for such a mode, in which every atom contributes to the same extent, the PR equals 1.
Conversely, if only one element in the eigenvector does not vanish, the numerator amounts to ξ^2, while the denominator equals $N\xi^2$, resulting in the lowest possible PR $= 1/N$. Therefore, the PR is a convenient measure to quantify the degree of (de)localisation of a given phonon mode. Here, a phonon mode is said to be localised if only a few atoms in the crystal participate in the motion of the mode, while delocalised modes are characterised by a large number of atoms moving. Although the PR has originally been used to describe the degree of phonon localisation in amorphous systems, it also turns out to be a useful quantity to distinguish inter- and intramolecular phonon modes, as will be discussed in Sec. 5.

2.3.1. Anharmonicities in a nutshell

Although anharmonic properties have not really been covered in this theses except for a tiny remark in Sec. 3.1.1, it is still beneficial to understand a few basic concepts in

the framework of anharmonic lattice dynamics. Based on the expansion of the PES in (Cartesian) atomic displacements(see Eq. (2.10)), one could consider higher-order terms as well. In second quantisation, the full Hamiltonian of the system reads [36, 55]:

$$\begin{aligned}\widehat{H} = \sum_{\lambda} \hbar\omega_{\lambda} \left(\frac{1}{2} + a_{\lambda}^{\dagger} a_{\lambda}\right) + \frac{1}{3!} \sum_{\lambda_1,\lambda_2,\lambda_3} \Phi^{(3)}_{\lambda_1,\lambda_2,\lambda_3} \widehat{A}_{\lambda_1} \widehat{A}_{\lambda_2} \widehat{A}_{\lambda_3} + \\ + \frac{1}{4!} \sum_{\lambda_1,\lambda_2,\lambda_3,\lambda_4} \Phi^{(4)}_{\lambda_1,\lambda_2,\lambda_3,\lambda_4} \widehat{A}_{\lambda_1} \widehat{A}_{\lambda_2} \widehat{A}_{\lambda_3} \widehat{A}_{\lambda_4} + \\ + \frac{1}{5!} \sum_{\lambda_1,\lambda_2,\lambda_3,\lambda_4,\lambda_5} \Phi^{(5)}_{\lambda_1,\lambda_2,\lambda_3,\lambda_4,\lambda_5} \widehat{A}_{\lambda_1} \widehat{A}_{\lambda_2} \widehat{A}_{\lambda_3} \widehat{A}_{\lambda_4} \widehat{A}_{\lambda_5} + \dots \end{aligned} \tag{2.43}$$

Truncating the expansion of the PES after the first term - the harmonic term - leads to the well-known set of equations for independent harmonic oscillators, for which the quantum numbers n (band index) and $\mathbf{q}$ (wave vector) have been condensed into one quantum number λ for reasons of brevity. The harmonic term contains a summation over $\hbar\omega_{\lambda}/2$ (the zero-point energy) as well as the ladder operators $a_{\lambda}^{\dagger}$ and a_{λ}, which create and annihilate a phonon with the (condensed) quantum number λ, respectively. As the harmonic term is diagonal in this space (i.e. both operators act on the same phonon such that $a_{\lambda}^{\dagger} a_{\lambda}$ can also be replaced by the number operator $\widehat{n}_{\lambda}$), only one quantum number appears in the summation, in contrast to the summations in case of the higher-order terms. The latter basically include summations over the product of the higher-order force-constants - high-dimensional objects whose number of indices depends on the order of the Taylor expansion of the PES - and the operators $\widehat{A}_{\lambda}$, which are a sum of the (harmonic) creation and annihilation operators[7]:

$$\widehat{A}_{\lambda} = a_{\lambda} + a_{-\lambda}^{\dagger} \tag{2.44}$$

Higher-order terms can be relatively easily considered via Greens' functions in many-body perturbation theory (and the Dyson equation). To this end, one typically calculates the phonon propagator for the operator $\widehat{A}_{\lambda}$, which leads to the problem of calculating the self-energy of the system [56]. One eventually ends up with drawing and evaluating Feynman diagrams corresponding to the scattering processes of multiple phonons that contribute to the real and imaginary part of the self-energy, which lead to a shift in the phonon frequencies and a finite linewidth (proportional to the inverse lifetime), respectively. Although the formalism to calculate the contributions (at finite temperatures using Matsubara Greens' functions), the biggest challenge is to obtain the higher-order force constants which act as (relative) weights for the Feynman diagrams. These objects typically grow very rapidly in number (even for smaller systems) so that force constants beyond third-order are hardly ever used in practice.
Although anharmonicities are only rarely treated on the basis of considering higher-order force constants explicitly, there are anharmonic effects that are more accessible by easier means. One such anharmonic effect is the dependence of the frequencies on

[7] The index $-\lambda$ corresponds to $(n, -\mathbf{q})$.

the unit-cell volume, V. The quantity that qualitatively describes the relative change in phonon frequency as a consequence of the relative change in volume, is the mode Grüneisen parameter $\gamma_{n,\mathbf{q}}$ [57]:

$$\gamma_{n,\mathbf{q}} = -\frac{V}{\omega_{n,\mathbf{q}}}\frac{d\omega_{n,\mathbf{q}}}{dV} \tag{2.45}$$

For many materials, frequencies typically increase upon decreasing the system's volume. According to the definition of the mode Grüneisen parameter, such a behaviour would result in a positive value of $\gamma_{n,\mathbf{q}}$. For some systems, however, the mode Grüneisen parameters can also be negative, which is sometimes referred to as "phonon softening" - i.e. the frequencies decrease upon decreasing the system's volume. This observation is especially well-known in metal-organic frameworks [58, 59, 60], and often leads to negative thermal expansion (at low temperatures), as both quantities are intimately related to each other (to first approximation)[7]:

$$\alpha_V = \frac{\langle\gamma\rangle_C C_V}{VB} \tag{2.46}$$

In the above equation of the volumetric thermal expansion coefficient, α_V, besides the unit-cell volume V, the bulk modulus B and the heat-capacity per unit-cell (at constant volume) C_V also the Grüneisen parameter $\langle\gamma\rangle_C$ enters. This quantity can be seen as an average of the mode Grüneisen parameters weighted with the mode contributions to the heat capacity (see next section; with k_B being the Boltzmann constant):

$$\langle\gamma\rangle_C = \frac{\frac{1}{N_q}\sum_\lambda \gamma_\lambda c_\lambda}{\frac{1}{N_q}\sum_\lambda c_\lambda} \qquad \text{with } c_\lambda = k_B\frac{(\hbar\omega_\lambda)^2/(k_BT)^2\exp\{\hbar\omega_\lambda/(k_BT)\}}{(\exp\{\hbar\omega_\lambda/(k_BT)\}-1)^2} \tag{2.47}$$

Thus, the thermal expansion of a crystal is a purely anharmonic effect and, to the first approximation, is a direct consequence of the volume-dependence of the phonon frequencies.

Strictly speaking, the mode Grüneisen parameters must be defined more generally for non-cubic systems because the volume is an ambiguous descriptor of the shape of the unit-cell. While in a cubic crystal the single lattice parameter can always be unambiguously translated in the unit-cell volume and vice versa, in systems with more than one lattice constant this is not the case. In a hexagonal crystal, for instance, the phonon frequencies might respond in different ways to a change in the lattice parameter c than to a change in lattice parameter a. Thus, in general, the mode Grüneisen parameter must be redefined as a tensorial quantity involving the derivative with respect to one of the six independent elements of the strain tensor ε_{ij} [61]:

$$\gamma_{ij}^{n,\mathbf{q}} = -\frac{1}{\omega_{n,\mathbf{q}}}\frac{\partial\omega_{n,\mathbf{q}}}{\partial\varepsilon_{ij}} \tag{2.48}$$

Using this tensorial Grüneisen parameter, one can even draw direct conclusions not only on the volumetric thermal expansion, but also on the thermal expansion tensor - i.e. study how the lattice parameters change separately as a function of temperature [61].

2.4. Phonons in the (Grand) Canonical Ensemble

Since insulators have only little contributions to important quantities such as thermodynamic potentials from the crystal electrons, the phonon contributions to the thermal properties typically dominate. In order to understand which assumptions are made to derive the well-known expressions for the free energy, entropy, heat capacity, etc. of phonons, one must treat the harmonic oscillators within quantum statistical physics. The basic considerations presented here are based on Refs. [36, 37]. First of all, it is convenient to define the reciprocal temperature β, which has the dimension of an inverse energy due to the Boltzmann constant k_B in the denominator.

$$\beta = \frac{1}{k_B T} \tag{2.49}$$

In statistical physics, one of the central quantities is the density operator, $\hat{\rho}$, which, for phonons with vanishing chemical potential, is related to the multi-body Hamiltonian according to the following equation[8]:

$$\hat{\rho} = \frac{1}{\mathcal{Z}} \exp(-\beta \hat{H}) \tag{2.50}$$

The Hamiltonian that is considered here is the harmonic part of Eq. (2.43), i.e. no correlation and no interaction of the $\mathcal{N}$ harmonic oscillators (index i, angular frequency ω_i) among each other is taken into account. In other words, the considered many-body Hamiltonian (of the entire system) - in absence of any couplings or anharmonicities - corresponds to a sum of single-particle harmonic oscillator Hamiltonians, $\hat{H}_i$ (with individual frequencies ω_i and number operators $\hat{n}_i$):

$$\hat{H} = \sum_i^{\mathcal{N}} \hat{H}_i = \sum_i^{\mathcal{N}} \hbar\omega_i \left(\hat{n}_i + \frac{1}{2}\hat{\mathbb{1}} \right) \tag{2.51}$$

The quantity $\mathcal{Z}$, which appears in the denominator of Eq. (2.50) for reasons of normalisation, is the so-called partition function. One can calculate the partition function $\mathcal{Z}$ by summing the repsective Boltzmann weight for every possible (quantum) state of the system. As the Hamiltonian represents a uncoupled system of harmonic oscillators, a general state $|\psi\rangle$ can be written as a product state of the $\mathcal{N}$ involved harmonic oscillator eigenstates, $|n_i\rangle$ [37]:

$$|\psi\rangle_{n_1,n_2,\ldots,n_\mathcal{N}} = |n_1\rangle\,|n_2\rangle \ldots |n_\mathcal{N}\rangle \tag{2.52}$$

To evaluate the partition function, one must sum the Boltzmann weights $\langle\psi_{n_1,n_2,\ldots,n_\mathcal{N}}| \exp(-\beta\hat{H})\,|\psi_{n_1,n_2,\ldots,n_\mathcal{N}}\rangle$ for all possible quantum states - i.e. for all possible combinations of the quantum numbers $n_1 \in \{0\ldots\infty\}$, $n_2 \in \{0\ldots\infty\}, \cdots, n_\mathcal{N} \in$

[8] For other particles for which the chemical potential μ does not vanish one would have to replace $\hat{H}$ by $\hat{H} - \mu\hat{N}$, with $\hat{N}$ being the total particle number operator. For $\mu \neq 0$, this ensemble would even correspond to the *grand* canonical ensemble. Here, as $\mu = 0$, the expressions for the canonical and the grand canonical ensembles become equivalent.

$\{0 \ldots \infty\}$. Mathematically, this sum is equivalent to the trace of the operator $\exp(-\beta\hat{H})$ evaluated in the space of all possible states $|\psi\rangle_{n_1,n_2,\ldots,n_\mathcal{N}}$. This trace could, in principle, be evaluated in any basis. Most conveniently, however, this is done in the eigenbasis of the Hamiltonian - i.e. product states of the eigenstates of the independent harmonic oscillators - so that the Hamilton operator in the exponent can be replaced by the corresponding (harmonic) eigenvalues involving the quantum (occupation) number n_i for the i^{th} harmonic oscillator (i.e. the eigenvalue of the number operator $\hat{n}_i$), which can be any positive integer and zero.

$$\begin{aligned} \mathcal{Z} = \mathrm{tr}\left\{\exp(-\beta\hat{H})\right\} &= \sum_{n_1}\sum_{n_2}\cdots\sum_{n_\mathcal{N}} \langle\psi_{n_1,n_2,\ldots,n_\mathcal{N}}| \exp(-\beta\hat{H}) |\psi_{n_1,n_2,\ldots,n_\mathcal{N}}\rangle \quad (2.53) \\ &= \sum_{n_1}\sum_{n_2}\cdots\sum_{n_\mathcal{N}} \exp\left(-\beta\sum_i \hbar\omega_i\left(n_i+\frac{1}{2}\right)\right) \quad (2.54) \end{aligned}$$

The second line in the equation above is easily obtained from the fact that each of these occurring operators $\exp(-\beta\hat{H}_i)$ only acts on the single-particle states of the same harmonic oscillator: $\langle n_i| \exp(-\beta\hat{H}_i) |n_i\rangle = \exp\left(-\beta\hbar\omega_i\left(n_i + 1/2\right)\right)$. Thus, the number operators were eventually replaced by the associated quantum numbers.
This expression can be further evaluated within a few steps. The first one is recognising that the sum over the harmonic oscillators i in the exponent can equivalently be written as a product of exponential factors[9]:

$$\exp\left(-\beta\sum_i \hbar\omega_i\left(n_i+\frac{1}{2}\right)\right) = \prod_i \exp\left(-\beta\hbar\omega_i\left(n_i+\frac{1}{2}\right)\right) \quad (2.55)$$

Since all the individual exponential factors in this product only depend on one specific quantum number n_i (and not on combinations of quantum numbers), Eq. (2.54) can be rearranged:

$$\begin{aligned} \mathcal{Z} &= \sum_{n_1}\sum_{n_2}\cdots\sum_{n_\mathcal{N}}\prod_i \exp\left(-\beta\hbar\omega_i\left(n_i+\frac{1}{2}\right)\right) = \\ &= \sum_{n_1}\exp\left(-\beta\hbar\omega_1\left(n_1+\frac{1}{2}\right)\right)\sum_{n_2}\exp\left(-\beta\hbar\omega_2\left(n_2+\frac{1}{2}\right)\right)\ldots \\ &\ldots \sum_{n_\mathcal{N}}\exp\left(-\beta\hbar\omega_\mathcal{N}\left(n_\mathcal{N}+\frac{1}{2}\right)\right) \quad (2.56) \end{aligned}$$

In short, this lengthy expression can be written as a product of mathematically equivalent (convergent) series. Finally, one can exclude the factor from the geometric series,

[9]Strictly speaking, the single-particle harmonic oscillators of the Hamiltonian ($\hat{H} = \sum_i \hat{H}_i$) must commute ($\left[\hat{H}_i, \hat{H}_j\right] = 0$) so that this step is justified, which is the case here [37].

which has its origin in the zero-point energy of the quantum harmonic oscillators:

$$\mathcal{Z} = \prod_i \left[\sum_{n_i} \exp\left(-\beta\hbar\omega_i \left(n_i + \frac{1}{2} \right) \right) \right] = \prod_i \left[\exp\left(-\beta\hbar\omega_i/2\right) \sum_{n_i} \left(\exp\left(-\beta\hbar\omega_i\right)\right)^{n_i} \right] \tag{2.57}$$

Evaluating the geometric series[10], one finds for the partition function [37]:

$$\mathcal{Z} = \prod_i \frac{\exp\left(-\beta\hbar\omega_i/2\right)}{1 - \exp\left(-\beta\hbar\omega_i\right)} \tag{2.58}$$

In every ensemble (canonical, microcanonical, grand canonical, constant pressure and temperature), the thermodynamic potential (the free energy, the entropy, the grand canonical potential, Gibbs free enthalpy), from which all further properties can be derived with simple operations, is proportional to the natural logarithm of the corresponding partition function [37].

$$\ln \mathcal{Z} = -\sum_i \left(\frac{\beta\hbar\omega_i}{2} + \ln\left\{1 - \exp\left(-\beta\hbar\omega_i\right)\right\} \right) \tag{2.59}$$

Up to this point, the summations have been carried out over all harmonic oscillators i in a system of a given size. In a perfect crystal with an ideally infinite extent, it is more sensible to define all thermodynamic quantities per unit-cell of the crystal. In other words, the summation over all harmonic oscillators i are replaced by a summation over phonon bands n and wave vectors $\mathbf{q}$, which are condensed into a single index λ, with a normalisation constant N_q. N_q is the number of wave vectors the sum runs over, which is equivalent to the number of unit-cells of the given crystal[11].

$$\sum_i \rightarrow \frac{1}{N_q} \sum_{\lambda=(n,\mathbf{q})} \tag{2.60}$$

Therefore, from this point on, the thermodynamic expressions given in the following, describe the respective properties per unit-cell. The thermodynamic potential for the (grand) canonical ensemble (i.e. constant volume and temperature) is the Helmholtz free energy. Knowing the partition function, one can easily calculate the free energy for phonons in a crystal [37]:

$$F = -k_B T \ln \mathcal{Z} = \frac{1}{N_q} \sum_{\lambda=(n,\mathbf{q})} \left(k_B T \ln\left\{ 1 - \mathrm{e}^{-\frac{\hbar\omega_\lambda}{k_B T}} \right\} + \frac{\hbar\omega_\lambda}{2} \right) \tag{2.61}$$

Next, I slightly rewrite the free energy to make it more obvious that it consists of a temperature-dependent part $A(T)$ and a contribution without any temperature-dependence

[10] With $\sum_{n=0}^{\infty} p^n = \frac{1}{1-p}$ if $|p| < 1$. Here, $p \equiv \exp(-\beta\hbar\omega_i)$.

[11] This can be understood very easily: If a crystal consists only of two unit-cells, there can only be two wave vectors that "fit" into the crystal: $q = 0$ and $q = \pi/a$ if a is the lattice parameter in that direction in which the crystal has the two unit-cells.

stemming from the zero-point energy (ZPE) of the harmonic oscillators. Since $A(T) \leq 0, \forall T$ ($A(T = 0\ \mathrm{K}) = 0$), the free energy has its maximum value, i.e. the ZPE, at the absolute zero and decreases continuously at higher temperatures.

$$F = \frac{1}{N_q} \sum_{\lambda=(n,\mathbf{q})} k_B T \ln \left\{ 1 - \mathrm{e}^{-\frac{\hbar\omega_\lambda}{k_B T}} \right\} + \frac{1}{N_q} \sum_{\lambda=(n,\mathbf{q})} \frac{\hbar\omega_\lambda}{2} = A(T) + \mathrm{ZPE} \tag{2.62}$$

At this point it is crucial to stress a few implications of the equation above. Since the expression for the ZPE does not include temperature, this part of F is a temperature-independent one already present at 0 K. Moreover, the thermal occupation of phonon bands is irrelevant for this quantity, as every mode λ contributes a part proportional to its frequency ω_λ to the ZPE. Thus, phonon modes with very high frequency typically show a larger relative contribution to the ZPE than the low-frequency modes.
Moreover, the entire temperature-dependence of F is contained in the term which has been referred to as $A(T)$ above. Analysing its functional form in terms of its frequency dependence, one can easily understand that $A(T)$ favours the low-frequency modes. This means that here, the thermal occupation plays a role again. In other words, the temperature behaviour of $A(T)$ (and, thus, also of F) is determined by the low-frequency phonon bands.

If there are several competing phases of a crystal (and the influence of pressure can be neglected[12]), the phase with the lowest free energy will be the dominant one in thermodynamic equilibrium [7]. Thus, both the initial *offset* determined by the ZPE as well as the temperature-dependence are relevant to describe the relative thermodynamic stability of different possible phases.
In order to better understand the (mathematical) composition of the free energy of the ensemble of quantum harmonic oscillators considered here, it is instructive to derive and discuss another important phonon property. This quantity is the internal energy U, which is defined as being the expectation value of the (many-body) Hamiltonian [37]. Thus, it is the average (thermodynamic) energy of the many-body system. In quantum statistical physics, expectation values are evaluated by computing the trace of the product of the desired operator with the density operator (properly normalised with the partition function $\mathcal{Z}$) [37]. After some mathematical tricks, it can be concluded, that the internal energy is easily obtained by differentiating the logarithm of the partition function with respect to the inverse temperature:

$$\begin{aligned} U = \left\langle \hat{H} \right\rangle &= \mathrm{tr}\left\{ \hat{H}\hat{\rho} \right\} = \frac{1}{\mathcal{Z}} \mathrm{tr}\left\{ \hat{H} \exp\left(-\beta \hat{H} \right) \right\} = -\frac{1}{\mathcal{Z}} \frac{\partial}{\partial \beta} \mathrm{tr}\left\{ \exp\left(-\beta \hat{H} \right) \right\} = \\ &= -\frac{\partial}{\partial \beta} \ln \mathcal{Z} \end{aligned} \tag{2.63}$$

[12] Otherwise one must consider the Gibbs free enthalpies $G(p,T) = F(V(p,T),T) + pV(p,T)$ after a Legendre transformation introducing the pressure p instead of the volume V as a relevant variable [7].

In particular, the trick used here to arrive at the last equality of the first line in the equation above is the following (expressed in terms of variables and not operators): $x\exp(-ax) = -\partial/\partial a\,(\exp(-ax))$. In other words, the expression for U has been rewritten by introducing a partial derivative with respect to the inverse temperature. Computing the required derivative, the internal energy is found to equal:

$$U = \frac{1}{N_q}\sum_{\lambda=(n,\mathbf{q})}\left(\frac{\hbar\omega_\lambda}{2} + \hbar\omega_\lambda\frac{1}{\exp(\beta\hbar\omega_\lambda)-1}\right) = \frac{1}{N_q}\sum_{\lambda=(n,\mathbf{q})}\left(\frac{\hbar\omega_\lambda}{2} + \hbar\omega_\lambda\left\langle n_\lambda\right\rangle(T)\right) \tag{2.64}$$

In the last equality, the average occupation number of the λ^{th} phonon has been introduced, which is the famous Bose-Einstein distribution. Here, $\langle n_\lambda\rangle(T)$ is a shorthand notation for the Bose-Einstein distribution for a frequency ω_λ at temperature T. With one last step of simplification, one can arrive at an expression for the internal energy which is very similar to the energy of the one-dimensional harmonic oscillator (see Eq. (2.12)):

$$U = \frac{1}{N_q}\sum_{\lambda}\hbar\omega_\lambda\left(\frac{1}{2} + \left\langle n_\lambda\right\rangle(T)\right) \tag{2.65}$$

In this way, it is obvious that the internal energy of the entire system of (statistically treated) quantum harmonic oscillators equals a sum of individual contributions, in which the original quantum numbers n_λ have been replaced by their respective thermodynamic expectation values $\langle n_\lambda\rangle$. Moreover, one can easily see that for each term in the summation over harmonic oscillators, there is a temperature-dependent part (depending on the Bose-Einstein distribution) and a temperature-independent part coming from the ZPE, which, thus, also contributes at $T = 0$ K.
The Bose-Einstein distribution, which has only been introduced as a shorthand notation for a function appearing in the derivation of the internal energy so far, can also be derived more rigorously by computing the expectation value of a (single-particle) particle number operator (using the density operator):

$$\left\langle n_\lambda\right\rangle = \mathrm{tr}\left\{\hat{n_\lambda}\hat{\rho}\right\} = \left(\prod_k\frac{1-\exp\left(-\beta\hbar\omega_k\right)}{\exp\left(-\beta\hbar\omega_k/2\right)}\right)\prod_i\sum_{n_i}n_\lambda\exp\left(-\beta\hbar\omega_i\left(n_i+\frac{1}{2}\right)\right) \tag{2.66}$$

The first product with multiplication index k corresponds to the (inverse) partition function (see Eq. (2.58)), while the second product (multiplication index i) corresponds to $\mathrm{tr}\left\{\hat{n_\lambda}\exp(-\beta\hat{H})\right\}$. It is quite obvious that all the series - i.e. the factors - in the latter product above are unaffected by the additional factor n_λ, except for the summation over exactly this variable. Thus, all other factors cancel with the respective factors in the partition function such that only the summation over the (discrete) quantum occupation number n_λ remains to determine the thermodynamic expectation value.

$$\begin{aligned}\left\langle n_\lambda\right\rangle &= \frac{1-\exp\left(-\beta\hbar\omega_\lambda\right)}{\exp\left(-\beta\hbar\omega_\lambda/2\right)}\sum_{n_\lambda}n_\lambda\exp\left(-\beta\hbar\omega_\lambda n_\lambda\right)\exp\left(-\beta\hbar\omega_\lambda/2\right) = \\ &= \left(1-\exp\left(-\beta\hbar\omega_\lambda\right)\right)\sum_{n_\lambda}n_\lambda\exp\left(-\beta\hbar\omega_\lambda n_\lambda\right)\end{aligned} \tag{2.67}$$

This convergent sum can be evaluated as shown in the Appendix in Eq. (A.5). Finally, the well-known Bose-Einstein distribution describing the average number of phonons with frequency ω_λ at a given temperature follows:

$$\langle n_\lambda \rangle = \left(1 - \exp\left(-\beta\hbar\omega_\lambda\right)\right) \frac{\exp\left(-\beta\hbar\omega_\lambda\right)}{\left[\exp\left(-\beta\hbar\omega_\lambda\right) - 1\right]^2} = \frac{1}{\exp\left(\beta\hbar\omega_\lambda\right) - 1} \tag{2.68}$$

One reason why the phonon contribution to the free energy is so important is that it includes also an entropic term, since the free energy, the internal energy, and the temperature are related to the entropy S according to the Legendre transformation [7, 37]:

$$\begin{aligned} F &= U - ST && (2.69)\\ dF &= dU - SdT - TdS = \\ &= -pdV + TdS - SdT - TdS = -pdV - SdT && (2.70)\\ &\equiv \left.\frac{\partial F}{\partial V}\right|_T dV + \left.\frac{\partial F}{\partial T}\right|_V dT && (2.71) \end{aligned}$$

Equivalently, the relation can be formulated for the total derivatives of the occurring quantities (here, the expression $dU = -pdV + TdS$ has been used for the total derivative of the internal energy [37])). By comparing the physical interpretation of the total derivative of F (see Eq.(2.70)) with the mathematical expression of the total derivative (see Eq. (2.71)), the pressure and the entropy can be identified as the (negative) partial derivative of F with respect to volume V and temperature T, respectively. Thus, the entropy can either be calculated from the difference of the internal and the free energy, or, directly, from the partial derivative of F with respect to the temperature [37].

$$\begin{aligned} S &= \frac{U - F}{T} && (2.72)\\ S &= -\frac{\partial F}{\partial T} = -\frac{\partial F}{\partial \beta}\frac{\partial \beta}{\partial T} = k_B\beta^2\frac{\partial F}{\partial \beta} && (2.73) \end{aligned}$$

Regardless of whether one way is chosen or the other, the entropy is found to equal to (,which can equivalently be rewritten using hyperbolic functions):

$$\begin{aligned} S &= \frac{k_B}{N_q}\sum_{\lambda=(n,\mathbf{q})} \left(\beta\hbar\omega_\lambda \langle n_\lambda \rangle (T) - \ln\left\{1 - \exp\left(-\beta\hbar\omega_\lambda\right)\right\}\right) && (2.74)\\ S &= \frac{k_B}{N_q}\sum_{\lambda=(n,\mathbf{q})} \left(\frac{\beta\hbar\omega_\lambda}{2}\coth\left(\frac{\beta\hbar\omega_\lambda}{2}\right) - \ln\left\{2\sinh\left(\frac{\beta\hbar\omega_\lambda}{2}\right)\right\}\right) && (2.75) \end{aligned}$$

It can be seen that the first term in Eq. (2.74) also appears in the expression of the internal energy (except for a missing factor T). Therefore, when subtracting TS from U, this term cancels in the free energy and only the second (temperature-dependent) term of the entropy in Eq. (2.74) and the (temperature-independent) ZPE from the internal

energy (see Eq. (2.65)) survive. Consequently, the entire temperature-dependent term in the free energy F stems from the entropy S[13], while the ZPE fully originates from the internal energy. Therefore, the entropy, which vanishes at the absolute zero (third law of thermodynamics) and grows with temperature, is responsible for the negative temperature gradient of the free energy.

Finally, a last quantity that should be briefly introduced and discussed is the heat capacity (per unit-cell) at constant volume, C_V, which describes the amount of energy required to increase the temperature of the system by a certain amount. This property is important because it can be experimentally evaluated very easily[14]. The heat capacity is defined as the temperature gradient of the internal energy with fixed volume. After a few mathematical simplifications, the heat capacity reads (including an alternative formulation using hyperbolic functions):

$$\begin{aligned} C_V &= \left.\frac{\partial U}{\partial T}\right|_V = k_B\beta^2 \left.\frac{\partial U}{\partial \beta}\right|_V = \\ &= \frac{k_B}{N_q}\sum_{\lambda=(n,\mathbf{q})} \frac{\left(\beta\hbar\omega_\lambda\right)^2 \exp\left\{\beta\hbar\omega_\lambda\right\}}{\left(\exp\left\{\beta\hbar\omega_\lambda\right\}-1\right)^2} \qquad (2.76) \\ &= \frac{k_B}{N_q}\sum_{\lambda=(n,\mathbf{q})} \frac{\left(\frac{\beta\hbar\omega_\lambda}{2}\right)^2}{\sinh^2\left(\frac{\beta\hbar\omega_\lambda}{2}\right)} \qquad (2.77) \end{aligned}$$

The terms appearing in the summations are the mode contributions to the heat capacity, i.e. the contribution of each phonon to the total magnitude of this quantity. As a function of phonon frequency, the mode contributions equal 1 for low frequencies ($\beta\hbar\omega_\lambda \to 0$) and 0 for high frequencies ($\beta\hbar\omega_\lambda \to \infty$). The transition - with regard to smoothness and position - depends on the temperature. Therefore, I often think of the mode contribution as a temperature-dependent low-pass filter considering only phonons with a small enough frequency. Interestingly, the heat capacity saturates with temperature. At very high temperatures, all the mode contributions equal unity, such that the heat capacity amounts to $3Nk_B$ per unit-cell. This is known as the famous Dulong-Petit law [7]. This law can be seen as the classical limit being characterised by a comprehensive equipartitioning of all available degrees of freedom - i.e. quantum occupation becomes irrelevant.

Moreover, one can make use of the expressions and rules from statistical physics to slightly rewrite the heat capacity. The mathematical steps used in the subsequent derivation are the following: rewriting the partial derivative with respect to T as a partial derivative with respect to β, rewriting the thermodynamic expectation value of $\hat{H}$ via

[13] This can also be rationalised by recalling the finding from Eqs. (2.71) and (2.70), namely that $S = -\partial F/\partial T$ (at constant volume).

[14] Strictly speaking, one rather measures the heat capacity at constant pressure, C_p, which is always somewhat larger than C_V, as shown in the Appendix A.9.

the density operator, and applying the product rule for the differential with respect to β [37].

$$\begin{aligned} C_V &= \left.\frac{\partial U}{\partial T}\right|_V = \left.\frac{\partial \left\langle \hat{H} \right\rangle}{\partial T}\right|_V = -k_B\beta^2 \left.\frac{\partial \left\langle \hat{H} \right\rangle}{\partial \beta}\right|_V = \\ &= -k_B\beta^2 \left.\frac{\partial}{\partial \beta}\right|_V \left(\frac{1}{\mathcal{Z}} \operatorname{tr}\left\{\hat{H}\exp\left(-\beta\hat{H}\right)\right\}\right) = \\ &= -k_B\beta^2 \left(-\frac{\partial \mathcal{Z}}{\partial \beta}\mathcal{Z}^{-2} \operatorname{tr}\left\{\hat{H}\exp\left(-\beta\hat{H}\right)\right\} - \frac{1}{\mathcal{Z}} \operatorname{tr}\left\{\hat{H}^2\exp\left(-\beta\hat{H}\right)\right\}\right) \end{aligned} \tag{2.78}$$

The second term of the last line above can be identified as the (thermodynamic) expectation value of $\hat{H}^2$. The first term must be rewritten in order to further simplify it:

$$-\frac{\partial \mathcal{Z}}{\partial \beta}\mathcal{Z}^{-2} \operatorname{tr}\left\{\hat{H}\exp\left(-\beta\hat{H}\right)\right\} = \left(-\frac{\partial \mathcal{Z}}{\partial \beta}\frac{1}{\mathcal{Z}}\right)\left(\frac{1}{\mathcal{Z}} \operatorname{tr}\left\{\hat{H}\exp\left(-\beta\hat{H}\right)\right\}\right) \tag{2.79}$$

The second factor in parentheses in the equation above can again be identified as the thermodynamic expectation value of $\hat{H}$, while the first factor can be rewritten as $-\frac{\partial \ln \mathcal{Z}}{\partial \beta}$, which also equals the thermodynamic expectation value of $\hat{H}$ according to Eq. (2.63). Thus, the term in Eq. (2.79) equals $\left\langle \hat{H} \right\rangle^2$. Finally, one sees that the heat capacity is proportional to the variance of the Hamiltonian:

$$\begin{aligned} C_V &= -k_B\beta^2 \left(-\frac{\partial \ln \mathcal{Z}}{\partial \beta}\left\langle \hat{H} \right\rangle - \left\langle \hat{H}^2 \right\rangle\right) = \\ &= -k_B\beta^2 \left(\left\langle \hat{H} \right\rangle^2 - \left\langle \hat{H}^2 \right\rangle\right) = \\ &= k_B\beta^2 \mathrm{var}\left(\hat{H}\right) \end{aligned} \tag{2.80}$$

In other words, the heat capacity quantitatively measures how much the energy of the system fluctuates -i.e. how much the energy of the individual harmonic oscillators deviates from the thermodynamic expectation value ($=U$). The more the energy fluctuates, the more energy is required to heat a system to a higher temperature.

At this point it should be stressed that it is important to choose the number of wave vectors $\mathbf{q}$ large enough in order to obtain properly converged bulk properties (as it has also been discussed in the Supporting Information of Ref. [1]). Fig. 2.1 shows the difference in the heat capacity and the Helmholtz free energy of crystalline naphthalene due to phononic contributions for the case in which only one wave vector at the centre of the first Brillouin zone, Γ, has been considered in the summation, and for the case of a densely sampled first Brillouin zone. Focussing on the free energy, one notices that at 0 K, the sampling density does not seem to have a large impact. This means that the free

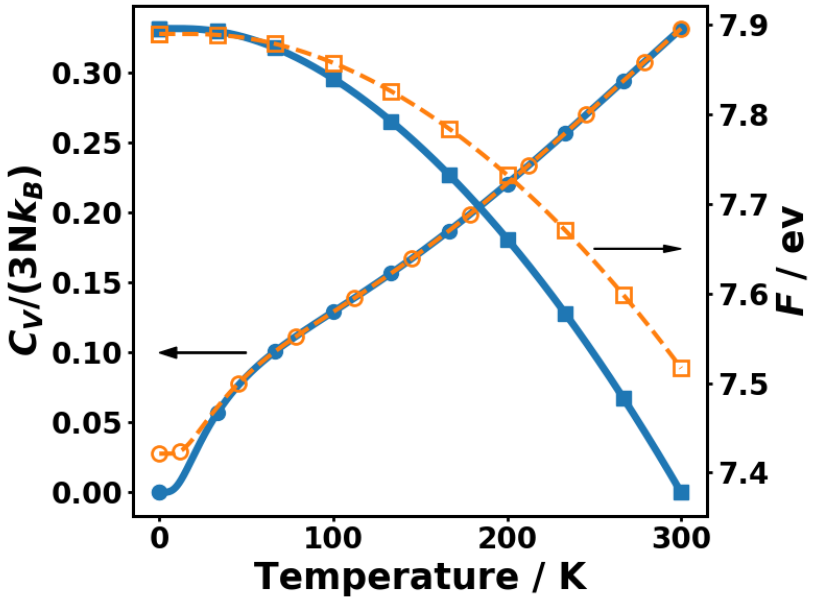

Fig. 2.1.: Vibrational free energy (F) and phonon contribution to the heat capacity (C_V) as a function of temperature in crystalline naphthalene. The solid blue curves with filled symbols have been calculated from a homogeneously sampled mesh of wave vectors, $\mathbf{q}$, whereas the dashed orange curves with empty symbols are based on Γ-modes only. This figure has been taken from the Supporting Information of Ref. [1].

energy at 0 K (=ZPE), which is proportional to the average frequency in the crystal, is mostly unaffected. This observation is most probably a consequence of the overwhelming amount of rather flat intramolecular bands in this system: for (nearly) vanishing band dispersion the average frequency is not affected whether one uses only the frequency at one wave vector or at several ones. The fact that the ZPE is in such a good agreement can be seen as a feature of systems containing molecular moieties in the crystallographic unit cell rather than for, e.g., more conventional inorganic semiconductors or metals. At higher temperatures, neglecting the band dispersion becomes obvious as the (negative) entropic contribution is obviously underestimated with a Γ-only sampling.
The heat capacity seems to be mostly affected at very low temperatures: while the heat capacity for a properly sampled first Brillouin zone vanishes at 0 K - in accordance to the third law of thermodynamics - the Γ-only heat capacity shows an artificial offset at 0 K. This offset comes from the fact that the three (physically meaningless) acoustic modes at Γ (corresponding to rigid translation of the entire crystal) have zero frequency. Using only the Γ-modes - i.e. neglecting the band dispersion - is equivalent to saying that the Γ-frequencies are observed for every wave vector of the first Brillouin zone. Thus, there is a significant contribution to the heat capacity stemming from the three "0-frequency bands" already at a temperature of 0 K resulting in a notable offset. Strictly speaking, the third law of thermodynamics is violated here. In order to correct for this violation, one would have to subtract $3k_B$ from the heat capacity per unit-cell, which, however, results in a constant offset of the curves at finite temperatures.

An important quantity when it comes to sampling of states in a crystal, is the density of states (DOS). The DOS is defined as delta-distributions (normalised with the number of wave vectors N_q) summed over all wave vectors and band indices.

$$\mathrm{DOS}(\omega) = \frac{1}{N_q} \sum_{n}^{3N} \sum_{\mathbf{q}}^{N_q} \delta\left(\omega - \omega_{n,\mathbf{q}}\right) \tag{2.81}$$

According to this definition, the DOS has the dimension of an inverse frequency and equals $3N$ when being integrated over the frequency. The main advantage of the DOS is that all the equations above, which originally contained a summation over wave vectors and bands indices, can be reformulated as frequency-integrals of the following general form:

$$\frac{1}{N_q} \sum_{\lambda} X(\omega_\lambda) \rightarrow \int d\omega \mathrm{DOS}(\omega) X(\omega) \tag{2.82}$$

This form allows to reinterpret some of the quantities introduced above. For instance, for the heat capacity per unit-cell, one can equivalently write:

$$C_V = k_B \int d\omega \mathrm{DOS}(\omega) \frac{(\beta\hbar\omega)^2 \exp\{\beta\hbar\omega\}}{(\exp\{\beta\hbar\omega\} - 1)^2} \tag{2.83}$$

$$= \int d\omega \mathrm{DOS}(\omega) f_C(\omega, T) \tag{2.84}$$

In this way, since the function $f_C(\omega, T)$ has already been discussed to be a temperature-dependent low-pass filter, the integral above can be interpreted as a (smoothly) truncated integral of the DOS: at 0 K, the low-pass f_C is zero everywhere such that nothing of the DOS is integrated, thus, resulting in a vanishing heat capacity. At infinite temperature, the band pass is unity everywhere, such that the entire DOS is integrated amounting to $3N$ (Dulong-Petit law).
This type of interpretation will become more relevant in Sec. 2.5.

2.4.1. Atom-resolved thermodynamic averages

Similar to the thermodynamic quantities presented in the previous section, certain properties can even be defined atom-wise within the framework of thermodynamics. One of this quantities will be discussed extensively in Sec. 4 so that it is worthwhile introducing it and similar ones already here. Using the harmonic oscillator ladder operators, one can write the time dependent position operator of an atom j in unit-cell A in the Cartesian direction α in the following way [36]:

$$u_j^\alpha(A)(t) = \sum_{\lambda=(n,\mathbf{q})}^{N_q,3N} \left(\sqrt{\frac{\hbar}{2m_j N_q \omega_\lambda}} \mathbf{e}_{j,\lambda}^\alpha \exp\left\{\mathrm{i}\mathbf{q}\cdot\mathbf{R}_A\right\} \times \right.$$
$$\left. \times \left(a_\lambda \exp\left\{-\mathrm{i}\omega_\lambda t\right\} + a_{-\lambda}^\dagger \exp\left\{+\mathrm{i}\omega_\lambda t\right\} \right) \right) \tag{2.85}$$

Using the same notation as before (with the joint index $\lambda = (n, \mathbf{q})$ and $-\lambda = (n, -\mathbf{q})$), it is apparent that besides the phonon frequencies, the corresponding eigenvectors enter the equation for the displacement (operator) above[15]. Although this quantity would, in principle, allow for tracking every degree of freedom in a crystal in a time-resolved manner, it is typically more useful to calculate the time-average of the square of the position operator. Using the well-known commutator rules for bosonic ladder operators (see Appendix A.2), the mean-squared thermal displacement (MSTD) follows [36]:

$$\left\langle \left| u_j^\alpha \right|^2 \right\rangle = \sum_{\lambda=(n,\mathbf{q})}^{N_q,3N} \frac{\hbar}{2m_j N_q \omega_\lambda} \left(1 + 2\left\langle n_\lambda \right\rangle(T)\right) \left| \mathbf{e}_{j,\lambda}^\alpha \right|^2 \tag{2.86}$$

Note that the dependence on the unit-cell has vanished as a consequence of the thermodynamic averaging. Moreover, the Bose-Einstein distribution has appeared as being the thermodynamic average of the number operator $\hat{n}_\lambda = a_\lambda^\dagger a_\lambda$. The MSTD quantifies the average (squared) displacement an atom undergoes as an effect of all the thermally activated phonon modes: the larger the MSTD of an atom in a certain direction, the more the atom moves in that direction at finite temperature. Moreover, the MSTD enters the important Debye-Waller factor [62, 63] which describes the loss of intensity

[15] Special care should be taken in order to not confuse the band index n appearing as a part of the summation index λ with the Bose-Einstein distribution $\langle n_\lambda \rangle(T)$.

in an X-ray diffraction experiment due to the thermal motion. In contrast to all the other quantities derived and discussed so far, the MSTD still shows a dependence on the eigenvector of the phonons. Thus, key to describing the MSTDs properly is correctly reproducing not only frequencies but also the eigenvectors - i.e. the atomic displacement patterns of every mode.
Similarly, based on the representation of the momentum operator in terms of annihilation and creation operators which is typically only found for a simple one-dimensional harmonic oscillator as in Ref. [7], one can write the momentum operator of atom j in unit-cell A in the Cartesian direction α as defined in Ref. [36]:

$$p_j^\alpha(A)(t) = \mathrm{i} \sum_{\lambda=(n,\mathbf{q})}^{N_q,3N} \left(\sqrt{\frac{\hbar m_j \omega_\lambda}{2N_q}} \mathbf{e}_{j,\lambda}^\alpha \exp\left\{\mathrm{i}\mathbf{q}\cdot\mathbf{R}_A\right\} \times \right. \\ \left. \times \left(a_\lambda^\dagger \exp\left\{-\mathrm{i}\omega_\lambda t\right\} - a_{-\lambda} \exp\left\{+\mathrm{i}\omega_\lambda t\right\} \right) \right) \tag{2.87}$$

Based on that, thermodynamically averaging[16] the absolute value of the momentum operator allowed to arrive at the mean-squared thermal momentum (MSTM), which has a similar form as the MSTD:

$$\left\langle \left| p_j^\alpha \right|^2 \right\rangle = \sum_{\lambda=(n,\mathbf{q})}^{N_q,3N} \frac{\hbar m_j \omega_\lambda}{2N_q} \left(1 + 2\left\langle n_\lambda \right\rangle (T)\right) \left| \mathbf{e}_{j,\lambda}^\alpha \right|^2 \tag{2.88}$$

Notably, the only characteristic in which the MSTD and the MSTM differ is that the former has the (angular) frequency in the denominator, while the latter has it in the numerator. In spite of being less practically relevant than the MSTD, I still derived the MSTM in order to show the effect of quantum mechanics and the resulting non-equal occupation of degrees of freedom. The MSTM offers a convenient way to calculate the average kinetic energy of a system:

$$\left\langle E_{kin,j} \right\rangle = \sum_{\alpha=\{x,y,z\}} \frac{\left\langle \left| p_j^\alpha \right|^2 \right\rangle}{2m_j} = \frac{\hbar}{4N_q} \sum_{\alpha=\{x,y,z\}} \sum_{\lambda=(n,\mathbf{q})}^{N_q,3N} \omega_\lambda \left(1 + 2\left\langle n_\lambda \right\rangle (T)\right) \left| \mathbf{e}_{j,\lambda}^\alpha \right|^2 \tag{2.89}$$

By doing so, the mass-dependence which is still present in the MSTM is gone so that the mean thermal kinetic energy of an atom j is only dependent on the associated eigenvector components and the phonon frequencies. Note that for the sake of convenience, a further summation over the Cartesian direction α has been carried out to calculate the total average kinetic energy for each atom. In order to demonstrate the effect, we will focus on a one-dimensional model system consisting of one heavy (M) and two

[16] The remainder of this subsection does not follow any text books, but is based on my own considerations and derivations.

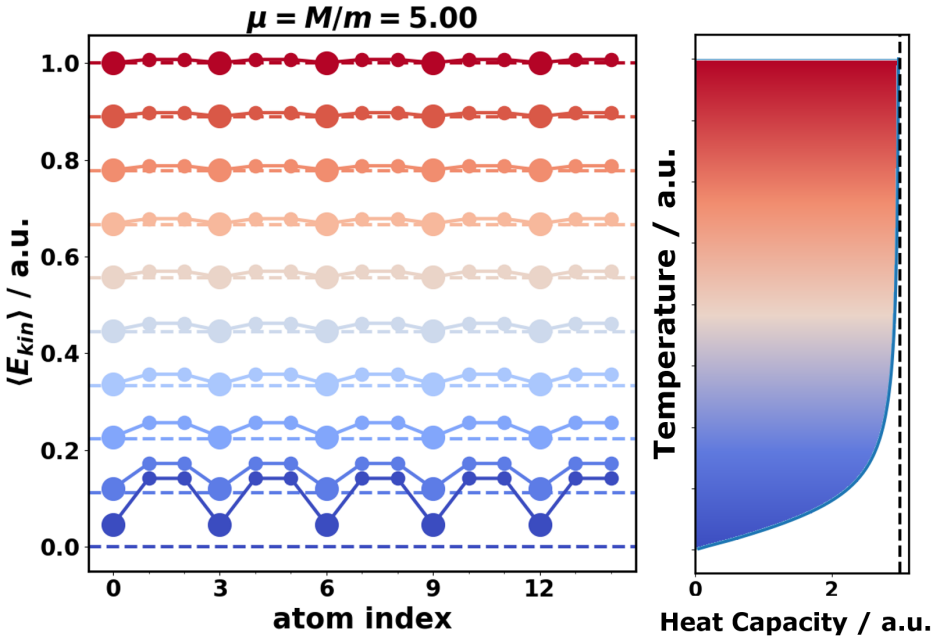

Fig. 2.2.: Average kinetic energy for each atom in a one-dimensional linear chain consisting of three atoms per unit cell: one heavy atom (large circle) and two lighter atoms with equal mass (small circles). The average kinetic energies are displayed for a range of temperatures as encoded in the colour (blue: low temperature, red: high temperature). The horizontal dashed lines correspond to the average kinetic energy according to the equipartition theorem ($= k_B T/2$). The right panel shows the heat capacity per unit-cell (and its Dulong-Petit limit indicated by the vertical dashed line) as a function of the temperature. The temperature and the average kinetic energy are plotted with an equivalent scale exploiting that direct proportionality in the classical limit ($E = k_B T/2$).

lighter atoms ($m = M/5$) (for more details see Appendix A.3). Figure 2.2 shows the average kinetic energy (in arbitrary units) for five supercells of the crystal for various temperature (the lower, blue curves correspond to low temperatures, while the upper, red curves correspond to high temperatures). First of all, it can be seen that in the entire temperature range, the average atomic kinetic energy of the heavier atom is (slightly) reduced compared to the lighter atoms, with the difference decreasing with higher temperatures. This means that in this quantum-regime the heavier atoms will always have a lower "effective temperature"[17] than the light atoms. The horizontal dashed lines in Figure 2.2 show the classically expected average kinetic energy - i.e. $E_{classical} = k_B T/2$. It is obvious that the kinetic energy of every atom in the crystal approaches this value with increasing temperature. In other words, at very high temperature, all degrees of freedom indeed become equivalent. At lower temperatures there is always a significant difference between the classical energies and the quantum-mechanically evaluated, atomically resolved ones - especially in the case of the light atoms. Interestingly, the kinetic energy at (almost) zero temperature does not vanish for any atom, which is a consequence of the ZPE of the harmonic oscillators. While the average kinetic energy of the heavy atoms approaches the classical values relative early in terms of temperature, the lighter atoms are still somewhat higher in energy at the highest temperature. This observation suggests a different degree of "classicity" for each inequivalent atom in the crystal. The right panel of Figure 2.2 shows the heat capacity of the system as a function of the temperature. The axes are aligned such that the temperature corresponds to the classical equipartitioned energies in the left panel. This comparison is instructive as it proves that the heat capacity is indeed a measure to quantify how classically the system behaves at a certain temperature: at the highest shown temperature it has already (approximately) reached the Dulong-Petit limit, as indicated by the vertical dashed line, in line with the observation that all the kinetic energies (almost) equal the classical value.

2.5. Relevant Frequency Ranges

Based on the discussion in Sec. 2.4, it is essential to understand that different thermodynamic properties depend on different spectral ranges of phonons. This topic has been discussed quite intensively in Ref. [1], which this subsection has been based on. The easiest way to identify the relevant frequency ranges for various properties is to replace the summation over band indices and wave vectors with a frequency integral introducing the DOS (see Eq. (2.82)). The remaining frequency-dependent parts in the integral can often be condensed into material-independent *spectral functions*. This general approach is demonstrated for the example of the mean-squared thermal displacements (MSTDs):

[17] Although, in general, the temperature is not proportional to the average kinetic energy in a system , this analogy is often used since it is the case in classical physics.

$$\left\langle \left| u_j^\alpha \right|^2 \right\rangle = \int d\omega \frac{\hbar}{2m_j\omega} \mathrm{DOS}(\omega) \left(1 + 2\left\langle n(\omega, T) \right\rangle\right) \left| \mathbf{e}_j^\alpha \right|^2 \tag{2.90}$$

$$\left\langle \left| u_j^\alpha \right|^2 \right\rangle = \int d\omega \frac{\hbar}{2m_j} \mathrm{DOS}(\omega) f_D\left(\omega, T\right) \left| \mathbf{e}_j^\alpha \right|^2 \tag{2.91}$$

Here, the factor $\omega^{-1}\left(1 + 2\left\langle n(\omega, T)\right\rangle\right)$ has been summarised in the spectral function f_D. It can be seen in Fig. 2.3(a) that f_D is restricted to very low frequencies - even for relatively high temperatures. For $T \to 0$, f_D converges to the hyperbolic function $1/\omega$, which can be seen as the most frequency-selecting limiting case.

As it has already been discussed in Eq. (2.84), the phonon heat capacity can be decomposed in a similar way, with the spectral function f_C acting like a temperature-dependent low-pass filter. The frequency and temperature behaviour is indicated in Fig. 2.3(b). Similarly to the spectral function of the MSTDs, also f_C preferentially selects low-frequency phonons. In contrast to f_D, f_C extends to much higher frequencies. In fact, its tail reaches higher frequencies than one would expect by estimating the occupied frequency with $\omega = k_B T/\hbar$: at 300 K, for instance, f_C decreases to half its maximum value at ~18.6 THz (see Sec. 4.2.5), while $k_B T$ only corresponds to ~6.2 THz. Due to the special form of the spectral function f_C, higher-frequency phonons start to play a role already at lower temperatures.

Besides the equation of the phonon heat capacity, the spectral function f_C also enters the expression of the thermal conductivity tensor obtained from the Boltzmann transport equation using the relaxation time approximation [64]:

$$\kappa_{\alpha\beta} = \frac{k_B}{N_q V} \sum_\lambda \eta_{\alpha\beta}^\lambda \tau_\lambda \tag{2.92}$$

$$\eta_{\alpha\beta}^\lambda k_B = f_C\left(\omega_\lambda, T\right) \left(\mathbf{v}_{g,\lambda} \otimes \mathbf{v}_{g,\lambda}\right)_{\alpha\beta} \tag{2.93}$$

Here, a new tensorial quantity, $\eta_{\alpha\beta}^\lambda$, has been introduced which contains all purely harmonic ingredients to the thermal conductivity tensor, while the phonon lifetime τ_λ is a result of anharmonic effects. As this thesis is (mostly) concerned with harmonic phonon properties, the tensor η should be analysed in slightly more detail. Apart from the spectral function f_C, it contains the dyadic product[18] of the group velocity vectors. Since the group velocities in molecular crystals typically decrease relatively rapidly with increasing frequency (see Sec. 4, 5), the product of group velocities drops even faster. Thus, due to this strong decaying behaviour of the group velocities in organic semiconductors, the spectral function f_C is typically not the limiting factor confining the spectral region of relevant phonon contributions. The mode-contributions to η_{xx} can be seen in Fig. 2.3(c) for the case of crystalline naphthalene.

Besides these three examples which nearly exclusively rely on the low-frequency phonons (at low temperatures), there are, however also quantities, for which also the higher-frequency phonons play a role. One such a a quantity is the Helmholtz free energy as

[18] The dyadic product of two vectors is defined as $\left(\mathbf{a} \otimes \mathbf{b}\right)_{ij} = a_i b_j$.

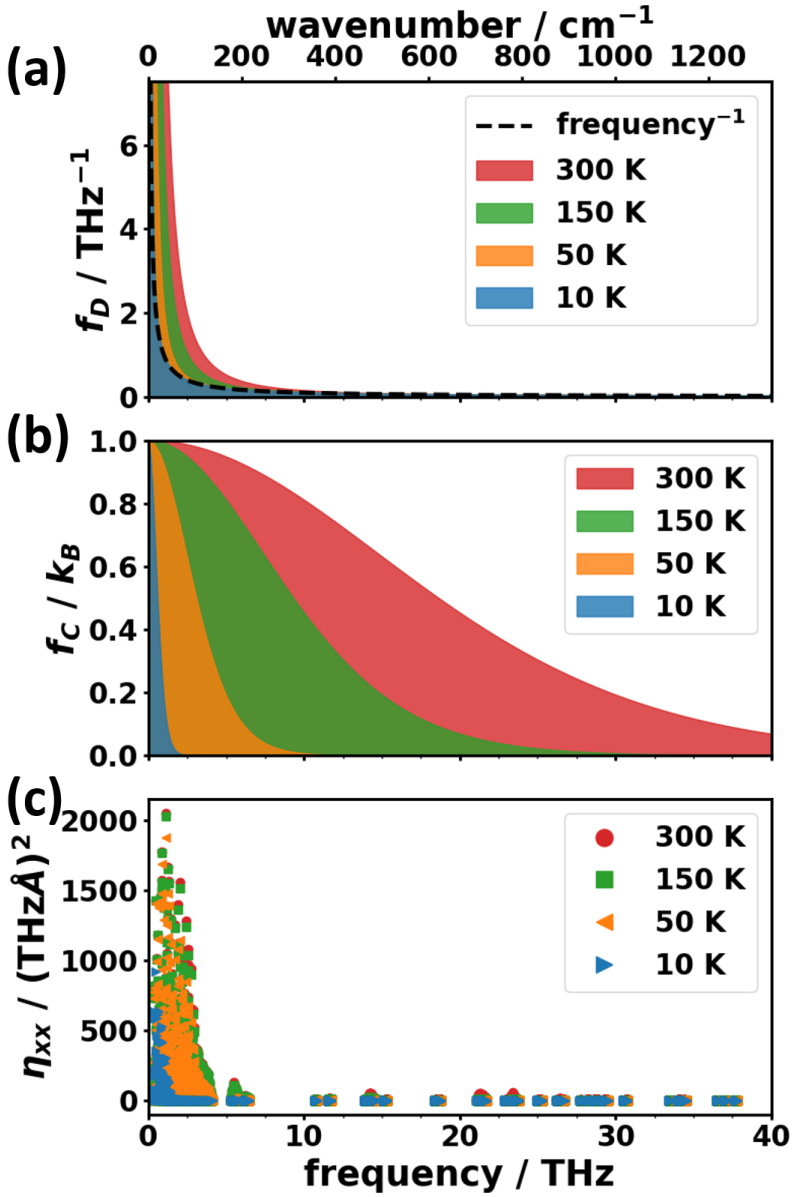

Fig. 2.3.: Frequency dependence of the spectral functions entering the equations of (a) the mean-squared thermal displacements, f_D (see Eq. (2.91)) and (b) the heat capacity, f_C (see Eq. (2.84)). (c) The mode contributions of the harmonic parts to the thermal conductivity, η_{xx} (for the xx-component; see Eq. (2.93)). This figure has been taken from Ref. [1].

derived in Sec. 2.4. Apart from the temperature-dependent entropic contribution, which also favours low-frequency phonons, the ZPE depends on all frequencies in the system to the same extent. For systems such as organic semiconductors, in which the phonon modes spread over a large spectral range - from the very-low frequencies of the acoustic modes (< 1 THz) up to the high-energetic C-H stretching oscillations at > 91 THz - one can imagine that the relative contributions to the ZPE - i.e. the main contribution to the free energy at (very) low temperatures - is much higher for the high-frequency modes (see Eq. (2.62)).

Therefore, when it comes to a quantitative comparison between different methods, it makes sense to split the analysis of frequencies and phonon-related properties into two separate regimes: a high-frequency and a low-frequency range. It is, however, relatively arbitrary where one draws the line between these two regimes. In the context of the methodology benchmark for crystalline naphthalene in the course of this thesis, the frequency 9 THz has been chosen to separate the low-frequency (≤ 9 THz) from the high-frequency (> 9 THz) considerations. This choice is, on the one hand, motivated by the fact that f_D and $\eta^{\lambda}_{\alpha\beta}$ are only significant within this frequency range and it is also the frequency, at which f_C drops to half its maximum at ~150 K. On the other hand, when comparing the Raman spectra for molecular and crystalline naphthalene (see Fig. 4.4), one can see that in the crystalline phase many Raman active modes below ~4 THz are present, which do not occur in the molecular phase. These modes, correspond to the intermolecular modes, which only appear in a crystalline environment in which neighbouring molecules interact by means of long-range interactions (van der Waals). Therefore, the chosen low-frequency regime contains all intermolecular modes as well as first low-lying optical intramolecular ones.

2.6. Density Functional Theory

After this discussion of various phonon-related properties, the current focus should be slightly shifted from the theoretical background to the practical simulations of phonon band structures. The only ingredient that one needs for phonon calculations are the harmonic force constants - i.e. the knowledge of how atomic forces change as a function of frequency. This means one must simply solve the electronic eigenvalue problem for several displaced atomic geometries one very mighty tool to do this also for practically relevant systems is density-functional theory (DFT) [65, 66]. Since DFT, which has gained a lot of popularity in the past decades, is already quite well-known and is only used in the context of this thesis as one of the possible tools to calculate the required forces, only the most basic ideas of DFT will be briefly recapitulated (using atomic units).
The main idea in DFT is that the ground state of a real quantum-mechanical system including all the complex correlations and interactions in an external potential uniquely determines this potential [65]. This means the ground state of the system can always be expressed as a functional of the electron density of the ground state. This leads to the following expression of the ground state energy (Hohenberg-Kohn variational principle):

$$
\begin{aligned}
E\left[n(\mathbf{r})\right] &= \min_{|\psi_\alpha|^2=n} \langle\psi_\alpha|H|\psi_\alpha\rangle \\
&= \int d\mathbf{r}\; n(\mathbf{r})V_{ext}(\mathbf{r}) + F\left[n(\mathbf{r})\right] \qquad (2.94)\\
\text{with} \qquad & F\left[n(\mathbf{r})\right] = \min_{|\psi_\alpha|^2=n} \langle\psi_\alpha|T+U|\psi_\alpha\rangle \qquad (2.95)
\end{aligned}
$$

Thus, the energy as functional of the ground state electron density, $n\left(\mathbf{r}\right)$, depends on the functional F. Formally, the latter corresponds to minimising the expectation values of the kinetic energy T and the electron-electron interaction U among all trial wave functions which result in the ground state density $n\left(\mathbf{r}\right)$.
Although this formalism is exact up to this point, the actual mathematical form of $F\left[n(\mathbf{r})\right]$ is unknown. An elegant way to reformulate the problem was introduced by Kohn and Sham [66]. Their idea is based on the following two steps. (i) It is more instructive to start with the case of non-interacting electrons ($U = 0$). The ground state energy for such a system is minimised if the ground state consists of single-electron orbitals ϕ_j (with $n(\mathbf{r}) = \sum_j \left|\phi_j(\mathbf{r})\right|^2$) which solve the following Schrödinger equation

$$
\left(-\frac{\nabla^2}{2} + V_{ext}(\mathbf{r}) - \epsilon_j\right)\phi_j(\mathbf{r}) = 0 \qquad (2.96)
$$

In analogy to the non-interacting case, they chose the following ansatz for the ground state energy incorporating the electron interaction ($U \neq 0$) in a new functional, the so-called exchange-correlation functional E_{XC}:

$$
\begin{aligned}
E\left[n(\mathbf{r})\right] &= \int d\mathbf{r}\; n(\mathbf{r})V_{ext}(\mathbf{r}) + \\
&+ \; T\left[n(\mathbf{r})\right] + \frac{1}{2}\int\int d\mathbf{r}\; d\mathbf{r}'\frac{n(\mathbf{r})n(\mathbf{r}')}{\|\mathbf{r}-\mathbf{r}'\|} + E_{XC}\left[n(\mathbf{r})\right] \qquad (2.97)
\end{aligned}
$$

In this famous *Kohn Sham equation*, the kinetic energy is taken from the non-interacting case and the electron-electron energy is expressed as a double integral corresponding to the coulomb repulsion of the charge densities. Moreover, the energy functional E_{XC} has been introduced. This so-called exchange-correlation energy contains the correlations, the exchange term and the difference between the used (non-interacting) kinetic energy and the interacting one. The problem of the unknown functional form of F has, thus, been shifted to the unknown functional E_{XC}. Using the energy of the Kohn Sham equation, one can again find that the energy is minimised for a set of one-electron orbitals (the so-called Kohn-Sham orbitals), which solve the following Schrödinger equation:

$$\left(-\frac{\nabla^2}{2} + V_{eff}(\mathbf{r}) - \epsilon_j\right)\phi_j(\mathbf{r}) = 0 \tag{2.98}$$

$$\text{with } V_{eff}(\mathbf{r}) = V_{ext}(\mathbf{r}) + \int d\mathbf{r}' \frac{n(\mathbf{r}')}{\|\mathbf{r} - \mathbf{r}'\|} + V_{XC}(\mathbf{r}) \tag{2.99}$$

$$\text{and } V_{XC}(\mathbf{r}) = \frac{\delta E_{XC}\left[n(\mathbf{r})\right]}{\delta n} \tag{2.100}$$

Thus, effectively, the interacting system is mapped onto an auxiliary system, which formally results in a solution which can be written as single-particle orbitals - similar to the non-interacting case, but with a different potential V_{eff} in the single-particle Schrödinger equation. Additionally, this effective potential contains the exchange-correlation potential V_{XC}, which is the functional derivative of the exchange-correlation energy functional with respect to the density. This energy, however, depends on the density that one desires to solve. Therefore, these equations must be solved self-consistently:

1. Start with a trial charge density n
2. From n calculate the effective potential V_{eff} for the single-particle Schrödinger equation using Eq. (2.99)
3. With V_{eff} solve to single-particle Schrödinger equation (Eq. (2.98)) for the Kohn-Sham orbitals ϕ_j. (In practice this is done by expanding the Kohn-Sham orbitals in basis functions $\phi_j = \sum_a C_{ja}\varphi_a$ and solving for the coefficients C_{ja}).
4. With the Kohn-Sham orbitals calculate the new density $n = \sum_j |\phi_j|^2$
5. Use the new density and start over with step 2. Repeat until the total energy converges.

It should be stressed at this point that still, the entire formalism is rigorously exact, i.e. no effective approximation has been made so far, as everything that goes beyond the interactions captured in the terms presented above is put into the exchange-correlation energy E_{XC}. The only approximation that remains is to use a certain (approximate) form for E_{XC}.
Naturally, over the years, people have come up with a number of exchange-correlation functionals, which are supposed to yield an improvement in one calculated property or another. The most basic functional is the local (spin) density approximation, L(S)DA, in which it is assumed that the exchange-correlation energy only depends on the (spin) density of the current electron configuration. The exchange part is approximated from the exact, analytically known exchange energy of an homogeneous electron gas, while the correlation part has been approximated by fitting curves to results from quantum Monte Carlo simulations of electron gases [67]. Unsurprisingly, the L(S)DA is more suitable for systems that are similar to the homogeneous electron gas - i.e. metals. For insulators, other approximations of the exchange-correlation functional involving the gradient of the

charge density as well - the so-called generalised gradient approximation (GGA) - fare much better, with the most prominent being the PBE functional named after Perdew, Burke, and Ernzerhof [68].
Beyond L(S)DA and GGA, there exist several hybrid functionals, which partially mix Hartree exchange into E_{XC} to a variable extent or mix the exchange and correlation parts of different functionals with various weights. One can imagine that some of the choices of the mixing parameters are made to reproduce one certain property with high accuracy while other disadvantages occur in turn. Although hybrid functionals, in principle, have the potential to achieve increased accuracy, one must be very careful to tune these parameters manually to obtain the desired results. Moreover, since all of them at least partly mix in the computationally expensive Hartree exchange energy, geometry optimisation in a crystal (necessary for phonon calculations) become quite expensive already for small systems because the exchange part has to be evaluated at each self-consistency step at each geometry step. Therefore, all of the presented data with periodic boundary conditions in this thesis have been obtained with the PBE functional.

2.6.1. *A posteriori* van der Waals corrections

One significant drawback of the (semi-)local approximations to DFT is, however, the non-explicit treatment of long-range van der Waals interactions. The physical origin of the van der Waals interaction is the correlation of electrons: due to an instant polarisation of the electron density around one nucleus (as a result of the charge fluctuation), the electron density of an neighbouring atom close by gets polarised (depending on its polarisability). To a first approximation, this can be described by a dipole-dipole interaction between an instantaneously formed dipole at one atom and an induced dipole at another one. The energy of a dipole equals (minus) the scalar product of the electric field $\mathbf{E}$ times the (induced) dipole moment vector $\mathbf{p}$ [7].

$$E_{dip} = -\mathbf{p}^{ind} \cdot \mathbf{E} \tag{2.101}$$

Since the field of the dipole on atom A induces a dipole on atom B and *vice versa* one can express the dipole moment on atom $A(B)$ via the corresponding polarisability α and the field of the other atom $B(A)$:

$$\mathbf{p}^{ind}_{A/B} = \alpha_{A/B}\mathbf{E}_{B/A} \tag{2.102}$$

The (dispersion) energy of these two dipoles, thus, equals:

$$E_{disp} = -\mathbf{p}^{ind}_{A} \cdot \mathbf{E}_B = -\mathbf{p}^{ind}_{B} \cdot \mathbf{E}_A \propto \alpha_A\alpha_B \left\|\mathbf{E}\right\|^2 \tag{2.103}$$

The electric field of a dipole is proportional to R^{-3}, with R being the distance from the dipole so that, in total, the energy can be written as:

$$E_{dip} = -C\alpha_A\alpha_B R^{-6} = -C_{6,\alpha\beta}R^{-6} \tag{2.104}$$

Together with an empirically found description of the (Pauli) repulsion of two atoms, a often used potential that describes the attractive and repulsive regime of the interatomic

interaction is the Lennard-Jones potential with the potential depth ϵ and the equilibrium distance $\sqrt[6]{2}\sigma$:

$$V(r) = 4\epsilon \left(\left(\frac{\sigma}{r}\right)^{12} - \left(\frac{\sigma}{r}\right)^{6} \right) \tag{2.105}$$

Although this potential is used very frequently in force field calculations and for gaining conceptual insights into van der Waals-bonded systems, it is of less importance for DFT calculations since the repulsive terms is already covered with the ordinary Kohn-Sham formalism. Thus, it suffices to be concerned about the attractive term in DFT. A van der Waals energy of that kind must be added to the (semi-)local DFT Kohn-Sham energy manually, which is often done in an *a posteriori* fashion. Similar to the variety in available exchange-correlation functionals, there exists also a broad spectrum of possible *a posteriori* van der Waals corrections for DFT [69, 70]. Alternatively, a few functionals also put the van der Waals interaction into the exchange-correlation functional like the vdW-DF functional of Dion et al. [71].

One of the simplest van der Waals correction is the D2 method of Grimme [72]. Within this method, the dispersion energy is approximated as a sum of pairwise contributions summed over all atoms of the unit-cell (double sum over atomic indices i, j) and all unit-cells A (of the second atom), with $r_{ij,A}$ being the distance between atom i in the "central unit-cell" and atom j in the unit-cell A in the crystal:

$$E_{disp} = -\frac{1}{2} \sum_{i,j,A} \frac{C_{6,ij}}{r_{ij,A}^{6}} f_{d,6}(r_{ij,L}) \tag{2.106}$$

In this simple approximation, the coefficients $C_{6,ij}$ are fixed parameters for each pair of atomic species. The values are tabulated for homonuclear cases (i.e. both atoms interacting via van der Waals forces belong to the same atomic species), while for heteronuclear cases, the coefficient is obtained from the mixing rule $C_{6,ab} = \sqrt{C_{6,aa} C_{6,bb}}$. This means that in this method any influences of the crystalline or molecular environment on the polarisability of the atom are neglected since always the same C_6 coefficients are used. Additionally, the dispersion energy contains a Fermi-type damping function, which relies on three global parameters as well as species-specific ones. It is supposed to damp the dispersion energy contribution continuously for small distances at which the covalent interactions are already covered within DFT.
A remarkable improvement of this approach is achieved by the D3 correction of Grimme [73]. In this correction, the dispersion energy includes an additional term proportional to $r_{ij,A}^{-8}$:

$$E_{disp} = -\frac{1}{2} \sum_{i,j,A} \left(\frac{C_{6,ij}}{r_{ij,A}^{6}} f_{d,6}(r_{ij,L}) + \frac{C_{8,ij}}{r_{ij,A}^{8}} f_{d,8}(r_{ij,L}) \right) \tag{2.107}$$

Apart from the additional term, the most important difference to D2 is the fact that the $C_{6/8}$ coefficients are made dependent on the local geometry: depending on the covalent radii of the involved atoms, fractional coordination numbers are calculated based on

which the actual C_6 coefficients are derived from a two-dimensional interpolation scheme. The C_8 coefficients are directly calculated from the corresponding C_6 parameters and second and fourth moments of the charge density of an atom. It is obvious that the coefficients evaluated in this way are much more likely to represent the actual situation as they are flexibly adapted to the actual local geometry. A further difference to the D2 method is the chosen damping function. In fact, the D3 correction is available with two different choices of damping functions: the so-called D3-zero and the D3 correction with Becke-Johnson damping (D3-BJ) [74]. Since the latter has been applied in the context of this thesis, the damping function should be briefly commented on. The two damping functions ($n = 6, 8$) are given by the following equation:

$$f_{d,n}(r_{ij}) = \frac{s_n r_{ij}^n}{r_{ij}^n + (a_1 R_{0,ij} + a_2)^n} \quad \text{with } R_{0,ij} = \sqrt{\frac{C_{8,ij}}{C_{6,ij}}} \tag{2.108}$$

In this function, s_n, a_1, and a_2 are global parameters which must be adjusted depending on the used exchange-correlation functional. This functional form of $f_{d,n}$ assures that the dispersion interaction is damped to zero at small distances, while it approaches s_6 (which is typically set to unity) for large distances. Moreover, the term in brackets in the denominator corresponds to the distance at which the damping function reaches half its maximum. Thus, the damping behaviour is not only controlled globally by the functional-dependent parameters, but also by means of the local atomic geometry affecting the coefficients $C_{6/8}$ and, thus, R_0. In contrast to the Fermi-type damping function used in the D2 correction, the dispersion interaction is, thus really damped to zero at zero distance, and, moreover, the damping is more gradual compared to the exponential term in D2.
An alternative approach to improve the D2 correction different than introducing an additional r_{ij}^{-8}-term is offered by the correction of Tkatchenko and Scheffler (TS) [75]. The expression of the dispersion energy is formally equal to that in Grimme's D2 correction, but the C_6 coefficients are not fixed, tabulated values. The concept of the TS correction is based on the relation that the product of the atomic polarisability of a free atom α_i^{free} and an "effective atomic volume" v_i yields the polarisability of the same atom in the given chemical environment α_i. Since the C_6 coefficients depend on the polarisability squared, the TS approach states:

$$C_{6,ii} = v_i^2 C_{6,ii}^{free} \tag{2.109}$$

The free atom quantities must, again, be tabulated. The effective atomic volumes, however, are calculated on the fly for the given chemical/crystalline environment according to a Hirshfeld partitioning of the electron density:

$$v_i = \frac{\int d\mathbf{r}\ r^3 w_i(\mathbf{r}) n(\mathbf{r})}{\int d\mathbf{r}\ r^3 n_i^{free}(\mathbf{r})} \tag{2.110}$$

Here, the density n_i^{free} is the spherically averaged electron density of an isolated (neutral) atom of species i, while w_i is the so-called Hirshfeld weight, which is the fraction of n_i^{free}

relative to all atoms in the system:

$$w_i(\mathbf{r}) = \frac{n_i^{free}(\mathbf{r})}{\sum_{k=1}^{N} n_k^{free}(\mathbf{r})} \tag{2.111}$$

In the TS approach, also the mixing rule for heteronuclear C_6 coefficients is a different one relying on the calculated atomic polarisabilities:

$$C_{6,ij} = \frac{2C_{6,ii}C_{6,jj}}{\frac{\alpha_j}{\alpha_i}C_{6,ii} + \frac{\alpha_i}{\alpha_j}C_{6,jj}} \tag{2.112}$$

Although the TS approach offers a (supposedly) more sophisticated way to calculate the C_6 coefficients, it still relies on a two-body description of the dispersion energy and, according to Ref. [76], it lacks a consistent description of long-range dipole-dipole interactions due to screening effects. These weaknesses are improved in the so-called many-body dispersion (MBD) correction [76, 77]. In the MBD approach, the dispersion energy is based on the frequency-dependent atomic polarisabilities $\alpha^0(\mathrm{i}\omega)$ calculated in the TS correction. However, these atomic polarisabilities are used to separately describe the short-range and long-range interactions in two different ways: the short-range atomic polarisability is obtained by solving the range-separated (rs) self-consistent screening (SCS) equation from classical electrodynamics.

$$\alpha^{rsSCS}(\mathrm{i}\omega) = \alpha^0(\mathrm{i}\omega) - \alpha^0\mathbf{T}_{SR}\alpha^{rsSCS}(\mathrm{i}\omega) \tag{2.113}$$

Here, $\mathbf{T}_{SR}$ is the short-range (SR) dipole-dipole interaction operator, which is obtained from the full dipole-dipole interaction operator via an additional Fermi-type damping factor (see Eq. (12) and (13) in Ref. [77]). The actual form of the dipole-dipole interaction tensor is obtained by considering the fluctuation dipoles as charged atom-centred quantum harmonic oscillators with Gaussian charge distributions. In the long-range regime, the correlation of oscillating (induced) dipoles is treated within the random phase approximation. Using the rsSCS polarisabilities, one defines a diagonal matrix $\mathbf{A}$ with $A_{mn} = -\delta_{mn}\alpha^{rsSCS}(\mathrm{i}\omega)$, with the help of which the MBD dispersion energy can be calculated in analogy to the correlation energy in the random phase approximation using the long-range (LR) part of the dipole-dipole interaction operator:

$$E_{c,MBD} = \frac{1}{2\pi}\int_0^\infty d\omega\, \mathrm{tr}\left\{\ln\left(\mathbb{1} - \mathbf{A}\mathbf{T}_{LR}\right)\right\} \tag{2.114}$$

Thus, in this van der Waals correction no explicit two-, three-, ..., N-body terms are considered within the MBD approach, as all possible interactions are accounted for due to the usage of the random phase approximation. Being a highly elegant solution to the problem, the MBD approach only relies on relatively few parameters: two parameters entering the Fermi-type damping function for the range separation (with one of them being kept fixed, while the other one has to be adapted for the used functional). The

only input needed for the calculation of the TS polarisabilities is reference data of free atoms (atomic polarisabilities, C_6 coefficients and van der Waals radii of free atoms), which can be tabulated and read from internal databases.

2.7. Density Functional Tight Binding

Although DFT is already orders of magnitude faster than (supposedly more accurate) wave function-based methodologies such as post-Hartree Fock methods, the computational efficiency of DFT is still far too low to handle systems that go beyond a certain size. For problems of that kind several more approximate methods[19] have been proposed to speed-up quantum-mechanical calculations yet preserving an acceptable accuracy of the results. One such approximate method is density-functional (based) tight binding (DFTB). Since this methodology has been tested with regard to its suitability to accurately reproduce (experimental) phonon band structures in organic semiconductors, the basic concepts of DFTB should be briefly summarised in this section. The equations and the arguments are based on the reviews of Koskinen and Mäkinen [78] and Oliveira et al. [32].

Starting point for deriving the DFTB formalism is the Kohn-Sham energy as presented in Eq. 2.97. Here, it is however necessary to include one additional energy term, which has been omitted in the introduction of DFT: the ion-ion repulsion E_{II}. A central idea in DFTB is the comparison of the actual ground state density $n(\mathbf{r})$, which minimises the DFT functional, with a density $n_0(\mathbf{r})$, which is the superposition of the free atomic charge densities ρ_a of all the atoms a in the system (at position $\mathbf{R_a}$) - i.e. n_0 is the charge density of an artificial system in which all the atoms are present but their charge densities are not affected by the presence of other atoms in the proximity (no charge transfer as a consequence of any bonding motifs):

$$n_0(\mathbf{r}) = \sum_a \rho_a(\mathbf{r} - \mathbf{R_a}) \tag{2.115}$$

One assumes that the difference charge density $\delta n(\mathbf{r})$ between the real ground state density n and n_0 is small.

$$n(\mathbf{r}) = n_0(\mathbf{r}) + \delta n(\mathbf{r}) \tag{2.116}$$

The next step is an expansion of the energy functional $E[n(\mathbf{r})]$ in powers of $\delta n(\mathbf{r})$:

[19] One might well consider DFT an approximate method. The amount of approximations and the degree of abstraction are, however, significantly higher in such "approximate methods" than in DFT.

$$E\left[n(\mathbf{r})\right] = E\left[n_0(\mathbf{r})\right] + \int d\mathbf{r}\, \frac{\delta E\left[n(\mathbf{r})\right]}{\delta n}\bigg|_{n_0(\mathbf{r})} \delta n(\mathbf{r}) + \tag{2.117}$$

$$+\frac{1}{2}\int d\mathbf{r}' \int d\mathbf{r}\, \frac{\delta^2 E\left[n(\mathbf{r})\right]}{\delta n \delta n'}\bigg|_{n_0(\mathbf{r}),n_0(\mathbf{r}')} \delta n(\mathbf{r})\delta n(\mathbf{r}') + \tag{2.118}$$

$$+\frac{1}{6}\int d\mathbf{r}'' \int d\mathbf{r}' \int d\mathbf{r}\, \frac{\delta^3 E\left[n(\mathbf{r})\right]}{\delta n \delta n' \delta n''}\bigg|_{n_0(\mathbf{r}),n_0(\mathbf{r}'),n_0(\mathbf{r}'')} \delta n(\mathbf{r})\delta n(\mathbf{r}')\delta n(\mathbf{r}'') + \ldots \tag{2.119}$$

The expansion of the energy functional is carried out up to second order in ordinary DFTB, while the third order term is included in the so-called DFTB3 method [79]. If this expansion (up to second order) - i.e. the functional derivatives with respect to the charge density - is applied to the energy terms of the Kohn-Sham equation, the following three energy terms can be identified:

$$E\left[n_0(\mathbf{r}) + \delta n(\mathbf{r})\right] = E_{BS}\left[n_0(\mathbf{r})\right] + E_{rep}\left[n_0(\mathbf{r})\right] + E_{CF}\left[n_0(\mathbf{r}), \delta n(\mathbf{r})\right] \tag{2.120}$$

The first terms is called the band structure energy, E_{BS}, and only depends on $n_0(\mathbf{r})$ (the superposition of free atomic charge densities). In essence, E_{BS} equals the sum of all the expectation values of the one-particle Hamiltonians in the Kohn-Sham formalism (see Eq. (2.98)), $\hat{h}$, considering a proper (spin) occupation f for all these orbitals i:

$$E_{BS}\left[n_0(\mathbf{r})\right] = \sum_i f_i \left\langle \widehat{h}\left[n_0(\mathbf{r})\right] \right\rangle \tag{2.121}$$

Thus, no information about the charge transfer density $\delta n(\mathbf{r})$ enters the band structure energy. The case is similar for the second term, which is labelled the *repulsive energy* E_{rep}:

$$E_{rep}\left[n_0(\mathbf{r})\right] = E_{XC}\left[n_0(\mathbf{r})\right] - \frac{1}{2}\int d\mathbf{r} \int d\mathbf{r}' \frac{n_0(\mathbf{r})n_0(\mathbf{r}')}{\|\mathbf{r}-\mathbf{r}'\|} - \int d\mathbf{r}\; n(\mathbf{r})V_{XC}\left[n_0(\mathbf{r})\right] + E_{II} \tag{2.122}$$

Although the repulsive energy could, in principle, be calculated for a given exchange-correlation functional, one typically neglects the exact form of E_{rep} and relies on fitted data for pairwise potential interactions depending only on the distance between the two atoms:

$$E_{rep} \approx \sum_{i<j} V_{rep}^{ij}\left(\|\mathbf{r}_i - \mathbf{r}_j\|\right) \tag{2.123}$$

This step might appear somewhat concerning at first glance, but it is typically justified that at least the ion-ion repulsion E_{II} and the double integral can be seen as sums over pairwise contributions. In practice, the functions V_{rep}^{ij} are fitted to high-accuracy reference data (at several distances) for all pairs of atomic species, which is often the crucial part determining the quality of a DFTB calculation [80]. This concept renders DFTB "less *ab-initio*", but drastically increases its speed.

The last term in the expression for the total energy in DFTB besides E_{rep} and E_{BS} is the charge fluctuation term E_{CF}:

$$E_{CF}\left[n_0(\mathbf{r}), \delta n(\mathbf{r})\right] = \frac{1}{2}\int d\mathbf{r} \int d\mathbf{r}' \left(\left.\frac{\delta^2 E_{XC}\left[n(\mathbf{r})\right]}{\delta n \delta n'}\right|_{n_0(\mathbf{r}),n_0(\mathbf{r}')} + \frac{1}{\|\mathbf{r}-\mathbf{r}'\|} \right) \delta n(\mathbf{r}) \delta n(\mathbf{r}')) \tag{2.124}$$

This more complicated double integral is, subsequently, evaluated based on the following assumptions:

1. The charge fluctuation density δn can be written as a sum of atomic contributions which consist of the absolute atomic charge difference Δq_i and a spatial distribution function $p_i(\mathbf{r})$: $\delta n(\mathbf{r}) = \sum_i \Delta q_i p_i(\mathbf{r})$. Note that these charge differences Δq_i are *a priori* unknown, but they are determined self-consistently (see below).

2. For products of those atomic contributions to the charge fluctuation density, which belong to the same atom ($i = j$), the charge fluctuation term is related to the Hubbard U (approximately equal to the ionisation energy minus the electron affinity).

3. For products of those atomic contributions to the charge fluctuation density, which belong to different atoms ($i \neq j$), the second derivative of the exchange-correlation functional in the equation above will vanish in case of local exchange-correlation functionals, and only the Coulomb contribution survives.

4. The spatial distribution functions $p_i(\mathbf{r})$ are assumed to be spherically symmetric Gaussian distributions. Constraining the spatial distributions to this special mathematical form, the integrals can be evaluated.

Finally, the charge fluctuation term is approximated as a (double) sum over pairwise contributions involving the absolute charge transfers Δq_i on each atom i and a function γ[20], depending on the distance R_{ij} between two atoms i and j:

$$E_{CF} \approx \frac{1}{2}\sum_{i,j} \gamma_{ij}\left(R_{ij}\right) \Delta q_i \Delta q_j \tag{2.125}$$

$$\gamma_{ij}\left(R_{ij}\right) = \begin{cases} U_i & \text{for } i = j \\ \operatorname{erf}\left(C_{ij} R_{ij}\right)/R_{ij} & \text{for } i \neq j \end{cases} \tag{2.126}$$

In the historically earlier versions of the DFTB formalism, the charge fluctuation term E_{CF} was neglected so that the entire system has actually been treated as a superposition of (free) atomic, spherically symmetric, charge densities. In the so-called self-consistent-charge (SCC) DFTB, which is the state-of-the-art flavour of DFTB nowadays, one, however, cares about the charge transfer Δq_i, which must be considered in a self-consistent

[20] Due to the Gaussian spatial distribution functions, the function γ contains the error function, $\operatorname{erf}(x)$, and the parameter C_{ij}, which is related to the standard deviations of the distributions $p_i(\mathbf{r})$ and $p_j(\mathbf{r})$.

iterative manner.
Although most of the expression for the DFTB energy is known at that point, one is still not able to evaluate the band structure energy - i.e. the expectation values of the single-particle Hamiltonians - because the Kohn-Sham states are not known yet. To do so, a next step of simplification is introduced by the tight-binding (TB) formalism, within which the DFTB energy is evaluated. This means that only the valence electrons of each atom are considered, while inner core electrons are supposed to be already treated within the repulsion energy. Based on a linear combination of atomic orbitals (LCAO), the a^{th} state of the system is expressed with a minimal local basis (i.e. only one atomic orbital function for each pair of (l, m) angular momentum quantum numbers):

$$\psi_a = \sum_{\mu} C_{\mu}^{a} \varphi_{\mu}(\mathbf{r}) \tag{2.127}$$

Using this sum of ansatz atomic orbitals for the single-particle KS-Hamiltonian, (and multiplying with $\varphi_{\nu}^{*}(\mathbf{r})$) from the left, one finds the final expression for the DFTB energy (with the Hamilton matrix $h_{\nu\mu} = \langle \varphi_{\nu} | \, \widehat{h} \, | \varphi_{\mu} \rangle$ and the overlap matrix $S_{\nu\mu} = \langle \varphi_{\nu} | \varphi_{\mu} \rangle$, which enters the expression for the charge transfer $\Delta q_{i,j}$, see Ref. [78]):

$$E = \sum_{a} f_a \sum_{\mu\nu} \left(C_{\mu}^{a} \right)^{*} C_{\nu}^{a} h_{\mu\nu} + \frac{1}{2} \sum_{i,j} \gamma_{ij} \left(R_{ij} \right) \Delta q_i \Delta q_j + \sum_{i<j} V_{rep}^{ij} \left(\| \mathbf{r}_i - \mathbf{r}_j \| \right) \tag{2.128}$$

This expression can be evaluated relative efficiently because in DFTB, the matrix elements of the Hamilton matrices and the overlap matrices are not calculated, but stored in so-called Slater-Koster files, as they only depend on quantities of free atoms. I.e. to successfully set-up a DFTB calculation, one must read those Slater-Koster files for each possible pair of atomic species. These files contain all the necessary matrix elements and the repulsive energy contributions as a function of the interatomic distance.
The DFTB energy is minimised by solving the generalised eigenvalue problem for the expansion coefficients C_{ν}^{a} (introducing Lagrange multipliers ϵ_a to keep the norm of the wave functions fixed):

$$H_{\mu\nu} C_{\nu}^{a} = \epsilon_a S_{\mu\nu} C_{\nu}^{a} \tag{2.129}$$

This equation involves a new Hamilton matrix $H_{\mu\nu}$, which contains the original matrix elements $h_{\mu\nu}$, the overlap matrix $S_{\mu\nu}$, and parts of the charge fluctuation energy including the charge transfer Δq_i of each atom (see Ref. [78]). It is important to note that this equation is the DFTB-equivalent to the Kohn-Sham equation in DFT and must be solved iteratively, with the variable quantities being the charge transfers: starting from guessed values for Δq_i on each atom, the matrix $H_{\mu\nu}$ can be determined. In a next step, this matrix is used in the equation above to solve for the expansion coefficients C_{ν}^{a}. These coefficients can be used to calculate the DFTB energy, but also determine the new charge fluctuation. Thus, one calculates new charge fluctuations from the expansion coefficients, plugs them into the generalised eigenvalue equation, obtains new expansion coefficients and so on, until the DFTB energy does not significantly change any more.

In summary, DFTB offers a fast framework relying on a self-consistent determination of charge transfer within a system. The higher computational speed is achieved by (i) a choice of a minimal basis set, (ii) the absence of the necessity to calculate any integrals of these basis functions, but rather read them from provided tables, and (iii) obtain the repulsion energy from pairwise, tabulated functions. This increase in speed comes, however, at a cost of making several assumptions: (i) the repulsion energy can be treated as a sum of pairwise contributions, (ii) the charge transfer (with respect to free isolated atoms) are treated only as spherically symmetric Gaussian distributions, (iii) only valence electrons are considered in the tight-binding formalism (accompanied by neglecting several overlap integrals), and (iv) the DFT-energy is expanded only up to second (third) order in DFTB(3).
Regarding the treatment of van der Waals interactions, DFTB must rely on the same corrections as in DFT, with some of them being more difficult to apply in the framework of DFTB. Here, Grimme's D3(-BJ) or D2 correction are most easily applicable since the C_6 coefficients are essentially based on tabulated data - completely in agreement with the spirit of DFTB - and only require an interpolation based on local coordination numbers in the case of D3(-BJ).

2.8. Classical Force Fields

If one is only interested in the properties and the dynamics of the atoms of a system, an alternative and even more approximate and empirical method is describing the nuclear interactions and, thus, the potential energy surface, directly, which are actually defined by the electrons. This can be done by using so-called force fields or force field potentials, which contain explicit expressions for each kind of interaction one wants do describe in a system. In other words, they provide fixed (and parametrised) expressions for (low-dimensional sections of) the potential energy surface.
For example, the *General Amber Force Field* (GAFF, see Ref. [81]) has a very simple functional form. Therefore, it is instructive to introduce the concept of force fields based on the comparably simple mathematical relations used in the GAFF. The GAFF considers the potential energy of a system as being describable as the sum of the following very simplistic terms:

$$\begin{aligned} E &= \sum_b K_b \left(l_b - l_b^0\right)^2 + \sum_a K_a \left(\theta_a - \theta_a^0\right)^2 + \sum_d \sum_n \frac{V_{n,d}}{2} \left[1 + \cos\left(n\varphi_d - \gamma_{n,d}\right)\right] + \\ &+ \sum_{i=1}^{N-1} \sum_{j=i+1}^{N} \left\{ 4\epsilon_{ij} \left[\left(\frac{\sigma_{ij}}{r_{ij}}\right)^{12} - \left(\frac{\sigma_{ij}}{r_{ij}}\right)^{6} \right] + \frac{q_i q_j}{4\pi\epsilon_0 r_{ij}} \right\} \end{aligned} \tag{2.130}$$

The first term in this expression is a sum of harmonic bond stretching potentials. I.e. for each bond b, a bond length l_b which differs from their equilibrium bond length l_b^0 adds a quadratic contribution (with bond stretching force constant K_b) to the energy. The next term in Eq. (2.130) is similar, but the summation runs over all bond angles a: every duplet of two adjacent bonds in a system is assigned a bond angle (i.e. the bond angle

is determined by three atoms), for which also a harmonic ansatz for its contribution to the total energy is made (equilibrium angle θ_a^0, force constant K_a).
The last term in the first line of Eq. (2.130) corresponds to the energy of all dihedrals d in the system - i.e. in an atomic bond sequence of atoms i, j, k, l which do not share a common plane, the (proper) dihedral angle refers to the angle between the plane spanned by atoms i, j, k and the plane spanned by atoms j, k, l. Since an angle like this is typically periodic and shows several minima, it is typically more intuitive to describe such an interaction in terms of a Fourier series. Here, besides the varying periodicity of the cosine terms (determined by $n\phi_d$), each of them additionally has a parameter $\gamma_{n,d}$ to account for the correct position of the energy minimum. For the sake of completeness, one must mention that there is another type of interaction that is described with the Fourier sum: improper torsions or out-of-plane bending. These terms typically cause an energetic penalty if one of four atoms, which are supposed to lie in a common plane, bends out of this plane. The typical picture of the atomic arrangement in such an improper torsion is the following: the central atom i has three bonds - to j, k, and l. Initially, they are in the same plane, but if one of them - e.g. atom l - bends out of the plane, this motion is penalised with an typically harmonic term, quadratic in the angle (or height) of the out-of-plane-bending. In GAFF, such an interaction is described via the dihedral Fourier series only including the term for $n = 2$.
These three terms in the GAFF are typically referred to as the "bonded terms" because they are supposed to describe interactions between covalently bonded sequences of two, three or four atoms. Force fields with these simple expressions for the bonded interactions are typically classified as Class I force fields. The complexity can, of course, tremendously increase by considering not only those simple harmonic interactions but parametrise them by anharmonic ones relying on more (fit) parameters. Besides the anharmonic description of bond stretches, bond angles etc. one could also introduce so-called cross terms, which couple different degrees of freedom in the system - e.g. an interaction of a bond stretch witch another bond stretch, or the coupling between one bond angle and a dihedral and so on. Including cross terms besides anharmonic bonded interactions, the force field is classified a Class II force field [82], such as *COMPASS* [83] or *MOF-FF* [84] (see Sec. 3). Beyond Class II force fields, the highest complexity of interactions such as hyperconjugation, polarisation etc. is exerted by Class III force fields, which have, however, not been considered in the context of this thesis.

Apart from the bonded terms, which describe the through-bond interactions, the second line in Eq. (2.130) contains the non-bonded terms responsible for the through-space interactions of atoms. Here, they are the van der Waals interaction - described via the Lennard-Jones potential which has already been introduced earlier - and a Coulomb term depending on the atomic charges $q_{i/j}$ of atoms i and j. The van der Waals interaction has been extensively discussed in Sec. 2.6.1 in the context of DFT *a posteriori* corrections so that it is obvious that the Lennard-Jones potential is only one of the possible choices to account for the dispersion forces. Apart from this special functional form, many other description as well as different mixing rules to obtain the heteronuclear parameters from the homonuclear ones have been designed showing different drawbacks

and merits. One of the largest problems in this context is the description of the repulsive part: while in electronic structure calculations, this term is accounted for naturally due to the electron (Pauli) repulsion, here, it is described using one of many (empirically found) functions such as high-order polynomials (like in the Lennard-Jones potential) or exponential functions (like in the so-called Buckingham potential [85]). Those alternative descriptions of the van der Waals interactions in FFs will, however, not be discussed here in more detail.
Eventually, one should spend a few words on the last term representing the Coulomb interactions, here described as a pairwise interaction of point charges depending on the distance like $1/r_{ij}$, which effectively makes them long-range interactions. In this expression, the concept of atomic charges is somewhat problematic. Since atomic charges are by no means physical observables, the definition of an atomic charge leaves a lot of space for interpretation[21]. One could use a proper partitioning scheme of electronic charge densities obtained from, e.g., a DFT calculation to calculate the atomic charges. Another more meaningful approach is to determine the atomic charges such that the total electrostatic potential fits that of a reference (so-called ESP charges, electrostatic potential). Alternatively to the description via point charges, some force fields use fixed charge distributions (e.g. Gaussian distributions similar as in DFTB) for the Coulomb term.

Finally, it should be stressed that, in contrast to the more common application of force fields, namely molecular dynamics (MD) simulations, in which the Newtonian equations of motions are integrated, here no MD simulations have been carried out. Therefore, it is neither necessary to discuss the integration schemes for the equations of motion nor the different available thermo- and barostats. In the context of this theses, force fields have only been used to calculate the 0 K-phonon band structure by means of finite displacements.

[21] A physically more accessible quantity is the so-called Born-effective charge, which is the first derivative of the polarisation with respect to an atomic displacement, as they directly enter the experimentally observable infra-red intensities [86].

3. Methodology and Computational Details

3.1. Phonon Properties for the Benchmark of Approximate Methodologies

In this subsection the relevant simulation settings for the benchmark of approximate methodologies are reported, with all of them focussing on crystalline naphthalene. Since the tested methodologies comprise three different levels of theory (employing three different available code packages), the parameters are presented separately. The dominant part of the content of this subsection has already been published in Ref. [1]. Nevertheless, graphics and data which were taken from Ref. [1] are explicitly labelled as such in the following.

3.1.1. Density-Functional Theory Calculations

The first level of theory is density-functional theory (DFT)[22]. Calculations at this level were carried out with the *Vienna Ab-Initio Simulation Package* (*VASP*) [38, 39, 40, 87] (version 5.4.1). All the used settings reported here are equal to the ones reported in Ref. [1]. The exchange-correlation energy was evaluated using the PBE functional [68]. To increase the computational efficiency, core electrons have been treated by means of the (recommended standard) pseudopotentials [41] for the projector-augmented wave method [88]. The occupation of electronic states was described using a Gaussian smearing width a width of $\sigma = 0.05$ eV. In calculations in which the primitive unit-cells were used, electronic wave vectors have been sampled on a $2 \times 3 \times 2$ **k**-mesh together with a plane wave energy cutoff of 900 eV in order to converge the total energy to an accuracy below 0.5 meV per atom in the unit-cell. Careful tests showed that this level is sufficient to obtain well-converged phonon frequencies: the Γ frequencies of naphthalene are essentially constant for more wave vectors beyond a $2 \times 3 \times 2$ mesh (see Fig. 3.1). Conversely, when supercells have been considered ($2 \times 3 \times 2$ supercells, see Sec. 3.1.4), only electronic states at the centre of the first Brillouin zone, Γ, were used.

The atomic coordinates and the unit-cell parameters were optimised simultaneously with the conjugate gradient algorithm under the side condition of constant unit-cell volume. This approach has been repeated for several volumes such that the total energy of the optimised geometries at each volume could be fitted to a Rose-Vinet equation of state [89]. This approach not only yields additional information including the bulk modulus and its pressure derivative, but also mostly omits Pulay stresses due to small inconsistencies between the plane wave basis set and the altered unit-cell volume in the course of the optimisation [90]. Finally, the unit-cell parameters and the atomic coordinates were optimised for the volume that minimises the energy according to the fitted equation of state.

As described in Ref. [1], this type of optimisation has been carried out separately

[22] It should again be stressed that all the following calculations and tests within the DFT level of theory were carried out by myself.

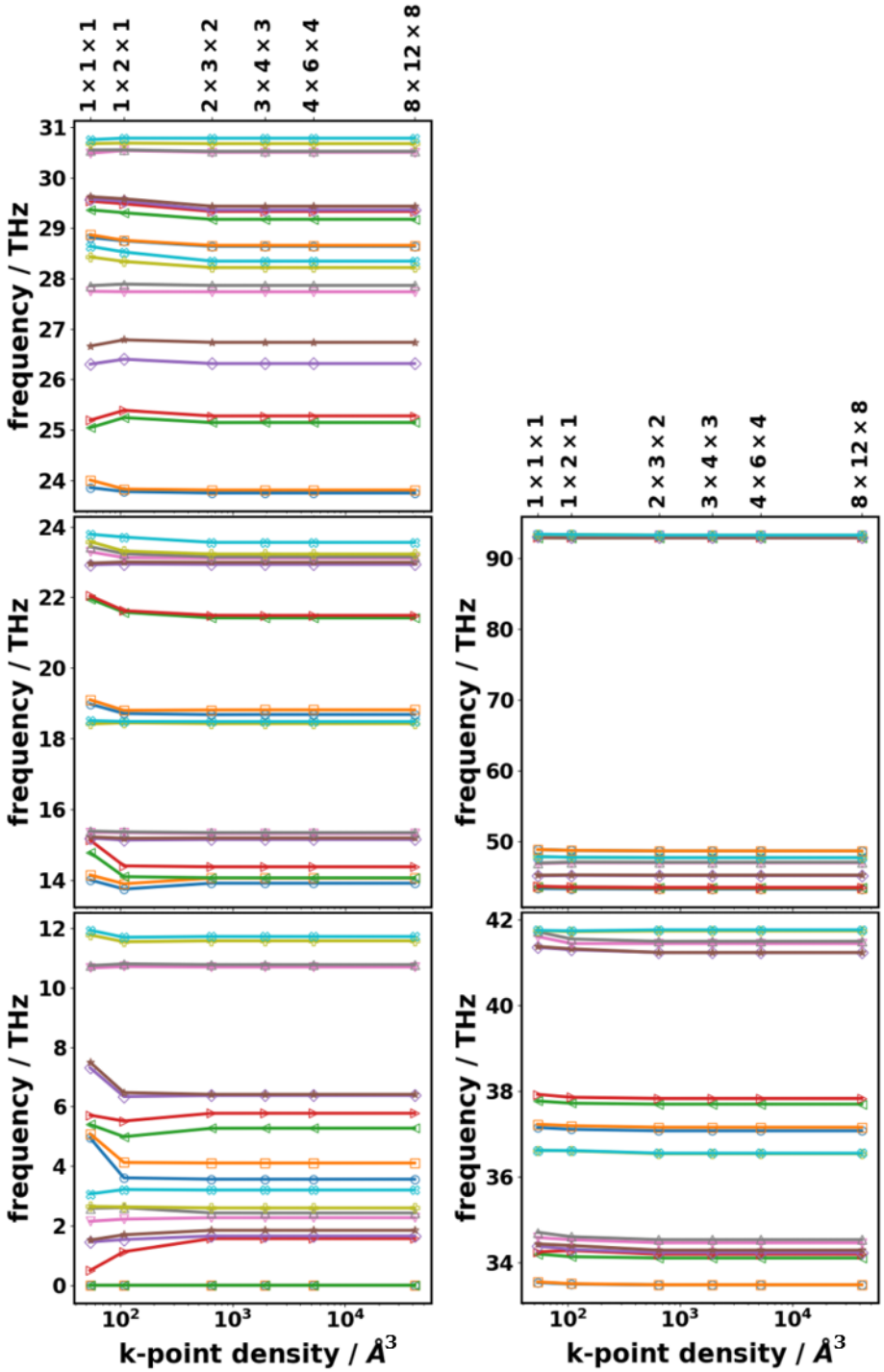

Fig. 3.1.: Convergence behaviour of PBE/D3-BJ-calculated Γ-frequencies in naphthalene as a function the sampling density of the electronic first Brillouin zone. The shown frequencies were obtained based on the same primitive unit-cell, for which the sampling density of electronic wave vectors was varied in the frequency calculations only, but not in the geometry optimisation. The secondary abscissa indicated the (Γ-centred) **k**-meshes, while the primary abscissa shows the corresponding density (= number of **k**-points per volume of the first Brillouin zone).

with the four tested van der Waals corrections: Grimme's D2 [72], D3 [73] with Becke-Johnson damping [74] (D3-BJ), the Tkatchenko and Scheffler (TS) scheme [75], and the many-body dispersion (MBD) method [76, 77], as implemented in *VASP*. For the sake of completeness, the (default) settings for the free parameters used in the D3-BJ correction in combination with the PBE functional implemented in *VASP* should be listed: $a_1 = 0.4289$ Bohr, $a_2 = 4.4407$, $s_6 = 1.0$, and $s_8 = 0.7875$, according to the *VASP* manual [91].

The plane wave energy cutoff (*VASP* tag `ENCUT`), the global precision parameter which mainly determines the Fourier integration grid (`PREC`), and the convergence criterion for the total energy in the self-consistent field (SCF) loop (`EDIFF`) have been carefully tested in terms of their impact on the Γ-frequencies in the PBE/D3-BJ unit-cell. Note that the atomic positions and unit-cell parameters in these tests have not been re-optimised with those tested simulation settings. For a more detailed description of these *VASP*-specific tags, please refer to the manual of the code [91].

In order to quantify the quality of the convergence with respect to those three simulation parameters, the root-mean-square (RMS) errors and the maximum absolute error in frequency compared to the supposedly most accurate settings (highest plane wave cutoff of 900 eV, global precision `Accurate`, and SCF convergence criterion of 10^{-8} eV), which were also used to optimise the lattice vectors and the atomic positions as described above, have been calculated. The resulting map of RMS errors and maximum absolute errors are shown in Fig. 3.2(a) and (b), respectively [1]. Fig. 3.2 shows that the Γ-frequencies depend much more strongly on the plane wave cutoff (`ENCUT`) than on the global precision (`PREC`) and the SCF convergence criterion (`EDIFF`) - as already shown in the Supporting Information of Ref. [1]. Furthermore, one can see that the RMS error and the maximum absolute (MA) error do not decrease with the cutoff in the same way: while the RMS error appears to decrease more gradually, which is visible in the intermediate RMS errors for a cutoff of 500 eV, the MA error experiences a much more considerable drop upon increasing the plane wave cutoff from 400 to 500 eV. Both error indicators, however, show occurrences in which the error does not monotonically decrease with the cutoff. Moreover, one can discern a surprising peculiarity: for smaller plane wave energy cutoffs, the global precision `Normal` results in reduced errors compared to the `Accurate` settings. The simulation with the supposedly worst simulation settings (top left in Fig. 3.2) yields smaller RMS and MA errors than other simulations with the same cutoff but tighter SCF convergence criteria.

Besides numerical accuracy, one is also interested in the gain in computing time when reducing the accuracy. For the given architecture on the dCluster of the Graz University of Technology by the time of writing (Intel Xeon E5-25650 CPUs) and using MPI-parallelisation over 64 total cores, the maximum reduction in CPU time for the lowest settings was about a factor of 3.7 (see Fig. 3.3). Here, it can be seen that for larger plane wave cutoffs, the difference in computational time between the global precision `Accurate` and `Normal` drastically increases.

In order to get a more graphical impression of the loosened numerical settings impact the phonon band structure. Fig. 3.4 shows a comparison of the low-frequency phonon band structure (calculated using a $2 \times 3 \times 2$ supercell) and the phonon DOS of the most

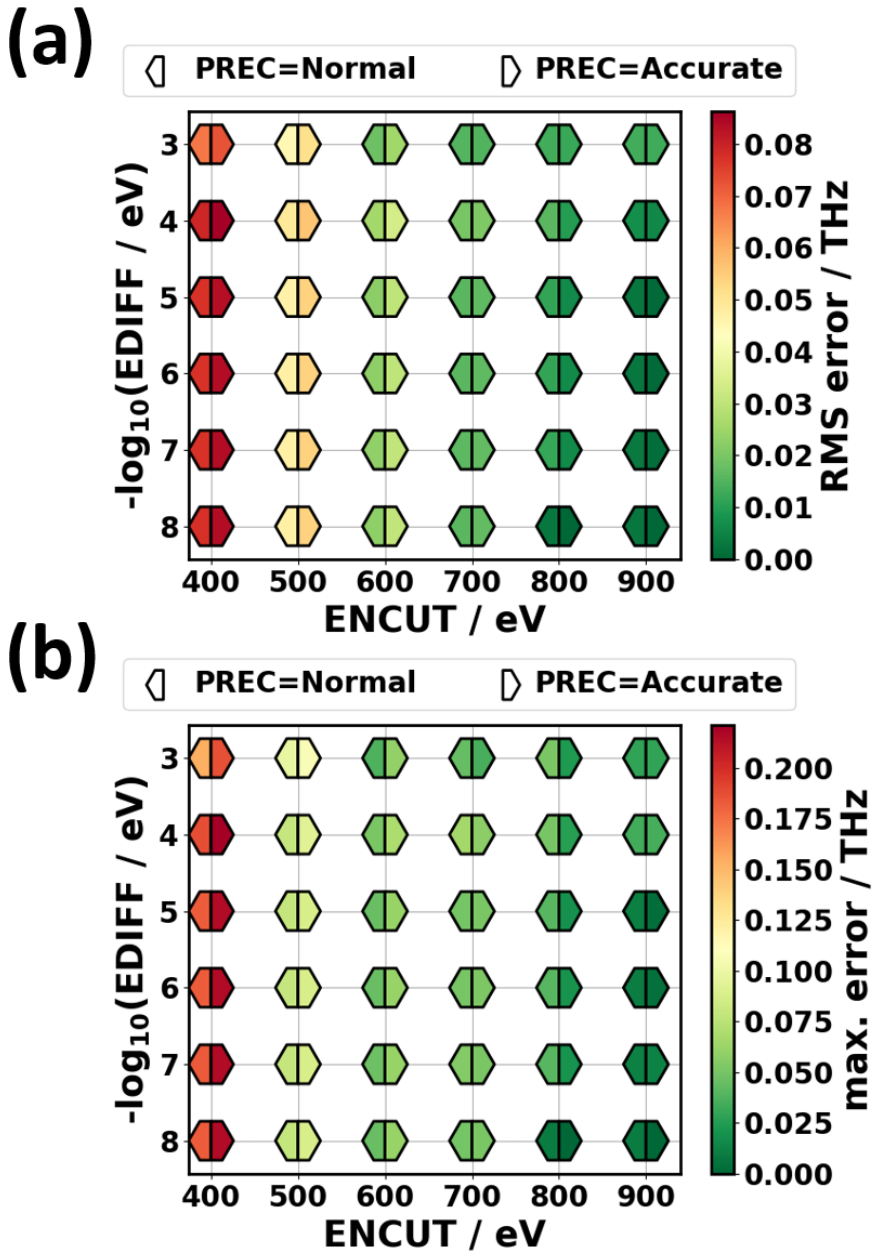

Fig. 3.2.: Accuracy map of Γ-frequencies as a function of the three *VASP*-specific parameters `PREC`, `ENCUT`, and `EDIFF`, determining the global precision settings, the plane wave energy cutoff and the SCF convergence criterion, respectively. (a) The root-mean-square error and (b) the maximum absolute error were calculated with respect to the Γ-frequencies with the tightest settings (`PREC`=`Accurate`, `ENCUT` = 900 eV, and `EDIFF` = 10^{-8} eV). This figure has been taken from the Supporting Information of Ref. [1].

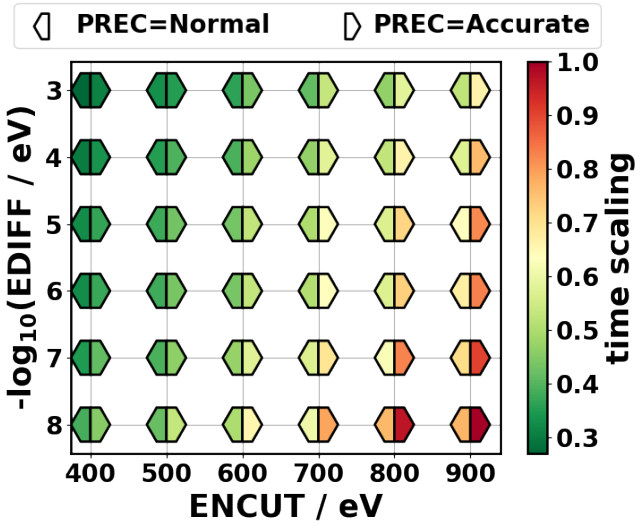

Fig. 3.3.: Map of relative saving in computational time for the calculation of Γ-frequencies in naphthalene as a function of the three *VASP*-specific parameters `PREC`, `ENCUT`, and `EDIFF`, determining the global precision settings, the plane wave energy cutoff and the SCF convergence criterion, respectively. The total CPU times have been divided by the largest required time, which was (not surprisingly) observed for the tightest numerical settings (bottom right).

accurate settings and the computationally most economic ("DFT eco") choice using the parameters resulting in the largest gain in computational time [1]. In spite of the fact that the DFT-eco results are actually highly underconverged, it can be seen that the agreement with the results from the most converged settings is still surprisingly good. The most pronounced discrepancies comprise a slight underestimation of the band gap between ~4.1 to 5.3 THz due to a small overestimation of the bands at the lower edge of the gap and small differences at and around the high-symmetry point A. The most obvious difference between the DFT reference and the economic settings is the band dispersion of the second-lowest (acoustic) band along XA, which is much flatter in DFT eco [1].

The extent of the discrepancy between the "DFT ref" and the "DFT eco" results can be more conveniently compared by calculating the RMS deviation of frequencies in the entire first Brillouin zone (sampled as homogeneously as possible at 125 **q**-points). When one does not limit the frequency range of the considered phonons, the RMS deviation amounts to ~0.08 THz (0.07 THz if only Γ-modes are considered). For the low-frequency bands only - i.e. up to 9 THz - the RMS deviation experiences a slight increase and is found to be ~0.11 THz, suggesting that the low-frequency intermolecular bands are obtained with less accuracy than the higher intramolecular modes [1].

At this point it must be stressed that although the error in the phonon band structures are comparably small (indeed much smaller than with any approximate methods as discussed in detail in Sec. 4), saving computational time by decreasing the numerical

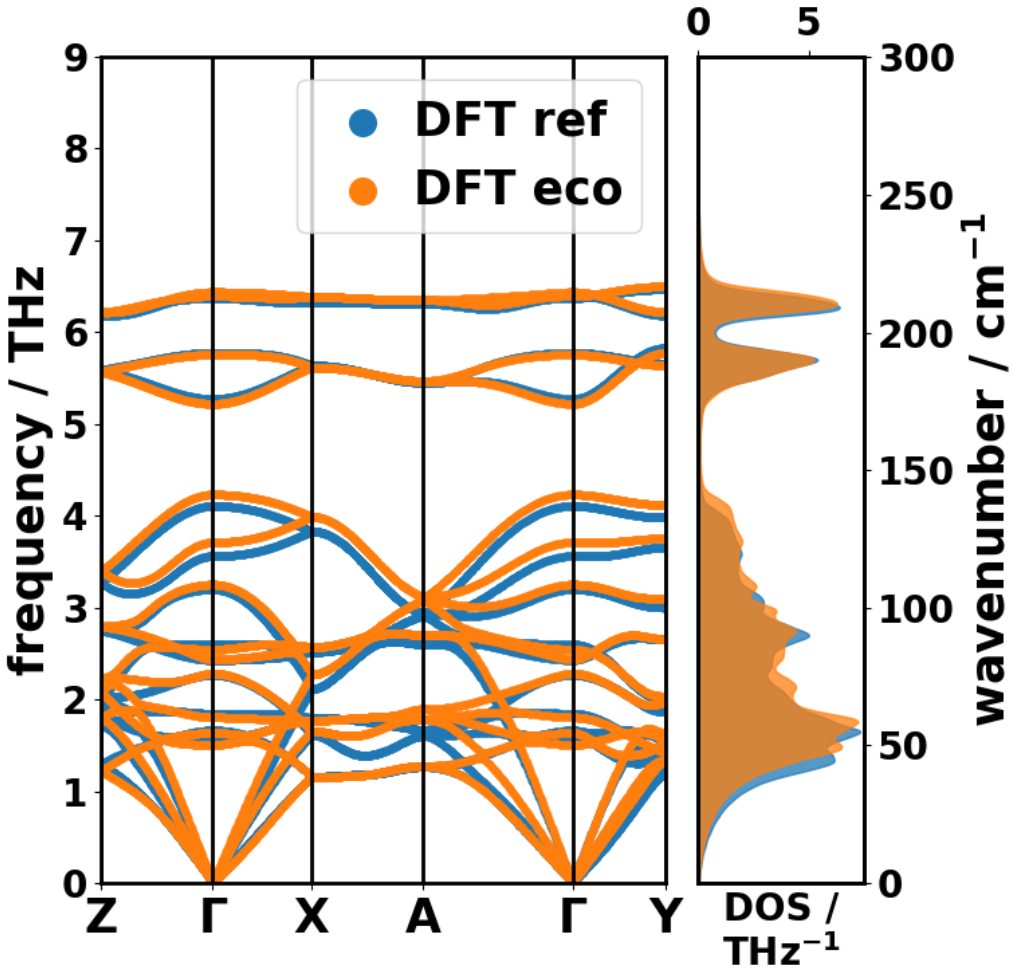

Fig. 3.4.: Phonon band structure and DOS of crystalline naphthalene obtained within DFT (PBE/D3-BJ) using well-converged simulation settings (DFT ref) and highly underconverged settings (DFT eco; for details see main text) using a 2×3×2 supercell. This figure has been taken from the Supporting Information of [1].

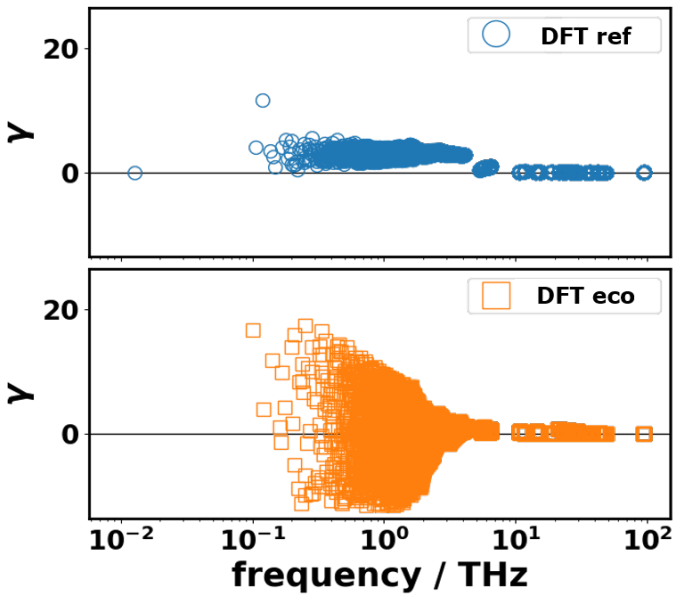

Fig. 3.5.: Mode Grüneisen parameters as a function of phonon frequency in crystalline naphthalene obtained within DFT (PBE/D3-BJ) using well-converged simulation settings (DFT ref) and highly underconverged settings (DFT eco).

accuracy has some dangerous disadvantages. One of them becomes apparent when calculating the mode Grüneisen parameters (see Eq. (2.45)). The Grüneisen constants are obtained by calculating phonons for a slightly increased and decreased unit-cell volume and approximating the derivative in Eq. (2.45) by a central difference scheme. Note that here, the equilibrium volume was increased/decreased by ~0.7%, and the four lattice parameters were optimised (together with the atomic positions) within these volumes. Moreover, the strained unit-cells optimised in that way were also used for the calculation of the Grüneisen parameters with the underconverged settings (i.e. the geometry optimisation was not carried out with the low-accuracy settings). Fig. 3.5 shows that operations such as the differentiation with respect to volume amplifies the errors in the band structure. Since for "DFT eco" one cannot observe a typical over- or underestimation of the Grüneisen parameters, one can conclude that the frequencies are also relatively arbitrarily over- or underestimated in the low-frequency region.

Regarding the used size of the employed supercells, diligent tests in the Supporting Information of Ref. [1] showed that a $2 \times 3 \times 2$ supercell results in converged interatomic force constants and, thus, converged phonon band structures (see. Fig. 3.6). Indeed, the harmonic force constants decay so rapidly with the distance of the corresponding pair of atoms, that relatively small supercells are already large enough to contain all relevant interaction (see Sec. 4.3.1). In fact, every supercell size beyond a $2 \times 2 \times 2$ supercell was found to be properly converged. Only the $1 \times 2 \times 1$ supercell yields massive discrepancies along ΓY, whereas the ZΓ direction is already perfectly converged. This can be rationalised by the fact that the used supercell is replicated along the **b** vector

which is coplanar with the reciprocal lattice vector $\mathbf{b}^*$. According to the condition of commensurate $\mathbf{q}$-points (see Eq. (2.21)), the high-symmetry point Z (corresponding to $\mathbf{b}^*/2$ in reciprocal space) is a wave vector commensurate with the supercell size and is, thus, directly calculated with the used supercell.

More technical details on the global parameters chosen in the phonon calculations throughout the various levels of theory can be found in Sec. 3.1.4.

The Raman activities of the isolated naphthalene molecule have been calculated using *Gaussian*16 (revision A.03) [92], whereas the activities for the crystalline phase were obtained based on finite Cartesian displacements exploiting the space group symmetries (to save computational time) using a tool developed in the course of my doctoral thesis in physics.

3.1.2. Density-Functional Tight Binding Calculations

Electronic structure calculations within the density functional tight binding (DFTB)[23] level of theory were conducted with the *DFTB+* package [93]. Again, all the parameters and settings described in this subsection are in agreement with the ones published in Ref. [1]. In order to increase the accuracy of this approximate approach, the atomic charges were being calculated self-consistently (Self-Consistent-Charge DFTB, SCC-DFTB). The publicly available *3ob-3-1* Slater-Koster files were used, including the special parameters provided by the *3ob:freq-1-2* extension in order to achieve the promised increase in accuracy concerning vibrational frequencies [94]. These Slater-Koster parameters were optimised for the DFTB3 functional, which includes a third-order expansion of the exchange-correlation energy in terms of the local charge fluctuation [79] (beyond the second-order expansion which is used in ordinary DFTB). In order to be consistent with the DFT settings, the D3-BJ van der Waals correction has been used employing the recommended parameters optimised for DFTB3: $a_1 = 0.746$ Bohr, $a_2 = 4.191$, $s_6 = 1.0$, and $s_8 = 3.209$, according to the *DFTB+* manual [95]. Concerning the discretisation of the first Brillouin zone, the same sampling as in DFT has been chosen. Moreover, all available angular momentum atomic orbitals for each species were included in the SCC-evaluation of the DFTB energy using a convergence criterion of 10^{-10} elementary charges.

The optimisation of the lattice parameters was found to be slightly more difficult than with *VASP*. In order to make use of the same approach based on an equation of state, multiple changes would have been required in the source code of *DFTB+*. Therefore, the optimisation of the four lattice parameters (the three lengths of the lattice vectors as well as the monoclinic angle β) was conducted in the following way: for a given monoclinic angle β, the atomic positions and the lengths of the lattice vectors were optimised with the conjugate gradient algorithm. (This constraint of constant angles is imposed by setting the keyword `FixAngles = Yes`). This procedure was repeated for several angles β_i such that a second-order polynomial could be fitted through the total energy-vs.-β data

[23] Also at the DFTB-level of theory, all phonon band structure calculations, geometry optimisations, convergence tests, etc. were carried out by myself.

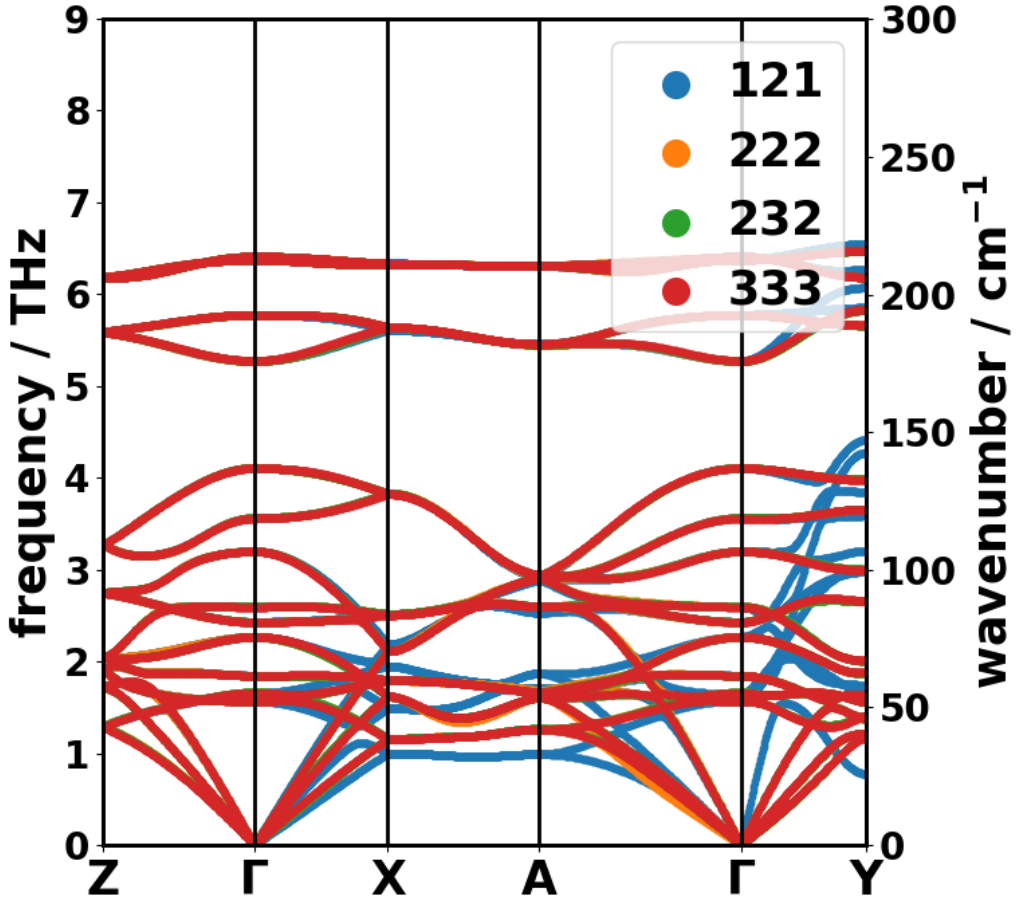

Fig. 3.6.: DFT-calculated (PBE/D3-BJ) phonon band structure of crystalline naphthalene as a function of the supercell size. This figure has been taken from the Supporting Information of Ref. [1].

(see Supporting Information of Ref. [1]). For the so found optimal monoclinic angle, a final optimisation of lattice vector lengths and atomic position was carried out. In all these (constrained) optimisations a maximum residual force of 10^{-8} eV/Å was set as the convergence criterion for the optimisation algorithm [1].
Note that all the later shown results based on this level of theory rely on "off-the-shelf" parameters - i.e. no system-specific reparametrisation of the Slater-Koster files has been done [1].

3.1.3. Force Field Calculations

The most important setting in force field-based calculations is the choice of the force field (FF) itself containing the predefined interaction terms including free parameters that must be obtained from some kind of reference data (more accurate levels of theory or experiments)[24]. One of the simplest FFs is the General AMBER Force Field (GAFF) [81] (AMBER: "Assisted Model Building with Energy Refinement") which is often applied for simulations of molecular crystals [14, 96, 97, 98]. This transferable FF was parametrised focussing on small organic molecules and only includes harmonic terms in all bonding interactions - i.e. bond stretching, bond angle bending, dihedral torsions - and completely neglects any interdependencies amongst those (i.e. there are no cross terms). The non-bonding interactions are the electrostatic interaction, described by a Coulomb potential based on assigned atomic point charges, and the van der Waals interaction, implemented via a pairwise 12-6 Lennard-Jones potential - i.e. a repulsive term proportional to r^{-12} and an attractive term proportional to r^{-6}, with r referring to the interatomic distance. The atomic point charges required for these interactions are not predefined neither are they physical observables, and so the user must provide reasonable values for these parameters. Here, the charges have been calculated from the (periodic) local electrostatic potential of the geometry fully optimised within the DFT level of theory as described above. The point charges were obtained with the *REPEAT* [99] method, which essentially determines (by means of least-squares fitting) those point charges in space which most closely reproduce the reference electrostatic potential.
The next level of sophistication can be reached by introducing anharmonic - i.e. polynomial terms beyond second order or functional dependencies which can only be expressed by an infinite series of polynomials such as the exponential function, for instance - terms in the mathematical model functions of the interactions as well as cross terms between those. Features like this are provided by the ready-to-use second-generation force field COMPASS ("*condensed-phase optimized molecular potentials for atomistic simulation studies*") [83]. Due to its increased level of sophistication compared to the much simpler GAFF, properties in organic semiconductors have often been simulated based on this FF [100, 101, 102, 103]. The many additional terms are supposed to result in a more fine-tuned description of the interatomic interactions and, thus, more accurate

[24] In contrast to DFT and DFTB, the phonon band structure calculations reported in Ref. [1] employing FFs were prevailingly carried out by Sandro Wieser (GAFF and MOF-FF band structures) and Hirotaka Kojima (COMPASS band structure). The parametrisation of the MOF-FF for naphthalene was conducted by Sandor Wieser and Johannes P. Dürholt under the supervision of Rochus Schmid.

phonon properties. In contrast to GAFF, COMPASS uses a 9-6 Lennard-Jones potential - i.e. the repulsive term is proportional to r^{-9} rather than to r^{-12} - to describe van der Waals interactions. Another difference is that COMPASS provides predefined atomic charges so that there is no need for calculating them from reference electrostatic potentials. Since the parameters of the FFs are tuned to work best with these standard atomic charges, no further attempts have been made to use charges different than the provided ones.
In contrast to both chosen "off-the-shelf" FFs discussed so far [1], which nearly exclusively get along without external input data, the final option which has been employed to most accurately reproduce phonon properties is our own reparametrisation of a force field based on the MOF-FF [84]. This FF has originally been designed for metal-organic frameworks (MOFs [104]), but has been adapted to naphthalene mostly by Sandro Wieser and Johannes P. Dürholt based on molecular reference data using the software *FFgen* [84, 105]. The computational details as well as the specific FF parameters, which are not too relevant for this thesis, can be found in Ref. [1] or directly in the associated repository[25]. Note that the nature of this force field is intransferable so that it must be reparametrised for every system of interest. During preliminary tests it turned out that additional cross terms (so-called bb13 terms[26]) had to be included to improve the accuracy of the frequencies. These terms are already included by default in COMPASS. A difference compared to COMPASS (and GAFF) is, however, the different treatment of van der Waals interactions by means of a damped Buckingham potential: the repulsive part is described via an exponential term rather than being proportional to r^{-9} (r^{-12}), while the attractive r^{-6}-term is additionally multiplied with a damping function [84]. Note that none of the van der Waals parameters have been refitted during the reparametrisation. Instead, the van der Waals coefficients were used which were originally implemented in the MOF-FF based on the MM3 force field [106]. Furthermore, also the atomic charges are treated in a more sophisticated manner in terms of Gaussian charge distributions. Finally, in our parametrization of the MOF-FF for naphthalene, five different atom types (three chemically different carbons and two different hydrogens) are distinguished, while GAFF and COMPASS only discriminate between atomic species (i.e. one chemically inequivalent carbon atom and one hydrogen).
Regardless of the choice of the FF, the harmonic force constants have been consistently calculated with the *LAMMPS* package [107] (and *Phonopy*) by Sandro Wieser and Hirotaka Kojima [1]. Previous to phonon calculations, the geometries - i.e. atomic coordinates as well as lattice parameters - were optimised to a maximum residual force below 10^{-7} eV/Å using the conjugate gradient algorithm. A cutoff distance of 12 Å was chosen at which the Coulomb and the van der Waals interactions were truncated. To prevent possible discontinuities at the cutoff, an additional smoothening function in the region between 10.8 and 12 Å distance was employed to ensure that the functional forms of the non-bonding interactions continuously approach zero (for more details see

[25] `https://github.com/cmc-rub/supporting_data/tree/master/85-Kamencek_JCTC_2020`
[26] For a geometric arrangement of four atoms bonded in the sequence 1-2-3-4, the bb13 terms express the interdependence of the stretching motion between the atom pair 1 and 2 with the atom pair 3 and 4.

Refs. [84, 108] or the LAMMPS documentation[27]).
Finally, it must be stressed that in contrast to many simulations relying on classical FFs, no molecular dynamics (MD) simulations were carried out - i.e. no atomic motion at finite temperatures has been simulated by integrating the equation of motion. Rather lattice dynamics simulations (at 0 K) were conducted with the FFs only being a different means for setting up the dynamical matrix of the system.

3.1.4. Phonon Calculations

In order to use the same phonon approach consistently throughout the studied levels of theory, the supercell approach as provided by the functionalities of the *Phonopy* code [27] was chosen[28]. The workflow after an accurate geometry optimisation has always been the same and is based on the one published in Ref. [1]:

1. Generate the symmetry-inequivalent Cartesian displacements of single degrees of freedom in a supercell: single atoms are displaced by a given distance (typically 0.01 Å) in the Cartesian directions from their equilibrium positions.

2. Use the desired level of theory (DFT, DFTB, FFs, etc.) to calculate the forces in the supercell induced by the displaced atom.

3. Collect the information about the forces for all displaced geometries (and produce the file `FORCE_SETS` which is required for further phonon calculations in *Phonopy*).

4. Based on the information of the forces and the displacement distance/direction, the harmonic force constants are generated by *Phonopy* according to the equations described in Sec. 2.3.

5. Finally, the so produced harmonic force constants can be used to set up the dynamical matrix, from which all phonon properties can be calculated.

All these basic steps require additional settings such as the choice of the supercell extents and the displacement amplitude. Regarding the first step, the supercells varied among the levels of theory. In DFTB and DFT, $2 \times 3 \times 2$ supercells were found to be large enough to include all relevant interatomic interaction (see Fig. 3.6) [1]. For the calculations based on classical FFs, $3 \times 3 \times 3$ supercells were used, since - based on tests with MOF-FF, the phonon bands obtained with a $2 \times 3 \times 2$ supercell still showed some minor deviations for the lowest acoustic bands (see Fig. 3.7).
Concerning the displacement amplitude, careful tests using distances from 0.0025 to 0.02 Å were conducted as shown in the Supporting Information of Ref. [1]. However, these relative large variation in displacement amplitude only resulted in a maximum

[27] Here, the pair style "buck6d/coul/gauss/long" is used: `https://lammps.sandia.gov/doc/pair_buck6d_coul_gauss.html`

[28] Having the converged harmonic force constants for each methodology - DFT, DFTB, and FFs - available, all the further calculations and analyses of phonon-related properties were carried out by myself.

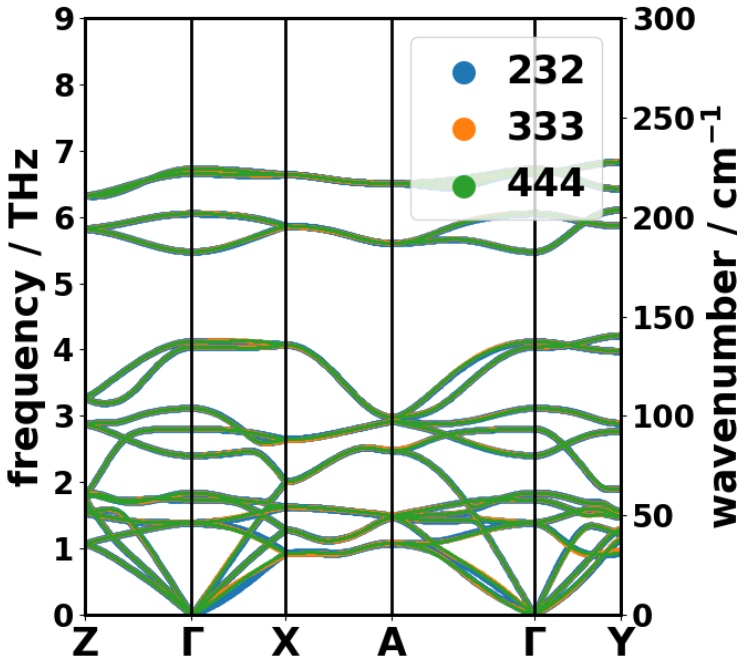

Fig. 3.7.: FF-calculated (MOF-FF) phonon band structure of crystalline naphthalene as a function of the supercell size. This figure has been taken from the Supporting Information of Ref. [1].

absolute (Γ-)frequency difference below 0.02 THz for the PBE/D3-BJ approach. Obviously, the system is relatively insensitive to this parameter (in combination with this level of theory) so that the default value of *Phonopy* (0.01 Å) was used for all approaches. The force constants were symmetrised using *Phonopy* to restore possibly lost symmetries due to numerical noise in the finite difference approach of obtaining the (harmonic) force constants. Group velocities were calculated analytically from the derivative of the dynamical matrices (see Eq. 2.34) with *Phonopy*.

To obtain (seemingly) connected phonon bands in band diagrams, the high-symmetry paths were sampled at 200 intermediate wave vectors $\mathbf{q}$. Whenever a homogeneous distribution of wave vectors over the entire first Brillouin zone is required - like for thermodynamic properties or densities of states (DOSs) - to carry out (unbiased) Brillouin zone integration/summation, a $9 \times 10 \times 9$ $\mathbf{q}$-mesh was used to account for the anisotropic extents of the first Brillouin zone [1]. This particular choice of the $\mathbf{q}$-mesh (810 wave vectors corresponding to 246 irreducible ones) results in a spacing of ~0.1 $Å^{-1}$ in each direction in reciprocal space. In the following section, a few arguments are made based in all the individual phonon modes sampled on this discrete mesh (such as frequencies and group velocities). Note that for the calculation of group velocities and mean-squared thermal displacements (MSTDs), these meshes were shifted away from Γ for different

reasons. Regarding the MSTDs, the spectral envelope function weighing the (thermally occupied) phonon contributions diverges at zero frequency. By omitting Γ, a possible divergence can be prevented [1]. Concerning the group velocities, shifted meshes were used to avoid biased comparisons with the reference because at Γ, the group velocities of optical bands are always zero. If unshifted meshes (including Γ) had been used, the sampled group velocities would have shown much better agreement with the reference because in both approaches there are a number of phonons (at Γ) with vanishing group velocities. Additionally, the definition of a group velocity at Γ for the three acoustic bands is somewhat problematic as discussed in Sec. 2.3 and in Ref. [1].
In contrast to the discrete sampling of the first Brillouin zone, the DOS requires a smooth curve as a function of frequency. To this end, the δ-distributions in Eq. (2.81) were replaced by Lorentzian functions with widths (σ) of 0.05 THz centred at the respective phonon frequency, in analogy to Ref. [1]. Note that 2σ corresponds to the full width at half-maximum[29].

3.1.5. Phonon Mode Assignment

In order to compare the frequencies of phonon modes corresponding to equivalent atomic motion but calculated with different approaches, it is necessary to assign those modes to each other in some way. Such an assignment is necessary because, due to insufficient accuracy, a mode with band index n in one approach might have band index $m \neq n$ in another approach. Thus, phonon frequencies must not simply be compared in order of increasing frequency. There, the so-called "Hungarian algorithm" of Kuhn [109] was exploited to solve this problem, which is called the *linear assignment problem*. The assignment procedure described in the following was developed to more reasonably analyse the data published in Ref. [1]. In general, the linear assignment problem, in which one wants to find the best assignment of features from two sets, is a minimisation of the following expression:

$$\min \sum_{ij} C_{ij} X_{ij} \tag{3.1}$$

In this expression, C_{ij} is a cost matrix, which describes the "cost" of assigning the i^{th} feature of the first set to the j^{th} feature of the second set. X_{ij} is the assignment matrix, whose elements are 1 if the i^{th} feature of set 1 is assigned to the j^{th} feature of set 2. The mathematical problem is, thus, to determine the elements of X_{ij} so that the above expression is minimised and every feature of set 1 is assigned to one and only one feature of set 2 - i.e. there is only one non-vanishing element in every row and every column of X_{ij} (equal to the numerical value 1).
The cost matrix could, in principle, be chosen arbitrarily and must be adapted to the

[29] In order to conserve the property of the DOS that an integration over the entire frequency range yields the number of phonon bands, $3N$, the substituted Lorentz functions must be normalised such that the integration over the Lorentz peak equals unity: $f(x|\sigma, x_0) = \frac{1}{\pi} \frac{\sigma}{(x-x_0)^2+\sigma^2}$.

given problem. Here, a cost matrix specifically designed for phonon assignment has been proposed by myself in Ref. [1].

$$C_{ij} = (1 - S_{ij}) + P_{ij} \tag{3.2}$$

In this equation, S_{ij} is the complex dot product matrix ("overlap matrix") of the phonon eigenvectors (of length $3N$, with N being the number of atoms per unit-cell) of the i^{th} mode of set 1 (=the reference) and the eigenvector of the j^{th} mode of set 2 (=the methodology whose modes are the target of the assignment procedure).

$$S_{ij} = \mathbf{e}_i^{(1)\dagger} \cdot \mathbf{e}_j^{(2)} \tag{3.3}$$

The term $(1 - S_{ij})$ is convenient for the cost matrix, since the eigenvectors form an orthonormal base for each wave vector $\mathbf{q}$ (as the dynamical matrix is hermitian, as discussed in Sec. 2.3). This means that for perfect agreement of the eigenvectors, the corresponding element of the overlap matrix S_{ij} is equal to unity, whereas the element vanishes if the mode corresponds to any other of the (orthogonal) eigenvectors. Therefore, the contribution to the cost matrix is 0 for perfect agreement and 1 for orthogonal eigenvectors. Additionally, a penalty matrix P_{ij} has been added to the cost matrix which penalises the assignment of modes with large frequency differences. Here, a Gaussian-type penalty was chosen of the following form:

$$P_{ij} = A \left(1 - \exp \left\{ - \frac{\left(f_i^{(1)} - f_j^{(2)} \right)^2}{2\sigma^2} \right\} \right) \tag{3.4}$$

Such a penalty with parameters A (amplitude) and σ (width) has turned out to be necessary since at certain (off-Γ) wave vectors, the agreement between phonon eigenvectors in naphthalene and the eigenvectors obtained with approximate methods was so bad that the assignment procedure resulted in frequency differences of unrealistically large value (above 50 THz). Visual inspection of these phonon modes showed that they were typically very different in nature, in spite of having been assigned to be equivalent. The penalty function, also considering the frequencies, tremendously improved the situation resulting in a reliable mode assignment algorithm. For all the reported mode assignments, the parameters $A = 0.5$ and $\sigma = 1$ THz were chosen [1].

3.2. Phonon Properties of Organic Semiconductors Other Than Naphthalene

Based on the results of Sec. 4, various further organic semiconductors were studied within the DFT level of theory employing the *VASP* code [38, 39, 40, 87] using the recommended standard PAW-pseudopotentials [41], the PBE functional [68] and the D3-BJ van der Waals correction [73, 74]. Since a detailed discussion of the chosen OSCs follows in Sec. 5, only the numerical settings shall be reported at this point. The studied systems are listed in Tab. 3.1, in which also abbreviations are introduced, which are

Tab. 3.1.: Abbreviations of the studied organic semiconductor systems. Moreover the chemical formulae, the molecular masses (M), the number of molecules per unit-cell (Z) as well as the number of atoms per unit-cell (N) are shown.

System	Abbreviation	Chemical Formula	M / amu	Z	N
Benzene (monoclinic)	1c_m	C_6H_6	78.11	2	24
Benzene (orthorhombic)	1c_o	C_6H_6	78.11	4	48
Naphthalene	2c	$C_{10}H_8$	128.17	2	36
Anthracene	3c	$C_{14}H_{10}$	178.23	2	48
Tetracene	4c	$C_{18}H_{12}$	228.29	2	60
Pentacene	5c	$C_{22}H_{14}$	278.35	2	72
Fluorene	F	$C_{13}H_{10}$	166.22	4	92
Pyrene	Py	$C_{16}H_{10}$	202.25	4	104
α-Quinacridone	αQ	$C_{20}N_2O_2H_{12}$	312.32	1	36
β-Quinacridone	βQ	$C_{20}N_2O_2H_{12}$	312.32	2	72
γ-Quinacridone	γQ	$C_{20}N_2O_2H_{12}$	312.32	2	72
Rubrene (monoclinic)	Ru_m	$C_{42}H_{28}$	532.67	2	140
Rubrene (orthorhombic)	Ru_o	$C_{42}H_{28}$	532.67	2	140
Biphenyl (planar)	2ph_plan	$C_{12}H_{10}$	154.21	2	44
Biphenyl (twisted)	2ph_tw	$C_{12}H_{10}$	154.21	2	44
Biphenyl (twisted, $Z = 4$)	2ph_tw4	$C_{12}H_{10}$	154.21	4	88
p-Terphenyl (planar)	3ph_plan	$C_{18}H_{14}$	230.30	2	64
p-Quinquephenyl (planar)	5ph_plan	$C_{30}H_{22}$	382.50	2	104

consistently used throughout Sec. 5.
Based on the same convergence criterion found applicable for naphthalene, the numerical settings (**k**-mesh and plane wave energy cutoff) were chosen system-specifically such that a convergence of the total energy below 0.5 meV per atom was reached. This level of convergence was shown to be adequate to achieve converged phonon frequencies [1]. Gaussian smearing ($\sigma = 0.05$ eV) for describing the occupation of electronic states and the global precision parameter `Accurate` (mostly determining the Fourier integration grid) were consistently used throughout the simulations of all systems. Also the optimum choice for the plane wave energy cutoff turned out to be 900 eV (`ENCUT`) for all systems to achieve the desired level of convergence and, simultaneously, keep the basis set size at a computationally efficient level. The used **k**-meshes, which were chosen such that the different first Brillouin zones were sampled as homogeneously as possible, can be seen in Tab. 3.3.

The original crystal structures - i.e. the starting geometries for the DFT-optimisation - of the listed systems were obtained by downloading crystallographic information files from the *Cambridge Structural Database* (`https://www.ccdc.cam.ac.uk/`). Tab. 3.2 shows the identifiers (and associated references) of the various crystal structures ob-

Tab. 3.2.: Database identifier and deposition numbers of the crystal structure entries in the *Cambridge Structural Database* (`https://www.ccdc.cam.ac.uk/`). Moreover, the temperatures at which the crystal structures were recorded, and the associated publications are listed. The tabulated entries were taken as the starting point for DFT-based geometry optimisations (see main text). The used abbreviations for the systems can be found in Tab. 3.1. The "2ph_tw" structure was created by applying rotations to the phenyl rings of the "2ph_plan" structure for reasons discussed in Sec. 5.

System	Database Identifier	Deposition Number	T / K	Ref.
1c_m	BENZEN03	1108752	295	[110]
1c_o	BENZEN01	1108750	138	[111]
2c	NAPHTA31	600182	5	[112]
3c	ANTCEN14	1103074	295	[113]
4c	TETCEN01	114446	175	[114]
5c	PENCEN04	170187	90	[115]
F	FLUREN01	1157853	295	[116]
Py	PYRENE10	1432441	90	[117]
αQ	QNACRD06	620257	295	[118]
βQ	QNACRD07	620258	293	[118]
γQ	QNACRD08	620259	293	[118]
Ru_m	QQQCIG13	726175	173	[119]
Ru_o	QQQCIG33	1565219	100	[120]
2ph_plan	BIPHEN	1111359	295	[121]
2ph_tw	-	-	-	-
2ph_tw4	BIPHEN06	1111365	22	[122]
3ph_plan	TERPHE01	1269381	295	[123]
5ph_plan	ZZZZNKU01	1319611	295	[124]

Tab. 3.3.: Sampling of the first Brillouin zone for electronic (**k**-mesh) and phononic (**q**-mesh) states in order to obtain group velocities and thermal properties. Moreover, the supercell dimensions (= the diagonal elements of the supercell matrices) are listed. For the systems with no given supercell dimension/**q**-mesh, no phonon calculations beyond the Γ-point have been carried out for several reasons as discussed in Sec. 5. The used abbreviations for the systems can be found in Tab. 3.1.

System	**k-mesh**	**supercell dimension**	**q-mesh**
1c_m	3×3×2	3×3×2	10×9×7
1c_o	2×2×1	2×2×2	10×9×7
2c	2×3×2	2×3×2	9×10×9
3c	2×3×2	2×3×2	9×10×7
4c	2×2×1	2×2×2	10×8×5
5c	2×2×1	2×2×2	10×8×4
F	2×1×3	2×1×3	7×3×10
Py	2×2×1	2×2×2	10×9×6
αQ	3×2×1	4×3×2	10×6×3
βQ	2×3×1	2×3×2	10×15×2
γQ	1×3×1	2×3×2	3×10×3
Ru_m	3×3×2	-	-
Ru_o	2×2×1	-	-
2ph_plan	2×3×2	-	-
2ph_tw	2×3×2	-	-
2ph_tw4	3×2×2	-	-
3ph_plan	2×3×1	-	-
5ph_plan	1×3×2	-	-

tained from the database in order to unambiguously recognise the input structures. It shall be noted, however, that for several of the considered molecular crystals, various polymorphs are reported and documented in the *Cambridge Structural Database*. For those systems, for which different polymorphs were not studied explicitly in this thesis, typically that polymorph measured at the lowest available temperature was chosen (as DFT calculations are formally carried out at 0 K). As will be discussed in more detail in Sec. 5, the dihedral angle between the phenyl rings in the oligophenylenes turned out to be somewhat problematic in the simulations. In this context, a twisted structure of biphenyl ("2ph_tw") was manually generated based on the database entry of a planar configuration ("2ph_plan") (see the detailed discussion of the observed complication in Sec. 5). For that reason, no database entry in Tab. 3.2 is associated with the 2ph_tw structure.
Based on these initial experimentally observed crystal structures, the atomic positions and lattice parameters were optimised employing the same convergence criteria and optimisation approach as described for naphthalene in Sec. 3.1.1. The used supercells for the phonon calculations (based on the finite displacement method as described in Sec. 2.3) are shown in Tab. 3.3. Since the increase in unit-cell volume in real-space determined by the supercell is accompanied by a reduction in reciprocal-space volume, the electronic **k**-sampling can be reduced with no loss of sampling density[30]. For supercells, the electronic first Brillouin zone has always been represented by the Γ-point only.
Regarding the choices of phonon wave vectors **q**, the high-symmetry paths between two high-symmetry points in the band diagrams were sampled by 200 intermediate points. For properties which require a homogeneous sampling of not only the high-symmetry paths but the entire first Brillouin zone, system-specific **q**-meshes were chosen depending on the extents of the corresponding reciprocal lattice vectors. The **q**-meshes used to calculate thermodynamic properties are listed in Tab. 3.3. The convergence behaviour of the DOSs, which appeared to be the more sensitive to the sampling than thermodynamic properties, is shown in the Appendix A.4 for those systems, for which the DOSs seems to be most affected by the **q**-sampling. Note that, consistent with the settings for naphthalene in Ref. [1] and in line with the considerations of Sec. 3.1, the shown **q**-meshes were shifted such that they do not include Γ for the calculation of the mean-squared thermal displacements and the group velocities, while for all other thermodynamic properties and the DOS, unshifted meshes were used.

[30] For example: If a $4 \times 6 \times 4$ **k**-mesh is used for the primitive cell, a $2 \times 3 \times 2$ **k**-mesh in a $2 \times 2 \times 2$ supercell provides the same sampling density of electronic wave vectors.

4. Methodological Benchmark: The Instructive Case of Naphthalene

The first question that arises when dealing with simulation is whether the simulation is capable of accurately describing the physical system of interest. As pointed out in Sec. 2, phonon properties can be calculated within many levels of theory. Identifying the "best" methodology and the optimal simulation settings has been a partial goal of this thesis. Additionally, the associated results have already been published in Ref. [1]. The data presented here not only contain the key messages of that article (reproduced in part with permission from Ref. [1]: `https://pubs.acs.org/doi/full/10.1021/acs.jctc.0c00119`, Copyright 2020 American Chemical Society), but also include additional information which had to keep unpublished due to length limitations. Thus, in the following, it will be explicitly stressed if data is discussed, which is **not** already published in Ref. [1].
Several methodologies, comprising DFT, DFTB, and FF-based approaches, have been employed to calculate the phonon band structure of crystalline naphthalene. The reason why the choice fell on this simple organic crystal is the availability of experimentally measured phonon band structures in the low-frequency region (below ~9 THz), which is the spectral range in which mostly intermolecular vibrations are found. These comprise the first 12 bands corresponding to the three translational and three rotational modes of each of the two molecules in the primitive unit-cell. To the best of my knowledge, the phonon band structure of crystalline naphthalene measured by Natkaniec et al. [24] already in 1980 is still the only available one of an organic semiconductor at present day.

4.1. Crystalline Naphthalene

As many organic semiconductors, naphthalene crystallises in a monoclinic crystal system with two molecules per unit-cell, which arrange in the typical herringbone fashion. The monoclinic unit-cell is built in such a way that the lattice vector **b** is perpendicular to **a** and **c** (see Fig. 4.1), the angle between which is the monoclinic angle β (~125°). The experimentally obtained lattice parameters are compared to the results of various simulation approaches in Tab. 4.1. Since the lattice vector **b** is much shorter (~5.9 Å) than **a** (~8.1 Å) or **c** (~8.6 Å), anisotropic (phonon) properties are to be expected. Moreover, the space group of the crystal ($P2_1/a$ = space group number 14) has the interesting side effect that all rank-2 tensors (such as the thermal/electrical conductivity, the Seebeck tensor, the thermal expansion tensor, etc.) are non-diagonal. For example, a temperature gradient in x direction will not only cause a heat flux in x but also in z direction as the thermal conductivity tensor element κ_{xz} does not vanish.
Another consequence of the monoclinic lattice is the fact that the lattice vectors - except for **b** - are not collinear with their reciprocal counterpart as it is the case for (simpler) lattices with mutually orthogonal lattice vectors. For that reason, the high-symmetry directions drawn in the band diagrams cannot easily be identified with real-space direc-

Tab. 4.1.: Comparison of simulated lattice constants of non-deuterated naphthalene with experimental data. The measurements have been conducted at a temperature of 5 K by Capelli et al. [112] with the digits in parentheses indicating the experimental error. This table has been taken from Ref. [1].

	$\|\mathbf{a}\|$ / Å	$\|\mathbf{b}\|$ / Å	$\|\mathbf{c}\|$ / Å	β / deg	unit-cell volume / Å^3
Experiment	8.080(5)	5.933(2)	8.632(2)	124.65(4)	340.41
DFT + D3-BJ	8.078	5.903	8.622	124.24	339.91
DFT + MBD	8.090	5.910	8.608	124.24	340.25
DFT + TS	8.052	5.860	8.616	123.89	337.47
DFT + D2	7.822	5.821	8.485	125.34	315.09
DFTB	7.573	5.733	8.457	125.04	300.61
COMPASS	8.002	5.771	8.500	124.64	322.96
MOF-FF	7.998	5.884	8.635	123.18	340.18
GAFF	7.850	5.979	8.610	124.05	334.88

tions. The only exception is the ΓZ direction, which corresponds to the direction along the lattice vector $\mathbf{b}$ (and also $\mathbf{b}^*$).

Each naphthalene molecule consists of 18 atoms (ten C atoms and eight H atoms) resulting in 108 (=2×18×3) degrees of freedom per unit-cell and exactly as many phonon bands. As already mentioned, the first twelve modes are dominated by intermolecular motion - i.e. relative motion of the two molecules as nearly rigid parts -, while the remaining 96 phonon bands are dominated by intramolecular motion - i.e. prevailingly distortions within the molecules.

Finally, it shall be mentioned that for comparing the simulated phonon band structure with the experimentally obtained one, it is necessary to consider deuterated naphthalene since the experiments were carried out for crystals of deuterated molecules. The reason for this is that deuterium has a much larger coherent scattering cross section for neutrons compared to the incoherent cross section than the more common protium isotope of hydrogen [21, 22, 23].

4.2. Low-Frequency Phonons ($\leq$ 9 THz)

4.2.1. Identifying an Accurate Reference Methodology

As discussed in detail in Sec. 2.5, different frequency ranges are typically more or less dominantly influencing certain thermal properties. Usually, the low-frequency phonons prevailingly govern the low-temperature characteristics due to the thermal occupation of the phonon bands. In line with these considerations, the first step in assessing the suitability of a simulation approach for predicting accurate phonon properties is to look at the low-frequency bands, an in-depth discussion of which can be found in Refs. [1, 29, 30, 112]. Since properties derived from the phonon band dispersion are not easily accessible and they cannot be calculated from the few experimentally available points in

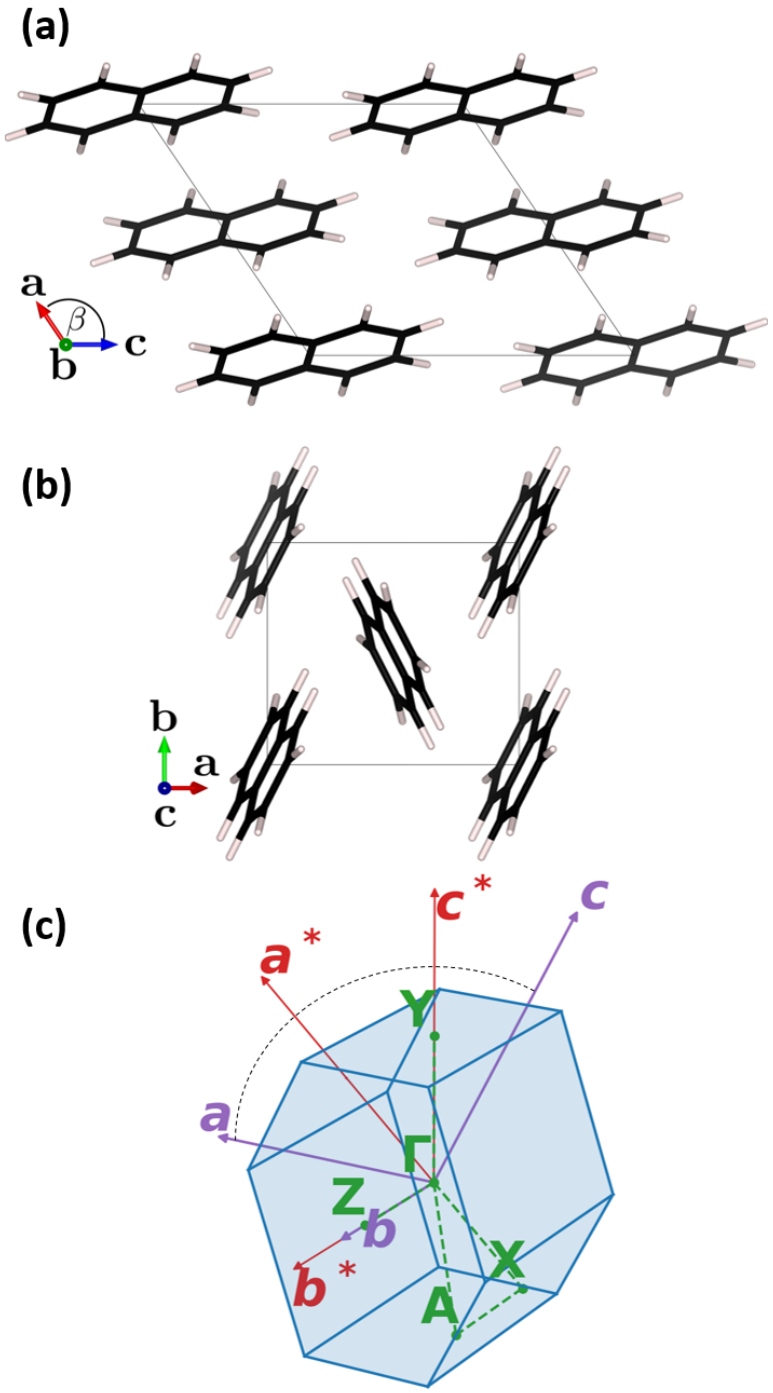

Fig. 4.1.: Unit-cell of crystalline naphthalene seen (a) along the lattice vector **b** and (b) along the lattice vector **c**. The first Brillouin zone is shown in panel (c) including the primitive real-space (**a**, **b**, **c**) and reciprocal-space lattice vectors (**a***, **b***, **c***) represented by red and purple arrows, respectively. Note that **a**, **c**, **a***, and **c*** lie in one plane, whereas **b**, and **b*** are collinear and perpendicular to this plane. The high-symmetry points Γ, A, X, Y and Z are those points used in the band diagrams in the following. This figure has been taken from Ref. [1].

the band structure[31], the chosen strategy to still have reliable reference data available for various properties consists of the following three steps:

1. Find a reliable and accurate methodology, which shows the best agreement with experimental data
2. Use the methodology found in 1. as a base to calculate phonon-related properties
3. Compare less sophisticated methodologies to those reference properties

In order to identify the accurate reference methodology, the presented work (and Ref. [1]) is extending the study Altvater-Brown et al. [30], who tested the impact of different DFT functionals on the calculated phonon band structure of naphthalene compared to the experimentally observed one. Note that they found that, when keeping the unit-cell size fixed to the experimental value, also neglecting van der Waals interactions at all, the PBE functional [68] without an additional *a posteriori* van der Waals correction provides a good agreement between measured and calculated phonon bands. This is similar to what has been observed for the agreement between simulated and measured Raman spectra - i.e. vibrations at the Γ-point of the first Brillouin zone only - of various organic crystals [125]. Since entirely disregarding van der Waals interactions does not allow for a consistent optimisation of the lattice parameters (the molecules would fly apart), this strategy is not pursued. Moreover, the computationally much more expensive hybrid functionals, are typically not the first choice in periodic *ab initio* calculations - especially if atomic positions and/or unit cells must be optimised like for phonon calculations. Thus, the presented strategy to identify a promising reference methodology is based on the well-established PBE functional in combination with the four different *a posteriori* van der Waals corrections introduced in Sec. 2.6.1: D2, D3-BJ, TS, and MBD.
The Γ-frequencies for deuterated naphthalene obtained with the four van der Waals corrections are shown in Fig. 4.2 in comparison to the experimental frequencies measured at the center of the first Brillouin zone. Note that in order to be comparable, the phonon frequencies were calculated for fully optimised unit-cells (atomic positions and lattice parameters), using the approach based on the Rose-Vinet equation of state as described in Sec. 3, consistently employing the respective van der Waals correction. The resulting lattice parameters are shown in Tab. 4.1.

MBD and D3-BJ nearly result in the same accuracy in terms of lattice parameters and in terms of frequencies at Γ, whereas the other two approaches (D2 and TS) yield notably different frequencies in the spectral region below ~8 THz - i.e. for the intermolecular modes. As these interactions between the molecules are dominantly governed by van der Waals interaction, it is reasonable that the respective modes are the ones affected the most by the choice of van der Waals correction. Analysing the lattice parameters,

[31] In order to be able to calculate thermal properties such as heat capacities or free energies from an experimentally measured phonon band structure, the band dispersion must be measured for a uniform mesh of wave vectors $\mathbf{q}$ in the entire first Brillouin zone for all phonon bands, which is difficult for systems with hundreds of bands such as organic semiconductors.

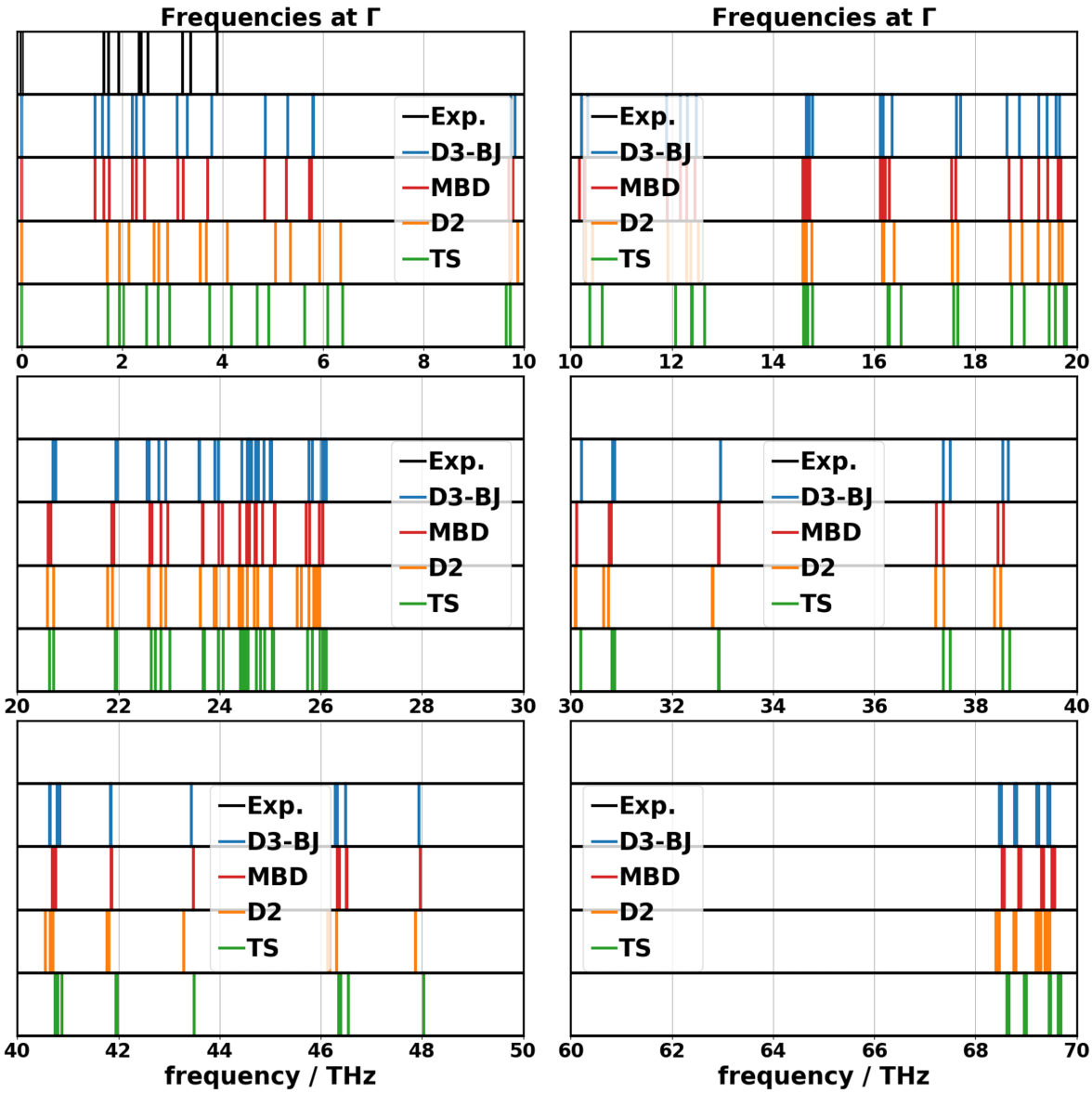

Fig. 4.2.: Comparison of the experimentally obtained ("Exp.") Γ-frequencies of deuterated naphthalene with the ones obtained within DFT employing the PBE functional and different van der Waals corrections. The various panels show different spectral ranges. The lattice parameters were fully optimised using the same correction. The experimental data were taken from the band structure measured in Ref. [24] at the centre of the first Brillouin zone. This figure has been taken from the Supporting Information of Ref. [1].

one can see that D2 considerably underestimates the unit-cell volume. As a result, the molecules are packed more densely. Thus, D2 tends to overestimate the intermolecular frequencies to some extent. The TS correction, however, yields lattice parameters at an accuracy comparable to this of MBD or D3-BJ, while the agreement with the experimental band structure data is the worst of the tested corrections. At higher frequencies all four corrections yield more similar values, although the D2 approach shows a small consistent underestimation of the frequencies of the intramolecular modes above ~40 THz.
For Γ-frequencies, the D3-BJ and the MBD approach were found to yield the best agreement with experimental data, with the MBD correction being computationally more expensive by about a factor of 3 (for naphthalene[32]). However, it is not clear *a priori* that this result also holds for the accurate description of the phonon band dispersion beyond the Γ-point. For that reason, the entire phonon band structure has been calculated (using $2 \times 3 \times 2$ supercells) and compared to experiments. As the MBD approach did not allow to calculate the entire band structure, which can most probably be ascribed to the large number of atoms in the used supercells ($12 \times 36 = 432$ atoms), the results of the three remaining candidates are shown in Fig. 4.3.

The overall agreement of the D3-BJ calculation with the experimental data is excellent. The root-mean-square deviation (RMSD) of frequencies (at the experimentally accessible wave vectors $\mathbf{q}$) amounts to ~0.13 THz (~4.3 cm^{-1}). Contrary to the D3-BJ results, the other two band structures are in less favourable agreement with the experiments. Although the functional form of the van der Waals interactions for both correction schemes is similar, D2 uses tabulated interaction coefficients, while TS calculates them based on atomic polarisabilities resulting from a Hirshfeld partitioning of the charge density of the system.
It can be seen in Fig. 4.3 that the TS correction results in a notably different band dispersion of the low-frequency optical phonon bands, while the frequencies of the acoustic bands can be obtained at a much higher level of accuracy. Most noticeably, the band gap between the first intramolecular band (at ~5 THz at Γ in the D2 and D3-BJ calculations) and the uppermost intermolecular band can hardly be discerned.
In contrast to the TS correction, the D2 approach underestimates the unit-cell volume by ~10 % as a result from too short lattice vectors by approximately 0.1 to 0.2 Å. Nevertheless, the agreement with the experiments is much better compared to the TS case, although the optical bands seem to experience a slight shift towards higher frequencies compared to the experiments, which can most probably be ascribed to the too small unit-cell volume[33].
The differences in the band structures obtained with the TS and the D2 correction discussed so far are also visible in the low-frequency phonon density of states (DOS)

[32] As the MBD approach includes potential terms beyond the typical pairwise van der Waals interactions, the calculation of higher many-body contributions becomes increasingly costly for larger numbers of atoms per unit-cell.

[33] Since naphthalene shows prevailingly positive mode Grüneisen parameters [29, 126, 127], the frequencies are supposed to increase with smaller unit-cell volume.

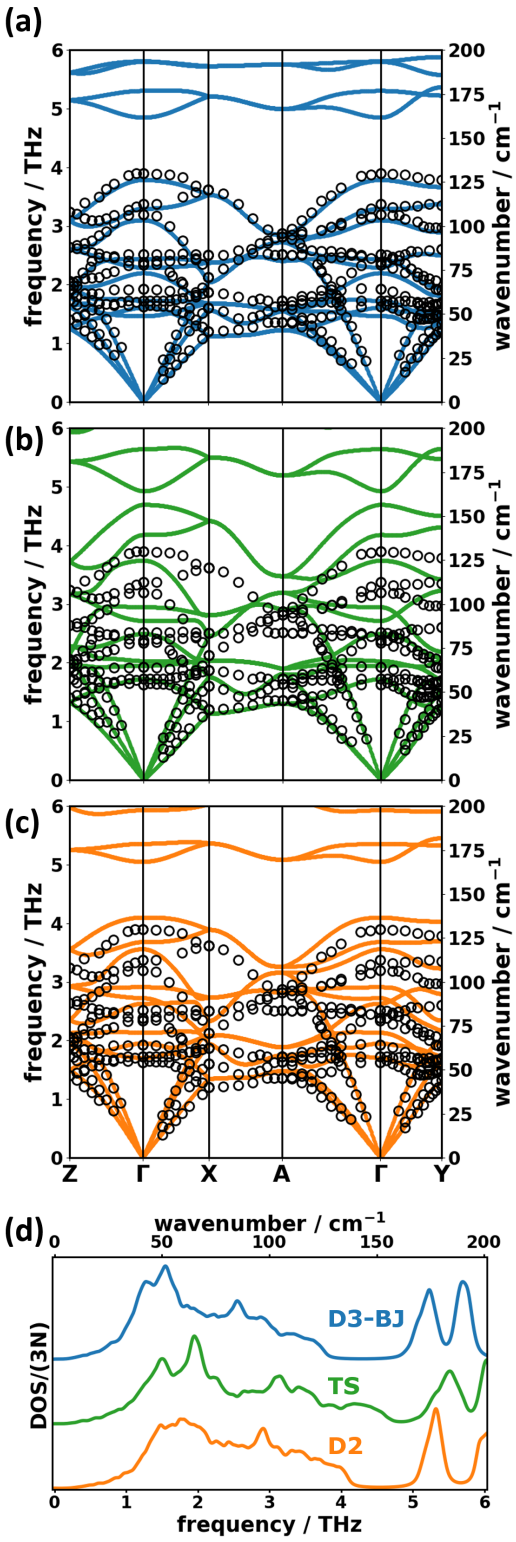

Fig. 4.3.: Comparison of the DFT-calculated phonon band structure of deuterated naphthalene using the (a) D3-BJ, (b) TS, and (c) D2 van der Waals corrections with experimental data (open circles) measured by inelastic neutron scattering at 6 K [24]. (d) Comparison of the normalised DOS - i.e. the DOS divided by the number of degrees of freedom $3N$. This figure has been taken from Ref. [1].

in Fig. 4.3(d). In this way of displaying the vibrational states in the entire first Brillouin zone rather than along specific high-symmetry paths, one can even draw more general conclusions about the methodology-dependent differences. The TS correction shows a tendency to shift many intermolecular spectral features to higher frequencies, which, in turn, results in the nearly complete closure of the band gap between inter- and intramolecular modes. In the DOS using the D2 correction these shifts are less pronounced, although the DOS of the acoustic region looks relatively different compared to the other two methodologies: the spectral features are more washed out, suggesting a more homogeneous distribution of phonon bands than for D3-BJ.
In addition to the excellent agreement between the calculated and the measured phonon band structures at very low-frequencies, the PBE/D3-BJ approach seems to be also well-suited to describe the high-frequency vibrations in organic crystals. This can be seen in Fig. 4.4 in which Raman spectra for the crystalline and the molecular (gaseous) phase of naphthalene are compared to the experimental data of Zhao and McCreery [128]. Please note that, in contrast to inelastic neutron scattering, there is no experimental need to use deuterated naphthalene for Raman spectra. Therefore, the vibrational spectra for the non-deuterated case are considered here.

Besides the excellent agreement between the simulated spectrum of the crystalline phase and the experiments, Fig. 4.4 additionally shows that the Raman spectra of the molecular and crystalline phases are essentially identical except for the low-frequency intermolecular regime (below ~5 THz). Moreover, the hybrid functional B3LYP [129, 130] results in a consistent overestimation of frequencies and, thus, worse agreement with the experiments.
Due to the fact that the PBE/D3-BJ approach has been identified to yield (i) the best agreement with low-frequency band structure measurements for deuterated naphthalene and (ii) high-frequency Raman scattering experiments for the non-deuterated case, this methodology is clearly the best (i.e. the most accurate and efficient) *high-level* methodology to reliably reproduce phonon properties from experiments in the entire spectral range. Therefore, this methodology can be used to benchmark other less sophisticated, more approximate approaches such as DFTB and FFs. Thus, the PBE/D3-BJ approach will be referred to as "DFT ref" in the following.

4.2.2. Phonon Band Structures from Density Functional Tight Binding

Computationally demanding phonon calculation can be sped up by various lower levels of theory, one of them being density functional tight binding (DFTB). However, this speed up usually comes at the cost of reduced accuracy. Firstly, it can be seen in Tab. 4.1 that the unit-cell optimisation within DFTB yields lattice constants which differ quite significantly from the experimental values. All lattice vectors are much shorter (**b** and **c** by ~2-3%, **a** even by ~6%) resulting in a much denser packing of the molecules. Since the low-frequency intermolecular modes are especially sensitive to the molecular packing, one expects large discrepancies in these phonon bands. Indeed, notable differences can be seen in Fig. 4.5(a) comparing the DFTB band structure and DOS to the reference (DFT ref).

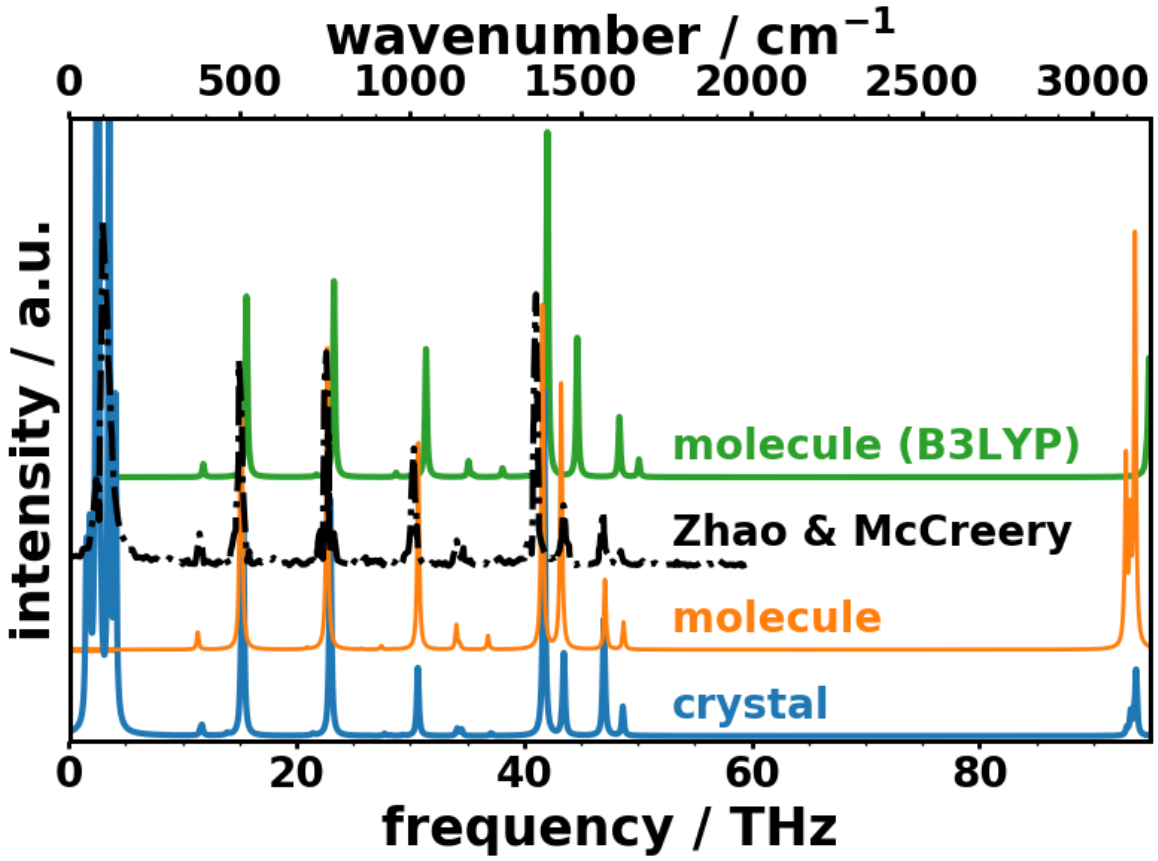

Fig. 4.4.: Comparison of simulated and experimentally measured Raman spectra of (non-deuterated) naphthalene. The spectra have been calculated for crystalline naphthalene using the PBE functional with the D3-BJ correction (blue line) and for molecular naphthalene using the same van der Waals correction with two different DFT functionals: PBE (orange line) and B3LYP (green line). The experimental data were measured by Zhao and McCreery [128] at room temperature using an excitation laser with a wavelength of 784 nm. The fact that the sample was a poly-crystalline powder was not specified in Ref. [128], but was privately communicated by Richard McCreery. This figure has been taken from the Supporting Information Ref. [1].

Compared to DFT ref, as a result of the denser packing, which goes hand in hand with an increased mechanical stiffness, the band widths and slopes of the acoustic bands are overestimated resulting in a more gradual increase of the DOS in that spectral region. Also the optical bands show pronounced differences compared to the reference. In DFTB, most of the phonon bands are typically shifted to higher frequency - often being accompanied with considerable distortions of the shapes of the bands. Consequently, not only are most of the low-frequency features shifted to higher frequencies, but also certain characteristics are not present at all: the band gap between inter- and intramolecular modes, for instance, is entirely closed in DFTB due to the strong upwards shift of the highest intermolecular band. Visualisations of these bands show that the motion these bands correspond to are essentially (intramolecular) twisting motions around the long molecular axes. Naturally, such motions are sensitively affected by the increased packing density.

At this point the question arises, if the bad agreement could be compensated by using better unit-cell parameters, which do, however, not correspond to the energetic minimum within the DFTB optimisation[34]. In principle, such an approach is equivalent to applying an external stress to the lattice. An approach like this has been suggested by Brandenburg and Grimme [131]. They proposed to use the unit-cell parameters from DFT and to only optimise the atomic positions at the DFTB level of theory for the accurate calculation of phonon frequencies in organic semiconductors. The suggested approach has been tested to validate if it can improve the calculated phonon properties. The data obtained from this strained unit-cell - i.e. the DFT unit-cell - are labelled as "DFTB@DFT" in the following. The respective band structure can be seen in Fig. 4.5(b).

Indeed, DFTB@DFT shows many improvements compared to the pure DFTB approach. Although the general shape of the bands is in a better qualitative agreement with the DFT reference, the quantitative one is still to be improved: it appears that DFTB@DFT has the tendency to underestimate frequencies - i.e. the (low-)frequency scale is rather compressed than expanded as in the pure DFTB approach. Since the mode Grüneisen parameters are prevailingly positive [29, 126, 127], the logical solution to correct for too low frequencies is decreasing the unit-cell volume such that the best agreement compared to DFT ref (in terms of the smallest observed root-mean-square deviations in frequencies) is achieved. This test is shown in Fig. 4.6 considering only the low-frequency modes $\leq$ 9 THz. Regardless of whether only the Γ-frequencies or phonon frequencies from the entire first Brillouin zone are considered, the best agreement with the reference data is achieved for a unit-cell with a volume of 95 % of the DFT value. This approach will be referred to as "DFTB@95%DFT". Note that in that test, the atomic positions were fully optimised for each rescaled unit-cell. It should be mentioned that the energy of the unit-cell volume found to minimise the frequency root-mean-square deviations (RMSD), the energy is ~30 meV higher than in the unit-cell fully optimised in DFTB, and the tensile stress amounts to ~-5 kbar.

[34] Please note that a local minimum on terms of the variation of the atomic positions can still be found such that phonon calculations still make sense.

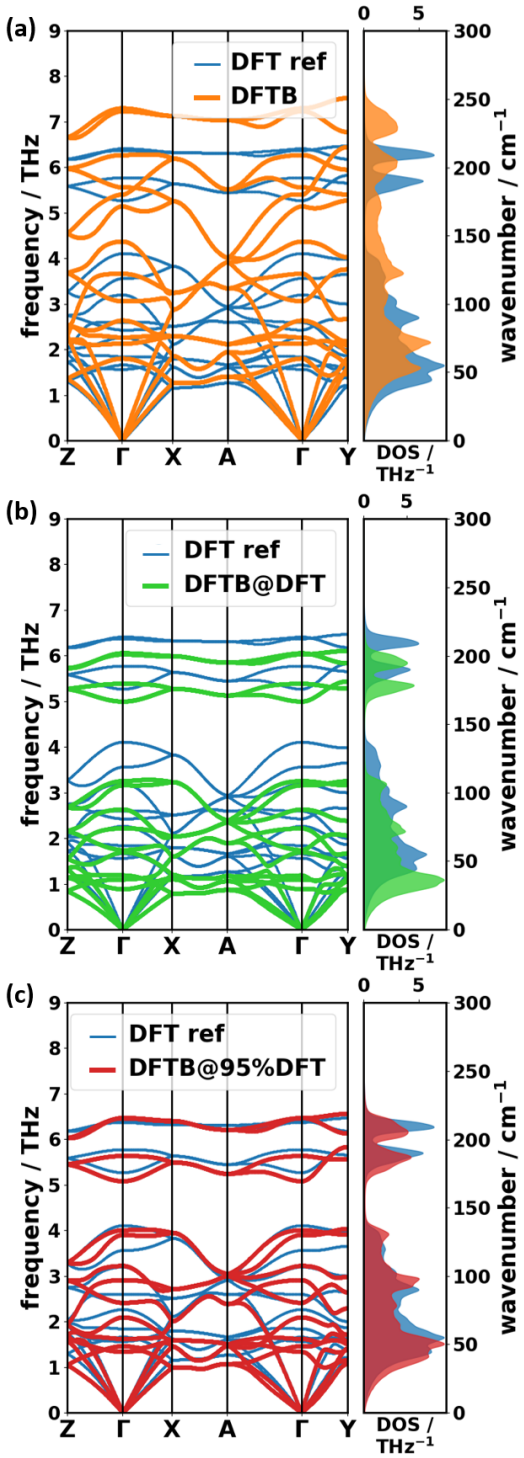

Fig. 4.5.: Phonon band structures and DOSs of various DFTB-based approaches compared to the DFT reference (DFT ref). (a) Unit-cell fully optimized within DFTB. (b) The lattice parameters were taken from DFT ref with only the atomic positions having been optimised within DFTB. (c) The DFT ref unit-cell was isotropically shrunk corresponding to a unit-cell volume rescaled by a factor of 0.95. For all three approaches the atomic coordinates have been optimised within DFTB/D3-BJ. This figure has been taken from Ref. [1].

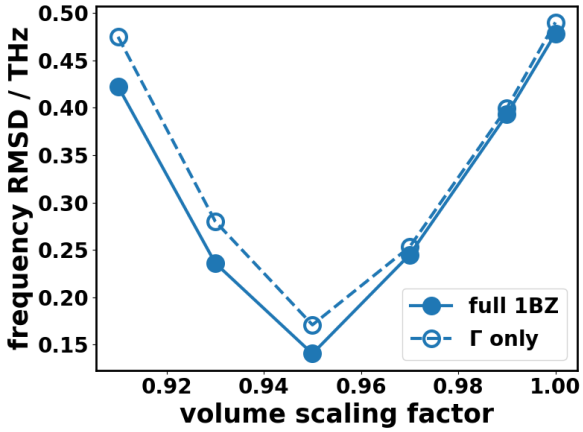

Fig. 4.6.: Root-mean-square deviation (RMSD) of frequencies ($\leq$ 9 THz) between the DFTB calculation and the DFT reference for naphthalene. The frequencies in the DFTB case have been calculated for lattice parameters based on the DFT unit-cell whose volume has been scaled by the shown scaling factors. The solid line with filled symbols represents the RMSD if the entire first Brillouin zone is considered, while the dashed line with open symbols represents the RMSD for Γ-frequencies only. This figure has been taken from the Supporting Information of Ref. [1].

The fact that the same optimum volume scaling factor can be discerned regardless of whether frequencies from the entire first Brillouin zone or only Γ-frequencies are considered is very promising, as it suggests that one only would need to carry out the much cheaper calculations of Γ-phonons in DFT to find the optimal scaling factor. This could be especially appealing in cases in which the computation of the entire phonon band structure in DFT is not feasible (for reasons of computational cost, for instance).
Finally, to asses, whether the rescaling of the unit-cell could be of general applicability, this approach has also been tested for two more systems: anthracene and fluorene[35]. Fig. 4.8(a) shows the comparison of the phonon band structure calculated with DFT and the pure DFTB approach. Like it is the case for naphthalene, the DFTB bands show significant discrepancies compared to the DFT bands. In general the DFTB bands appear to have much larger band widths and again the band gap between ~5-7 THz (in the DFT calculation) is filled with states to a large extent. As a result, also the phonon DOS has lost most of its spectral low-frequency features compared to the one calculated with DFT.

[35]The shown results for these two systems have not been published in Ref. [1].

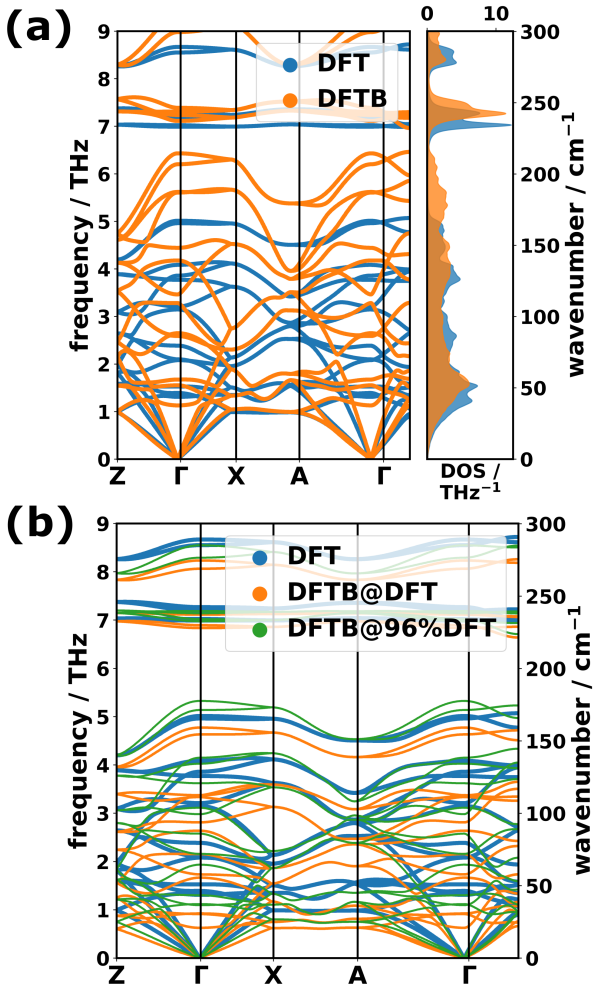

Fig. 4.7.: (a) Comparison of phonon band structures and DOSs of crystalline anthracene calculated with DFT (PBE/D3-BJ) and DFTB. The DFTB data have been obtained for a unit-cell which has been optimised purely within DFTB. (b) Comparison of band structures of crystalline anthracene calculated with DFT (PBE/D3-BJ) and DFTB, for which unit-cells have been used which were obtained from (isotropic) rescaling of the DFT unit-cell volume by the scaling factors 1.0 ("DFTB@DFT") and 0.96 ("DFTB@96%DFT"), respectively.

Here again, using a rescaled version of the DFT unit-cell provides a means of improving the phonon bands. DFTB band structures computed with (rescaled) DFT unit-cells can be seen in Fig. 4.7(b). In contrast to the case of naphthalene, it is hard to tell at first glance, which scaling factor achieves the best agreement with the DFT reference, as some of the scaling factors result in better agreement of the acoustic bands, while others yield better (intermolecular) optical modes. In order to unambiguously assess the quality of

agreement, the RMSD of frequencies (below 9 THz) can be calculated. The dependence of the frequency RMSD (considering only the low-frequency region $\leq$ 9 THz) can be seen in Fig. 4.8. According to the shown graph, a rescaling of the DFT unit-cell volume by 96 % yields the best quantitative agreement with the DFT reference. Like in the case of naphthalene, the same result is consistently achieved regardless of whether the entire first Brillouin zone or only Γ is considered.

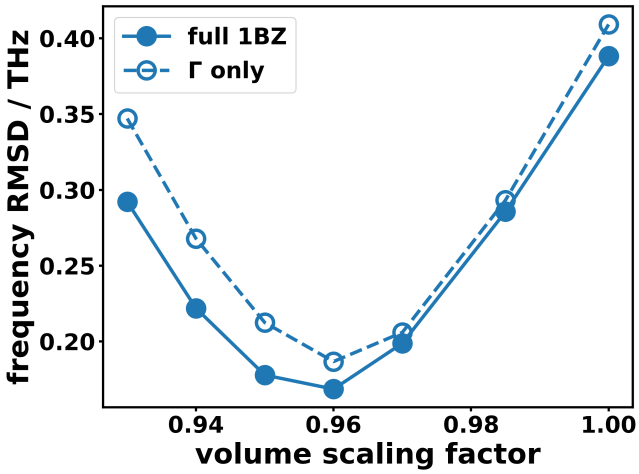

Fig. 4.8.: Root-mean-square deviation (RMSD) of frequencies ($\leq$ 9 THz) between the DFTB calculation and the DFT reference for anthracene. The frequencies in the DFTB case have been calculated for lattice parameters based on the DFT unit-cell whose volume has been scaled by the shown scaling factors. The solid line with filled symbols represents the RMSD if the entire first Brillouin zone is considered, while the dashed line with open symbols represents the RMSD for Γ-frequencies only.

An optimal scaling factor in the same range could also be identified for fluorene. Fig. 4.9(a) shows the comparison of the phonon band structure of fluorene calculated with DFT with two DFTB-based approaches: pure DFTB (using lattice parameters from a DFTB optimisation) and using a rescaled DFT unit-cell with only the atomic coordinates being optimised within DFTB. It can be seen that the agreement between the DFT and the pure DFTB bands is rather unfavourable, whereas a suitable rescaling of the DFT unit-cell results in a notable improvement as it has been shown to be the case for naphthalene and anthracene as well. The scaling factor of 0.97 might, however, be slightly more fine-tuned to achieve an improved degree of agreement as can be seen in Fig. 4.9(b).

However, it should be stressed that before applying this approach in a general way, further tests must be carried out considering more (diverse) systems. Moreover, the here presented way of scaling the lattice vectors isotropically might be less favourable for more anisotropic systems than the three discussed ones. Also the description of anharmonicities might not necessarily be the same in DFTB and DFT - indeed, they

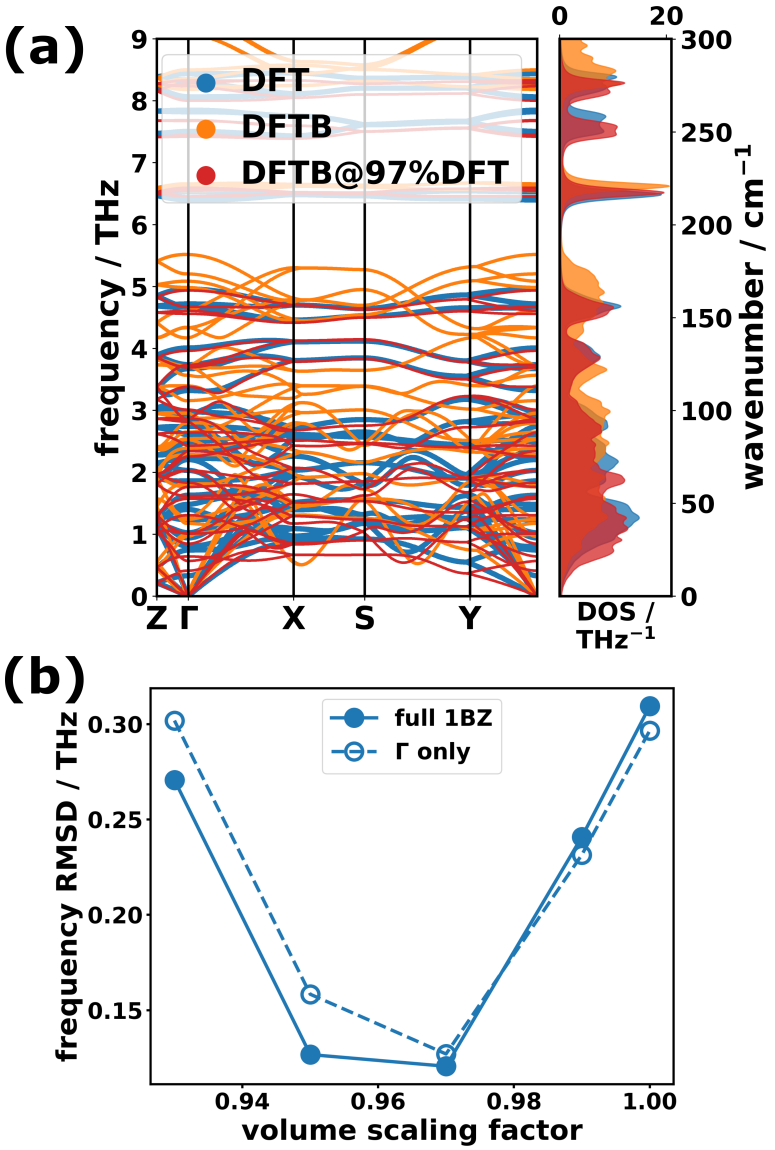

Fig. 4.9.: (a) Comparison of phonon band structures and DOSs of crystalline fluorene calculated with DFT (PBE/D3-BJ) and DFTB. The DFTB data have been obtained for a unit-cell which has been optimised purely within DFTB ("DFTB") and for a unit-cell which was obtained from (isotropic) rescaling the DFT unit-cell volume by a factor of 0.97. (b) Root-mean-square deviation (RMSD) of frequencies (≤ 9 THz) between the DFTB calculation and the DFT reference for anthracene. The frequencies in the DFTB case have been calculated for lattice parameters based on the DFT unit-cell whose volume has been scaled by the shown scaling factors. The solid line with filled symbols represents the RMSD if the entire first Brillouin zone is considered, while the dashed line with open symbols represents the RMSD for Γ-frequencies only.

are very likely to differ significantly. The most elegant but least straightforward alternative to improve the accuracy of DFTB would be a reparametrisation of Slater-Koster parameters to achieve a better transferability.

4.2.3. Phonon Band Structures from Classical Force Fields

Computationally much less expensively but more approximately, the interatomic (harmonic) force constants for phonon calculations can also be computed using classical force fields. In this approach, the forces between atoms are not mediated by the electronic interactions in the system such that no quantum-mechanical considerations are necessary. The entire interatomic interaction is, in principle, *hard-coded* in pre-defined terms depending on the bonding lengths, angles and dihedrals - i.e. the geometric arrangement of the atoms in the system. In this benchmark of phonon properties, the suitability to reproduce experiments/the reference data of three force fields (FFs) with different level of sophistication has been tested [1].
As detailed in Sec. 3.1.3, GAFF was developed for organic compounds with all bonding interactions being described by harmonic terms - without cross terms. Conversely, COMPASS considers much more complex mathematical shapes of the interaction potentials even including cross terms (resulting in much more parameters that were fitted by the developers of the force field). Therefore, a remarkable increase in accuracy is expected as the transferable nature of the force field offers so many more screws to turn to describe the involved interatomic bonding situation. Finally, MOF-FF has been specially parametrised based on an isolated naphthalene molecule such that one expects the most accurate results from this intransferable FF.
Before discussing the phonon properties obtained with these three FFs in more detail, one should note that the lattice parameters from the full unit-cell optimisation are in close agreement with the experiment and the DFT reference. Interestingly, the unit-cell volume obtained with the MOF-FF is essentially the same as the DFT reference in spite of the fact that only the intramolecular interactions have been fitted based on an isolated naphthalene molecule, while the intermolecular interactions determining the molecular packing were left untouched. Both, MOF-FF and GAFF show only small deviations from the reference in the lattice parameters: at most ~-2 % and ~-3 %, respectively, for the length of the lattice vector **a**, which crucially determines the intermolecular distance between the two inequivalent molecules in the unit-cell. For COMPASS, the largest deviation (~-3 %) is observed for the length of lattice vector **b** determining the smallest distance between a molecule and its periodic image in a neighbouring unit-cell. In spite of the good accuracy of the lattice parameters, the geometry optimisation using the FFs results in structures with reduced symmetry: while (considering a tolerance of 10^{-5} Å) with COMPASS and GAFF all symmetries are lost (space group $P1$), with MOF-FF at least inversion symmetry in the crystal structure (space group $P\bar{1}$) is conserved. Computationally this reduction of symmetries compared to the original (experimental) space group ($P2_1/c$) means that much more symmetry-inequivalent Cartesian displacements must be calculated to obtain the full dynamical matrix: for the correct space group, only 54 inequivalent atomic displacements have to be considered, while for space group

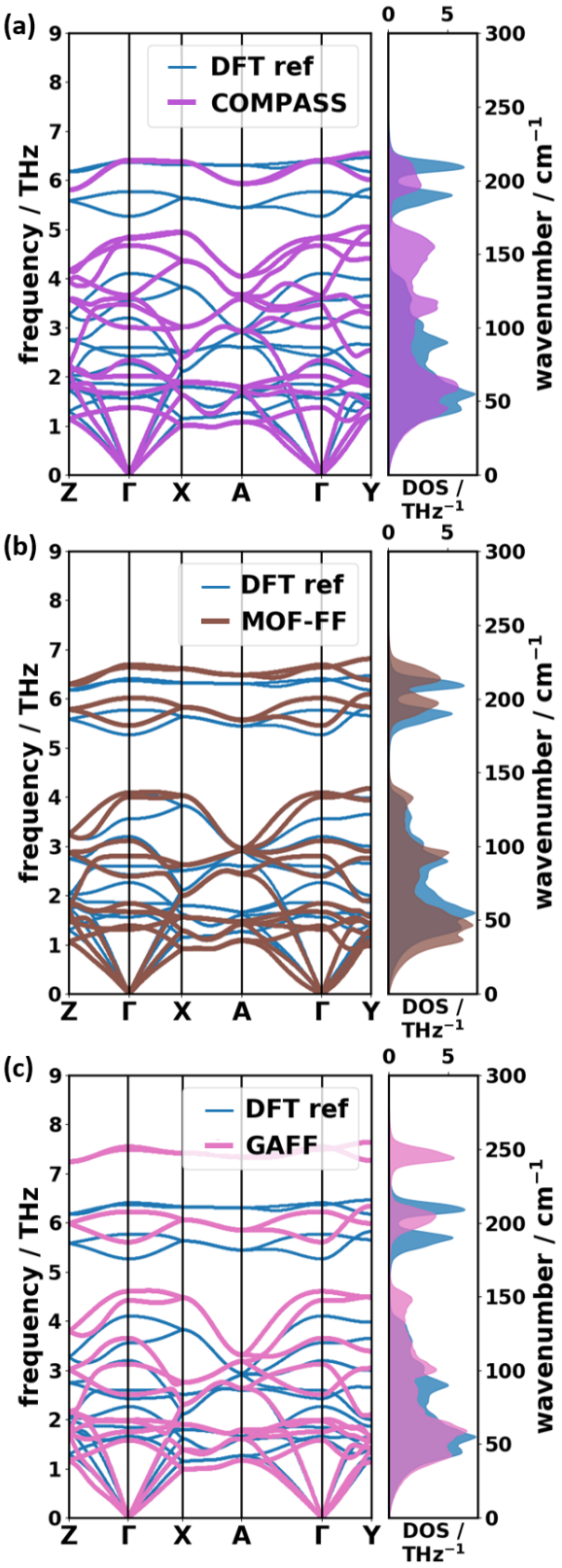

Fig. 4.10.: Phonon band structures and DOSs of various FF-based approaches compared to the DFT reference (DFT ref). (a) COMPASS [83] (b) our parametrisation of the MOF-FF [84], and (c) GAFF [81]. This figure has been taken from Ref. [1].

$P1$ ($P\bar{1}$) 216 (108) displacements are necessary to compute. This issue is, however, not a real problem for the computational cost using FFs, as the gigantic speed-up caused by not treating quantum-mechanics explicitly more than compensates the loss of symmetries.
The low-frequency phonon band structures are shown together with the corresponding DOSs in Fig. 4.10. While COMPASS is obviously suitable to accurately describe the acoustic bands and the corresponding region of the DOS (the onset of the DOS up to ~1.2 THz perfectly agrees with the reference), the optical bands show only few similarities with the DFT reference regarding energy scale, dispersion and band gaps. In particular the highest shown bands - i.e. the first intramolecular bands - severely deviate from the reference. This finding can be ascribed to the fact that for these motions, it is the bonding interactions rather than the van der Waals interaction which counts, suggesting that the parametrisation of COMPASS might still be improvable for high-accuracy phonon calculations.
Compared to COMPASS, our parametrisation of the MOF-FF shows a much better agreement with the reference band structure in the entire low-frequency region, as most of the spectral features are reproduced. While the bands below ~2 THz are slightly shifted towards lower frequencies, the first intramolecular bands fit particularly well to the DFT reference. The latter is not unexpected as, in contrast to the *universally applicable* COMPASS FF, this FF has been parametrised especially to mimic interatomic interactions in a naphthalene molecule.
Surprisingly, the acoustic and low-frequency intermolecular bands calculated with the GAFF are in excellent agreement with the reference. Up to frequencies of 4.5 THz, the agreement is even comparable with the much more sophisticated MOF-FF, while for the acoustic bands, GAFF even outperforms MOF-FF. The fact that mostly non-bonding interactions (van der Waals, Coulomb interaction) are responsible for those low-frequency intermolecular motions suggests that the 12-6-Lennard Jones description as implemented in the GAFF is slightly more suited to account for these interactions. For higher frequencies, at which intramolecular motions start to dominate, the agreement visibly deteriorates, which can be ascribed to the only harmonic description of bonding interactions in the GAFF.
All the general observations and comparisons of the band structures discussed up to now, equally apply to comparisons of the deuterated crystals with the experimental data as shown in Fig. 4.11.

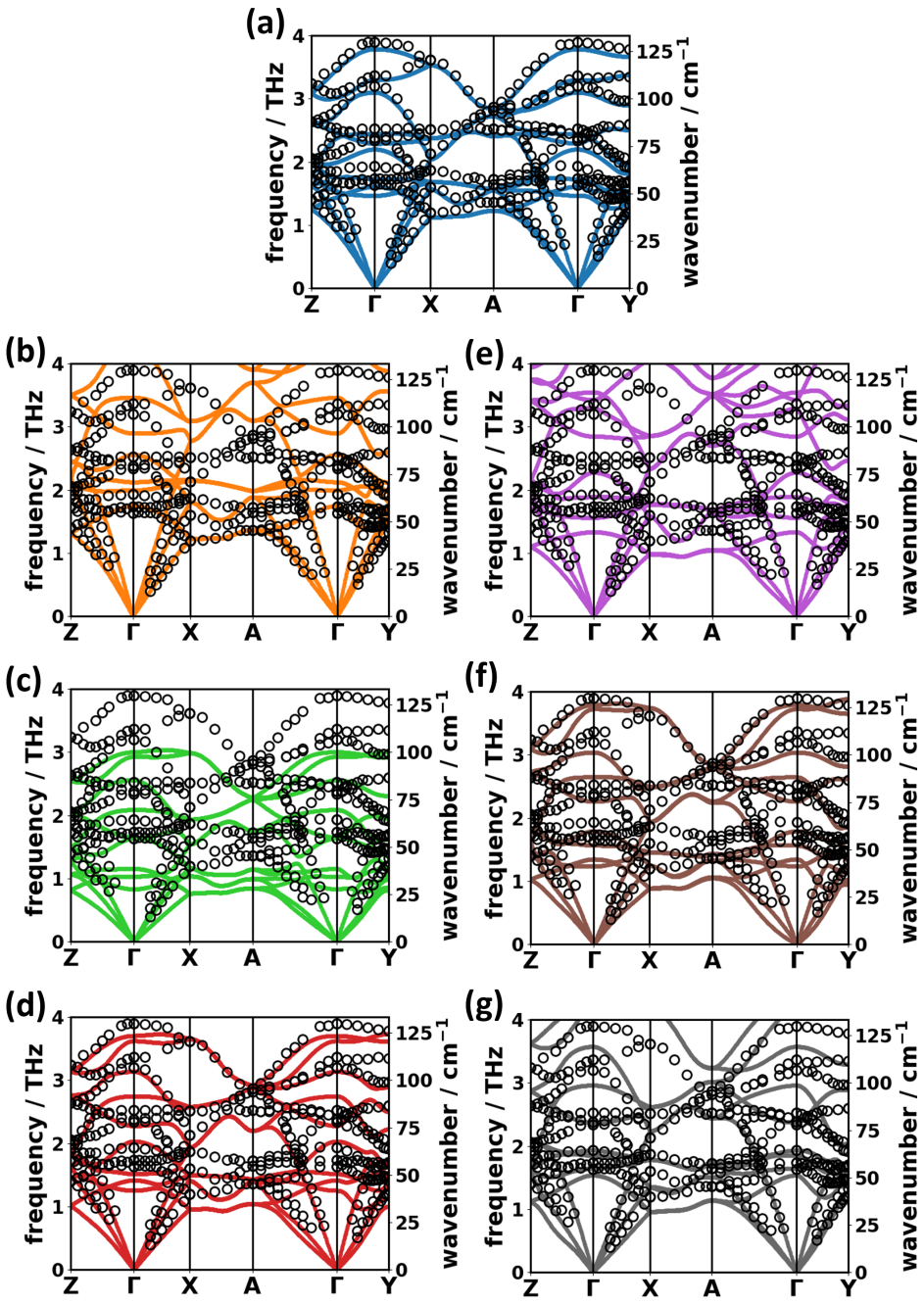

Fig. 4.11.: Phonon band structures (solid lines) of deuterated naphthalene calculated with (a) DFT (PBE/D3-BJ), (b) DFTB (with DFTB-optimised lattice vectors), (c) DFTB@DFT (DFTB with DFT-optimised lattice vectors), (d) DFTB@95%DFT (DFTB with DFT-optimised lattice vectors which were rescaled such that the volume amounts to only to 95 % of the original DFT-volume), (e) COMPASS (an anharmonic, transferable FF), (f) MOF-FF (an anharmonic, intransferable FF), and (g) GAFF (a harmonic, transferable FF) in comparison with the experimental data points (open circles). The latter were measured at a temperature of 6 K by Natkaniec et al. [24]. This figure has been taken from the Supporting Information of Ref. [1].

4.2.4. Quantitative Benchmark of Low-Frequency Phonon Properties

Although the previous discussion of discrepancies in the phonon band structures of various approximate methodologies provides valuable insights, it lacks quantitative assessment. In order to generate more specific insights into the accuracy and performance of these methodologies, it is more reasonable to focus not only on the band structure along certain high-symmetry paths, but rather on the entire first Brillouin zone. Since the simulations consider crystals of infinite extension, the space of wave vectors $\mathbf{q}$ becomes continuous. Still, one must discretise the $\mathbf{q}$-space for numerical calculations. As described in Sec. 3.1, the sampling must be as homogeneously distributed as possible all over the first Brillouin zone. Here, a $9 \times 10 \times 9$ $\mathbf{q}$-mesh was chosen to yield converged thermodynamic properties for which an integration over the first Brillouin zone is required.
In the course of the following discussion, most of the arguments will be based on statistical measures to quantify the deviations from the DFT reference data. A quantity that is often used to describe the discrepancies with respect to a reference is the root-mean-square deviation (RMSD) of a certain property x:

$$\mathrm{RMSD}_x = \sqrt{\frac{1}{N}\sum_{i}^{N}\left(x_i - x_{ref,i}\right)^2} \tag{4.1}$$

However, these RMSD values are not capable of indicating whether there is a general trend to over- or underestimate the reference property as the sign is lost when squaring the differences in (4.1). This knowledge is especially important when band structure-related properties (such as frequencies) enter thermodynamic expressions to calculate physical observables because under- and overestimated frequencies might compensate each other, for instance. In order to judge if a methodology is robust against such effects, it is useful to also consider the average deviations (AD) of the property x:

$$\mathrm{AD}_x = \frac{1}{N}\sum_{i}^{N}\left(x_i - x_{ref,i}\right) \tag{4.2}$$

A last step is still required to reasonably compute these statistical measures. Since the band index of a certain vibration can vary amongst the systems[36] comparing, e.g., frequencies, one must identify the corresponding phonon bands according to the approach described in Sec. 3.1.5 based on the algorithm of Kuhn [109] and the phonon eigenvectors (or polarisation vectors).

Starting with the basic ingredient for all phonon-related properties, the frequencies, Fig. 4.12(a) shows the frequency differences of the tested methodologies compared to the reference frequency (after the phonon mode assignment) as a function of this reference

[36] This means that a given vibration with a specific atomic motion can be the n^{th} band in the reference and the m^{th} band in an approximate method (with $n \neq m$) depending on how dense the bands lie and how accurately they can be reproduced by the compared method.

frequency, while panel (b) shows the cumulative RMSD_f values (for the frequencies) up to a cutoff-frequency as a function of that frequency cutoff. The values of RMSD_f at the highest shown frequency (9 THz) are listed in Tab. 4.2 together with the average deviations AD_f to quantitatively assess potential trends in the deviations from the reference.

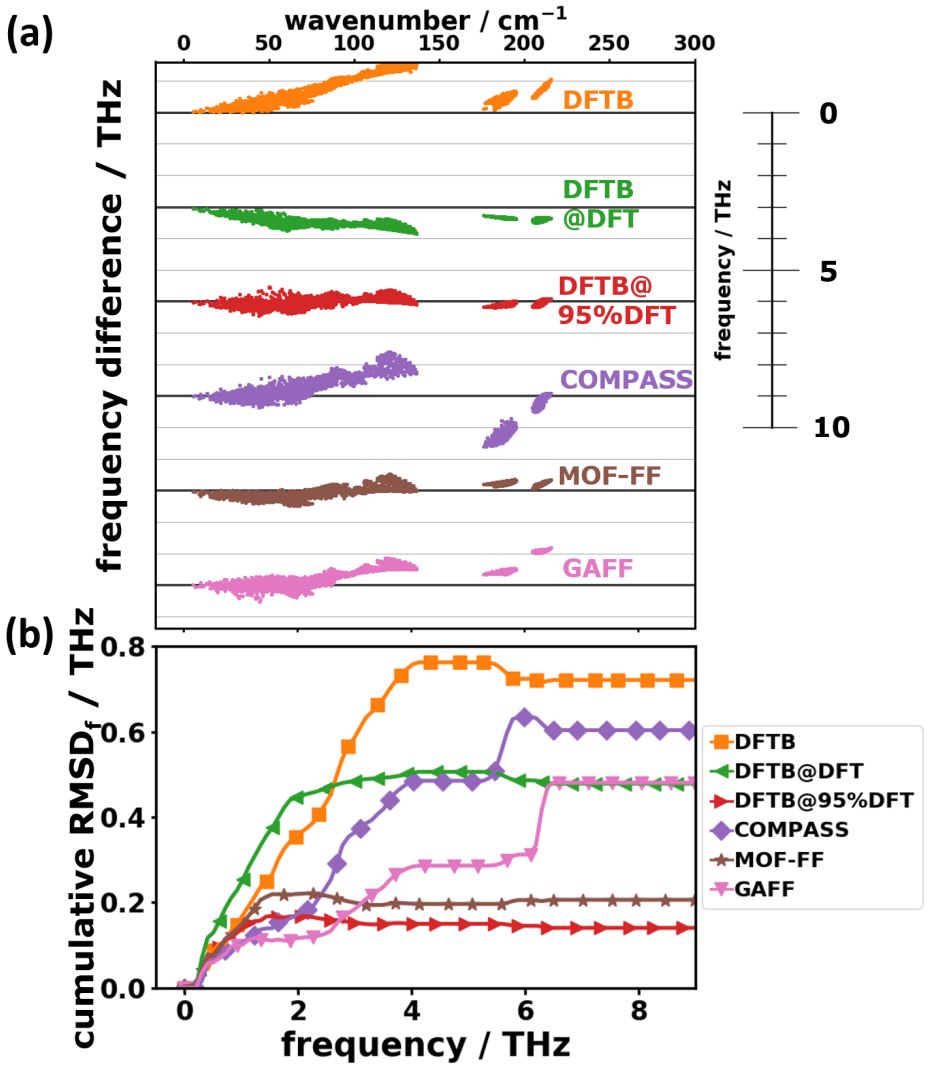

Fig. 4.12.: (a) Frequency differences of the tested approximate approaches with respect to the DFT reference (PBE/D3-BJ) as a function of the reference frequency in the low-frequency region. The frequency differences of each tested methodology are plotted with respect to its own zero line (thick black horizontal lines). (b) Cumulative root-mean-square deviations of frequencies considering phonon modes up to a certain cutoff frequency as a function of that cutoff. The symbols in (b) do not represent the actually calculated data points, which lie much more densely, but rather serve as guides to the eye. This figure has been taken from Ref. [1].

In line with the qualitative discussion of the band structures above, the pure DFTB approach shows a consistent shift of phonon modes towards higher frequencies (by up to ~1.5 THz). The frequency differences increase in a nearly linear fashion for the intermolecular modes up to ~4 THz, resulting in a particularly large RMSD_f and a large positive AD_f. In contrast to that, the DFTB@DFT approach rather experiences a shift towards lower frequencies, which is also indicated by the negative AD_f. Below 2 THz, however, the cululative RMSD_f is the highest of all approaches consistent with the observation from the band diagrams that the band dispersion of the acoustic bands is particularly underestimated. Both error descriptors can be significantly decreased by rescaling the unit-cell (DFTB@95%DFT) resulting in the smallest RMDS_f of all tested approaches in the low-frequency regime.
Regarding the frequencies obtained with the three FFs, COMPASS shows the tendency to overestimate the intermolecular modes up to ~4 THz. The frequencies of the first intramolecular modes are, however, underestimated so severely that the overall AD_f is relatively small considering that the RMSD_f is the second largest of all approaches. The frequency differences can be found within a relatively large spread of approximately ±1.5 THz around the reference. The particularly bad description of the first intramolecular bands starting at ~6 THz is the reason for the abrupt increase in the cumulative RMSD_f. With MOF-FF, this broad distribution of frequency differences can be notably reduced such that the RMSD_f is only slightly higher than for DFTB@95%DFT. Owing to the absence of any tendencies of over- or underestimations, the AD_f is the smallest of all approaches. Consistent with the conclusions drawn from the comparison of the band structures, the GAFF calculation shows excellent agreement with the reference data for very low frequencies up to ~2.5 THz. In this spectral region also the RMSD_f value is the smallest of all approaches in spite of the simplicity of the underlying force field. However, the error increases relatively rapidly above that frequency due to a consistent overestimation of phonon frequencies resulting in an essentially equivalent overall RMSD_f as DFTB@DFT.

In the following, the phonon group velocities $\mathbf{v_g}$ are discussed in terms of their (vector) norms, $v_g = \|\mathbf{v_g}\|$. First insights are generated from the analysis of the density of group velocities (DOGV). In analogy to the definition of the density of states according to Eq. (2.81), the DOGV is defined as follows [1]:

$$\mathrm{DOGV}(v_g) = \frac{1}{3N}\frac{1}{N_q}\sum_{n}^{3N}\sum_{\mathbf{q}}^{N_q}\delta\left(v_g - v_{g_{n,\mathbf{q}}}\right) \tag{4.3}$$

Note that the used definition of the DOGV differs from that of the DOS by the additional factor of $(3N)^{-1}$. This factor is used in order to normalise the integral of the DOGV over all group velocities to unity instead of $3N$. Therefore, the DOGV has all the properties of a probability density (non-negativity and normalisation [132]). Here, only the low-frequency modes up to 9 THz have been considered in the sum. Consequently, the normalisation factor was chosen not to be $3N$ but the number of low-frequency bands entering the summation. The DOGVs of all approaches are shown and compared to the DFT reference in Fig. 4.13. Conceptually, the DOGVs are very similar in all approxim-

Tab. 4.2.: Average differences (AD_x) and root-mean-square deviations ($RMSD_x$) of various phonon-related properties, x, with respect to the DFT reference. Here, the subscript x refers to different quantities: f ... frequencies, v_g ... vector norm of the group velocities, u^2 ... mean square thermal displacements (MSTD). While the numerical averaging in the calculation of AD_x and $RMSD_x$ for frequencies and group velocities has been carried out over phonon modes in the entire first Brillouin zone (sampling as described in Sec. 3.1), the averaging for the MSTD has been carried out over atoms. This table has been taken from Ref. [1].

		DFTB	DFTB@DFT	DFTB@95%DFT	COMPASS	MOF-FF	GAFF
Frequencies	$RMSD_f$ / THz	0.72	0.48	0.14	0.60	0.20	0.48
(≤ 9 THz)	AD_f / THz	0.62	-0.46	-0.05	0.07	-0.03	0.31
Frequencies	$RMSD_f$ / THz	1.43	1.50	1.46	2.10	0.76	4.14
(entire range)	AD_f/ THz	-0.55	-0.84	-0.73	0.17	0.06	1.10
Group velocities	$RMSD_{v_g}$ / THzÅ	5.2	3.3	3.8	5.8	3.6	4.1
(≤ 9 THz)	AD_{v_g} / THzÅ	3.8	-0.9	1.2	3.3	1.6	1.7
MSTD	$RMSD_{u^2}$ / Å^2	0.024	0.076	0.019	0.005	0.033	0.002
(150 K)	AD_{u^2} / Å^2	-0.023	0.074	-0.019	-0.002	0.033	0.001
MSTD	$RMSD_{u^2}$ / Å^2	0.048	0.152	0.039	0.009	0.066	0.004
(300 K)	AD_{u^2} / Å^2	-0.046	0.147	0.037	-0.004	0.066	0.003

ate methods - i.e. the DOGVs show maxima for relatively low group velocities in the range of up to 10 THzÅ and vanish for high group velocities beyond ~30 THzÅ, although some of the low-frequency modes show higher group velocities (up to ~50 THzÅ). The reason the DOGV still (approximately) vanishes for these high group velocities is the fact that only a few bands (of the 108 in total) show these large extents of dispersion and typically only close to the centre of the first Brillouin zone.
However, a closer look at the various DOGVs from the different approaches reveals that the densities of large group velocities are typically overestimated - i.e. the maxima of the DOGVs are typically shifted to larger values of v_g - while, consequently, the density of lower group velocities is rather underestimated. Interestingly, the DFTB@DFT approach yields the best agreement with the reference DOGV for very small group velocities up to about 4 THzÅ. Unfortunately, the analysis of the DOGV does not allow to draw conclusions about the spectral regions in which the band dispersion is typically over- or underestimated. Here, a statistical analysis similar to the one applied for frequencies above provides more quantitative insight. The cumulative RMSD_{v_g} in the low-frequency regime as well as the group velocities of all sampled phonon modes as a function of the associated frequency are shown in Fig. 4.14. Note that for reasons of visibility, the RMSD_{v_g} has been multiplied by a factor of 5. The computed average and RMS deviations are listed in Tab. 4.2. In line with the observation from the DOGVs, the typical shifts to higher group velocities are in agreement with the prevailingly positive AD_{v_g} in all cases except for DFTB@DFT. This approach also shows the best quantitative agreement in low-frequency group velocities, since the RMSD_{v_g} and the AD_{v_g} are the smallest of all approximate methods. However, the cumulative RMSD_{v_g} is particularly large in the spectral region up to ~0.5 THz. This means that the band dispersion of the acoustic phonons, which are typically the most important ones for phonon transport properties, is described with a relatively bad accuracy.
Except for DFTB@DFT, the cumulative RMSD_{v_g} values shown in Fig. 4.14 stay relatively constant throughout the entire low-frequency region suggesting that there is not a large variation in the accuracy of the description of the group velocities in this spectral regime. However, the absolute values of the RMSD_{v_g} (~3...~6 THzÅ; see Tab. 4.2) are relatively large compared to the actual group velocities. This suggests that the performance of the approximate methods is still improvable when it comes to accurately describing group velocities, and none of them really offers a reliable alternative to DFT-based calculations.

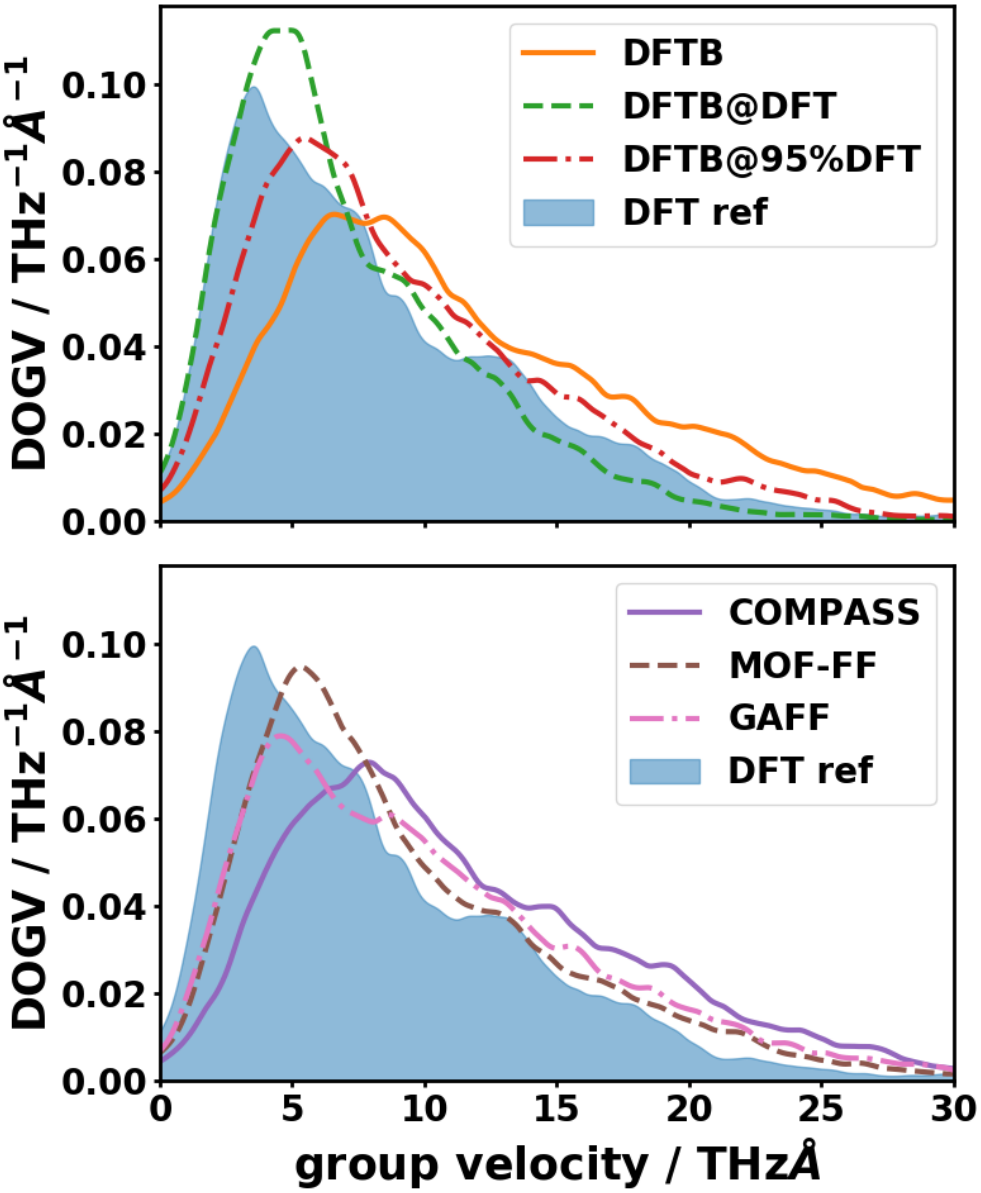

Fig. 4.13.: Density of group velocities (DOGV) as a function of the vector norms of the phonon group velocity. The DOGVs have been calculated according to the definition of Eq. (4.3) replacing the delta distributions by functions with a finite width. Here, Lorentzian peaks with a full width at half maximum of 1 THzÅ were chosen, centred at the group velocities of the sampled low-frequency (≤ 9 THz) modes. The blue shaded area represents the DOGV of the DFT reference. This figure has been taken from Ref. [1].

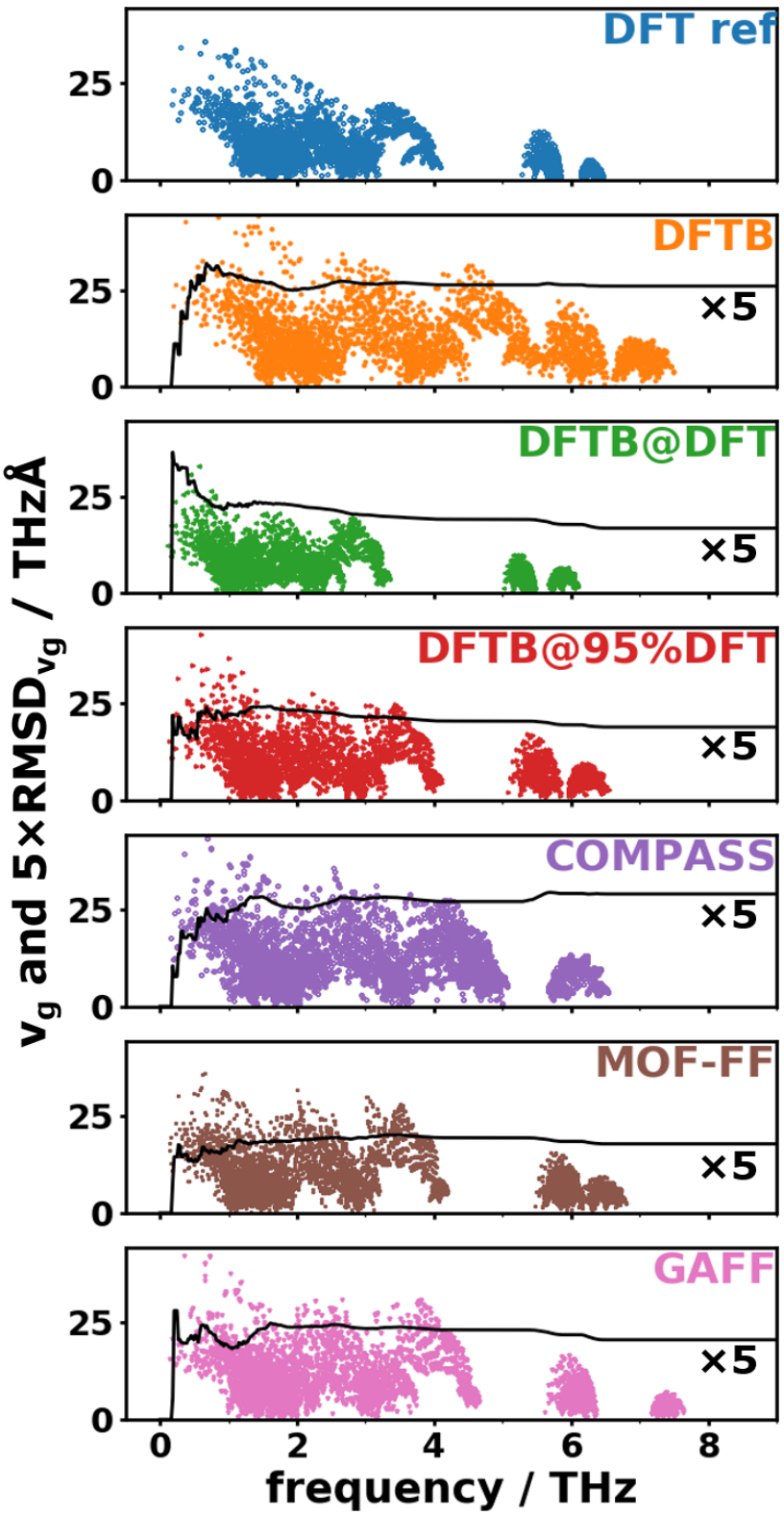

Fig. 4.14.: Vector norms of phonon group velocities as function of the associated phonon frequency. Here, the phonon modes were sampled on a discrete mesh as described in Sec. 3.1. The solid black lines show the cumulative RMSD_{v_g}, which has been scaled by a factor of 5 for reasons of visibility. This figure has been taken from Ref. [1].

4.2.5. Assessment of the Suitability of Approximate Methods to Describe Physical Observables Based on the (Low-Frequency) Phonon Band Structure

It has already been shown in Sec. 2.4 that many physically observable quantities prevailingly depend on low-frequency phonon modes. This results from the thermal occupation of phonon states. For the same reason, it is reasonable to analyse how the already discussed differences in the low-frequency phonon band structure affect thermodynamic properties. To this end, the physical observables will be compared to the properties calculated based on the DFT reference phonons. The first of the discussed quantities is the mean-squared thermal displacement (MSTD), which is defined in Eq. (2.86). This quantity describes the average squared displacement of an atom from its 0 K equilibrium position at finite temperature. It has already been shown by George et al. that the DFT/D3-BJ approach is highly suitable to reproduce experimental MSTDs [133], which can be extracted from high-quality X-Ray diffraction experiments, for instance. Although, in general, the MSTD has three Cartesian components for each atom in the crystal, which define the three axes of the so-called thermal ellipsoids, the discussion is restricted to a scalar quantity, which is simply the sum of the three Cartesian components of the MSTD.
Figure 4.15(a) shows the atom-resolved MSTD for each methodology calculated for a temperature of 300 K. It can be seen that the MSTDs vary to some extent between the chemically different carbon atoms. Also in the MSTDs of the chemically inequivalent hydrogen atoms, slight variations can be discerned. In general, the MSTDs of the hydrogen atoms are on average about 70 % larger because of the smaller atomic mass of this species. This circumstance can be seen qualitatively in the thermal ellipsoids in Fig. 4.15(b), which show the surfaces within which the atoms can be found with 75 % probability at all times.
Regarding the suitability of the approximate methods to yield accurate values for the MSTDs, Fig. 4.15(a) shows that the best agreement with the DFT reference is achieved with COMPASS and the GAFF. Quantitatively, this is evident by the small RMSD_{u^2} as listed in Tab. 4.2. The pure DFTB approach results in underestimated MSTDs (in line with a negative AD_{u^2}), whereas they are overestimated by the DFTB@95%DFT, MOF-FF, and DFTB@DFT approaches, in increasing order of AD_{u^2}. In the latter case, the extent of overestimation is particularly bad, as the MSTDs are too large by about a factor of 2. The key to understanding the reason for this behaviour is Eq. (2.86). The spectral function which weights the DOS and the eigenvector contributions to the MSTD is $(1 + 2n(\omega))/\omega$. Both factors, one of them containing the Bose-Einstein distribution n and the other one ω^{-1}, favour low frequencies so that the description of the acoustic phonons is of crucial importance. Note that the factor $(1 + 2n(\omega))/\omega$ can also be rationalised by semi-classical arguments by equalling the potential energy of a harmonic oscillator (determined by the amplitude u_0, its mass m, and the angular frequency ω) with the quantised energy of the quantum harmonic oscillator [134]:

$$\begin{aligned} \frac{m\omega^2}{2}u_0^2 &= \hbar\omega\left(n+\frac{1}{2}\right) \\ u_0^2 &= \frac{\hbar}{m\omega}\left(1+2n\right) \end{aligned} \tag{4.4}$$

More rigorously, the spectral function $(1 + 2n(\omega))/\omega$ has its origin in the definition of the position operator in terms of creation an annihilation operators in a harmonic oscillator and their commutation relations as shown in Sec. 2.4.
Consequently, the surprisingly good agreement between COMPASS and GAFF with the reference can be ascribed to their accurate descriptions of acoustic phonon bands and the resulting onset of the DOS in that spectral region. In DFTB, the acoustic frequencies are significantly overestimated resulting in a too gradual increase of the DOS, which, in turn, causes a decrease of the occupation of those modes at a given temperature. The diminished thermal occupation of the acoustic band is the reason why there are fewer contributions to the MSTDs leading to underestimations of this quantity. In contrast, for those methodologies which tend to underestimate the band dispersion of the acoustic bands (most significantly DFTB@DFT), too many contributions enter the sum (integral), resulting in overestimated MSTDs.

Concerning the temperature dependence of the differences in MSTDs, Tab. 4.2 shows, that the absolute magnitudes of the deviations approximately increase by a factor of 2 from 150 to 300 K. However, the ratios between the RMSD_{u^2} and the MSTDs stay about the same. This can be understood by the following considerations. The only term that contains the temperature in the equation for the MSTD is the Bose-Einstein distribution. For $\hbar\omega \ll k_B T$, one can approximate the exponential function appearing in the Bose-Einstein distribution:

$$n(\omega|T) = \frac{1}{\exp\left\{\frac{\hbar\omega}{k_B T}\right\} - 1} \approx \frac{1}{1 + \left(\frac{\hbar\omega}{k_B T}\right) - 1} = \frac{k_B T}{\hbar\omega} \tag{4.5}$$

Thus, for the acoustic phonons with frequencies, for which $\hbar\omega$ is small compared to $k_B T$, one expects a linear scaling with the temperature.

Besides the thermal displacements of the atoms, another important thermodynamic property directly related to the phonon band structure is the heat capacity (at constant volume) C_V. As shown in Sec. 2.4, C_V is the derivative of the internal energy with respect to the temperature for fixed unit-cell volume. Introducing the DOS and an integral over a continuous frequency instead of the summation over bands and discrete wave vectors, one can alternatively interpret the heat capacity as an integral of the DOS multiplied with a (smooth) low-pass filter whose cutoff frequency $f_{1/2}$ scales with temperature as[37]:

[37] The proportionality is obtained by finding the argument $x = \frac{\hbar\omega}{k_B T}$ at which the low-pass filter drops to the value 1/2 - i.e. by numerically solving the equation $\frac{(x^*/2)^2}{\sinh^2(x^*/2)} = \frac{1}{2}$ for x^*, which yields $x^* \approx 2.98286714$. Solving for the frequency yields $f_{1/2} = \frac{k_B x^* T}{h}$.

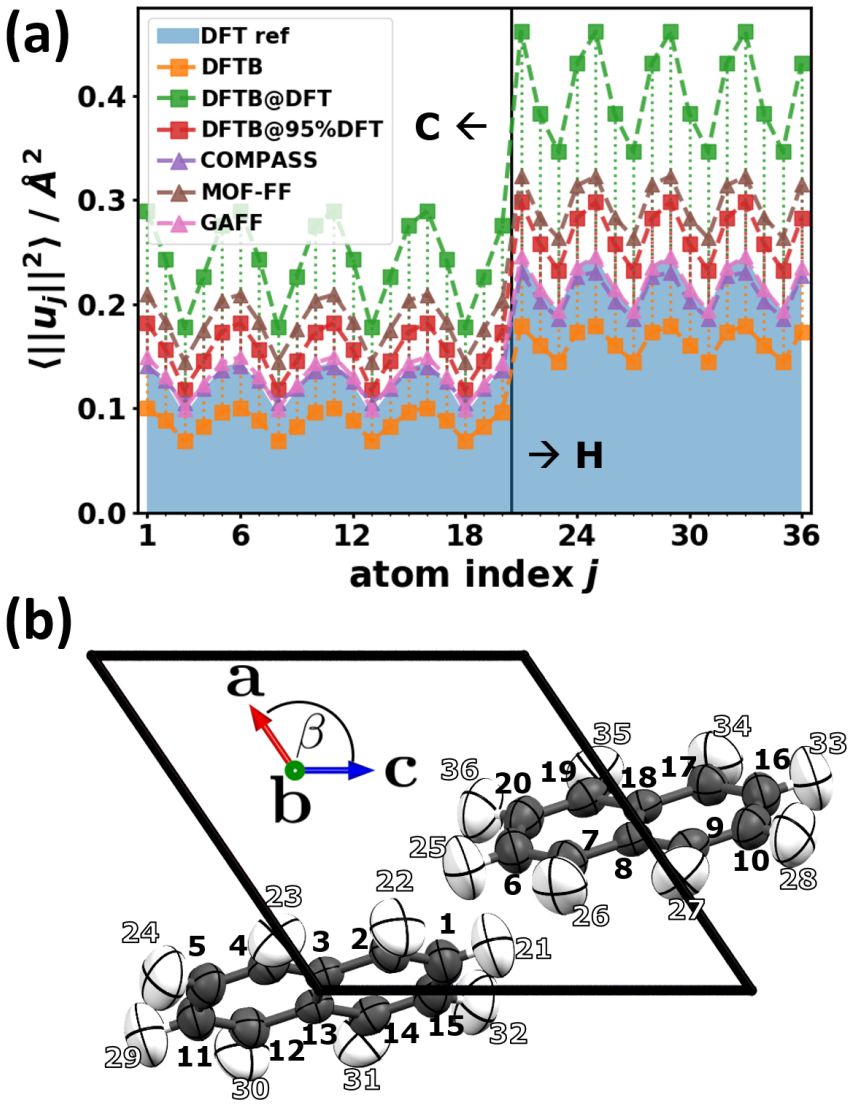

Fig. 4.15.: (a) Mean-square thermal displacements (MSTDs) $\langle \|u_j\| \rangle$ at a temperature of 300 K as a function of the atom index. The shaded area corresponds to the DFT reference, while both, lines connecting MSTDs and the vertical lines, are only guides to the eye and facilitate the visual perception of the differences with respect to the reference. (b) Atom indices in the unit-cell of naphthalene used as the abscissa in (a). The MSTDs are three-dimensionally visualised by plotting the thermal ellipsoids with *Mercury*[135]. These can be obtained by using spatial Gaussian probability distributions for the atomic positions, with the MSTDs being related to the covariance matrices in those distributions [136]. Consequently, thermal ellipsoids can be calculated for every probability. Here, they are drawn such that the atoms can be found within the thermal ellipsoids with a probability of 75 %. This figure has been taken from Ref. [1].

$$f_{1/2} = 0.06215285 \frac{\mathrm{THz}}{\mathrm{K}} \cdot T \tag{4.6}$$

This means that at a temperature of 100 K, the DOS is (approximately) integrated over frequencies $\leq$ 6.2 THz. This statement, however, is not strictly true, since the low-pass filter function does not have a sharp cutoff at $f_{1/2}$, but a smooth one with a certain width, which also increases with temperature. Therefore, at low temperatures, C_V is dominated by the low-frequency phonon modes. The earlier defined low-frequency region in the naphthalene band structure ($\leq$ 9 THz) is, thus contained in the integration at ~150 K. This is the temperature range of C_V which should be the subject of the following discussion.

Fig. 4.16(a) shows the heat capacities per unit-cell of all tested methodologies as a function of temperature. Note that the heat capacities have been normalised by the limiting value $3Nk_B$ at $T \to \infty$ - i.e. the value of C_V in the classical limit (so-called Dulong-Petit law), with $3N$ being the number of phonon bands (=3× the number of atoms per unit-cell = degrees of freedom per unit-cell) and k_B being the Boltzmann constant. In order to facilitate the assessment of the performance of the approximate methodologies compared to the reference data, Fig. 4.16(b) shows the difference in C_V of each approach with respect to the reference as a function of temperature. In all approaches, the largest deviations can be found at temperatures below ~75 K. In line with the discussion of the phonon band structure and the MSTDs, the DFTB approach shows an underestimation of the heat capacity in the entire shown temperature range, since the low-frequency DOS increases too gradually, owed to the too high band dispersion of the acoustic bands and the typical shift of spectral features to higher frequencies. Likewise, COMPASS and GAFF, which yielded the best agreement for the MSTDs, show also the smallest deviations for C_V, but only up to very small temperatures (~15 K). This temperature corresponds to a $f_{1/2}$ value of approximately 1 THz - i.e. it involves mostly the acoustic bands, which are described acceptably well with these two force fields. For higher temperatures - i.e. as soon as more optical bands start to contribute to C_V - the agreement deteriorates. The reason why the the errors change much more with the temperature than it was the case for the MSTDs are the different "low-pass filters" of both quantities. The low-pass filter relevant for C_V extends to much higher frequencies than the one in the equation of the MSTDs. Thus, optical bands become important for the heat capacity already at lower temperatures[38]. Therefore, the trends in the differences in C_V (underestimation with COMPASS and GAFF) are even reversed at higher temperatures because of the underestimation of many optical frequencies. For COMPASS, this reversion happens particularly early (due to the severe underestimation of frequencies of the lowest intramolecular modes): at ~80 K the over- and underestimation of frequencies causes a total cancellation of errors so that the reference heat capacity is reproduced ($\Delta C_V = 0$). This compensation of errors is consistent with the particularly

[38] This can be qualitatively understood by recalling that in statistical physics, the heat capacity is related to the variance of the energy (see Sec. 2.4) in a system (at a given temperature). Higher-frequency phonons have higher contributions to those energy fluctuations and, thus, contribute more strongly than one would expect from the thermal occupation only.

small average deviation of frequencies, AD_f, for COMPASS (see Tab. 4.2). Due to this cancellation of errors, the COMPASS force field achieves acceptable values for the heat capacity in the entire shown temperature range, although one might see this more as a coincidence than a real achievement.

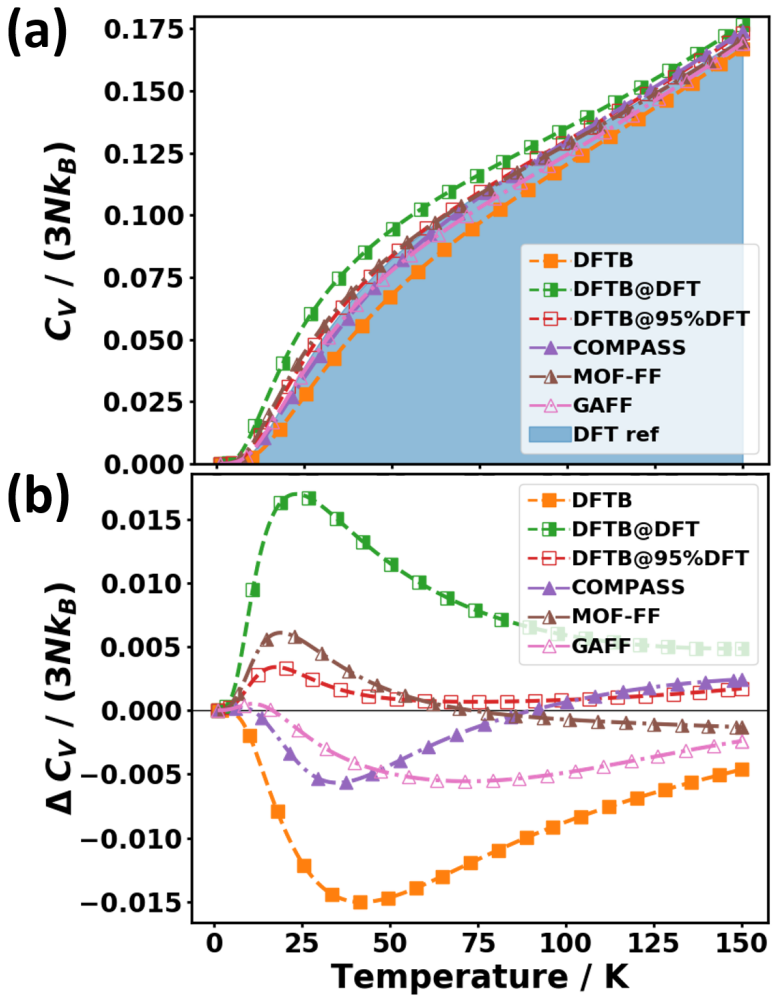

Fig. 4.16.: (a) Phonon contribution to the heat capacity C_V per unit-cell normalised by the Boltzmann constant k_B and the number of phonon modes ($3N$) as a function of temperature for all the tested methods. The blue shaded area corresponds to the DFT reference. (b) Difference in C_V relative to the heat capacity obtained with the DFT reference data. The symbols in both panels do not represent the actually calculated data points, which lie much more densely, but rather serve as guides to the eye. This figure has been taken from Ref. [1].

For MOF-FF and DFTB@95%DFT, the differences in C_V with respect to the reference are significantly smaller in the entire temperature range, which is consistent with

the generally very satisfying performance of these two approaches in the low-frequency region for both, inter- and intramolecular modes. The most notable discrepancies for the heat capacity are found for the DFTB and DFTB@DFT approaches, with the former underestimating and the latter overestimating C_V in a consistent way. Similar to the previously discussed cases, this behaviour can be traced back to the significant overestimation (underestimation) of frequencies with the DFTB (DFTB@DFT) approach. Eventually, the relative deviations from the reference heat capacity amount to up to 20 % at ~45 K in DFTB and as much as 43 % in DFTB@DFT at ~25 K. Still, the absolute errors are very small corresponding to roughly 1.6 % of the saturation value determined by the Dulong-Petit limit. The reason for that is that at 150 K, the heat capacity has only reached approximately 17 % of the classical limit, which is (hypothetically) approached above ~3500 K (i.e. at much higher temperatures than the melting point of crystalline naphthalene at 353 K [137]). This unrealistically high temperature required to establish classical circumstances - i.e. satisfying the equipartition theorem - is a result of the very high frequencies of C-H stretching modes (above ~90 THz). In order to extend the low-pass filter so much that these frequencies are fully covered in the integration, these extreme temperatures are required (see Fig. 4.17).

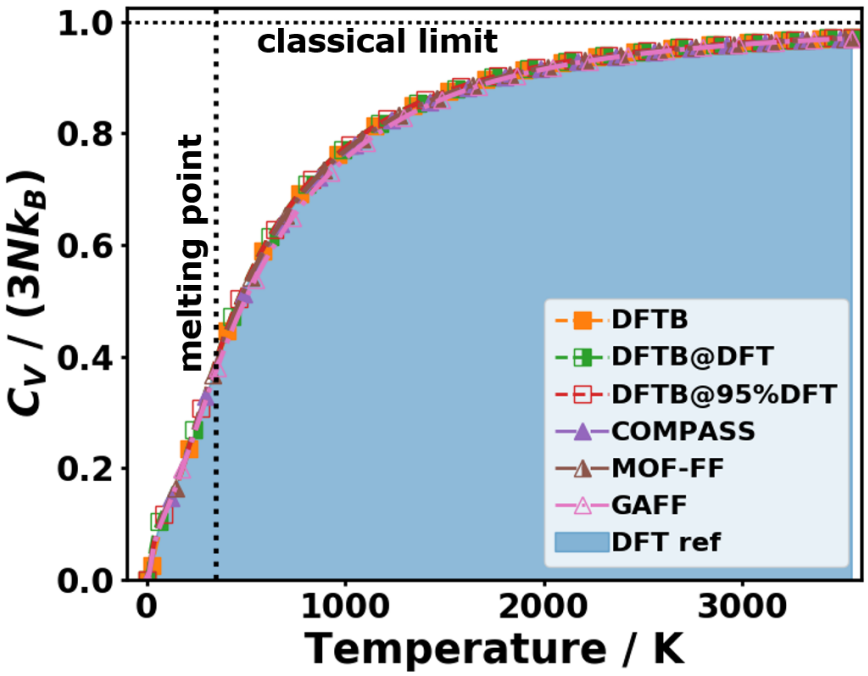

Fig. 4.17.: Saturation behaviour of the phonon heat capacity C_V as a function of temperature for the tested approaches. The vertical dotted line indicates the melting point of crystalline naphthalene (353 K [137]), while the horizontal line shows the classical limit for $T \to \infty$. This figure has been taken from the Supporting Information of Ref. [1].

4.3. High-Frequency Phonons (> 9 THz)

The discrepancies in the heat capacities discussed in Sec. 4.2.5 already indicate that for certain thermodynamic properties, especially at elevated temperatures, the higher-lying optical phonons increasingly gain in importance. Because of the fundamental differences in the nature of those higher optical phonon modes compared to the ones in the low-frequency region, with the former being dominated by intermolecular motion, while the latter are governed by intramolecular distortions within the molecules, it is worthwhile paying attention to the performance of the various approaches in that spectral regime separately. In terms of interactions, for the intermolecular modes, the non-bonding interactions (electrostatic Coulomb interaction and van der Waals forces) are important, while the bonding interactions - i.e. the much stronger covalent bonding motifs - are responsible for the intramolecular modes. For that reason, the performance of the approximate methods in this spectral region is very likely to deviate from the discussion considering the low-frequency regime. The fact that these two types of vibrational modes are dependent on fundamentally different physical interactions is also the reason why the choice of the van der Waals correction in DFT does not play such a big role for those higher frequencies, as shown earlier in Fig. 4.2.
Regarding experimental validation, no phonon band structures above ~4.1 THz are available. Thus, one must resort to Raman spectra showing phonon modes at the centre of the first Brillouin zone, Γ. As already discussed, Fig. 4.4 shows the excellent agreement of the DFT (PBE/D3-BJ) reference methodology with the experimental spectrum measured by Zhao and McCreery [128], regardless of whether a molecular or a periodic system is simulated. The simulated spectrum for the crystal, however, shows a pronounced difference at the low-frequency end of the spectrum: in contrast to the isolated molecule, the (Raman-active) intermolecular modes are accessible with the periodic simulation. The overall agreement between the calculations with PBE/D3-BJ even outperforms the results of using the hybrid functional B3LYP [129, 130]. Therefore, the reference methodology ("DFT ref") is still valid to be seen as such.

4.3.1. Quantitative Benchmark of High-Frequency Phonon Properties

A comparison of the DOSs obtained with the various tested methodologies is shown in Fig. 4.18 for the entire range of occurring frequencies in the system. Several conclusions can be drawn from that figure: (i) all the three DFTB-based approaches show relatively similar spectral features above 9 THz regardless of the chosen lattice parameters. This observation emphasises once more that these high-frequency intramolecular modes are relatively unaffected by the crystal packing, which, in turn, is determined by the different unit-cell volumes. (ii) The lower edge of the large band gap (~49 - 92 THz) is in excellent agreement with the DFT reference. These frequencies correspond to in-plane C-C stretching in the molecules, which are obviously accurately described within DFTB. In contrast, COMPASS and GAFF significantly overestimate these frequencies, with the latter showing the more severe effect. However, MOF-FF slightly underestimates these C-C stretching frequencies. This observation suggests that the parameters in none of the

force fields are optimally tuned for these modes. (iii) The C-H stretching modes, which can be seen as the sharp peaks above 90 THz in the DOSs appear to be quite difficult to describe for most of the approaches: except for MOF-FF, which is the only approach that yields satisfying agreement with the reference, all the other methodologies show a distinct underestimation of those frequencies, with GAFF being the worst, followed by the three DFTB approaches, and COMPASS. The latter shows, however, a much more wide-spread accumulation of C-H peaks than the relatively narrow distributions of frequencies in all other methodologies.

A severe disadvantage of the comparison of the DOSs of different approaches is, however, that the DOS is not capable of telling which types of vibrational states can be found at a certain frequency but only if and how many states are present at a given frequency. This means that, hypothetically, the DOS could not resolve the error in an approximate methodology if an intermolecular mode happened to coincidentally have the same frequency as another intramolecular mode (in the worst case). Therefore, it is not enough to only discuss differences in the DOS, but one really has to make sure that one compares frequency differences corresponding to the equivalent atomic motion patterns. To account for the real nature of the modes, again the algorithm of Kuhn [109] has been employed based on a cost function dependent on the (complex) dot product of phonon eigenvectors as described in Sec. 3.1.5.

Fig. 4.19 shows the typical outcome of such an assignment of phonon modes for a given wave vector $\mathbf{q}$ (here they are shown for Γ). The leftmost column of Fig. 4.19 shows the penalty matrices introduced to overcome mode assignments with unrealistically high frequency differences. Some of the aspects discussed before can also be seen in these penalty matrices, which have large elements at all entries P_{ij} at which the frequency of the i^{th} mode in the DFT reference is far from the j^{th} frequency in an approximate method. Therefore, the penalty in the region of the C-H stretching modes (starting with mode number 93) is large for all methods except for COMPASS and MOF-FF.

Typically the most important factor in the mode assignment is the overlap between eigenvectors of the DFT reference with eigenvectors of an approximate methodology. In order to facilitate the discussion and improve the visibility of those matrices for the reader, the overlap matrices for MOF-FF and GAFF are shown again in Fig. 4.20 with increased size.

The overlap matrix for MOF-FF looks very encouraging with large values being found nearly exclusively on the main diagonal of the matrix. This observation is equivalent to saying that MOF-FF has the tendency that the i^{th} mode corresponds also to the i^{th} reference mode. In particular, the first ~ 70 phonon modes are in nearly the same order as the reference (with small deviations around mode 30). Also the DFTB-based approaches fare relatively well in this comparison (see Fig. 4.19) such that modes appear typically in the same order as in the reference and the similarity of the atomic motion with the reference is high.

Besides these rather promising results, the situation is much worse for GAFF and COMPASS. Looking at the overlap matrix for GAFF in more detail (see Fig. 4.20(b)), one notices that above band index ~20, the number of larger off-diagonal elements in the overlap matrices continuously increases and in some cases there are entire rows and

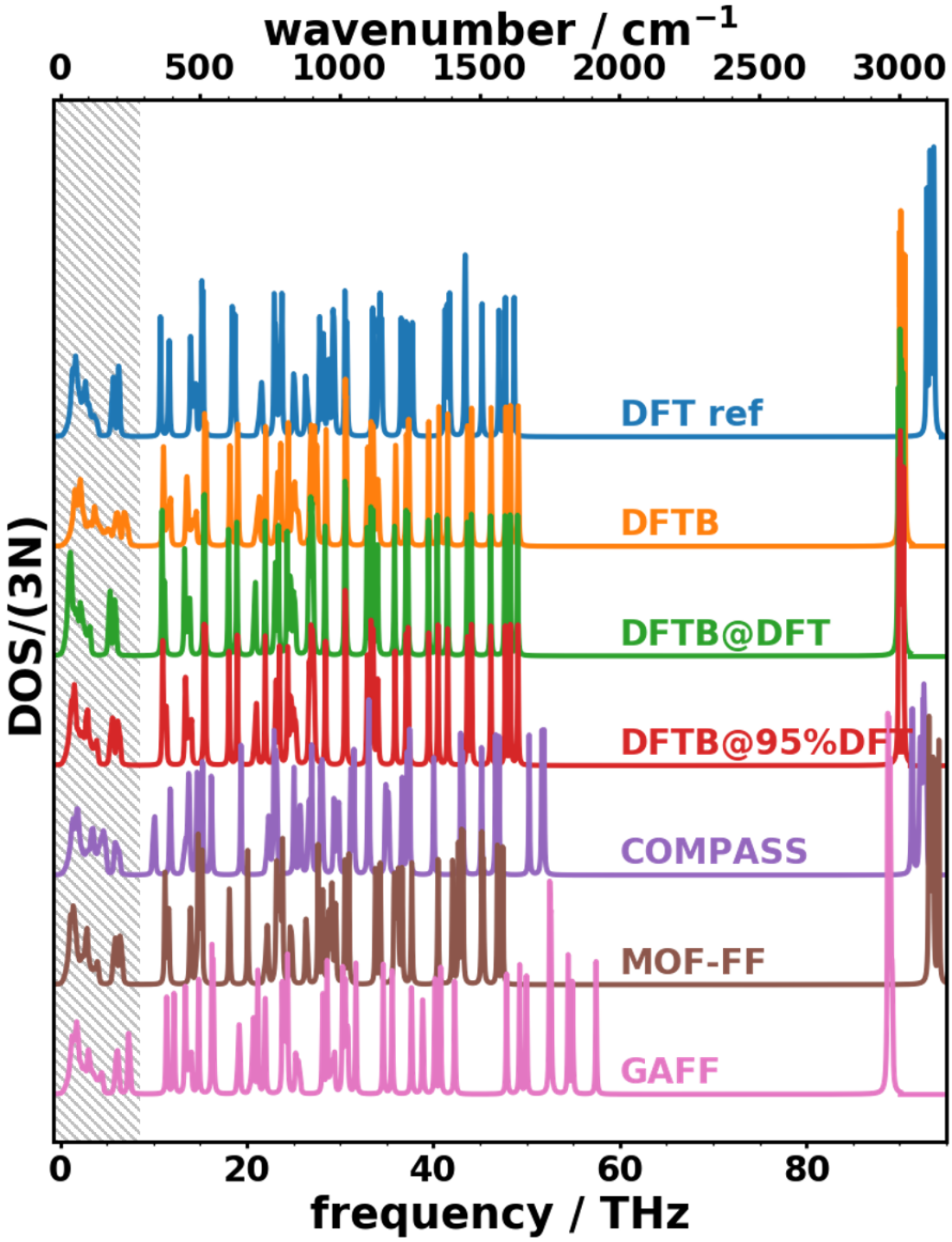

Fig. 4.18.: Phonon densities of states as a function of frequency of crystalline naphthalene for all tested approaches. The hatched area indicates the low-frequency regime discussed in Sec. 4.2. This figure has been taken from Ref. [1].

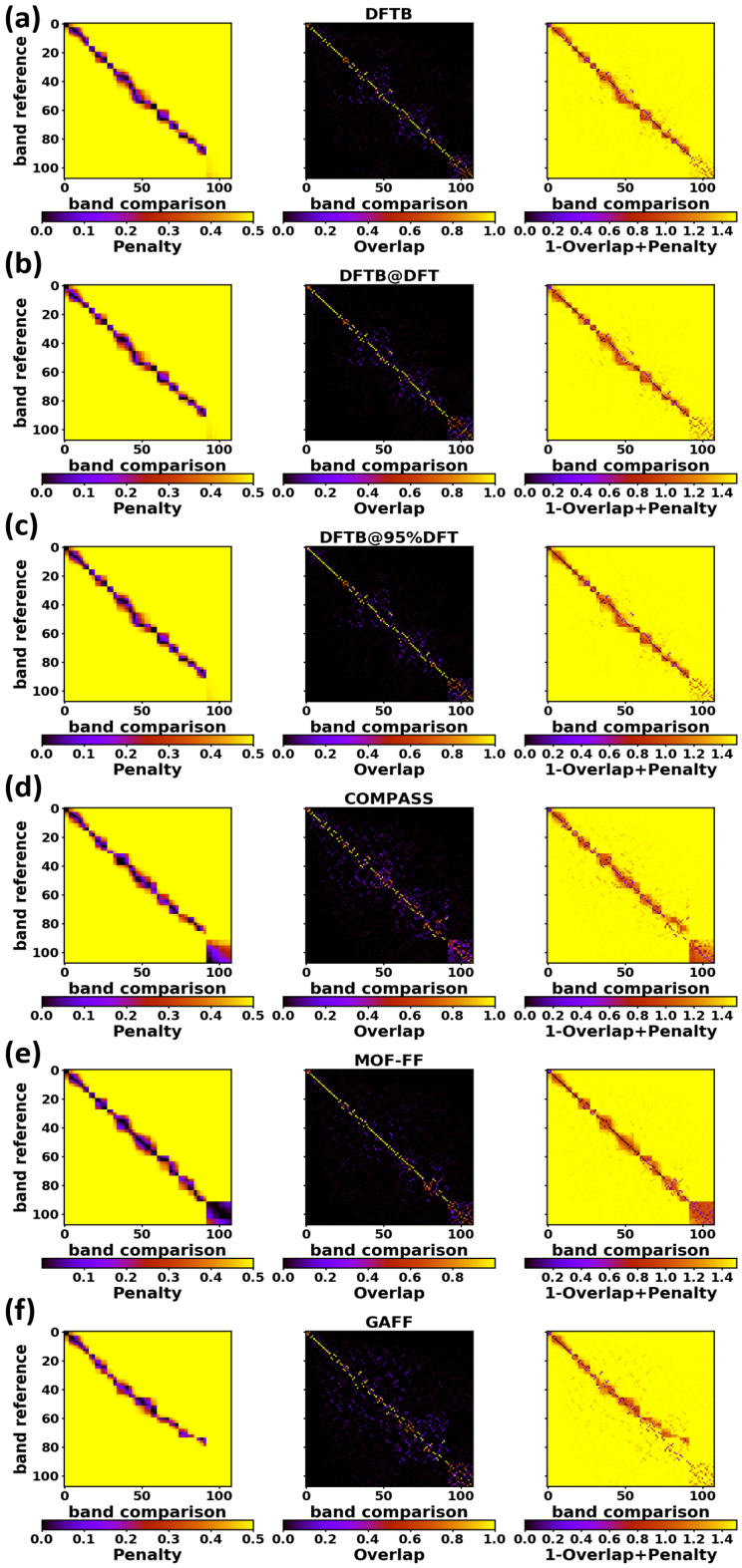

Fig. 4.19.: Penalty (left), overlap (centre), and cost matrix (right) of the (a) DFTB, (b) DFTB@DFT, (c) DFTB@95%DFT, (d) COMPASS, (e) MOF-FF, and (f) GAFF phonon modes at Γ compared to the DFT reference. The shown matrices are defined according to the equations in Sec. 3.1.5. This figure has been taken from the Supporting Information of Ref. [1].

columns, for which only several smaller overlaps can be calculated. This means that those methodologies partly produce phonon modes which correspond to motion that does not agree well with any of the vibrations in the reference. Finally, it should be remarked that the overlap matrices show notably large off-diagonal elements at wave vectors different from Γ. A detailed **q**-resolved analysis of this behaviour lies, however, beyond the scope of this thesis.

Once equivalent vibrations have been identified and the order of the modes has been adjusted accordingly, one can carry out quantitative comparisons of frequencies and frequency differences in terms of (cumulative) RMSD_f and AD_f in the same way as for the low-frequency regime. Fig 4.21 shows the frequency differences of assigned phonon modes in the entire first Brillouin zone and the cumulative RMSD_f as a function of the cutoff frequency. The AD_f and the RMSD_f values taking into account the entire spectrum are listed in Tab. 4.2.

The frequency differences displayed in Fig. 4.21 show that the discrepancies with respect to the DFT reference are much more severe than in the low-frequency region. In particular, COMPASS and GAFF show massive difficulties for phonon bands with frequencies above ~20 THz. There, frequency differences sometimes amount to 10 THz with varying sign. For both methodologies, this results in a steep increase in the cumulative RMSD_f. The situation even becomes much worse starting at ~40 THz. Although COMPASS has a relatively low overall AD_f, the cumulative RMSD_f is the second largest of all approaches (after GAFF). This means that the frequency differences are arbitrarily positive and negative and, on average, cancel each other to a large extent. The analysis of the displacement patterns of these modes with the largest deviations reveals that it is the C-C stretching and C-H in-plane bending motions which are most poorly described. These modes sometimes show frequency differences amounting to up to 15 THz. A possible reason to explain these discrepancies in spite of the rather complex nature of the force field including several cross-terms and anharmonic interactions, could be the fact that all chemical species in the unit cell are treated equally. That is, no distinction is made between atoms of the same species which should be chemically inequivalent due to their local environment. This assumption in the force field is very likely to be poorly justified as it does not reflect the real situation very well.

Also in this region (for GAFF between 35 and 50 THz), one can observe a tremendous overestimation of frequencies. On the one hand, this can be attributed to the fact that any cross-terms are omitted in this force field, which are needed to accurately describe the involved intramolecular motions for these modes. On the other hand, one can see that the harmonic force constants for the C-C interactions are much larger than in the DFT reference (see below).

In nearly the entire frequency range - except for the region between ~10 and 30 THz - MOF-FF shows the smallest RMSD_f of all approaches. This is not utterly surprising as the MOF-FF has been specifically parametrised based on the intramolecular geometry and the force constants of a naphthalene molecule, while all the other methods rather rely on publicly available parametrisation - either in terms of standard pseudopotentials, Slater-Koster parameters or ready-to-use force field parametrisations. Therefore, the harmonic C-C force constants are in excellent agreement with the DFT reference

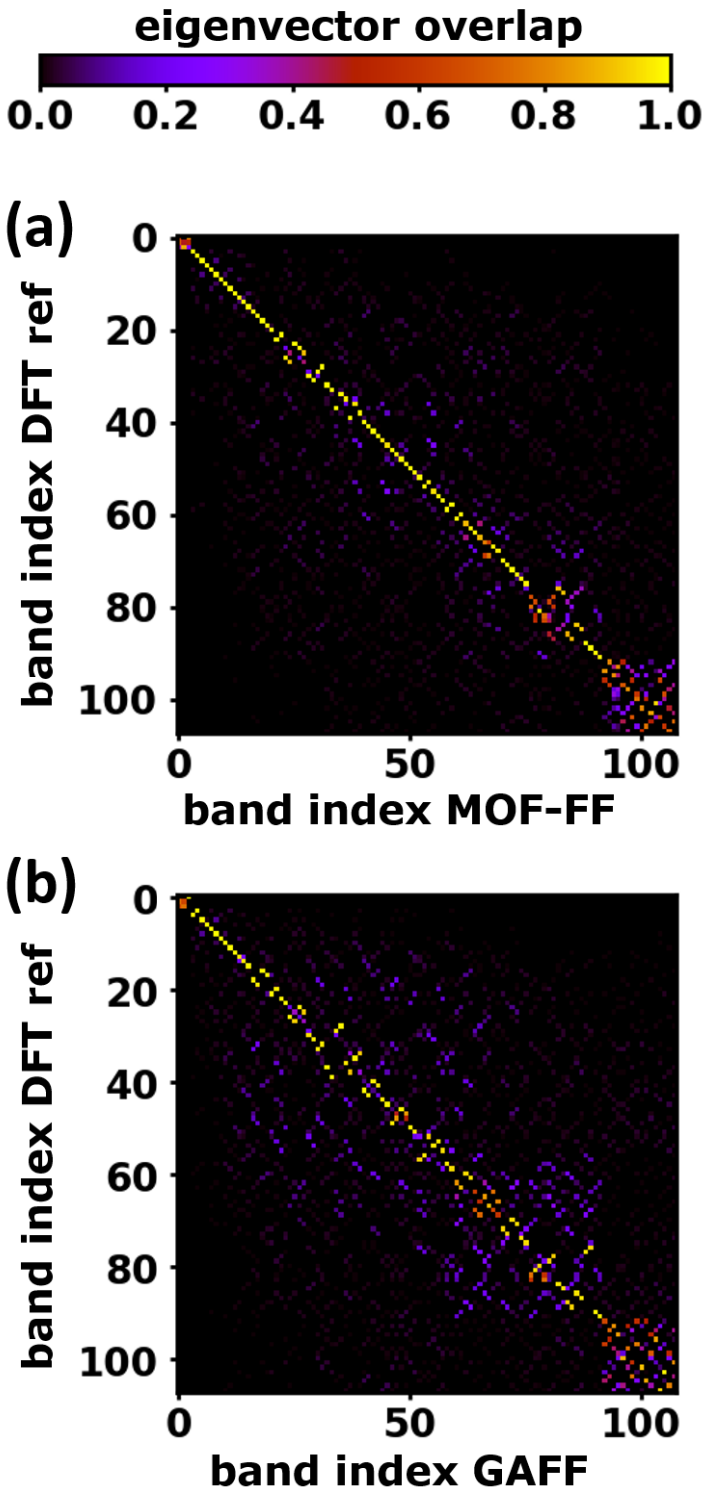

Fig. 4.20.: Overlap matrix of Γ-eigenvectors of the DFT reference with the eigenvectors obtained with (a) MOF-FF and (b) GAFF. The shown panels are enlarged views of panels (e) and (f) of Fig. 4.19 for enhanced visibility. The overlap matrix S_{ij} is defined as the complex dot product of the i^{th} eigenvector of the reference with the j^{th} eigenvector of the methodology to be compared (see Eq. (3.3)). This figure has been taken from Ref. [1].

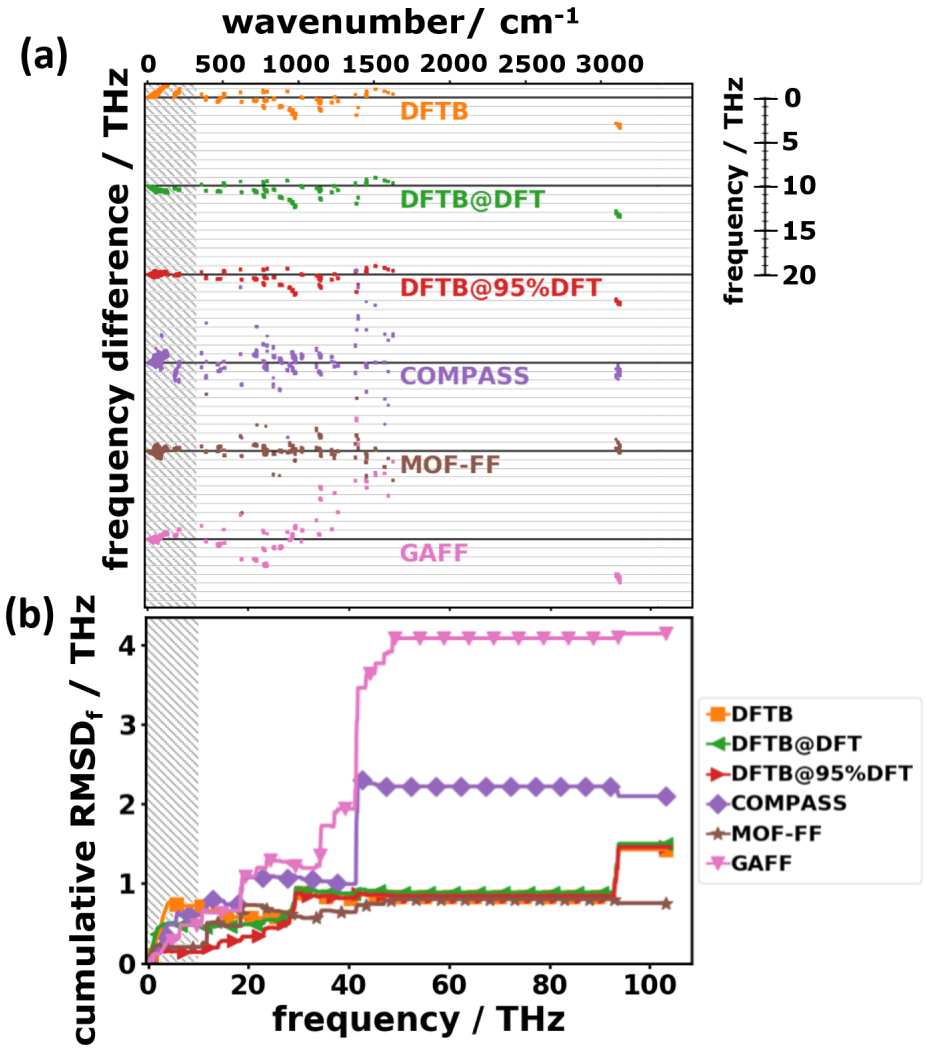

Fig. 4.21.: (a) Frequency differences of the tested approximate approaches with respect to the DFT reference (PBE/D3-BJ) as a function of the reference frequency for the entire spectral range of phonon frequencies in the system. The frequency differences of each tested methodology are plotted with respect to its own zero line (thick black horizontal lines). (b) Cumulative root-mean-square deviations of frequencies considering phonon modes up to a certain cutoff frequency as a function of that cutoff. The hatched area indicates the low-frequency regime discussed in Sec. 4.2. The symbols in (b) do not represent the actually calculated data points, which lie much more densely, but rather serve as guides to the eye. This figure has been taken from Ref. [1].

(see below). Similarly to the case of COMPASS, there is no systematic over- or underestimation of frequencies in certain spectral regions resulting in the smallest AD_f of all tested methodologies considering the entire frequency range.
Before a more detailed analysis of the harmonic force constants is presented, the performance of the DFTB-based approaches should be briefly commented on. Above the low-frequency region, all DFTB approaches slightly tend to under- rather than to overestimate the intramolecular frequencies. This notion is supported by the consistently negative values of the AD_f. For an almost comprehensive part of the frequency range, the cumulative $RMSD_f$ of the DFTB-based approaches is comparable to that of MOFFF: it is approximately constant from ~30 THz until the frequency of the C-H stretching vibrations. At this point the cumulative $RMSD_f$ values of the DFTB approaches experience a sharp increase due to the underestimation of those phonon frequencies by about -3 THz. The reason for this pronounced underestimation can be rationalised by the C-H harmonic force constants which are notably smaller in DFTB than in the DFT reference as will be discussed in the following excursus.

Some more details on the harmonic force constant:
The harmonic force constants (HFCs), which are the actually calculated quantities before their Fourier transform (=the dynamical matrix) yields the frequencies, typically can be analysed to understand the origin of the observed over- or underestimation of intramolecular modes. In simple cases, one can qualitatively correlate the discrepancies in phonon frequencies with notable differences in the HFCs.
The only complication with the analysis of the HFCs is, that these quantities are tensors of rank 2. In order to facilitate the following discussion, the arguments are based on the traces rather than on all nine elements of the tensors, since the trace of a tensor is invariant under arbitrary rotations. The choice of the trace as descriptor for the magnitude of the HFCs is insofar convenient as it allows to disregard orientational differences between the atoms in different approaches. It can be seen in Fig. 4.22 that the traces of the HFCs decay rapidly to zero within short distances of ~3 Å regardless of the type of the associated pair of atoms (carbon-carbon, carbon-hydrogen, or hydrogen-hydrogen). This observation implies that all relevant interactions are captured within the spatial extents of the considered supercells resulting in converged dynamical matrices. Moreover, the dependence of the HFCs on the distance does not seem to be very sensitive to the actual used method, as all approximate methodologies as well as DFT ref show a similar decaying behaviour of the HFCs with the interatomic distances. At this point it is useful to separate those values appearing at zero distance from all the others by introducing a different nomenclature. In the following, the HFCs at zero distance will be referred to as self-harmonic force constants (SHFCs) because these are the HFCs of an atom with itself. According to the acoustic sum rules (ASR, see Eq. (2.31)), the SHFC of an atoms is the negative sum of interactions of that atom with all the other atoms in the supercell. For that reason, the SHFCs are typically much larger than the HFCs and have different signs. The SHFCs are convenient measures to assess the contributions from atoms beyond the nearest covalently bonded neighbour: if there is only one dominant HFC between an atom and another one, then the SHFC will be equivalent to

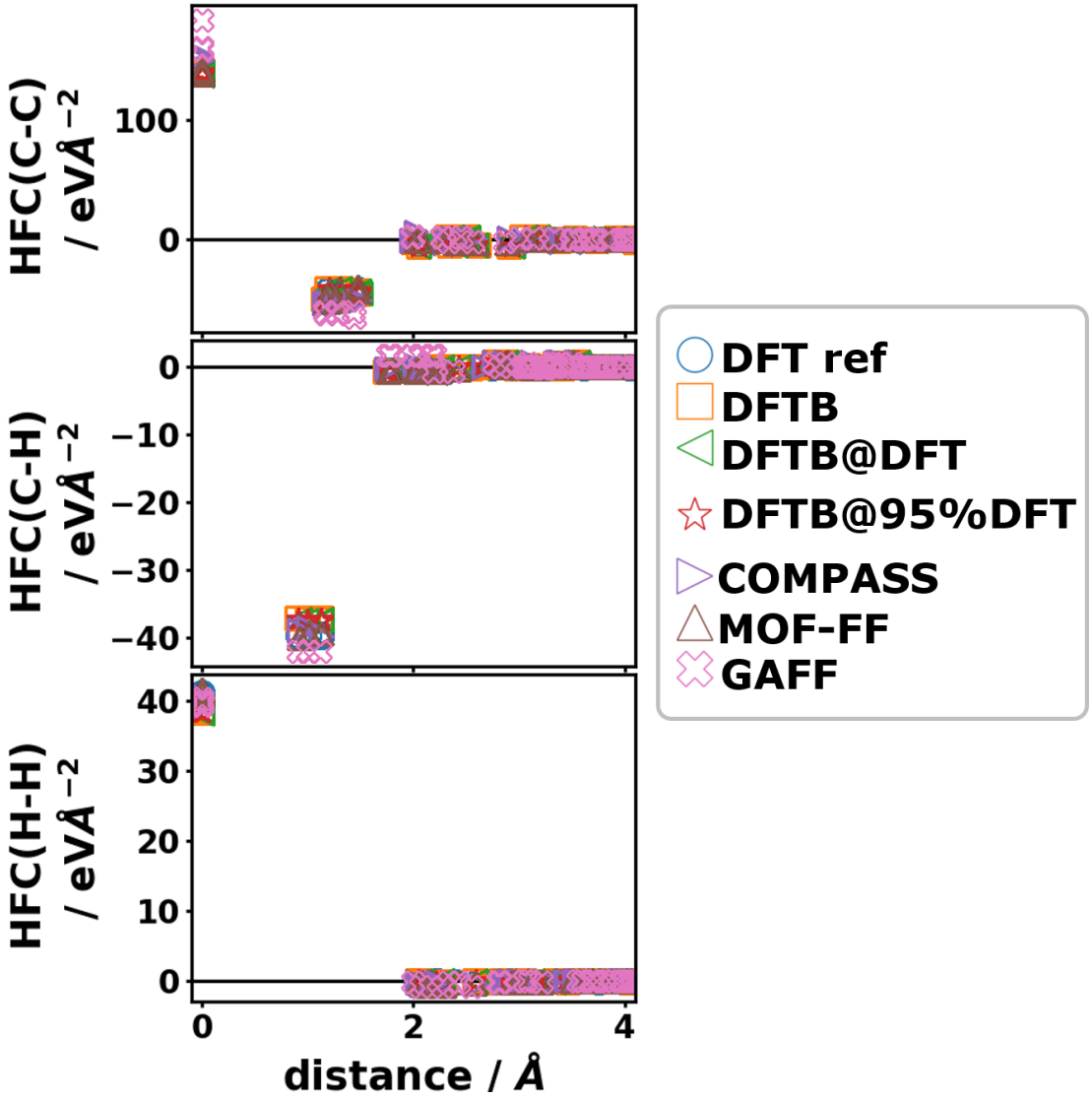

Fig. 4.22.: Traces of the harmonic force constant tensors (HFCs) of carbon-carbon, carbon-hydrogen, and hydrogen-hydrogen interactions as a function of the distance between the involved atoms considering periodic boundary conditions. The distance axis has been limited to the shown range for reasons of visibility. The maximum distance of probed HFCs ranges beyond 15 Å. This figure has been taken from the Supporting Information of Ref. [1].

the negative value of that dominant (and only relevant) HFC. If this is not the case, this means that there are significant long-range interactions present contributing to the SHFC. This circumstance will be exploited below.
Besides the SHFCs, the HFCs are apparently largest for atom pairs which are covalently bonded (C-C and C-H). The HFCs between atoms of different molecules or atoms in the same molecules which are far apart show significantly smaller magnitude. For example, the H-H HFCs can be found to be smaller by two orders of magnitude compared to the C-C or the C-H HFCs because they are not bonded covalently. This can be seen even better in Fig. 4.23: while the largest C-C (C-H) HFCs amount to ~-50 (40) eVÅ^2, the largest H-H HFCs only reach values of up to ~-0.2 eVÅ^2. At this point it is especially interesting to compare the (S)HFCs obtained with different methods.
Panels (a) and (b) of Fig. 4.23 show that all considered DFTB-based approaches as well as MOF-FF yield relatively similar values for the C-C HFCs and SHFCs, while one can observe distinct discrepancies in COMPASS and GAFF. Both obviously overestimate the magnitude of the nearest-neighbour C-C HFCs (GAFF much more severely as COMPASS), which contributes to the overestimation of the C-C SHFCs. In the case of COMPASS, the overestimation of C-C SHFCs can mostly be ascribed to the too large magnitudes of the C-C HFCs, while in GAFF also an overestimation of C-H HFCs has an contribution. These are much better described in COMPASS and even better in MOF-FF, which has been parametrised to molecular naphthalene data.
All the DFTB approaches, however, show notable underestimations of the C-H HFCs resulting in the too low frequencies of C-H stretching vibrations. In case of the DFTB-based approaches, the underestimation of these C-H HFCs (and the resulting discrepancies in the SHFCs) are the only obvious drawback in the description of intramolecular frequencies within this level of theory. Compared to the reference C-H HFCs, GAFF shows deviations of a similar magnitude as DFTB, but with a different sign. This would actually imply a spectral shift of C-H vibrations to higher frequencies. However, the situation for GAFF is slightly more involved. For all approaches except for GAFF, the H-H SHFCs (shown in Fig. 4.23(d)) approximately equal the sum of the nearest-neighbour C-H HFCs and H-H HFCs (Fig. 4.23(c) and (e), respectively). In other words, this means that in all cases except for GAFF, the hydrogens nearly exclusively show relevant interactions only with the carbon atoms, which which they are covalently bonded, and with the nearest hydrogen neighbours (through non-bonding interactions). This is not true for GAFF: although it overestimates both C-H and H-H HFCs, the H-H SHFCs are still underestimated, which strongly suggests interactions beyond the distance of covalently bonded atoms, as the SHFC must equal the (negative) sum of all HFCs.

Indeed, the HFCs of the next-nearest C-H interactions are found to be much larger than in all the other tested approximate methodologies. Only by adding them to the nearest-neighbour H-H HFCs and C-H HFCs, the underestimated H-H SHFCs can be explained. The interatomic distances of these next-nearest C-H neighbours is in the range of ~1.8 to ~2.3 Å. These overestimated force constants are increased by about a factor of -3.6 with respect to the reference. A detailed view of the distance-resolved HFCs showing these overestimated C-H HFCs can be found in Fig. 4.24.

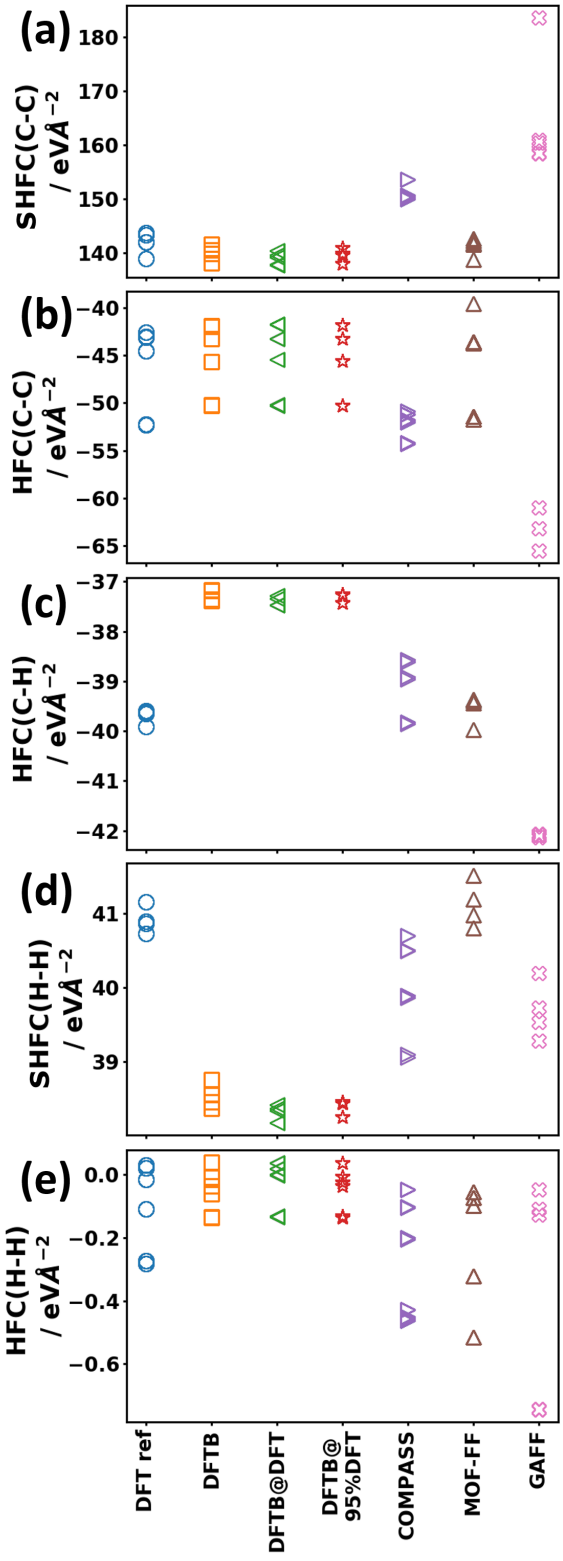

Fig. 4.23.: Traces of the harmonic force constants obtained from the different tested approaches: (a,d) Self-HFCs for carbon and hydrogen atoms, respectively. (b,c,e) HFCs for the nearest neighbour interactions sorted according to the involved atomic species (C-C, C-H, H-H). This figure has been taken from the Supporting Information of Ref. [1].

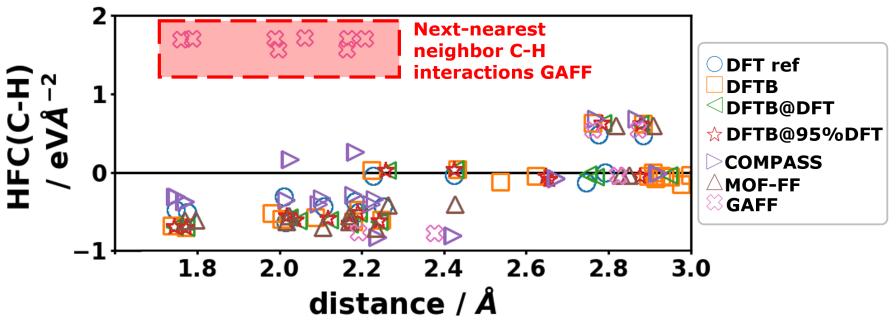

Fig. 4.24.: Enlarged view of a limited region of the middle panel of Fig. 4.22 showing the traces of the harmonic force constants of C-H interactions obtained from the different tested approaches as a function of the distance of the involved pair of atoms considering periodic boundary conditions. The distance axis is limited to values such that only interactions of C and H atoms are shown which are farther apart than the observed covalent bonding distances. The significantly overestimated C-H HFCs from GAFF are indicated with the red box. This figure has been taken from the Supporting Information of Ref. [1].

These complex circumstances of over-and underestimation in C-H HFCs in GAFF leads to the C-H bending vibrations showing massively increased frequencies, while the frequencies of the C-H stretching vibrations come out too low.

4.3.2. Assessment of the Suitability of Approximate Methods to Describe Physical Observables Based on the Entire Phonon Spectrum

Following the discussed tendencies of the various approximate methodologies to over- or underestimate phonon frequencies in certain spectral ranges, an analysis of the performance to accurately describe thermodynamic (phonon) properties can be carried out. First of all, the temperature dependence beyond the limited temperature range already discussed in Sec. 4.2.5 should be commented on. The heat capacity as well as the difference with respect to the DFT reference, ΔC_V, as a function of temperature are shown in Fig. 4.25. Note that at 300 K, the cutoff frequency $f_{1/2}$ amounts to ~18.6 THz, with the tail of the envelope function reaching beyond 40 THz. For that reason, the discrepancies discussed in Sec. 4.3.1 increasingly affect the heat capacities at elevated temperatures. The mentioned overestimation of frequencies between 30 and 50 THz in GAFF result in a pronounced underestimation of the heat capacity starting at 200 K because the corresponding phonon bands are missing in the integration, decreasing the value of the integral (see Eq. (2.84)) as a result. This can most obviously be seen in the difference plot in Fig. 4.25(b).
COMPASS yields a comparably small ΔC_V owing to the cancellation of errors which also results in the small overall AD_f. Also MOF-FF exhibits an excellence performance when it comes to reproducing the DFT reference values for the heat capacity. In contrast to COMPASS, both the RMSD_f and the AD_f adopt relatively small values, implying

that in MOF-FF, the good agreement is really an achievement of the well-parametrised force field rather than a result of an accidental cancellation of errors.

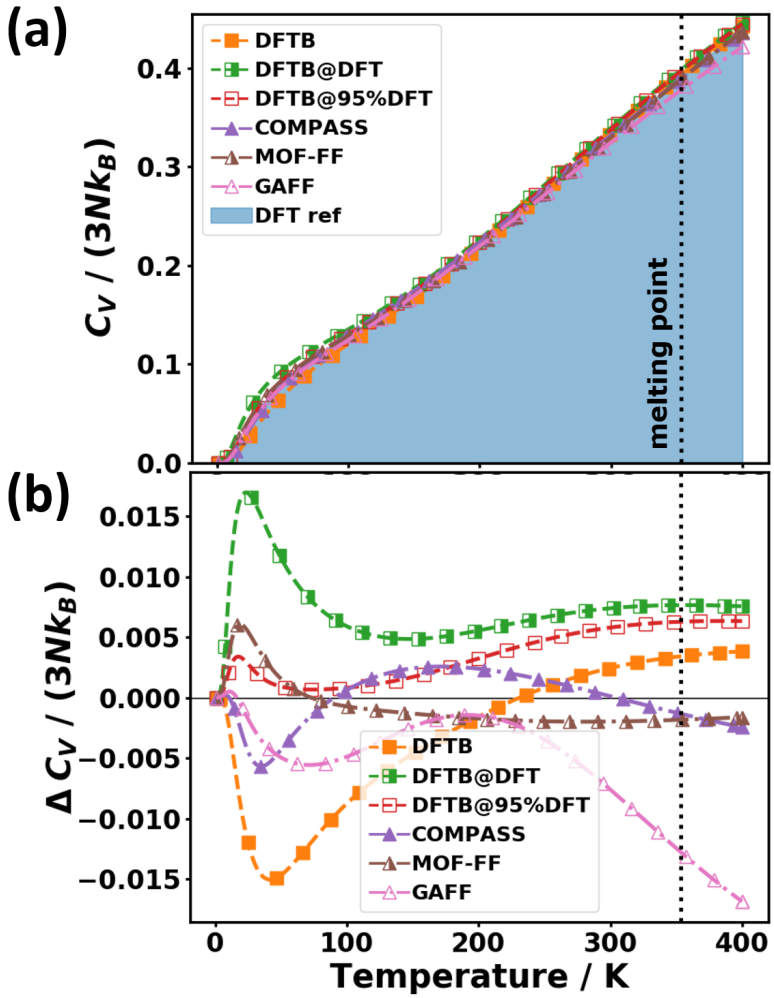

Fig. 4.25.: (a) Phonon contribution to the heat capacity C_V per unit-cell normalised by the Boltzmann constant k_B and the number of phonon modes ($3N$) as a function of temperature for all the tested methods over an extended temperature range. The blue shaded area corresponds to the DFT reference. (b) Difference in C_V relative to the heat capacity obtained with the DFT reference data as a function of temperature. The vertical dotted line indicates the melting point of the naphthalene crystal (353 K at ambient pressure [137]). The symbols in both panels do not represent the actually calculated data points, which lie much more densely, but rather serve as guides to the eye. This figure has been taken from Ref. [1].

For the three approaches based on DFTB, the typical observation that phonon frequencies above ~10 THz are slightly underestimated leads to positive ΔC_V values at

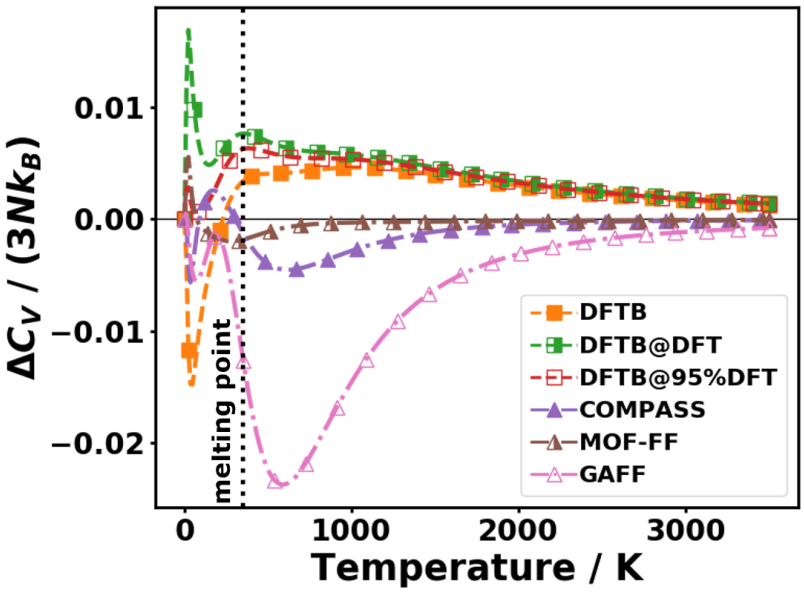

Fig. 4.26.: Difference in C_V with respect to the DFT reference as a function of temperature shown for an unrealistically high temperature range. The melting point of the naphthalene crystal (353 K at ambient pressure [137]) is indicated by the vertical dotted line. The symbols in both panels do not represent the actually calculated data points, which lie much more densely, but rather serve as guides to the eye. This figure has been taken from the Supporting Information of Ref. [1].

higher temperatures. The absolute values of the deviations from the reference strongly depends, however, on the performance in the low-frequency region - i.e. whether the low-frequency bands are typically underestimated (DFTB@DFT) or overestimated (DFTB). In the latter case, the two types of errors partially cancel in the summation (integration) for calculating the heat capacity, while they add up and amplify the total error for DFTB@DFT. This is also evident by the fact that for DFTB, ΔC_V changes sign at about 225 K suggesting that at this temperature the overestimation of the low-frequency bands is cancelled by the underestimation of high-frequency modes entering the sum (integral) for C_V. However, DFTB@95%DFT shows a relatively small difference in the heat capacity with respect ot the DFT reference at low temperatures owing to the good agreement of the low-frequency phonon band structure. At higher temperatures - starting at ~150 K, the error increases due to the underestimated frequencies in the same spectral region as the other two DFTB approaches. Based on the impression conveyed by Fig. 4.25(b), it can also be hypothesised that the ΔC_V values of all DFTB approaches converge to the same value at higher temperatures.

This can be seen when plotting the (hypothetical) heat capacity differences for very high temperatures, far beyond the melting point of the system. Although not being physically meaningful, it is still instructive to trace the errors to higher temperatures to

examine the limiting behaviour of the error. Fig. 4.26 shows the difference in the heat capacities with respect to the DFT reference (normalised by the number of phonon modes and the Boltzmann constant). This plot reveals that, indeed, the DFTB approaches converge to the same ΔC_V at about 1000 K. GAFF shows the largest deviations of all approaches climaxing at about 600 K, before the error starts to decrease again for higher temperatures. The fact that the error vanishes for $T \to \infty$ is a consequence of the Dulong-Petit limit: the heat capacity (per unit-cell) converges towards the value $3Nk_B$ at high temperatures such that the errors must converge to zero. The fastest convergence is obviously achieved by MOF-FF and COMPASS. While the former shows excellent agreement for the high-frequency modes, the latter exhibits a more or less arbitrary under- and overestimation of frequencies resulting in a cancellation of errors upon summation.
In spite of the above-discussed deviations from the reference heat capacity, it must be stressed that the heat capacity is a relatively robust quantity overall, since the relative error at 300 K in none of the cases exceeds 0.5 %.

Apart from the heat capacity, another crucial thermodynamic quantity is the Helmholtz free energy. This quantity is the thermodynamic potential of the canonical ensemble (NVT ensemble), from which all thermodynamic properties can be calculated by computing its partial derivatives. For this reason, the Helmholtz free energy is relevant for considerations of thermodynamic stability (in the canonical ensemble - and in the grand canonical ensemble if the chemical potential vanishes like for phonons). For large electronic band gaps between the valence and the conduction band, the temperature dependence of the electronic free energy can be neglected and the electronic contribution would only cause an offset of the total free energy. Therefore, it suffices to take the phonon contribution into account. Moreover, it is typically hard to quantitatively compare total energies from different levels of theory (even from the same level of theory using different pseudopotentials or different codes which define the energy zero point in a different way).
The analytical expression for the vibrational free energy, F (see Eq. (2.62)), can be written as a temperature-dependent term and a term in which only the phonon frequencies enter. The latter is the zero-point energy (ZPE) of the harmonic oscillators, which is independent from the thermal phonon occupation and, thus, also relevant at 0 K, while the temperature-dependent part vanishes for $T \to 0$. This suggests that for the ZPE, all frequency ranges are equally important and deviations of phonon frequencies directly lead to differences in the ZPE. This is especially important at lower temperatures at which the ZPE dominates over the temperature-dependent term of F. Only upon increasing the system's temperature, the temperature-dependent contribution to F starts to dominate, which considers the thermal occupation of phonon modes - i.e. the temperature dependence is prevailingly determined by the low-frequency phonons.
Fig. 4.27(a) shows the temperature dependence of F for the tested approaches, while the differences in free enrgy, ΔF compared to the DFT reference are shown in panel (b). At and close to 0 K, it is apparent that MOF-FF and COMPASS show the closest agreement with DFT ref. All three DFTB-based approaches exhibit too small ZPE, while

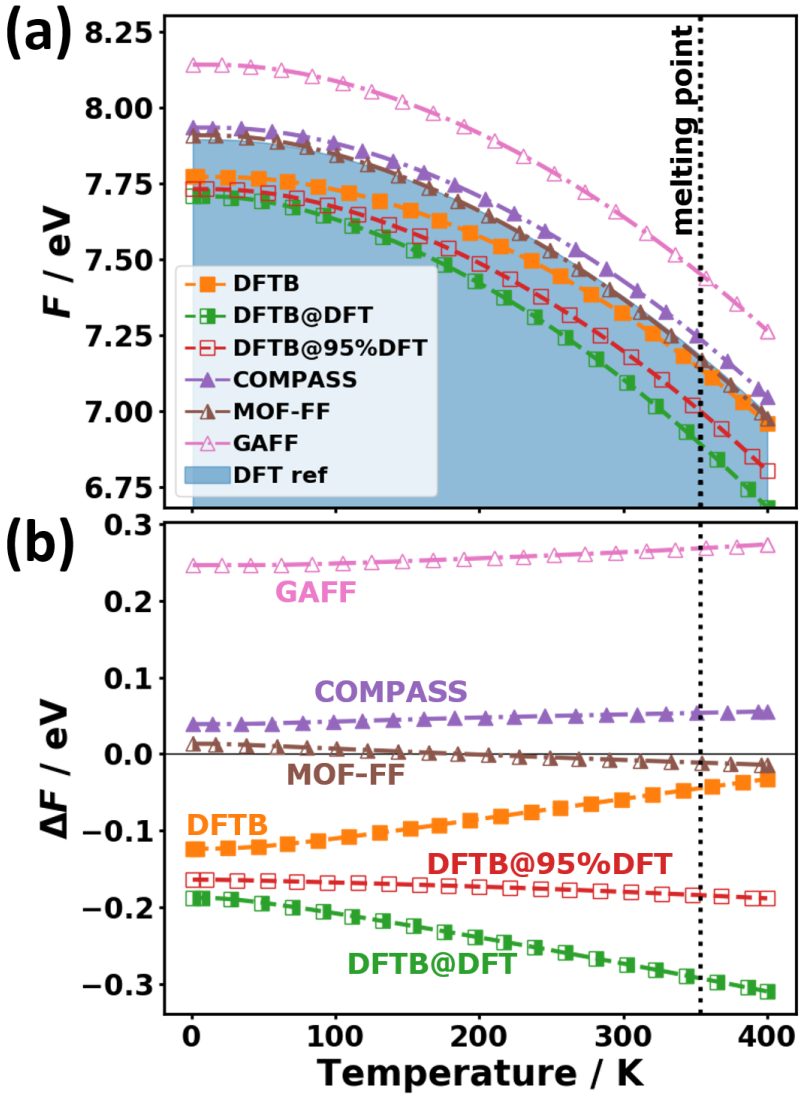

Fig. 4.27.: (a) Phonon contribution to the free energy, F and (b) differences in F with respect to the reference calculation as a function of temperature. The vertical dotted line indicates the melting point of the naphthalene crystal (353 K at ambient pressure [137]). The symbols in both panels do not represent the actually calculated data points, which lie much more densely, but rather serve as guides to the eye. This figure has been taken from Ref. [1].

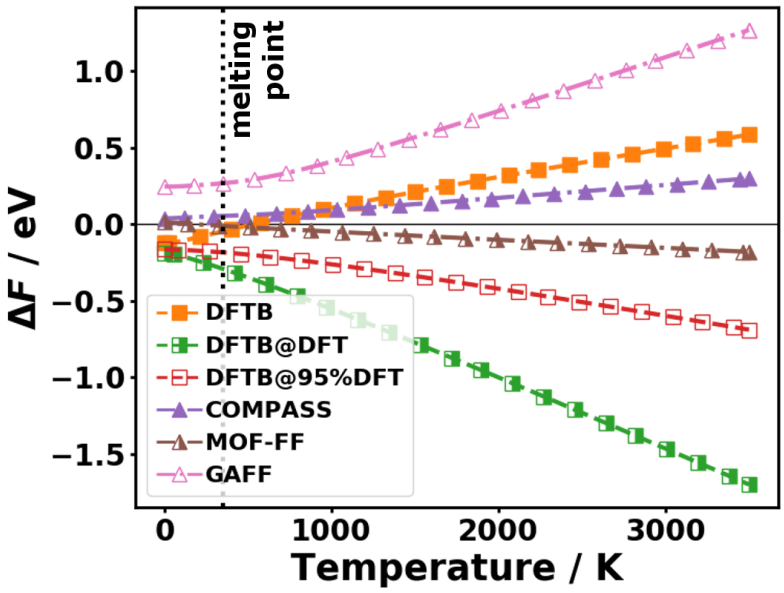

Fig. 4.28.: Differences in the vibrational free energy with respect to the reference calculation as a function of temperature shown for an unrealistically high temperature range. The melting point of the naphthalene crystal (353 K at ambient pressure [137]) is indicated by the vertical dotted line. The symbols in both panels do not represent the actually calculated data points, which are much more densely, but rather serve as guides to the eye. This figure has been taken from the Supporting Information of Ref. [1].

for GAFF, it is too large. These observations are perfectly in line with the AD_f values considering the entire frequency range (see Tab. 4.2), which is not surprising as the ZPE can be thought of as being proportional to the average frequency $\bar{\omega}$ in the system:

$$\mathrm{ZPE} = \frac{1}{N_q} \sum_{\lambda=(n,\mathbf{q})} \frac{\hbar\omega_\lambda}{2} = \frac{3N\hbar}{2}\bar{\omega} \qquad \text{with } \bar{\omega} = \frac{1}{3NN_q} \sum_{\lambda=(n,\mathbf{q})} \omega_\lambda \tag{4.7}$$

Consequently, the difference in ZPEs are proportional to the AD_f values. Therefore, COMPASS again profits from the cancellation of errors resulting in an excellent ZPE - only slightly worse than MOF-FF. Conversely, the severe underestimation of the (many) C-H vibrations to quite a considerable extent by DFTB results in the decreased ZPE, while in GAFF the many overestimated C-C stretching and C-H in-plane bending vibrations significantly increase the ZPE (and the AD_f). The absolute errors in the ZPE are notable amounting to up to 0.25 eV, which can already exceed the energetic differences typically occurring for different polymorphs [18].

Regarding the temperature-dependence of the free energies obtained with the approximate methods, one can see in Fig. 4.27 that the deviations from the DFT reference only relatively weakly depend on the temperature in case of the three force fields and DFTB@95%DFT. Since the temperature-dependence is mostly determined by the low-

frequency phonons (at low temperatures), this is a result of the relatively good agreement in the low-frequency region. Therefore, the ΔF values nearly stay at the offset determined by the difference in the ZPE.
For DFTB and DFTB@DFT, the situation is quite a different one. One can observe a pronounced decrease in the absolute magnitude of the deviation ΔF in case of DFTB and an increase in case of DFTB@DFT. This behaviour can be attributed to the fact that in both cases, the underestimation of the ZPE has its origin in the large number of underestimated high-frequency intramolecular modes. While this effect can be partly compensated at finite temperatures by the overestimated low-frequency bands in DFTB, the two effects add up in DFTB@DFT.
Finally, the high-temperature behaviour of ΔF shall be briefly commented on. The difference in free energy relative to the DFT reference is displayed in Fig. 4.28. In contrast to ΔC_V, the difference in F does not converge to zero nor to any other value because the free energy itself does not converge for $T \to \infty$. Over the huge shown temperature range of up to 3500 K, MOF-FF and COMPASS only exhibit differences in the free energy of ± 0.3 eV, which suggests that these two approaches are capable of quite reliably describing the free energy over a wide temperature range. The tendency of ΔF of a given methodology to increase or to decrease with temperature qualitatively agrees with the sign of the low-frequency AD_f ($\mathrm{signAD}_f = \mathrm{sign}\frac{d(\Delta F)}{dT}$).

4.4. Summary and Conclusions of the Methodological Benchmark

In order to briefly summarise the comprehensive performance tests and to see weaknesses and strengths at first glance, Fig. 4.29 shows a relative comparison of the tested approaches in various categories comprising the main quantities of interest: frequencies, group velocities, mean-squared thermal displacements, heat capacities and free energies. For mode-resolved quantities such as frequencies and group velocities as well as for atom-resolved ones such as the MSTDs, it is useful to resort to statistical analysis and report a RMSD value. For frequencies, however, the average deviation, AD_f, is taken into account as well, as this error indicator is able to predict cancellations of errors in thermodynamic properties. Additionally, the AD_f is capable of quantitatively assessing the difference in ZPE (AD_f of the entire spectral range) and qualitatively predicting the temperature behaviour of the difference in free energy (AD_f of the low-frequency regime).
The reference values for all the tested DFTB- and FF-based approaches is the DFT reference methodology relying on the PBE functional and the D3-BJ van der Waals correction. This level of theory has been shown to outperform different methodologies (PBE/D2, PBE/TS) when it comes to reproducing experimental phonon band structures of (deuterated) naphthalene. Moreover the PBE/D3-BJ approach even yields a better agreement with measured (powder) Raman spectra than using the B3LYP functional (and the same van der Waals correction).

Overall, the best performance is exhibited by the second-generation force field MOF-

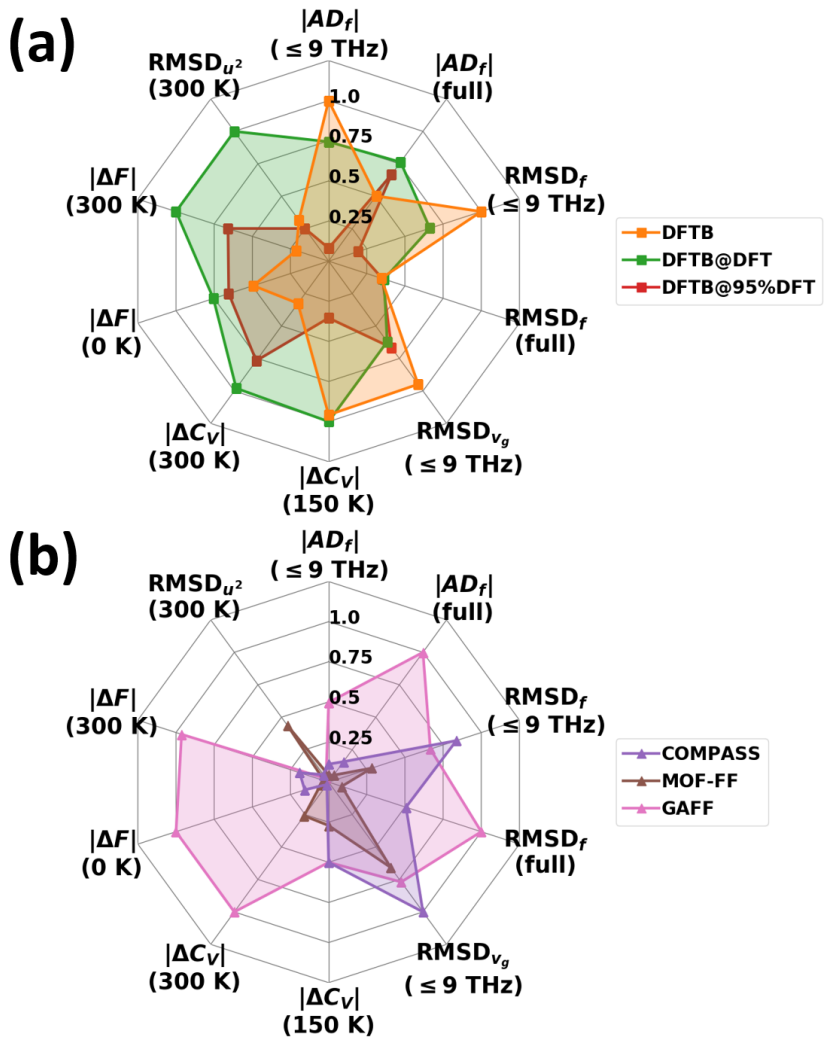

Fig. 4.29.: Radar charts showing the summarised relative performances of (a) DFTB- and (b) FF-based methodologies compared to the DFT reference results. The axes for each category are normalised in such a way that 1 corresponds to the maximum observed error indicator amongst all tested approaches. The quantities considered in this comparison comprise the average deviations in the calculated frequencies with respect to the DFT (PBE/D3-BJ) reference, AD_f, and the root-mean-square deviations of frequencies, $RMSD_f$, both separately calculated for the low-frequency region (≤ 9 THz) and the entire spectral range (full). Moreover, the plots include the RMSD value of vector norms of phonon group velocities in the low-frequency regime ($RMSD_{v_g}$) and the absolute deviations in thermodynamic properties (phonon contributions to the free energy F and the heat capacity C_V) at various temperatures. Furthermore, the RMSD values of the mean-squared thermal displacements ($RMSD_{u^2}$) are displayed, which are computed as the mean quadratic difference of thermal displacements with respect to the reference considering all atoms in the unit-cell. This figure has been taken from Ref. [1].

FF, which was specifically parametrised based on molecular naphthalene *ab initio* data. The MOF-FF is only outperformed in the category of the mean-squared thermal displacements (MSTDs) by almost every other approach except for the DFTB@DFT method. This finding can be ascribed to the fact that (especially the force fields GAFF and COMPASS) show a slightly better description of the acoustic phonon bands compared to MOF-FF. A possible strategy to improve the performance of the MOF-FF even more is, thus, to modify the description of the van der Waals interaction in that force field.
Besides the accurate description of the acoustic bands, the COMPASS force field produces thermodynamic properties with a high degree of agreement with the DFT reference (heat capacities and free energies), despite the fact that the $RMSD_f$ is relatively large. Therefore, one can conclude that the good performance of COMPASS in describing properties which involve a summation over frequencies has its origin in a fortuitous cancellation of errors rather than in an accurately parametrised description of inter- and intramolecular interactions. The (arbitrary) under- and overestimations of frequencies often compensate each other resulting in a low difference in the zero-point energy (ZPE) and the heat capacity, for instance.
Conversely, for GAFF one can identify a typical tendency to overestimate frequencies - especially in the frequency range from ~30 to ~50 K. As a result, the heat capacity is underestimated because higher temperatures are required to achieve occupation of the higher-lying phonon bands. In line with this overestimation of frequencies, the free energy is overestimated in the entire temperature range starting from 0 K with the ZPE, which is too high by ~0.25 eV (per unit-cell) with the error increasing with temperature.
DFTB, in spite of the considerably increased computational cost compared to the classical force fields, typically does not achieve an increase in accuracy without special precautions: the best agreement in terms of the $RMSD_f$ value for low frequencies of all tested approaches is obtained by the DFTB@95%DFT approach. Here, the strategy is to rely on the DFT-optimised lattice parameters rather than on a pure DFTB-based optimisation and, additionally, to (isotropically) scale the unit-cell volume down to a value slightly below 100 % of the DFT unit-cell volume. Optimal scaling factors, which reduce the low-frequency $RMSD_f$ to a minimum[39], have been shown to be rather similar for naphthalene, anthracene, and fluorene. This approach is, however, far from generally applicable before much more comprehensive testing has been carried out. At higher frequencies, the unit-cell parameters become less relevant and all DFTB approaches yield essentially identical high-frequency intramolecular frequencies. However, compared to the DFT reference band structure, these are typically slightly underestimated - except for the very accurate C-C stretching vibration - which results in notably underestimated zero-point energies. Regarding the temperature dependence of the error in the free energy, it was shown that it is strongly dependent on the low-frequency AD_f: for DFTB, which typically overestimates the low-frequency intermolecular modes (due to closer packing because of the reduced unit-cell volume), one can observe a partial cancellation of errors as the positive slope of the error in the free energy as a function of temperature compensates the negative offset due to the underestimated ZPE at some

[39]Regardless of whether frequencies in the entire first Brillouin zone or only Γ-frequencies are considered.

point.
Since the radar charts in Fig. 4.29 only show a relative comparison between the methodologies it is worthwhile to individually comment on the general suitability of the approximate methodologies to describe certain properties in absolute values. Furthermore, it should be briefly summarised which of the quantities are more robust and less prone to possible inaccurate descriptions of phonon band structures than others. The heat capacities, for instance, are described relatively accurately in all approaches. Even in the worst case (GAFF), the error never exceeds 0.5 % of the reference value at room temperature [1].
Conversely, the free energy is a more sensitive quantity, for which the errors are generally larger reaching up to ~3 % for several of the tested approaches. The discrepancies with respect to the reference can amount to ~250 meV per unit cell, which is larger than typically reported energy differences between different organic polymorphs [17, 18, 19, 138]. The reason for this enhanced susceptibility to frequency errors is the fact that the vibrational free energy can be decomposed into the temperature-independent ZPE and a temperature-dependent contribution. While the former, already at 0 K, takes into account all frequencies in the crystal and, thus, sets the energy scale, the latter is mostly determined by the low-frequency modes. In order to achieve a good performance of a methodology for this quantity, a constantly high accuracy of phonon frequencies is required[40]. The MOF-FF is able to achieve that goal so that, as a consequence of the accurately described phonon frequencies, the vibrational free energy only varies within ±0.01 eV compared to the DFT reverence over a wide range of temperatures [1].
The quantities most sensitive to an accurate description of the (acoustic) phonon bands are the mean-squared thermal displacements (MSTDs). The most severe overestimation (factor of 2) is exerted by the DFTB@DFT approach, while, surprisingly, COMPASS and GAFF yield the most satisfying agreement with the DFT reference. This extreme level of sensitiveness of the MSTDs has its origin in the fact that they are prevailingly affected by the acoustic phonon bands. These frequencies are typically so low (in the range of 1 THz) that already deviations which would be considered small in other spectral regions have a huge relative impact. This effect distorts the description of the thermal motion of the atoms. GAFF and COMPASS fare especially well when it comes to the description of the acoustic bands so that their MSTDs are in close agreement with the reference [1].

The results presented in this chapter suggest that there are indeed promising low-cost alternatives to state-of-the-art DFT available for calculating phonon properties in organic semiconductors employing approximate methods. However, the above discussion also implies that no "off-the-shelf" approximate method is likely to compete with well-established *ab initio* approaches in terms of accuracy to a fully satisfying extent [1]. It is believed that system-specifically parametrised, non-transferable force fields such as

[40] Or an symmetrically distributed scattering of frequencies around the *real* frequencies resulting in a cancellation of errors when the summation over frequencies is performed, as it is the case for COMPASS.

the MOF-FF are most likely to have the potential to achieve that goal (one day). In spite of the supposedly high potential, there is still room for improvement especially regarding the implemented description of the van der Waals interactions. The presented results suggest that a large improvement of the low-frequency bands and the properties sensitive to those modes (especially the group velocities) can be achieved by a more accurate energy term for those non-bonding interactions. Regarding the DFTB-based approaches tested to achieve the best phonon properties possible, it can be concluded that the Slater-Koster parameters used in this work, which are supposedly the most frequently applied and the most advanced publicly available ones, are probably not optimal for the usage in molecular crystals. It might be advisable to consider a reparametrisation to improve the results and increase the suitability of this approach, which should be technically more straightforward (at least if only the repulsive Energy is refitted) than FFs because different interatomic interactions should be resulting from quantum mechanics "automatically" without the need to parametrise every type of interaction separately with predefined terms. Very lately, Stöhr, Sandonas and Tkatchenko have presented a new way of improving many (anharmonic) potentials in a number of molecules by replacing the conventional pairwise repulsive energy by a local many-body interaction repulsive energy via machine learning approaches [80]. It remains to be seen how far and if approximate methods will advance to make reliable phonon calculations more accessible.

5. Phononic Properties in Various Organic Semiconductors

Since the DFTB-based approaches were found inadequate for reliable and accurate calculations of phonon-related properties (based on the used 3ob-3-1 Slater-Koster files [94]) and the intransferable nature of MOF-FF would have required a lot of additional work parametrising the force field, the method of choice to study structure-to-property relations is the PBE/D3-BJ approach. Based on the extraordinarily good agreement with experimental evidence for naphthalene presented in Sec. 4, this level of theory is chosen to be applied to other organic semiconductors.
In order to try to draw reasonable conclusions, the molecules shown in Fig. 5.1 were systematically selected to be studied. In particular, simple structure-to-property relations were supposed to be established as a function of the molecule length in oligoacenes (Fig. 5.1(a-e)) and oligophenylenes (Fig. 5.1(a,i-k)). Furthermore, one is interested in how the different spatial arrangement of the four phenyl rings in pyrene compared to tetracene (Fig. 5.1(d) and (f), respectively) or the relatively bulky functionalisation of tetracene by four additional phenyl rings (resulting in rubrene; Fig. 5.1(l)) affect the phonon properties. Fluorene (Fig. 5.1(g)) has been chosen to see what happens if the two six-membered phenyl rings cannot undergo torsional oscillations so easy any more as in the biphenyl molecule where the rings are only connected by a single bond. Finally, quinacridone (Fig. 5.1(h)) can be seen as a functionalised and substituted version of pentacene such that the impact of this chemical variation on the phonon properties can be investigated. Moreover, in this system one is supposed to observe other intermolecular bonding motifs than in the other crystals (hydrogen bridges), which are likely to notably affect the phonon band structures.

Unfortunately, the situation in the crystalline systems is much more involved than the simple structural formulae in Fig. 5.1 might convey. Very often, several packing arrangements or small geometric differences must be considered for molecular crystals of one given molecule. The different crystal structures for the studied molecular crystals are shown in Tab. 3.1 together with the abbreviations used in the following, the chemical formulae of the molecules, the molecular masses (M), the number of molecules per unit-cell (Z), and the number of atoms-per unit-cell (N)[41]. Even for benzene, the simplest of the studied organic crystals, there are two different phases: an orthorhombic and a monoclinic phase with four and two molecules per unit cell, respectively. According to simulations of the phase diagram of crystalline benzene with quasi-harmonic lattice dynamics [139, 140] (the results in both references being in excellent agreement with experimental data), the orthorhombic phase should be the dominant, thermodynamically stable phase at ambient pressure. The other, monoclinic phase, however, allows to draw more reasonable connections to naphthalene and anthracene, both of which crystallise in monoclinic Bravais lattices. Even this small number of symmetries which are still present in those systems with monoclinic space groups are lost in case of tetracene and

[41] N could alternatively be easily calculated from the chemical formulae and Z. The reason why it is listed is rather a matter of convenience.

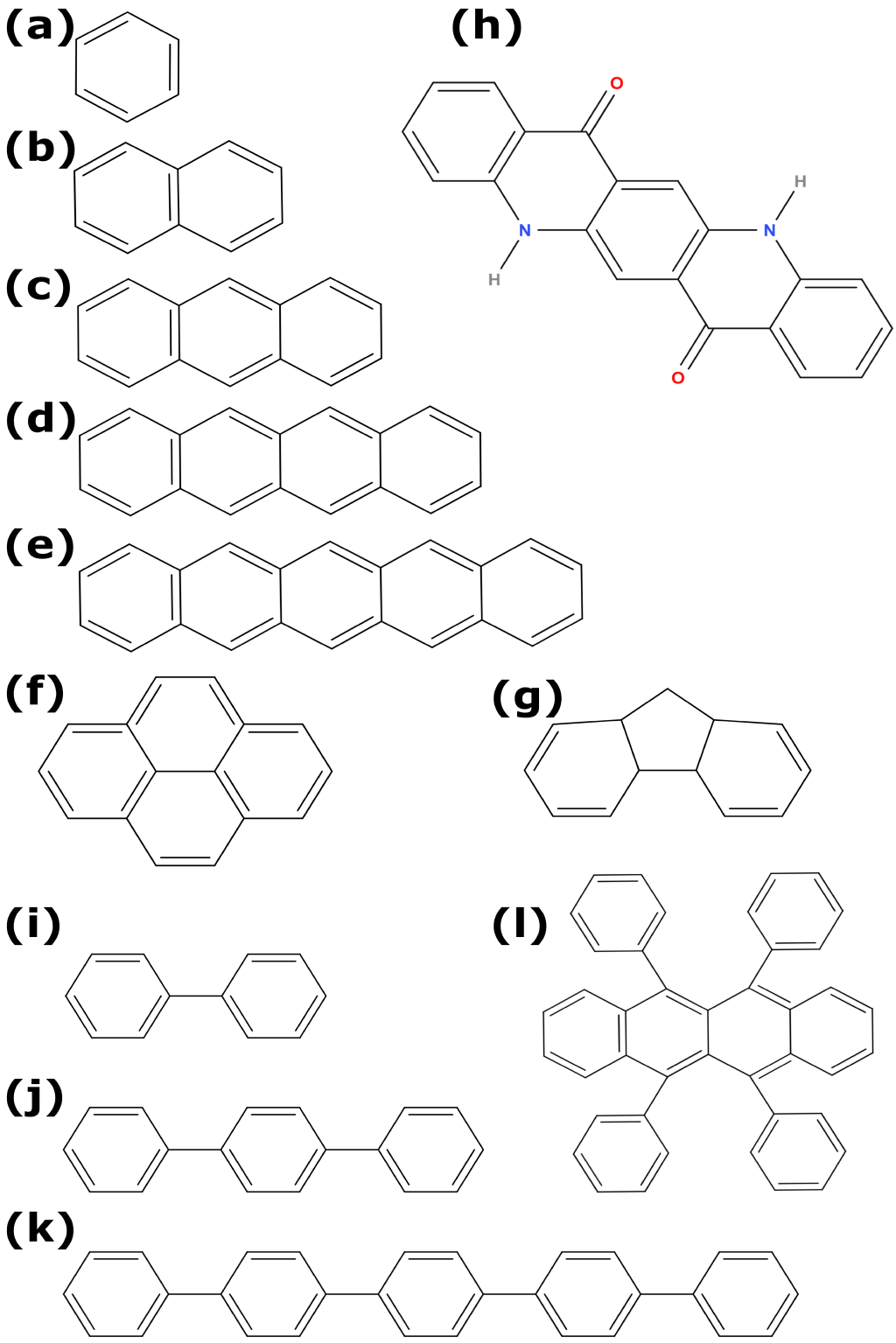

Fig. 5.1.: Structural formulae of (a) benzene, (b) naphthalene, (c) anthracene, (d) tetracene, (e) pentacene, (f) pyrene, (g) fluorene, (h) quinacridone, (i) biphenyl, (j) (para-)terphenyl, (k) (para-)quinquephenyl, and (l) rubrene. The hydrogen atoms bonded to carbons have been omitted for reasons of visibility.

pentacene, whose crystal systems are already triclinic with unit-cell angles distinctly different from 90° (see Tab. 5.1).
While for fluorene (orthorhombic) and pyrene (monoclinic) comparably unique polymorphs are relevant, quinacridone even forms three different phases with varying space groups and numbers of molecules per unit-cell, Z. Also rubrene crystallises in several polymorphs. Two of them, a monoclinic one with space group $P2_1/c$, typical of many organic semiconductors, and an orthorhombic one have been considered in the context of this thesis.
The most problematic structures turned out to be the various oligophenylenes (biphenyl, para-terphenyl, para-quinquephenyl). Usually, when searching for structures in e.g. the *Cambridge Structural Database*, one finds many crystal structure files for geometries, in which all phenyl rings lie perfectly in one plane. In reality, this is typically not the case [141, 142, 143]. The deposited crystal structures might be the result of the averaging nature of X-ray diffraction: in some unit-cells the inter-ring torsion angle is most probably positive, while it is negative (by the same absolute magnitude) in others so that in an X-ray diffraction experiment, on sees the average. Interestingly, although the planar configuration should not correspond to an energetic minimum in molecular biphenyl as shown in Ref. [141], here, still no imaginary frequencies at Γ are observed suggesting that the used structures indeed represent a minimum of the potential energy surface (within DFT using the PBE/D3-BJ methodology). Nevertheless, the system might be *dynamically* unstable resulting in imaginary phonon frequencies for non-vanishing wave vectors. This very complex situation has been accounted for from a phononic point of view by considering not only the planar configurations ("2ph_plan","3ph_plan", and "5ph_plan"), but also twisted ones in biphenyl. When imposing a non-vanishing inter-ring torsion angle in biphenyl, one can additionally find a unit-cell doubled in size along the lattice vector **b** containing four molecules ("2ph_tw4") showing an arrangement of torsion angles that cannot be achieved with only two molecules per unit-cell ("2ph_tw").
For all the systems listed in Tab. 3.1, a full optimisation according to the procedure described in Sec. 3.2 was carried out based on the experimental starting structures listed in Tab. 3.2. This resulted in the lattice parameters (and space groups) shown in Tab. 5.1.

Moreover, the systems' packing densities (Z/V), mass densities (ρ) and the four fit parameters extracted from the fitted equation of state (volume V, bulk modulus B, pressure derivative of the bulk modulus B' and the equilibrium energy E_0) are listed in Tab. 5.2. The fitted equilibrium energy E_0 divided by the number of molecules per unit-cell Z is particularly relevant to energetically compare different polymorphs containing different numbers of molecules per unit-cell.
The table shows, for instance, that the orthorhombic phase of benzene indeed has a lower energy per molecule by ~18 meV than the monoclinic phase. Moreover, the orthorhombic phase's packing and mass densities are slightly lower, despite the increased bulk modulus - i.e. the increased (isothermal) mechanical resistance of a system's volume V against compression due to hydrostatic (=isotropic) pressure p (or, more strictly speaking, the isotropic pressure p required to induce a certain relative change in volume V; see Eq.(5.1)):

Tab. 5.1.: Lattice constants (lengths of lattice vectors a, b, and c, and angles between the lattice vectors α, β, and γ) as a result of the unit-cell optimisation within the PBE/D3-BJ level of theory for the studied systems. Moreover, the space groups of the optimised crystal structures are listed. The used abbreviations for the systems can be found in Tab. 3.1.

System	**Space Group**		**Lattice Constants**					
	int. Symbol	**Number**	**a / Å**	**b / Å**	**c / Å**	**α /**	**β /**	**γ /**
1c_m	$P2_1/c$	14	5.632	5.558	7.768	90.00	111.17	90.00
1c_o	Pbca	61	6.756	7.318	9.288	90.00	90.00	90.00
2c	$P2_1/c$	14	8.078	5.903	8.622	90.00	124.24	90.00
3c	$P2_1/c$	14	8.426	5.930	11.110	90.00	125.43	90.00
4c	$P\bar{1}$	2	6.016	7.776	12.911	77.10	72.58	85.52
5c	$P\bar{1}$	2	6.271	7.638	14.314	76.76	88.99	84.08
F	Pnma	62	8.310	18.715	5.599	90.00	90.00	90.00
Py	$P2_1/c$	14	8.335	9.143	13.429	90.00	100.10	90.00
αQ	$P\bar{1}$	2	3.833	6.451	14.566	100.67	96.86	101.42
βQ	$P2_1/c$	14	5.710	3.900	29.822	90.00	96.44	90.00
γQ	$P2_1/c$	14	13.553	3.861	13.280	90.00	99.34	90.00
Ru_m	$P2_1/c$	14	8.676	10.065	15.542	90.00	90.54	90.00
Ru_o	Cmce	64	13.755	13.755	14.129	90.00	90.00	30.14
2ph_plan	$P2_1/c$	14	7.770	5.514	9.427	90.00	93.65	90.00
2ph_tw	Pc	7	7.770	5.514	9.427	90.00	93.65	90.00
2ph_tw4	Pc	7	7.811	11.014	9.431	90.00	93.87	90.00
3ph_plan	$P2_1/c$	14	7.732	5.527	13.534	90.00	93.76	90.00
5ph_plan	$P2_1/c$	14	22.071	5.513	7.723	90.00	99.06	90.00

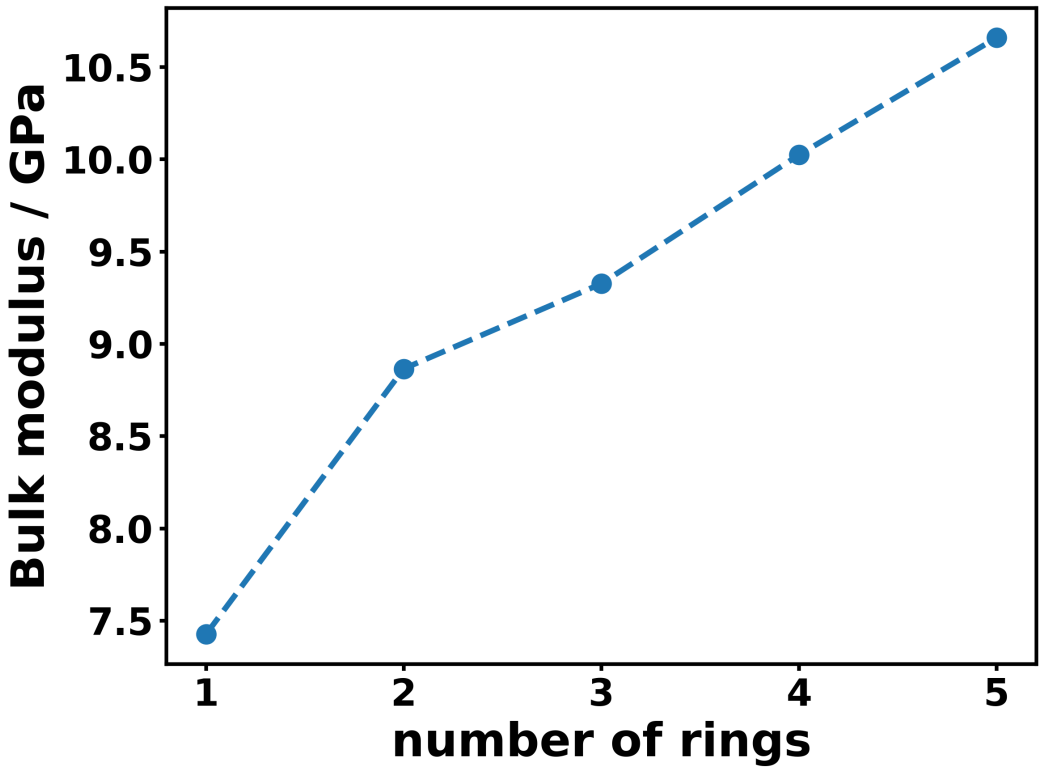

Fig. 5.2.: Bulk modulus from the fitted equations of state as a function of the length of the oligoacene molecules. For benzene (1 ring), the monoclinic phase is considered in this plot because it has the same number of molecules per unit-cell as the larger oligoacenes.

$$B = -V \left.\frac{\partial p}{\partial V}\right|_T \tag{5.1}$$

For the calculated crystalline oligoacenes, the total energy per molecule seems to decrease by about 44 eV for each additional ring. The bulk modulus increases (roughly linearly) with the molecular length for the oligoacenes (see Fig. 5.1).

In passing it should be noted that the bulk modulus calculated in that way is typically slightly overestimating the experimental values, as it was reported for naphthalene [29]. A more accurate way to determine the bulk modulus would be a full evaluation of the elastic tensors of the systems, from which the linear compressibility and the bulk modulus can be extracted [144].

It can also be seen that the energetic stability for the polymorphs of quinacridone is (in order of increasing energy): γQ, βQ, and αQ. The energies per molecule lie in a very narrow energy window (within ~0.07 eV) so that the phononic contributions (zero-point energy and thermally activated phonon occupation) might change the picture of the relative thermodynamic stability. Especially the β- and the γ-polymorph are very close in energy - in line with the experimental results in the literature [145]. Moreover,

Tab. 5.2.: Parameters extracted from the fitted equations of state (Rose-Vinet type): unit-cell volume (V), equilibrium energy (E_0), bulk modulus (B), and derivative of the bulk modulus with respect to pressure (B'). Moreover, derived quantities such as the molecular packing density (Z/V), the mass density (ρ), and the equilibrium energy per molecule (E_0/Z) are listed. The used abbreviations for the systems can be found in Tab. 3.1.

System	$\frac{Z}{V}$ / nm^{-3}	ρ / kgm^{-3}	V / $Å^3$	B / GPa	B′	E_0 / eV	$\frac{E_0}{Z}$ / eV
1c_m	8.82	1144.04	226.75	7.426	7.69	-153.84	-76.918
1c_o	8.71	1129.84	459.21	7.523	8.29	-307.75	-76.936
2c	5.88	1252.28	339.91	8.865	8.91	-242.15	-121.074
3c	4.42	1308.58	452.33	9.326	9.09	-330.17	-165.083
4c	3.56	1349.85	561.66	10.024	9.16	-418.11	-209.053
5c	3.01	1392.53	663.84	10.659	8.15	-506.04	-253.020
F	4.59	1267.92	870.76	8.721	8.43	-623.91	-155.977
Py	3.97	1333.30	1007.56	9.061	8.40	-735.54	-183.884
αQ	2.92	1514.93	342.34	9.895	18.82	-259.08	-259.080
βQ	3.03	1571.60	659.99	12.077	7.22	-518.27	-259.133
γQ	2.92	1512.51	685.78	9.481	9.10	-518.31	-259.154
Ru_m	1.47	1303.55	1357.09	9.762	11.29	-972.20	-486.100
Ru_o	1.49	1317.88	1342.34	11.113	17.42	-972.21	-486.107
2ph_plan	4.96	1270.64	403.05	9.051	8.07	-293.22	-146.611
2ph_tw	4.96	1270.65	403.05	9.292	8.75	-293.22	-146.611
2ph_tw4	4.94	1265.22	809.56	7.029	32.33	-586.45	-146.612
3ph_plan	3.47	1325.20	577.16	13.399	22.04	-432.72	-216.359
5ph_plan	2.16	1368.84	928.01	13.703	26.53	-711.62	-355.812

the β-polymorph shows a slightly increased packing density, accompanied by a notably increased bulk modulus (by roughly 30 %).
For the two tested phases of rubrene (Ru_m and Ru_o), the minimum energy per molecule from the fitted equation of state turns out to be essentially the same. This case most strongly motivates taking the phonon contribution to the free energy into account. The situation is very similar for the three considered modifications of biphenyl (planar: 2ph_plan, twisted: 2ph_tw, and twisted with four molecules per unit-cell: 2ph_tw4), for which the minimum energy is essentially indistinguishable (except for small rounding differences).

This very brief discussion emphasises the importance of considering temperature effects and the relative stability of different polymorphs, which is often not possible to predict accurately from the electronic contributions only. Therefore, the full phonon band structure must be available, from which various thermodynamic properties can be derived. In general, the Γ-phonons are not sufficient to calculate any thermodynamic properties, which is, however, still relatively often done in literature (e.g. in Refs.

[28, 29]). It has already been stressed in Sec. 2.4 and visualised in Fig. 2.1 that this approach usually results in some discrepancies in the calculated thermodynamic properties in that way. Thus, in the following, phonon contributions to the thermodynamic properties based on the full phonon band structure will be reported. In order to understand those, one must, as a first step, discuss and understand the low-frequency band structure in detail. This will be the main focus in Sec. 5.1, before the derived thermodynamic quantities can be reasonably discussed in Sec. 5.2.

Unfortunately, certain technical difficulties prevented the successful calculation of the phonon modes beyond the centre of the first Brillouin zone, Γ, for a few systems (as implied in Tab. 3.3 in Sec. 3.2):

1. Rubrene
   Both considered polymorphs of rubrene contain 140 atoms per unit-cell. The smallest reasonable size of a supercell would have been a $2 \times 2 \times 2$, resulting in 1120 atoms per supercell. For systems with that size, the DFT calculations typically become prohibitively expensive and massively inefficient due to the scaling behaviour with respect to the number of atoms. Systems of that size would favour the use of DFPT-based phonon calculations for which no supercells (just a dense enough **q**-mesh) are required to obtain the entire phonon band structure.

2. Biphenyl
   The static interring-twisting configuration of the phenyl rings in biphenyl appeared to pose a significant challenge on the simulations carried out in the framework of lattice dynamics. Despite many attempts of increasing the supercell size in the most simple (and most symmetric) planar configuration with two molecules per unit-cell (2ph_plan), imaginary (acoustic) phonon modes persisted at various points of the first Brillouin zone (see Fig. 5.3). Note that not imaginary frequencies are found at Γ. Maybe even larger supercells are required (especially in the **b**-direction, arriving at sizes as large as $3 \times 4 \times 3$ and beyond) to achieve entirely non-imaginary phonon bands, which would have meant a significant increase in computational cost. Also here, DFPT might provide a solution to this problem.
   What seemed to be more promising than increasing supercell sizes was to slightly modify the structure because, besides lacking convergence of supercell size, imaginary phonon modes can also indicate (dynamic) structural instabilities. This decision was motivated by the fact that in the ΓA-direction, the acoustic bands cause (due to the phase shift as a result of the non-vanishing wave vector) a wave in which the atomic motion contains an interring-twisting of the biphenyl molecules. The fact that these frequencies are found to be imaginary suggest that at this wave vector, the system's energy is effectively decreased - even below that of the supposed equilibrium geometry. Since also the gas phase shows a distinct inclination angle of the two phenyl rings, the possibility of a crystal structure with twisted biphenyl molecules was considered, ending up in the 2ph_tw system.
   Due to the reduced symmetry of 2ph_tw compared to 2ph_plan, the number of symmetry-inequivalent Cartesian displacements necessary to obtain the harmonic

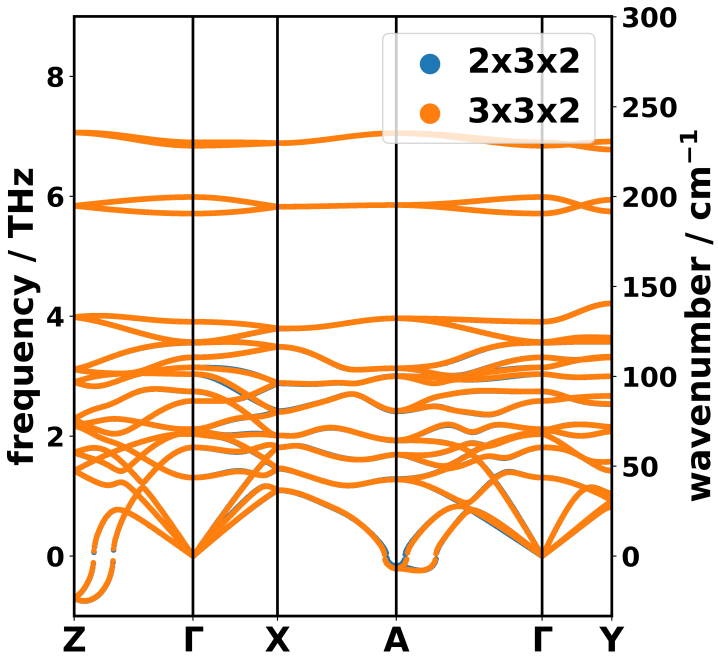

Fig. 5.3.: Phonon band structure of crystalline biphenyl (planar configuration) calculated with PBE/D3-BJ for two sizes of supercells. Independent from the supercell size, the band structure shows pronounced imaginary phonon bands around A and Z (and further high symmetry points which are not shown).

force constants increase by a factor of 2 (from 66 to 132) as the inversion symmetry is lost when twisting the molecules. Therefore, the phonon calculations would have cost additional computational resources without any guarantee that this structure would solve the problem. The concern that this structure was maybe still not the optimal choice was additionally supported by the fact that in the Cambridge Structural Database, all entries of twisted biphenyl unit-cells contained four molecules (which were predominantly deposited for the deuterated molecules, so that they might have been the results from elastic neutron scattering experiments, in which one has a clearer view of the hydrogen positions). Such a twisted structure containing four molecules per unit-cell (2ph_tw4) has been fully optimised within PBE/D3-BJ and even its Γ-phonons have been calculated. However, a (supercell-based) calculation of the phonon band structure was seen uneconomical because (i) the larger number of atoms in the system (with the same space group as 2ph_tw) results in a larger number of symmetry-inequivalent Cartesian atomic displacement (264 instead of 132 or 66 for 2ph_tw and 2ph_plan, respectively) and (ii) each of these many more displacements would have required much more computational time (at least four times more if the computational time only scaled quadratically with the number of atoms). For those reasons, the phonon calculations based on supercells in real space could not overcome the many problems in the seemingly simple biphenyl system.

3. Oligophenylenes
   Following the problems exhibited by the much simpler situation in crystalline biphenyl, similar problems were observed for p-terphenyl (3ph) when trying to calculate the phonon band structure. Here, the situation is much more involved because even in one molecule the three rings can be tilted in different ways (alternating or helical tilting). Extrapolating those problems to p-Quinquephenyl (5ph), the complexity of the ring twisting configuration explodes. Therefore, for 5ph all attempts to calculate the phonon band structure have been cancelled, and for 3ph, no further configuration besides the planar one with two molecules per unit-cell has been considered, since the problem has not been solved successfully even for biphenyl.

In the following, the low-frequency band structure of both phases of benzene, naphthalene[42], anthracene, tetracene, pentacene, fluorene, pyrene and the three phases of quinacridone are discussed.

5.1. Low-Frequency Band Structures

5.1.1. Benzene

The simplest organic molecule covered in this thesis is benzene crystallising either in a monoclinic (1c_m) or an orthorhombic (1c_o) crystal structure. In order to more reasonably discuss the band dispersion, the unit-cells as well as the corresponding first Brillouin zones of both phases are shown in Fig. 5.4. In anticipation of the later discussed phonon properties, the atoms in the crystal structure are plotted in terms of the calculated thermal ellipsoids based on the simulated phonon band structures using the *Mercury* software [135].

Although both phases show the typical herringbone stacking common for organic crystals, the phonon band structures shown in Fig. 5.5 cannot be compared on a one-to-one basis because of the different Bravais lattice. In general, it can be seen that the "low-frequency" region earlier defined for naphthalene is restricted to even a lower spectral range in benzene. The reason is clearly that the intramolecular bands are found at higher frequencies, whereas the intermolecular bands reach similar frequencies as in naphthalene. The reason why the gap between intra- and intermolecular modes is increased so significantly is simply that the flexibility of a molecule typically increases with its spatial extent - i.e. it is much harder to deform the shorter benzene molecule than the more compliant naphthalene molecule. The increased *molecular* flexibility with larger molecule lengths should, however, not be confused with the fact that the bulk modulus, which could be thought of as a measure for the *crystal* stiffness, still increases with the length of the oligoacene as shown in Fig. 5.2. The reason for the increased bulk modulus is the packing of the molecules in the unit-cell and the interactions between those, which are supposed to increase with the molecule size because the van der Waals interactions

[42] Only for the sake of completeness, as it has been the topic of the intensive discussion in Sec. 4.

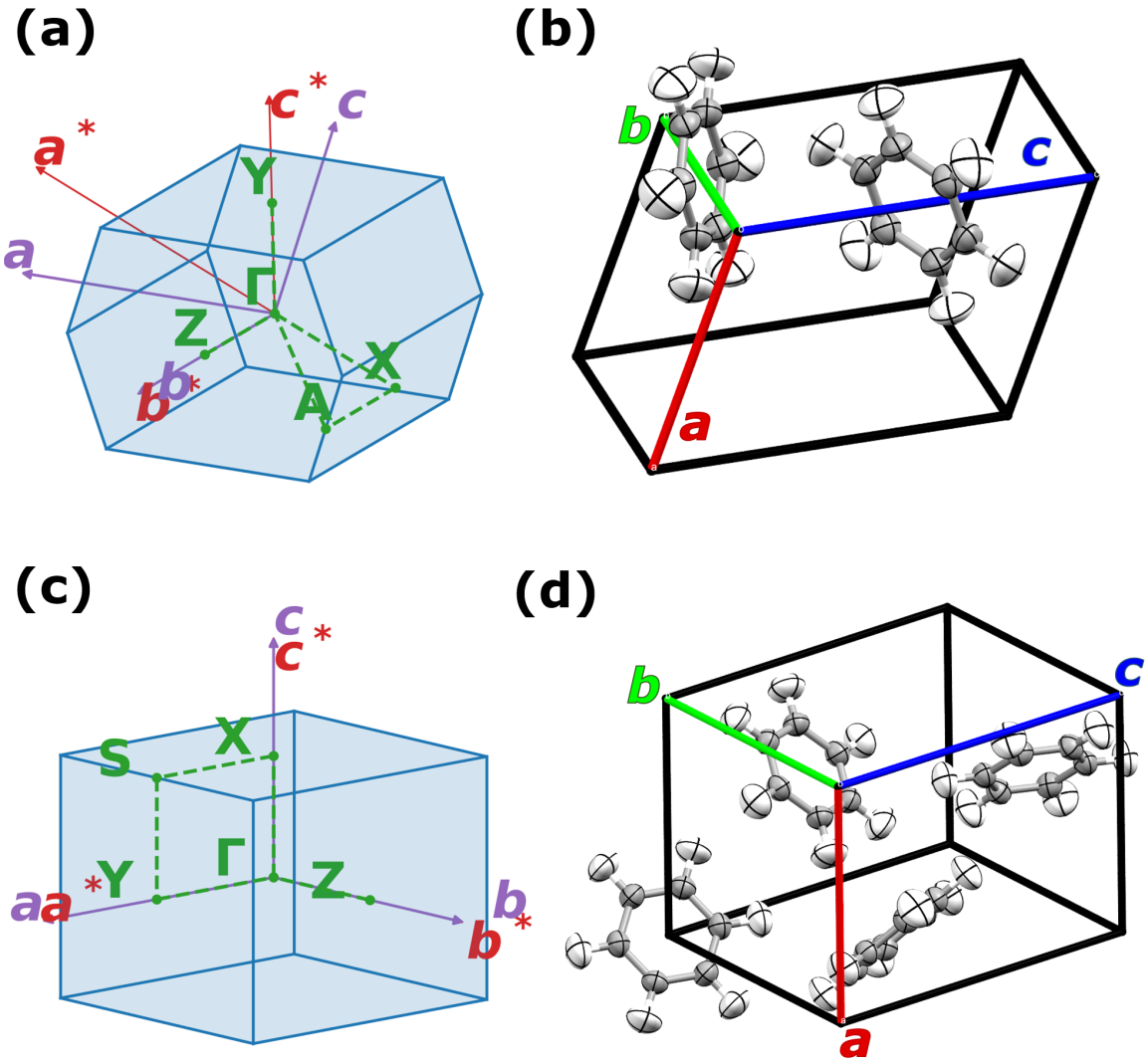

Fig. 5.4.: (a,c) First Brillouin zone including the high symmetry points used in the band structure diagrams and (b,d) real-space unit-cell of crystalline benzene in the monoclinic (1c_m) and the orthorhombic (1c_o) phase, respectively. The atoms are drawn in terms of the thermal ellipsoids for a probability level of 50 % and a temperature of 0°C since the melting point of benzene is about 5.5°C at ambient pressure [137].

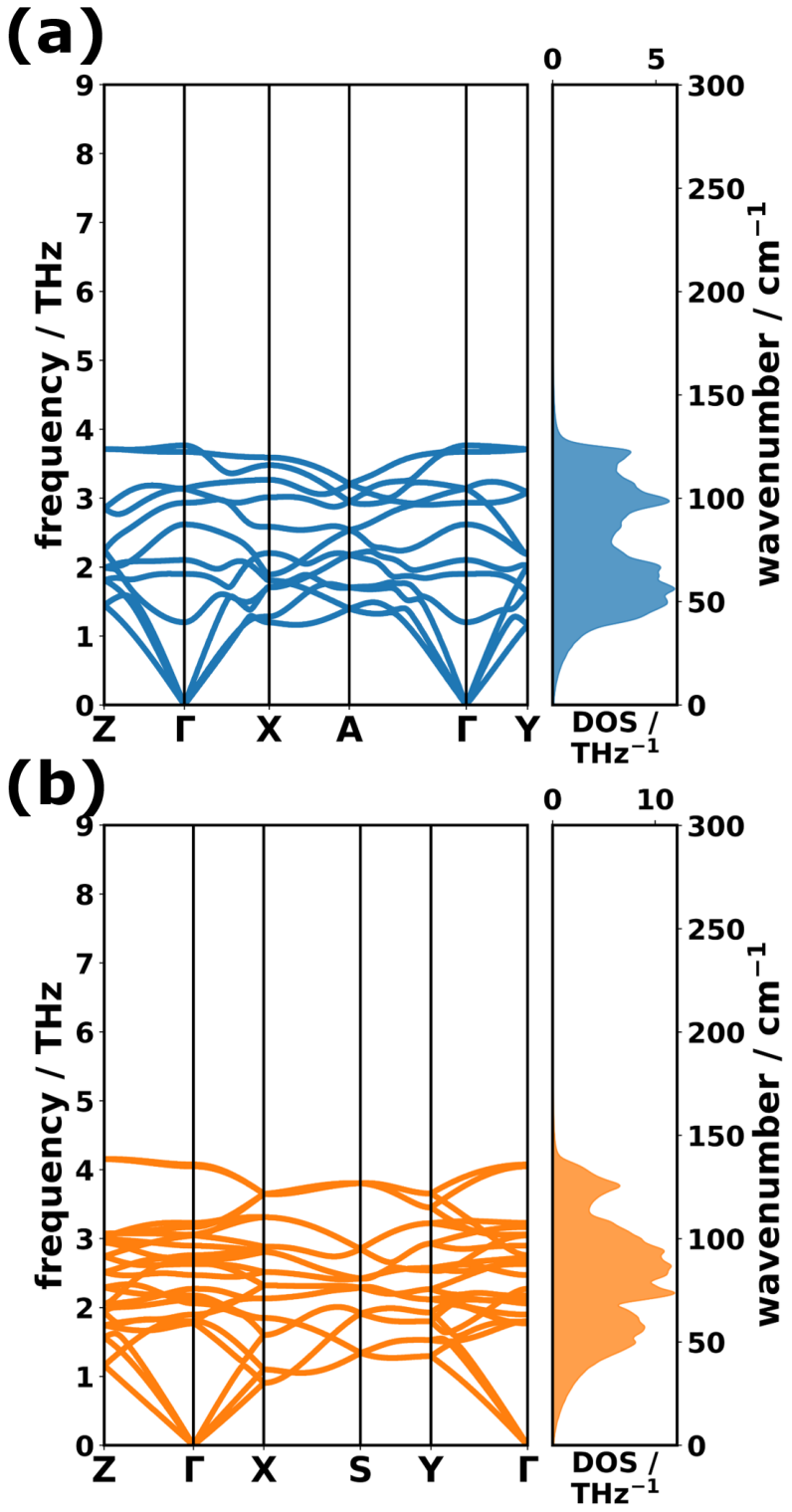

Fig. 5.5.: PBE/D3-BJ-calculated phonon band structure and DOS of (a) monoclinic (1c_m) and (b) orthorhombic (1c_o) benzene.

become stronger. In contrast, the *molecular* flexibility of those molecules, here, is assessed only in an intramolecular way: it is easier to share a given external deformation of a molecule among many bonds instead of demanding that only a few bonds distort to the entire extent of the total deformation. This can be thought of as a series of springs, for which every single spring has to elongate much less for a given total elongation. As a result, the total spring constant of such a series of springs is smaller than that of every single spring in it. Thus, for small molecules like benzene, one would expect a relatively pronounced separation between the inter- and intramolecular phonon modes.
In the case of 1c_m, one can easily check that the shown phonon bands really correspond to all intermolecular bands in the crystal. Since 1c_m has two molecules per unit-cell, there must be 12 intermolecular bands because every molecule has six degrees of freedom (three translational and three rotational ones). The identification of the nature of these bands' motion requires, however, other means, as will be discussed later. In the case of 1c_o, counting the bands is slightly harder since the bands lie so densely, but their number amounts to 24, consistent with the four molecules per unit-cell in this structure.
It is, however interesting to note that the intermolecular regime for both phases extends to ~4 THz, similar as in naphthalene. This implies that the highest inter**molecular** force constant between the benzene molecules amounts to only ~61 % of that in naphthalene. This number is based on the following consideration: if the frequency is (approximately) equal, one can equate the ratio of intermolecular force constant Φ and molecular mass M for both systems, which corresponds to the squared (angular) frequency:

$$\begin{aligned} \omega_{1c}^2 &= \omega_{2c}^2 \\ \frac{\Phi_{1c}}{M_{1c}} &= \frac{\Phi_{2c}}{M_{2c}} \\ \Rightarrow \frac{\Phi_{1c}}{\Phi_{2c}} &= \frac{M_{1c}}{M_{2c}} \approx 0.601 \end{aligned} \tag{5.2}$$

This result is consistent with the notion that the low-frequency modes are determined by van der Waals interaction, which increases in strength with the lateral extension of the molecule. Therefore, one would only expect the intermolecular frequency range to increase for larger oligoacenes (with similar packing density) if the intermolecular force constants increase more rapidly than the molecular mass.
A difference between the band structures of the two phases is the fact that the highest intermolecular frequencies in 1c_o are slightly larger than in 1c_m. This is consistent with the observation that the bulk modulus is slightly higher, suggesting stronger intermolecular interaction. Additionally, the increased number of molecules per unit-cell in 1c_o results in many relatively flat bands between 2 and 3 THz. The very same spectral region is relatively poor in bands in the case of 1c_m, resulting in a pronounced minimum in the DOS, whereas one can see a notable maximum in the DOS of 1c_o.
A similarity in both DOSs is the relatively large frequency range in which the DOS has a Debye-like quadratic shape (up to ~1.5 THz). This is a consequence of the band dispersion of the acoustic bands showing a nearly linear **q**-dependence throughout the entire

shown high-symmetry paths. Only in a few instances they are interrupted by intermolecular optical bands with the same irreducible representation of the symmetry of the atomic motion such that an avoided crossing occurs. Obviously, this phenomenon seems to be more common for the 1c_m system. A few notable examples in 1c_m include the avoided crossing of the highest (longitudinal) acoustic band along ΓX at about 1.8 THz, the second-highest (transverse) acoustic band along ΓY at ~1.5 THz or the multiple avoided crossings in ΓA-direction, whereas one can only observe an avoided crossing along ΓY in 1c_o. Basic understanding of group theory reveals the reason for the more common occurrences of avoided crossings in 1c_m. Due to the reduced symmetry in this system (space group $P2_1/c$) there are fewer irreducible symmetry representations[43] than in the 1c_o system with more symmetries (space group Pbca). Therefore, the probability that two bands with the same irreducible representation cross is notably increased in 1c_m.

The dispersion of the acoustic bands can relatively easily be observed when colouring the bands according to the corresponding mode participation ratio (PR) (see Eq. (2.42) in Sec. 2.3). Obviously, the acoustic bands correspond to motion in which all the atoms in the crystal participate in the wave. Thus, the acoustic bands have a very high PR, at Γ even exactly 1 as shown in Fig. 5.6. In passing it should be noted that the PR (for *simple* phonon modes) is supposed to decrease for non-vanishing wave vectors because these waves have finite wavelengths and, thus, there must be parts in the structure that do not move significantly at every instance.

The PR-coloured bands in Fig. 5.6 facilitate the recognition of the (high-PR) acoustic bands. This enhanced visual recognition reveals that the acoustic bands in ΓZ direction in the 1c_m system show the largest bandwidths of all the shown directions in the band diagram (~2.3 THz). The real-space equivalent of this direction is along the short lattice vector **b** - i.e. the direction in which the molecules pack most closely in a parallel way. A similar effect can be seen for the orthorhombic phase as well: the bandwidths in ΓZ and ΓY are approximately the same, but in ΓX, it is notably reduced. In real-space, the ΓX-direction corresponds to the lattice vector **c**, which is the largest lattice parameter. Thus, the reduced packing distance in this direction decreases the effective stiffness of the system, which, in turn, reduces the acoustic band dispersion.

[43] At Γ, the symmetry (point) groups are C_{2h} and D_{2h} in 1c_m and 1c_o, respectively. The character tables of these point groups (see e.g. Ref. [146]) contain four and eight irreducible representations (irreps), respectively. For wave vectors different than Γ, the symmetry is even further reduced, ending up in less symmetric point groups with even fewer irreps. Therefore, avoided crossings of two bands, which requires the same irrep of the involved bands, are less likely in 1c_o.

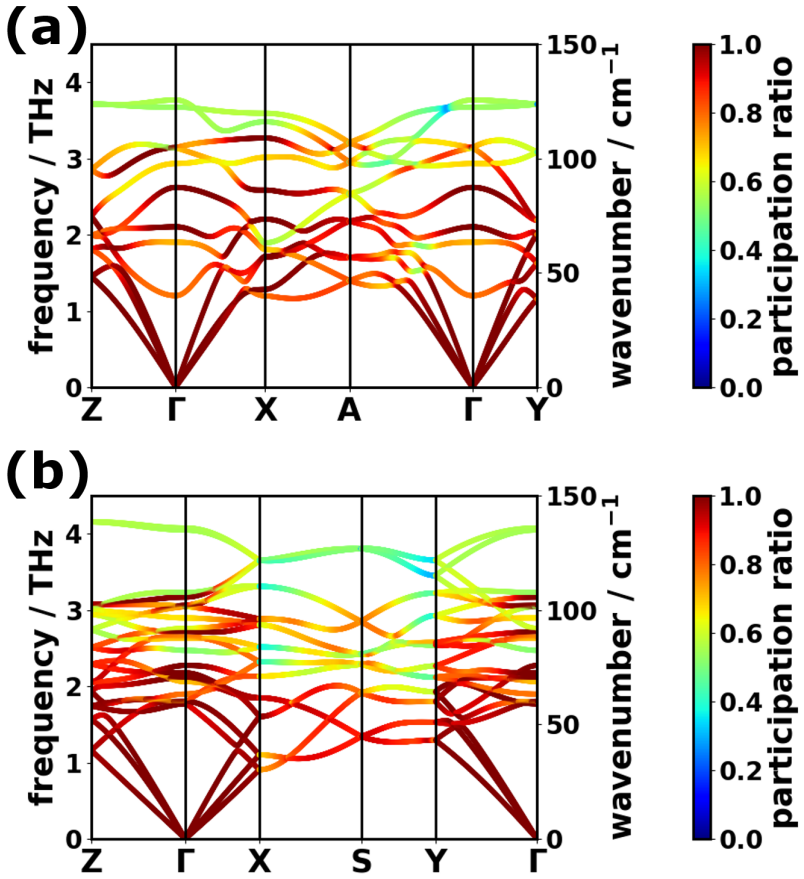

Fig. 5.6.: PBE/D3-BJ-calculated phonon band structure coloured according to the mode participation ratio of (a) monoclinic (1c_m) and (b) orthorhombic benzene (1c_o).

Besides facilitating the recognition of the acoustic bands, the PR-colouring allows to identify optical phonons with particularly high degree of atomic motion: in 1c_m, modes of that kind can, e.g., be found at Γ for the frequencies 2.10, 2.62, and 3.14 THz. Visualising the corresponding displacement patterns of these modes reveals that these high-PR optical phonons correspond to intermolecular modes in which the two molecules per unit-cell translationally oscillate with respect to each other keeping the internal molecular geometry mostly unaffected. In other words, the molecules oscillate "rigidly". These $3(Z-1)$ **r**igid **i**nter**m**olecular translational **m**odes (with Z being the number of molecules per unit-cell), which I will refer to as "RIMMs" in the following, are often severely affecting the charge transport properties of organic semiconductors so that for many systems they might be referred to as the *killer phonon modes* [10]. The other $3Z$ intermolecular bands[44] with slightly decreased PRs correspond to rigid rotations of

[44]In general, a system with Z molecules per primitive unit-cell has $6Z$ intermolecular modes, since each molecule brings in 3 translational and 3 rotational degrees of freedom. Of the in total $6Z$ intermolecular modes, three correspond to the three acoustic modes of the crystal, resulting in

the molecules, which show less atomic motion because at least the axis of rotation has to stand still (resulting in lower PRs). RIMMs (characterised by rigid translational motions) can also be observed in the band structure of 1c_o (See Fig. 5.6(b)). Due to the increased number of molecules per unit-cell, one can observe nine RIMMs in that system: at 1.81, 1.85, 2.11, 2.18, 2.71, 3.05, 3.07, and 3.20 THz at Γ. The frequencies of these RIMMs will be focussed on during the later discussion in the course of a comparison among the longer oligoacenes.

5.1.2. Naphthalene

Since the low-frequency band structure of naphthalene has been the topic of the intensive discussion in Sec. 4, this section should be kept relatively short and rather serve as a consistent continuation of the discussion of the oligoacenes. Fig. 5.7 shows the first Brillouin zone and the real-space unit-cell (including the thermal ellipsoids) of naphthalene. It can be seen that the molecules again pack in a herringbone fashion.

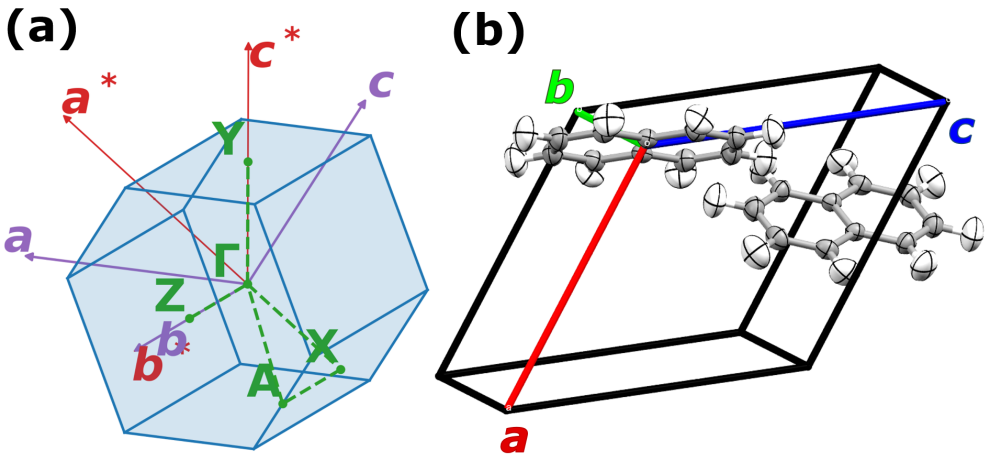

Fig. 5.7.: (a) First Brillouin zone including the high symmetry points used in the band structure diagrams and (b) real-space unit-cell of crystalline naphthalene (2c). The atoms are drawn in terms of the thermal ellipsoids for a probability level of 50 % and a temperature of 0°C. The melting point of naphthalene is about 80°C at ambient pressure [137].

$6Z-3$ optical intermolecular modes. Those can again be split into $3(Z-1)$ optical intermolecular modes characterised by translational motion (="RIMMs"), and into $3Z$ intermolecular rotational modes.

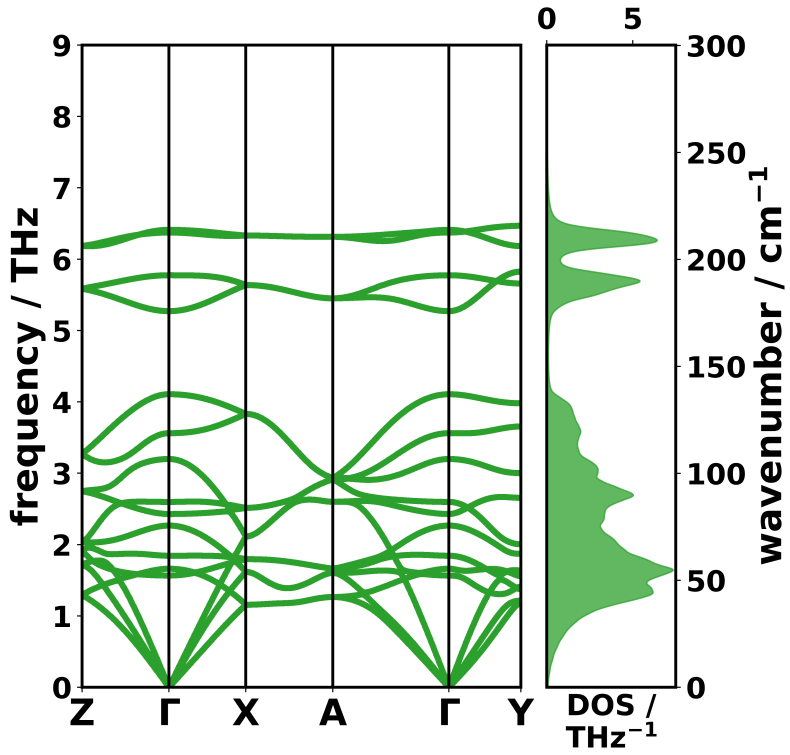

Fig. 5.8.: PBE/D3-BJ-calculated phonon band structure and DOS for naphthalene (2c).

In contrast to benzene, first intramolecular bands appear at already relatively low frequencies (between ~5.2 and 6.5 THz). They correspond to bending and twisting motions of the rings around the long molecular axis (see Appendix A.5). Bands with relatively little dispersion as those appear as comparably sharp peaks in the DOS (see Fig. 5.8) separated from the more continuous low-frequency part of the DOS (due to the intermolecular modes) by a much smaller band gap (slightly above 1.2 THz) compared to the discussed benzene polymorphs. Similarly to benzene, one can identify a region in the DOS (up to ~1.4 THz) with a typical Debye-like shape caused by the (approximately) linear dispersion of the acoustic phonons.
The closest distance between the molecules is found in the direction of the lattice vector **b**, which corresponds to the ΓZ-direction in reciprocal space. In this direction, however, the stacking is parallel rather than herringbone-type because only a molecule and its periodic replica are involved (rather than the two inequivalent molecules). Following the observations made for benzene, one expects a higher acoustic band dispersion in this direction, as the stacking is much denser. This is, however, not true for naphthalene which can most probably be ascribed to the reduced symmetry of the naphthalene molecule compared to benzene: i.e., naphthalene has a distinct long molecular axis, which adds an additional component of anisotropy besides the anisotropic stacking. Therefore,

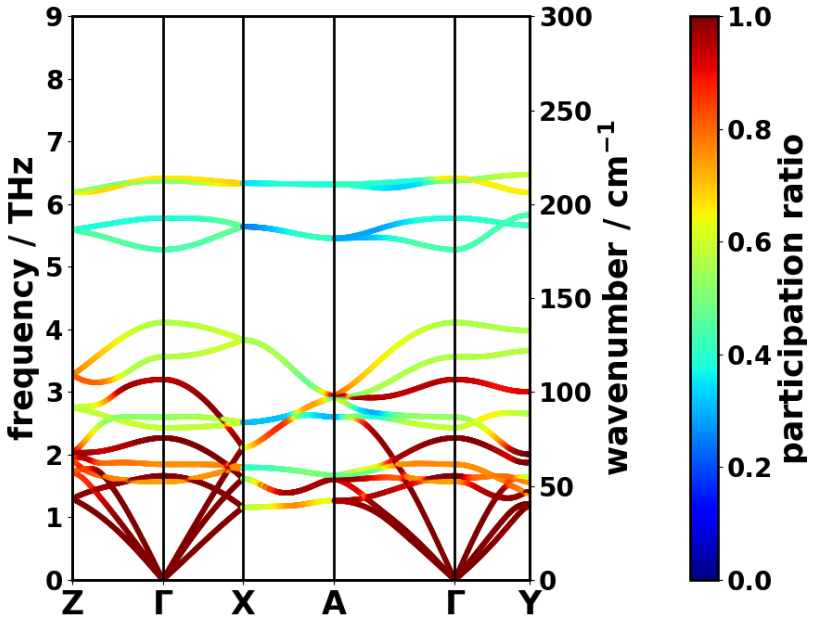

Fig. 5.9.: PBE/D3-BJ-calculated phonon band structure of naphthalene (2c) coloured according to the mode participation ratio.

motions in certain directions experience more van der Waals interactions than others. As a result, the acoustic band widths are relatively similar along ΓZ and ΓX. Only in ΓY it seems, at first glance, that the band widths of the longitudinal acoustic band - i.e. the acoustic band with the highest frequency near Γ - is notably reduced. The mode-PRs (see Fig. 5.9) reveal, however, that this is more a consequence of avoided crossings with optical intermolecular bands with a relatively high degree of phonon hybridisation, as a comparably wide gap is opened in between the bands involved in the avoided crossing. The high PRs of the bands at about 2 THz at the high symmetry point Y suggest that this is the rest of the longitudinal acoustic (LA) band along this direction.

Besides facilitating the visual recognition of the band dispersion, the PR-coloured bands very clearly show the RIMMs (at Γ at 1.66, 2.27 and 3.20 THz). In contrast to the case of benzene, one can more easily distinguish between the physical origin of these three modes in naphthalene due to the reduced molecular symmetry. Visualising the displacement patterns, it can be seen that the lowest of these RIMMs corresponds to the (nearly) rigid relative displacements of the two molecules along their long molecular axes, close to lattice vector **c** (see Fig. 5.10(a)). Compared to the frequencies of the corresponding modes in benzene, the frequency is decreased, which is most probably a result of the higher molecular mass. Also the second-lowest RIMM (see Fig. 5.10(b)) is slightly reduced in frequency with respect to the 1c_m system, whereas the highest RIMM (at ~3.2 THz at Γ; see Fig. 5.10(c)) is found at about the same frequency as in

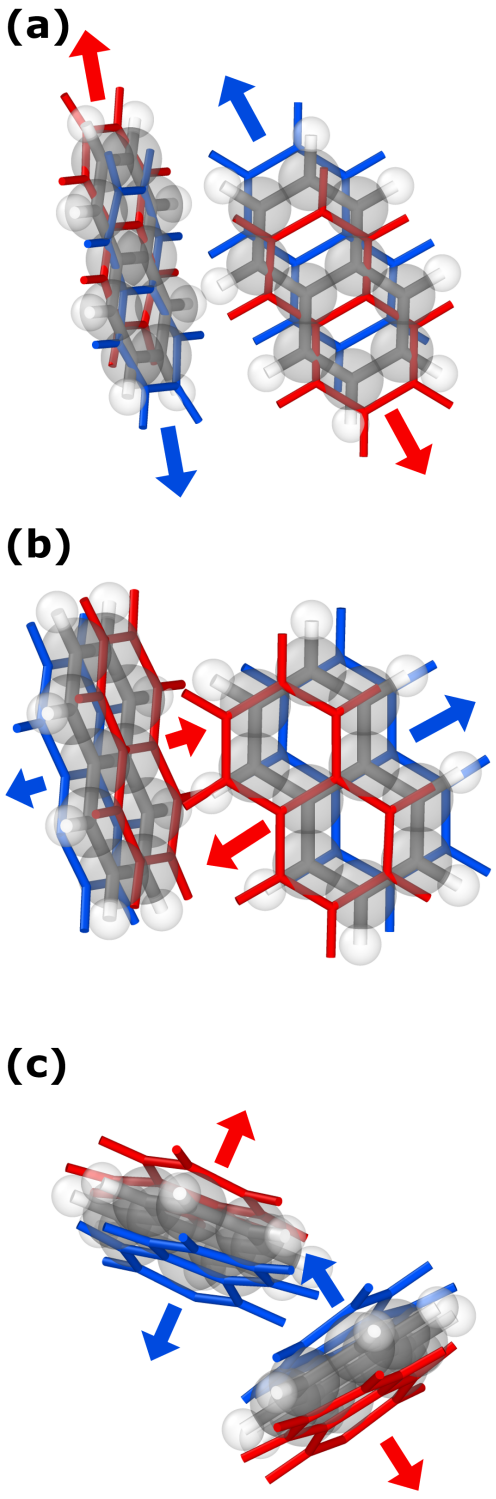

Fig. 5.10.: Γ-point displacement patters of the rigid intermolecular modes at (a) 1.66 THz, (b) 2.27 THz, and (c) 3.20 THz in naphthalene. The red and blue wireframe structures correspond to the positive and negative amplitudes of the vibration, respectively.

1c_o and only negligibly higher than in 1c_m. As shown in the displacement pattern, this RIMM corresponds to a vibration, which periodically de- and increases the herringbone stacking distances. According to the argumentation using Eq. (5.2), this suggests slightly higher intermolecular force constants in this direction than in benzene (as the frequency is approximately the same in spite of the increased mass).

Quantitatively, one can estimate[45] the extent to which these intermolecular force constants must increase in naphthalene compared to benzene given the observed frequencies of the RIMMs. To this end, the following approximation can be employed (using the same nomenclature as for Eq. (5.2), but with an additional band index n) to quantitatively assess the ratio of intermolecular force constants based on the ratios of the (squared) frequencies and the molecular masses:

$$\begin{aligned} \omega_{n,1c/2c}^2 &= \frac{\Phi_{n,1c/2c}}{M_{1c/2c}} \\ \Rightarrow \left(\frac{\omega_{n,2c}}{\omega_{n,1c}}\right)^2 \frac{M_{2c}}{M_{1c}} &= \frac{\Phi_{n,2c}}{\Phi_{n,1c}} \end{aligned} \tag{5.3}$$

Evaluating Eq. (5.3) for the three RIMMs (in order of increasing frequency) in naphthalene compared to 1c_m benzene, the ratio of intermolecular force constants for these modes amount to 1.01, 1.23, and 1.70, respectively. This result is interesting, as the first RIMM, which corresponds to the anti-phase displacement of the two molecules along their long molecular axes, is obviously mostly shifted in frequency due to the mass difference of benzene and naphthalene, as the estimated molecular force constants for such a displacement are approximately equal. The other two RIMMs show higher ratios of the corresponding frequencies, which cannot be ascribed to the mass difference only, as can be seen by the notably increased intermolecular force constants ($\Phi_{n,2c}/\Phi_{n,1c} > 1$). This curiosity will be checked in the larger oligoacenes in the following subsections in order to test, whether there is a systematic trend behind this observation.

5.1.3. Anthracene

In terms of its structure, the monoclinic anthracene crystal is relatively similar to that of naphthalene. In order to fit the larger molecules inside the unit-cell, the lattice vectors must be longer: **a** and **c** by ~0.3 Å and 2.5 Å, respectively, while **b** is essentially the same (see Tab. 5.1). The unit-cell including two molecules (drawn in terms of the atomic thermal ellipsoids) as well as the corresponding first Brillouin zone are shown in Fig. 5.11.

[45] Note that this is only a crude estimation because here, the molecular mass is used as the mass of the corresponding harmonic oscillator, while actually the mode effective mass (see Eq. (2.40)) should be used. The high participation ratio, however, shows that the entire molecule is moving and, thus, the molecular mass provides an acceptable quick means to estimate the effective mass.

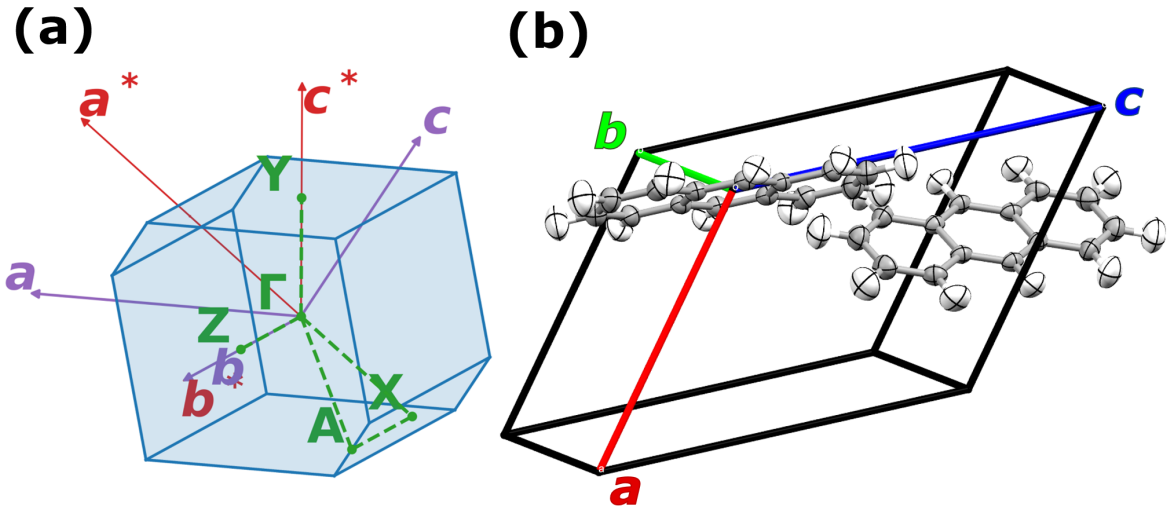

Fig. 5.11.: (a) First Brillouin zone including the high symmetry points used in the band structure diagrams and (b) real-space unit-cell of crystalline anthracene (3c). The atoms are drawn in terms of the thermal ellipsoids for a probability level of 50 % and a temperature of 0°C. The melting point of benzene is about 216°C at ambient pressure [137].

Again, the DOS (see Fig. 5.12) exhibits a Debye-like behaviour up to ~1 THz owing to the linear band dispersion of the acoustic bands. Similarly to naphthalene, the band widths of the acoustic bands are approximately the same in ΓX, ΓZ, and ΓY, with the latter showing several avoided crossings involving acoustic bands near the Brillouin zone boundary. A considerably higher band dispersion is only reached in ΓA (like in naphthalene), which can partly be ascribed to the increased length of this high-symmetry path in reciprocal space.
As a result of the enhanced molecular flexibility due to the increased size of the molecule, intramolecular distortions such as bending or twisting are expected to be observed at increasingly lower frequencies as a function of the number of rings in the oligoacene. Moreover, one can see several sharp peaks in the DOS in Fig. 5.12 starting at ~7 THz. At first glance, it seems as if the spectral band gap between the inter- and intramolecular modes had increased compared to the previously discussed DOS and the band structure of naphthalene. Also the DOS of anthracene supports this (wrong) impression because of its continuous nature up to ~5 THz. Analysing the band structures in Fig. 5.12, one can, however, find that this supposedly intermolecular spectral region up to 5 THz contains 16 bands, although there should only be twelve. This finding implies that there are already four intramolecular modes so low in frequency that they overlap with the actual intermolecular region. These bands can be discerned by means of the low PRs: the two bands with a frequency of ~5 THz at Γ (intramolecular torsions) and those with frequencies of ~3.2 and 3.8 THz at Γ (in-phase and anti-phase bending of the two molecules, respectively). It is, however, interesting that these low-frequency intramolecular bands show a significant degree of dispersion, unlike most of the higher modes starting

at ~7 THz, which display a non-negligible band dispersion only in exceptional cases. Therefore, these dispersing low-frequency bands might be potential candidates for the effective contribution to phonon-related transport properties such as the thermal conductivity.
Anthracene also displays three RIMMs like 1c_m and 2c above. The frequencies (ratios of force constants compared to 1c_m) for the equivalent types of motion shown in Fig. 5.10 are: 1.4 THz (1.0), 2.1 THz (1.47), and 3.1 THz (2.29). These frequencies are in agreement with the trends observed for naphthalene: the frequencies of the first two RIMMs are decreased, with the lower one being nearly exclusively the result of the enhanced molecular mass. For the higher one of these two, the mass ratio (with respect to 1c_m) alone is not able to explain the frequency reduction compared to both 1c_m and 2c. Instead, for that and the highest RIMM, a notable increase of the responsible intermolecular force constant is suspected. This increase is particularly large for the highest RIMM showing nearly the same frequency as in 1c_m and 2c. Therefore, the corresponding intermolecular force constant is supposed to entirely make up for the higher molecular mass of anthracene.

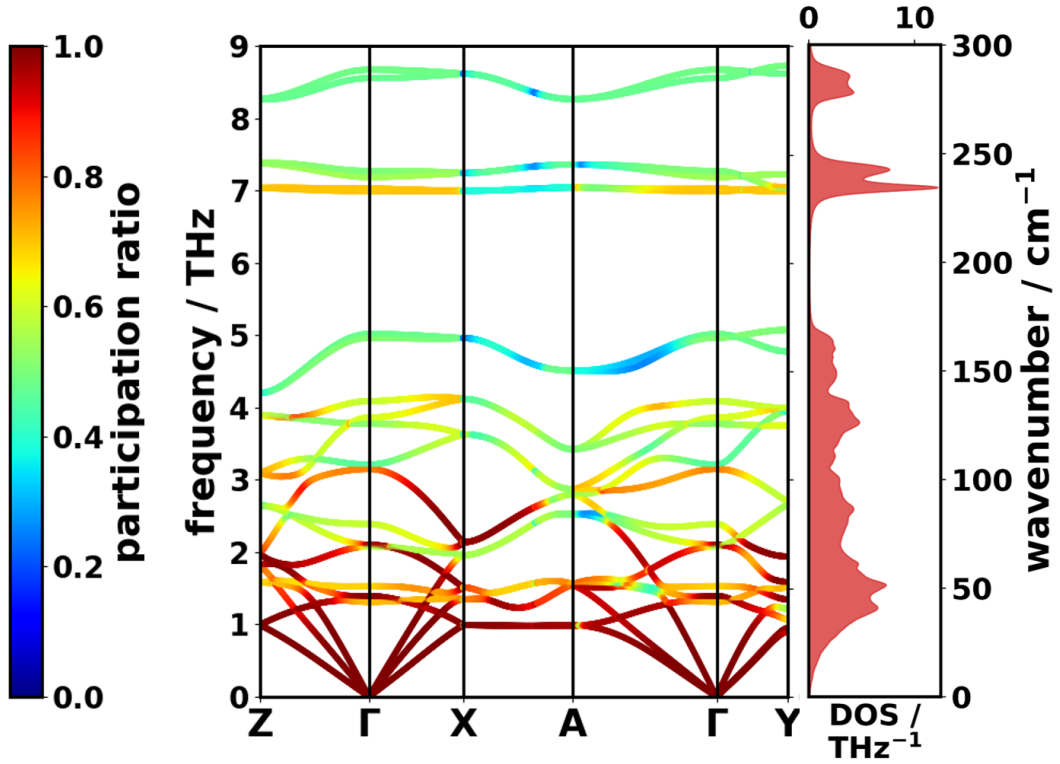

Fig. 5.12.: PBE/D3-BJ-calculated phonon band structure (coloured according to the mode participation ratio) and DOS of anthracene (3c).

5.1.4. Tetracene

Extending the discussion to a system with one more ring, one arrives at the tetracene crystal packing in a triclinic Bravais lattice. The unit-cell containing the thermal ellipsoids (for 0°C) as well as the corresponding first Brillouin zone are shown in Fig. 5.13. The long molecular axis is approximately oriented along the lattice vector **c**, whose orientation is similar to its reciprocal analogue $\mathbf{c}^*$. Due to the triclinic lattice, correlating the high-symmetry paths to real-space direction is much more involved. Moreover, it is not reasonable any more to draw continuous band diagrams as the only "high-symmetry" paths are those emerging from Γ. The DOS and the phonon band structures (coloured according to the PRs) are shown in Fig. 5.14.

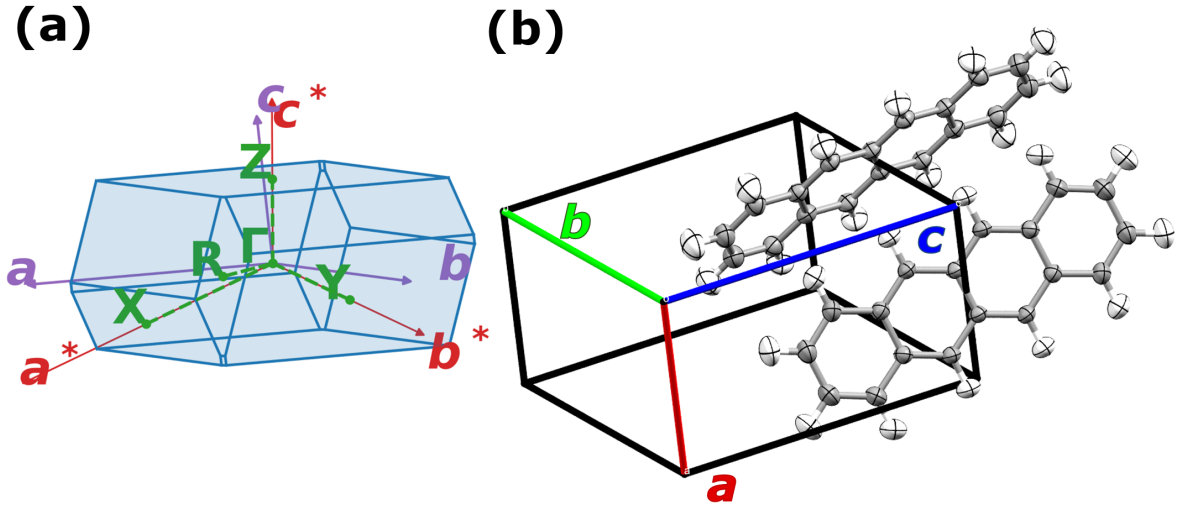

Fig. 5.13.: (a) First Brillouin zone including the high symmetry points used in the band structure diagrams and (b) real-space unit-cell of crystalline tetracene (4c). The atoms are drawn in terms of the thermal ellipsoids for a probability level of 50 % and a temperature of 0°C. The melting point of tetracene is about 357°C at ambient pressure [137].

Besides the reduced symmetry and the caused obstacles in the interpretation of the band diagrams, the entire phonon situation is drastically affected compared to the shorter oligoacenes. The only feature that is at least similar to anthracene is that, starting at about 5 THz, one can find relatively localised (low PR) and dispersionless bands. Since a band with little or no dispersion is equivalent to a high number of phonon states per frequency interval, the corresponding DOS typically shows a (sharp) peak. Equivalently, for bands with a large bandwidth, the phonon modes are spread over a wide frequency window, resulting in a much flatter shape of the DOS. The lowest intramolecular peak around 5 THz again conveys the wrong impression of an extended intermolecular spectral regime characterised by a continuous DOS. The bands corresponding to that peak in the DOS as well as the two bands below at ~4.2 and 4.5 THz at Γ (with particularly

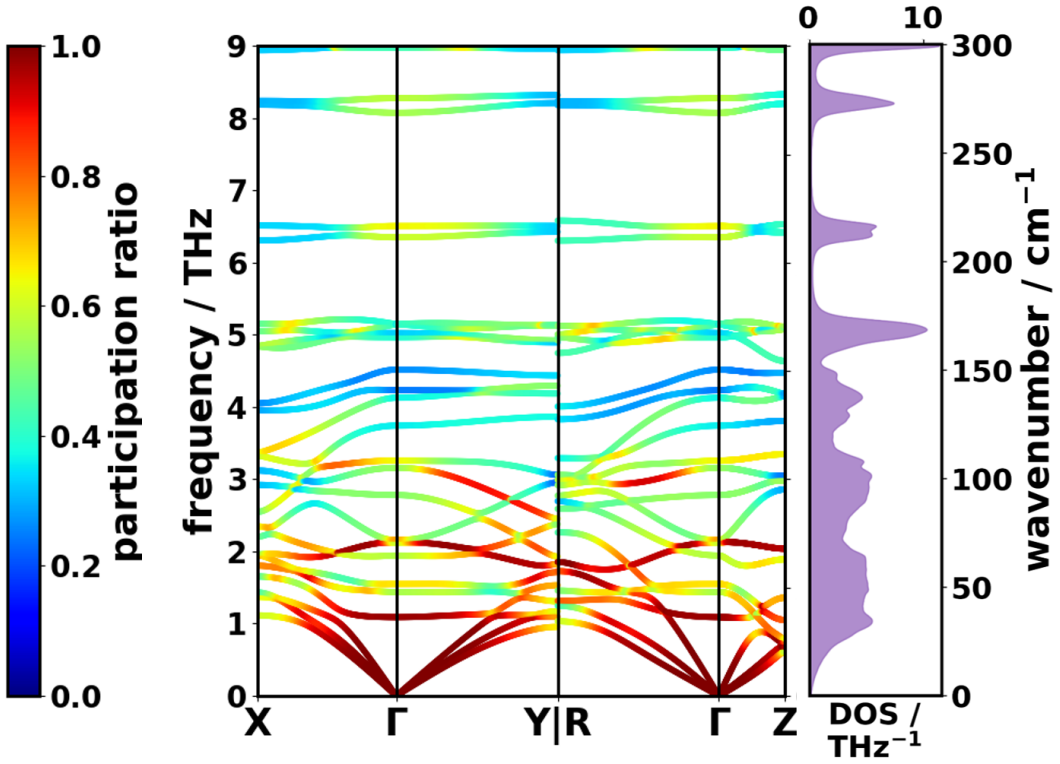

Fig. 5.14.: PBE/D3-BJ-calculated phonon band structure (coloured according to the mode participation ratio) and DOS of tetracene (4c). Here, the DOS was obtained for a denser mesh than for the thermal properties (according to Tab. 3.3) using a 20×17×9 **q**-mesh (see Appendix A.4).

low PR), again correspond to intramolecular motion which require only little energy due to the flexibility of the longer molecule, resulting in those low frequencies.

The onset of the DOS at very low frequencies does not show the same perfect agreement with a parabolic behaviour (Debye model) as the DOSs of the previously discussed systems exhibit. Instead, the parabolic shape is confined to a narrower frequency interval (up to ~0.5 THz). At approximately that frequency, the onset of the DOS shows a slight kink. This is a result of the relatively different band widths of the acoustic bands: while ΓX, ΓY, and ΓR show similar band widths, the acoustic bands in ΓZ-direction arrive at the Brillouin zone boundary at much lower frequencies. In other (not shown) directions, this might as well be the case, resulting in the deviations from the parabolic Debye-like behaviour of the DOS, which is - strictly speaking - only valid for an isotropic crystal. The condition of isotropy is expected to become increasingly invalid for such low-symmetry triclinic systems. Interestingly, although the band width in ΓY-direction is very similar to the others, the slope of the bands is massively reduced as a consequence of the longer distance of this high-symmetry path in reciprocal space. Acoustic phonon

transport is, thus, supposed to be particularly bad in this specific direction, which is roughly perpendicular to the long molecular axes (for the geometric relations see Fig. 5.13).
Moreover, the phonon transport properties are supposed to be reduced significantly by the high density of avoided crossings in the band structure. For each occurrence of such a phonon hybridisation, dispersive parts of the involved band (high group velocities) are replaced by less dispersive segments - depending on the hybridisation strength. Bands of a system with such a low-symmetry space group as tetracene ($P\bar{1}$) is particularly prone to avoided crossings because there are hardly any irreducible symmetry representations available for the phonon eigenvectors (at Γ, there are only two irreducible representation for the point group C_i [146]) so that nearly every pair of crossing bands is supposed to hybridise causing an avoided crossing. These phenomena are frequently found to be unfavourable for phonon transport [147, 148, 149].

Also the RIMMs are partly affected by such a hybridisation process: the RIMM with the highest frequency (~3.2 THz) and the one with the second-highest frequency (~2.2 THz) happen to hybridse with other bands near Γ. Therefore, the displacement patterns of these modes involve notable bending of the molecule as well. Still, their frequencies and ratios of intermolecular force constants are consistent with the trends observed so far: the highest RIMM-frequency (in spite of the additional bending character) is close to the frequency in the corresponding RIMM in all smaller oligoacenes, which suggests an increase of the intermolecular force constant by a factor of ~2.94 compared to 1c_m. The frequency of the second-highest RIMM is, again, slightly lower than in 1c_m (but higher than in 3c) so that one can estimate an intermolecular force constant larger than the equivalent one in 1c_m by a factor of ~1.97. The RIMM at the lowest frequency (1.1 THz) (oscillatory displacement along the long molecular axes; see Fig. 5.10(a)) exhibits the largest PR and also the least additional molecule bending. According to the considerations of Eq. (5.3), the intermolecular force constant in tetracene is smaller (0.78) compared to 1c_m. It is obvious that tetracene does not lie as perfectly in the trend of the shorter oligoacenes, which consistently showed a ratio of ~1 for this force constant. This slight discrepancy can most probably be ascribed to (i) the particular situation that there are modes with the same symmetry (irreducible representation) present, which cause a hybridisation, and (ii) the increased molecule flexibility which induces low-frequency bending modes. The fact that it is much easier to bend the molecule is also the reason why it is relatively difficult to assess the inter- or intramolecular nature of the modes just from visual inspection. In fact, a slight degree of additional molecule bending can be found for most of the low-frequency modes (at Γ).

5.1.5. Pentacene

The situation is similar for pentacene (5c), whose triclinic unit-cell (with the atoms being displayed in terms of their thermal ellipsoids at 0°C) and the first Brillouin zone are shown in Fig. 5.15. In analogy to tetracene, several sharp peaks appear in the low-

frequency regime of the DOS above ~5 THz. These modes correspond to bending, twisting etc. of higher order[46]. Most pronouncedly, one can observe a massive peak in the DOS in the spectral region between ~3.5 and 4.5 THz. This is a result of the relatively dense accumulation of weakly dispersing bands in that region including several forms of bending and twisting of the flexible molecules as well as the highest intermolecular modes (intermolecular rotations around the long molecular axis). The latter can also be seen when following the two bands with increased dispersion, which emerge at ~3.3 THz at X .
Due to the highly anisotropic shape of the first Brillouin zone, the acoustic bands arrive at the zone boundary at very diverse frequencies. The band widths in ΓZ are, for instance, notably decreased compared to the other shown high-symmetry paths. As a result, the DOS shows a kink below 1 THz (similarly to tetracene) rather than exhibiting the parabolic Debye-like shape as for the shorter oligoacenes.
Since pentacene crystallises in the same space group as tetracene, many avoided crossings of the bands are expected for the same reasons as discussed in Sec. 5.1.4. Most obviously, examples of avoided crossings can be seen for the acoustic bands near Z and near X.

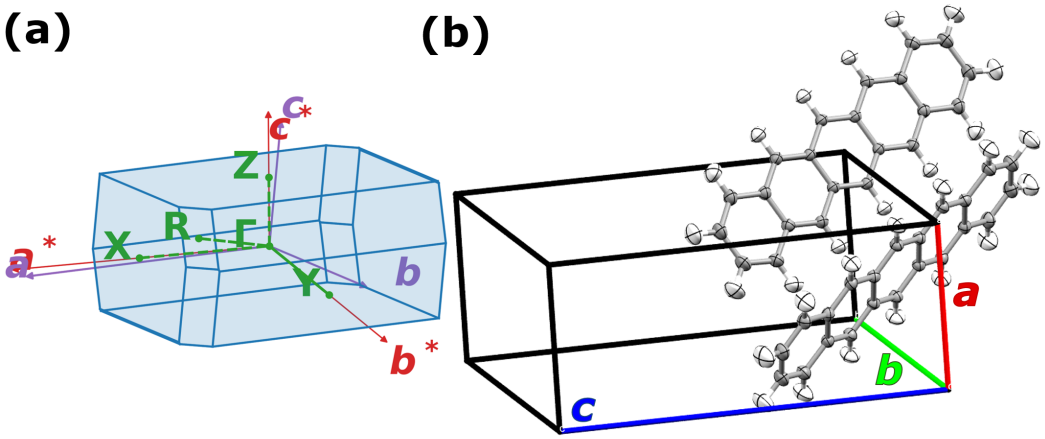

Fig. 5.15.: (a) First Brillouin zone including the high symmetry points used in the band structure diagrams and (b) real-space unit-cell of crystalline pentacene (5c). The atoms are drawn in terms of the thermal ellipsoids for a probability level of 50 % and a temperature of 0°C.

[46] By "higher-order" bending/twisting, an oscillation is referred to, which is characterised by more nodes. For example: a first-order bending of a stick which is kept fixed at its ends shows two nodes (at the ends, where it is fixed). A second-order bending introduces a further node in the middle of the stick such that the left half bends upwards while the right part simultaneously bends downwards (and vice versa).

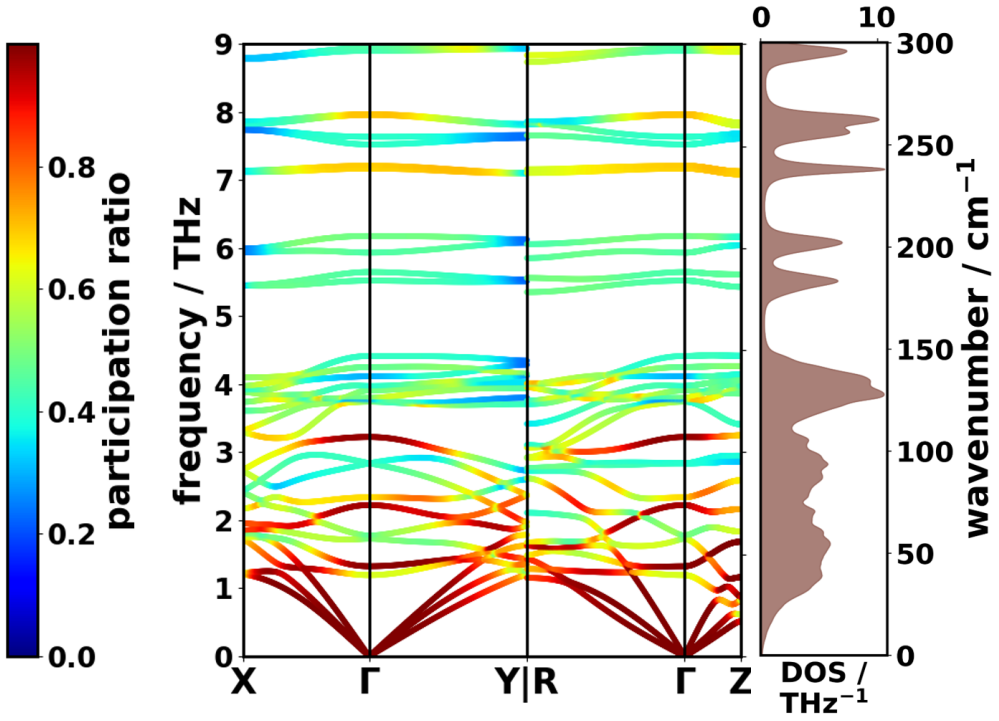

Fig. 5.16.: PBE/D3-BJ-calculated phonon band structure (coloured according to the mode participation ratio) and DOS of pentacene (5c). Here, the DOS was obtained for a denser mesh than for the thermal properties (according to Tab. 3.3) using a 20×15×10 **q**-mesh (see Appendix A.4).

Concerning the nature of the low-frequency phonon modes, the situation is even more complex than in tetracene, as one observes a pronounced intermixing of spectral regions of inter- and intramolecular modes. For example, (first-order) bending modes can already be discerned at ~1.78 and 2.84 THz (at Γ). These interfere with the intermolecular modes at certain points in the first Brillouin zone. Additionally, the highest intermolecular modes are overlapping with the many flat bands between 3.5 and 4.5 THz, as mentioned before. However, the RIMMs can still be identified based on the high PRs (1.3, 2.2, and 3.2 THz). Surprisingly, the recognition of those modes is even much less involved than in tetracene. Comparing their frequencies to the corresponding ones in the 1c_m system, the ratios of intermolecular force constants $\Phi_{n,5c}/\Phi_{n,1c}$ can be identified according to Eq. (5.3). They amount to 1.38, 2.54, and 3.74 (in order of increasing frequency). These values are again consistent with the observations for the shorter oligoacenes discussed so far: the ratio of the intermolecular force constants of the RIMMs with the highest and second-highest frequency scales nearly linearly with the number of rings (see Fig. 5.17) because of the enhanced van der Waals interaction caused by the larger lateral extent of the oligoacenes.
Since the frequency for the highest RIMM ($n = 3$) stays approximately constant among

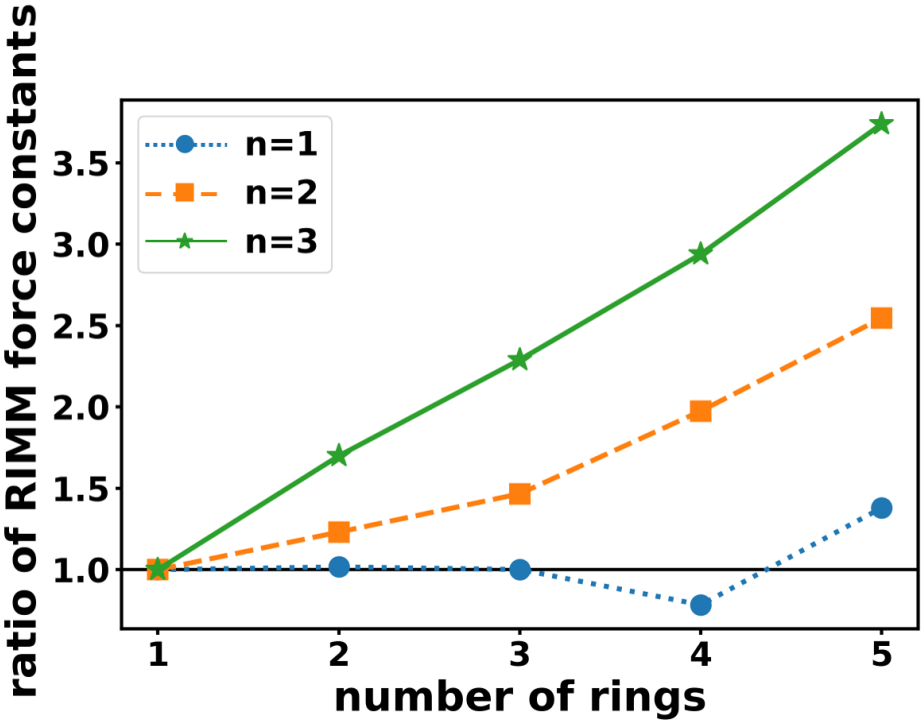

Fig. 5.17.: Ratios of intermolecular force constants $\Phi_{n,Nc}/\Phi_{n,1c\_m}$ for the rigid intermolecular modes (RIMMs) compared to the monoclinic benzene structure 1c_m as a function of the number of rings per molecule ($1 \leq N \leq 5$). The slight deviations in the force constants ratio of the lowest RIMM ($n = 1$) from unity for tetracene ($N = 4$) and pentacene ($N = 5$) are most probably a result of the phonon hybridisation near Γ and the different crystal structure.

the studied oligoacenes, this means that the increasing molecular mass is counterbalanced by the increasing intermolecular force constants - i.e. the increasing strength of the van der Waals interaction with the molecule length. For the intermediate RIMM ($n = 2$ in Fig. 5.17), one can observe a slight decrease in frequency with increasing molecular length in spite of the increasing intermolecular force constants. Here, the effect of the increasing mass cannot be cancelled by the stronger interaction. The RIMM with the lowest frequency (displacement along the long molecular axes; $n = 1$ in Fig. 5.17) exhibits a less unambiguous trend: as can be seen in Fig. 5.17, the ratio of the corresponding intermolecular force constants with respect to 1c_m is close to unity for 2c and 3c, but scatters around this value for the larger oligoacenes 4c and 5c. Most probably this behaviour can be ascribed to the fact that tetracene and pentacene show much higher molecular flexibility so that the assumptions made in this quantitative estimation - namely that the molecules move rigidly, with the "effective mass" equalling the entire molecular mass - do not hold exactly any more. Additionally, the difference in crystal class and the involved geometric details of the molecular packing might have a

contribution to the deviation from the trend. Moreover, the errors are naturally largest for the smallest frequency/force constant. Therefore, it is believed that the vibrations along the long molecular axes are determined by an intermolecular force constant that is roughly the same as in simple benzene. This can be rationalised by the notion that in those modes, the effective loss/gain in interaction and, thus, the curvature in the PES is approximately the same when oscillating along the long molecular axis regardless of the length of the molecule: the loss/gain in interaction strength is determined by the geometric overlap, which predominantly varies only at the very ends of the molecules. Conversely, in the other RIMM motions, the increased van der Waals forces result in enhanced intermolecular interactions: (i) for displacements along the short molecular axis ($n = 2$), the geometric overlap is varied along the entire length of the molecule; (ii) for displacements increasing/decreasing the packing distance ($n = 3$), the geometric overlap is determined by the entire molecular area. Thus, for the lowest RIMM, the drop in frequency observed for longer oligoacenes can (nearly) exclusively be ascribed to the higher molecular mass, while for the higher ones, the increased van der Waals interactions play a role as well. For the highest RIMM, the two effects even cancel each other resulting in a constant frequency of the associated modes.

5.1.6. Fluorene

The increasing overlap of the inter- and intramolecular regions observed in the oligoacenes starting at anthracene is supposed to deteriorate properties that rely on the band dispersion of low-frequency modes: as more weakly dispersing bands are present in the low-frequency regime, the average group velocity (for similar length scales - i.e. lattice constants) is decreased.

A potential pathway to separate these two regimes more strictly again could be increasing the stiffness of the molecules. Here, fluorene containing a five-membered ring (including an sp^3-hybridised carbon interrupting the aromatic electronic structure of the molecules) in between two six-membered rings could show enhanced molecular stiffness. The reason for this hypothesis is that - in contrast to anthracene - the "central" ring is shorter (i.e. it contains fewer bonds). However, the sp^3-hybridised carbon is supposed to (on average) form slightly weaker bonds to the neighbouring atoms compared to the sp^2-hybridised carbons in anthracene. As the latter is hypothesised to play only a minor role, the molecule should become less flexible, which, in turn, is supposed to shift the intramolecular bands to higher frequencies. Unfortunately, the unit-cell of fluorene contains four molecules, which raises the complexity of the analysis. However, the increased (orthorhombic) symmetry reduces the *a priori* probability of avoided crossings, which can be seen as unbeneficial for transport properties [147, 148, 149].

The orthorhombic unit-cell (containing the thermal ellipsoids) as well as the corresponding first Brillouin zone are shown in Fig. 5.18. The four molecules arrange in layers perpendicular to the lattice vector $\mathbf{b}$, along which the long molecular axes of all molecules are oriented. This layer-like molecular packing, with these layers being much more separated from each other than in the oligoacenes, suggests a weak interlayer coupling compared to the interactions within a layer. The most obvious difference in

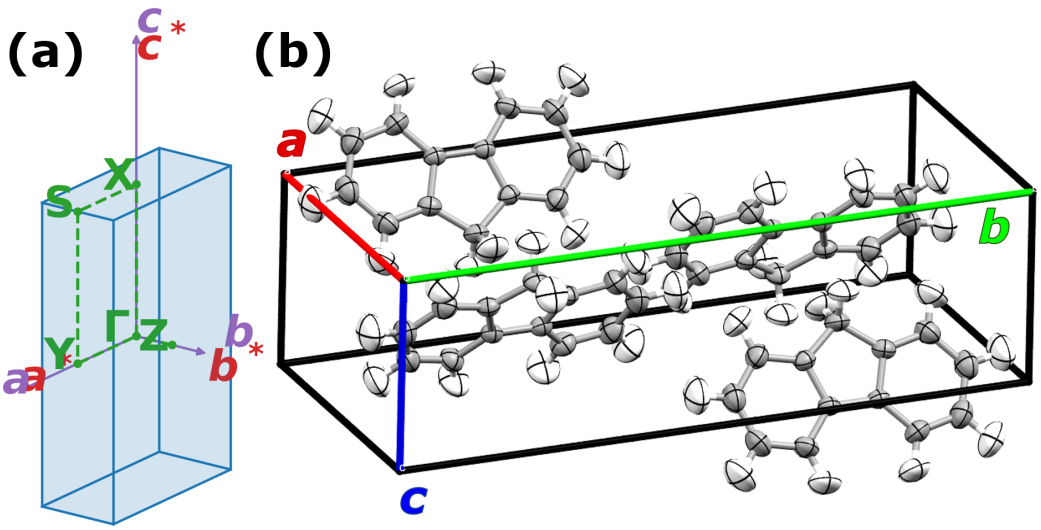

Fig. 5.18.: (a) First Brillouin zone including the high symmetry points used in the band structure diagrams and (b) real-space unit-cell of crystalline fluorene (F). The atoms are drawn in terms of the thermal ellipsoids for a probability level of 50 % and a temperature of 0°C.

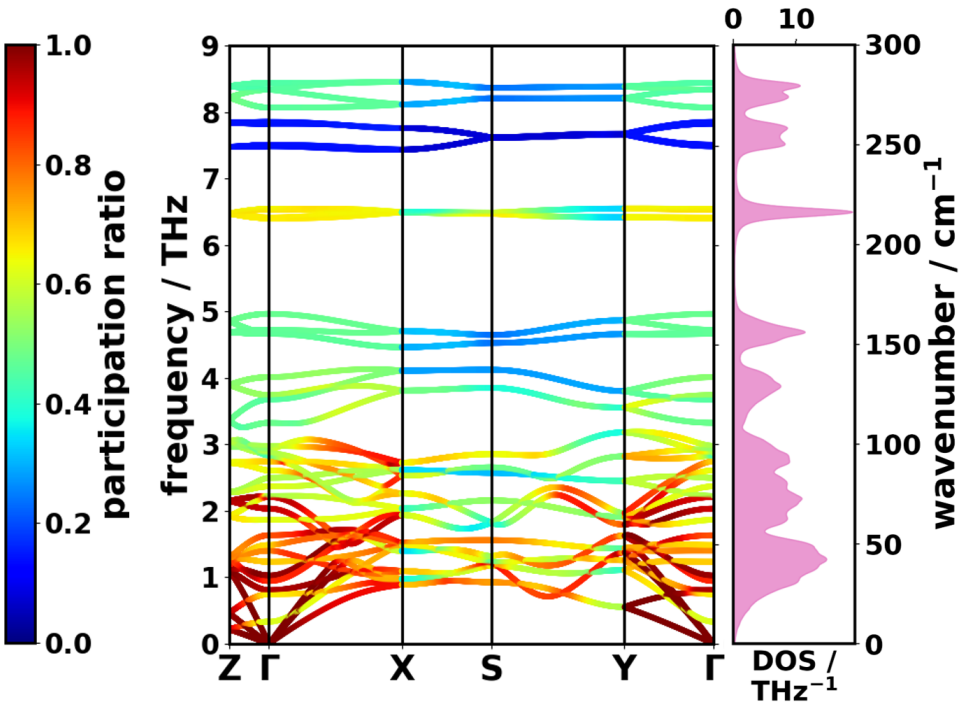

Fig. 5.19.: PBE/D3-BJ-calculated phonon band structure (coloured according to the mode participation ratio) and DOS of fluorene (F). Here, the DOS was obtained for a denser mesh than for the thermal properties (according to Tab. 3.3) using a 13×6×20 **q**-mesh (see Appendix A.4).

this layered structure of fluorene and that in the oligoacenes is the angle between the long molecular axes and boundary planes of those layers: while in fluorene, this angle amounts to (nearly) 90°, one observes a notably reduced angle between the long molecular axes and layer boundaries in the oligoacenes. In the latter case, part of the van der Waals interaction acts between the layers, whereas this is hardly possible in fluorene. This circumstance is expected to result in a decreased band dispersion of the transverse acoustic bands of wave vectors perpendicular to the layer boundaries. Such wave vectors would correspond to the direction of the reciprocal lattice vector $\mathbf{b}^*$ ($\widehat{=}\Gamma$Z).
This expectation is fulfilled by the band structure, which can be seen in Fig. 5.19. Along the very short ΓZ-path, the band dispersions of the two (lower-lying) transverse acoustic (TA) bands are considerably decreased compared to the longitudinal acoustic (LA) band. Partly owing to the longer distances in reciprocal space, the band widths of the acoustic bands are typically larger in the other directions. In general, the difference in band dispersion between the TA and the LA bands seems to be more pronounced in fluorene than in, e.g., orthorhombic benzene, which is very likely a result of the sheet-like packing of the molecules.
Moreover, the DOS displays no real band gaps below ~5 THz - similar to anthracene. The intended separation of inter- and intramolecular modes is, thus, only partly successful: in spite of the (supposedly) vanishing gap in the DOS[47], the phonon bands of the intramolecular modes are well separated from the intermolecular ones. The latter can be easily discerned in the band structure with the aid of the mode-PRs. Up to ~3 THz, one can find relatively high PRs. All bands up to this limit correspond to intermolecular modes. The (only very small) separation between inter- and intramolecular modes can rather be ascribed to the fact that the bands of the intermolecular modes do not reach high enough frequencies that they can overlap with the lowest intramolecular ones. The latter can be found to start at frequencies similar as in anthracene. Here, the intermolecular bands are much more confined to lower frequencies - particularly densely in the spectral region from ~0.8 to 1.5 THz, which results in the pronounced peak in the DOS. Interestingly, the presence of this large and broad spectral feature can be ascribed (partly) to the fact that several bands, including the acoustic bands as well, do not show significant degrees of dispersion. Most probably, this is a consequence of the structure consisting of (weakly) coupled layers. In fact, bands for wave vectors, which correspond to directions that lie in planes parallel to the layer boundaries (i.e. perpendicular to the lattice vector $\mathbf{b}$), show only little dispersion.

5.1.7. Pyrene

A further organic semiconductor, which (i) does not show the same strict layer-like structure with only little interlayer coupling as fluorene (and, thus, is supposed to not show

[47] In fact, the DOS should vanish in the spectral proximity of ~3 THz, where, according to the band diagram, one finds a tiny band gap (~0.05 THz) between the intermolecular regime and the first intramolecular modes. The fact that the DOS still does not perfectly vanish in this gap is essentially an artefact from the finite broadening of the DOS using Lorentzian functions with a full-width-at-half-maximum of 0.1 THz (see Sec. 3.1.4).

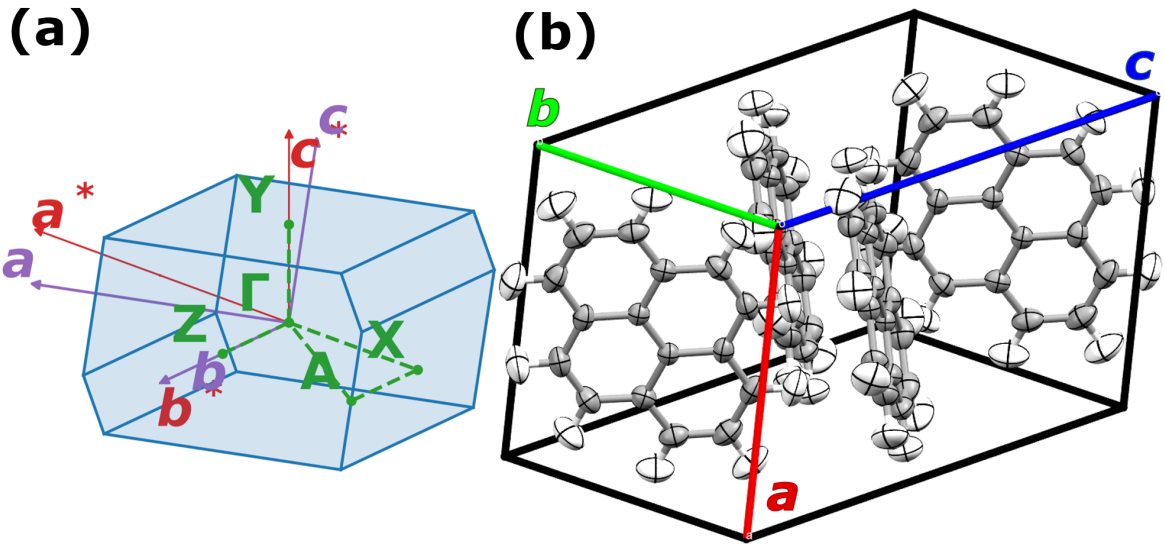

Fig. 5.20.: (a) First Brillouin zone including the high symmetry points used in the band structure diagrams and (b) real-space unit-cell of crystalline pyrene (Py). The atoms are drawn in terms of the thermal ellipsoids for a probability level of 50 % and a temperature of 0°C.

that many acoustic bands with little dispersion) and (ii) is expected to be structurally less flexible than those molecules with a more pronounced long axis, is crystalline pyrene consisting of four (aromatic) molecules per unit-cell. The monoclinic structure containing the atoms as thermal ellipsoids is shown in Fig. 5.20 together with its first Brillouin zone. The low-frequency phonon band structure is displayed in Fig. 5.21.

Due to the larger lateral extent of the aromatic pyrene molecules compared to the more strip-like oligoacenes one expects that e.g. the bending of the long molecular axis is shifted to higher frequencies (low-PR bands below 4 THz). Furthermore, the large spatial extent of the molecules leads to *trampoline*-modes (low-PR bands below ~7 THz, see Fig. 5.22(a)). Such trampoline modes, which might be considered as a two-dimensional bending, have not been observed in the low-frequency band structures of any of the other organic semiconductors discussed so far. The molecule itself can be roughly seen as a "stiffened" version of biphenyl, which, in contrast to the single additional (five-membered) ring in fluorene, stabilises the relatively flexible interring twisting configuration from two sides. This is the reason why the intramolecular modes characterised by those torsional motion (see 5.22(b)) are found at frequencies between ~4.5 and 5.5 THz. Interestingly, these bands show a significant degree of dispersion along ΓX and ΓA. In terms of band widths they even exceed those of the TA bands, for which they only amount to 0.6-0.8 THz.
Generally, the difference in band widths of the LA and TA bands is relatively large compared to, e.g., tetracene or pentacene. Especially in ΓZ-direction (= $\mathbf{b}^*$), the lowest TA band shows a considerably smaller band dispersion and width than the LA band. This is similar to fluorene, where this was an effect of the layer-like crystal packing. Here, the

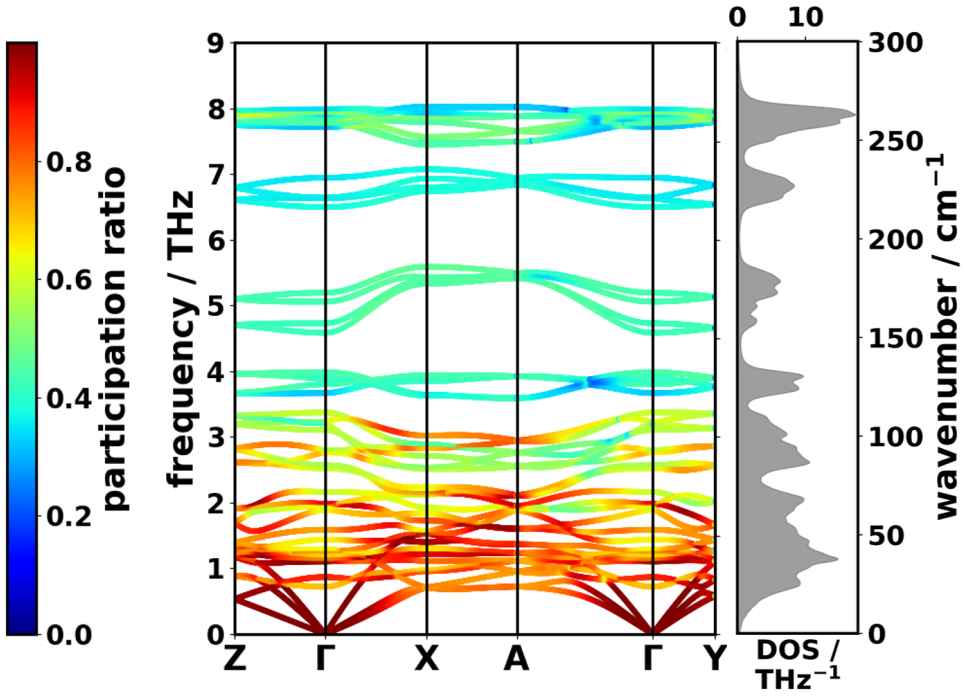

Fig. 5.21.: PBE/D3-BJ-calculated phonon band structure (coloured according to the mode participation ratio) and DOS of pyrene (Py).

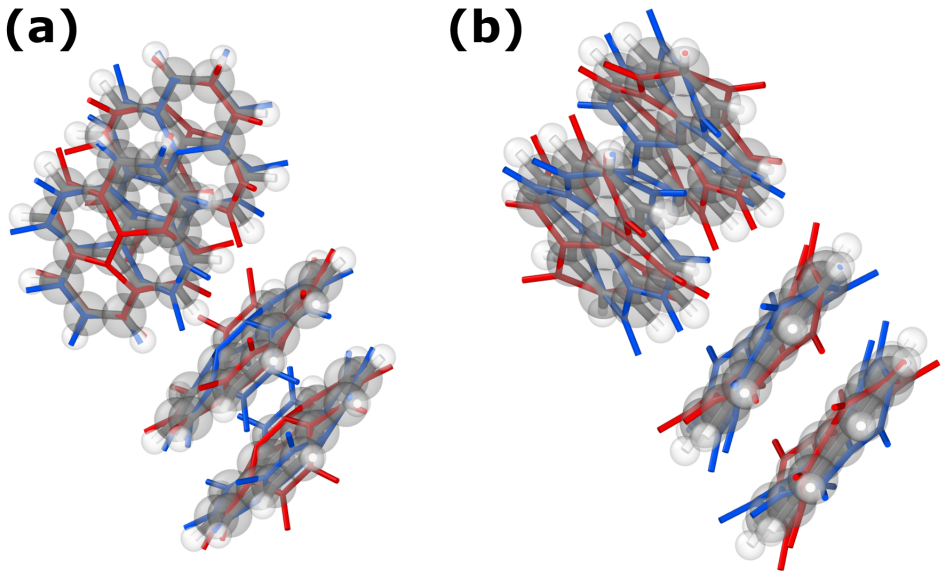

Fig. 5.22.: Γ-point displacement patters of the (a) trampoline modes at 6.5 to 7.0 THz and (b) intramolecular torsions at 4.5 to 5.5 THz in pyrene. The red and blue wireframe structures correspond to the positive and negative amplitudes of the vibration, respectively.

atomic displacement - i.e. the phonon polarisation - is oriented such that the molecules move nearly within their original planes, which is energetically not so unfavourable as motions effectively altering the packing distance between the molecules.
Due to the consistent, relatively small bandwidths of the TA bands, the DOS in the low-frequency regime shows a parabolic Debye-like shape up to ~0.8 THz. After that point, several peaks are present in the DOS as a result of the densely lying intermolecular bands (especially around ~1.2 THz). By means of visual inspection of the corresponding phonon animations, one can see that the entire intermolecular regime is condensed in the spectral region below ~3.4 THz, with no intramolecular bands appearing in that range. This observation can also be made from the PR-coloured band structure: the bands with the highest mode PRs can be found for the lowest 24 bands, while all (intramolecular) bands above are typically more localised. Based on the conclusions drawn from the discussion about the oligoacenes, the dominant effect for shifting (most of) the frequencies in the intermolecular regime appears to be the influence of the molecular mass rather than the interaction strength. Also here, the higher molecular mass (202.25 amu, which lies between the mass of anthracene and tetracene) is hypothesised to be responsible for condensing the intermolecular region to the observed frequency range and, thus, separating the inter- and intramolecular regimes.

5.1.8. Quinacridone

The most complex organic semiconductor discussed in this thesis is quinacridone. Not only does it have the same number of atoms per molecule as pentacene, but also exists in several polymorphic arrangements, three of which are covered here and are shown in Fig. 5.23 along with their corresponding first Brillouin zones. Moreover, the molecular packing in these phases are more complicated than in the OSCs discussed so far because the molecules do not only interact via van der Waals interaction but also via hydrogen bonds. In spite of the fact that the α-phase only has one molecule per unit-cell - a feature that none of the discussed systems so far has shown - the analysis is complicated by the triclinic Bravais lattice. Conversely, both remaining phases (β and γ) exhibit a monoclinic crystal system, but contain two molecules per unit-cell. Note that both phases show extreme ratios of lattice parameters: in γQ, the ratio between the longest and the shortest lattice vector amounts to roughly 3.5, while in βQ one even finds a ratio of ~7.6. Consistently, the first Brillouin zones have a distinctly anisotropic shape.

Looking at the crystal structure of βQ, one might immediately expect that the two inequivalent molecules per unit-cell arrange in such a way that each of them and their respective periodic replica lie almost perfectly in common planes (this is shown more clearly in the Appendix A.6). Additionally, one can observe a structural similarity to fluorene: the crystal can again be decomposed into two inequivalent repeated layers (with boundaries approximately parallel to the plane defined by the lattice vectors **a** and **b**, see Appendix A.6), with the long molecular axes of the molecules being roughly perpendicular to those layers. As in fluorene, the layers are rather strictly separated from each other so that a large interlayer interaction is less likely. Therefore, similar effects are to be expected in the phonon band structure as for fluorene. In addition to

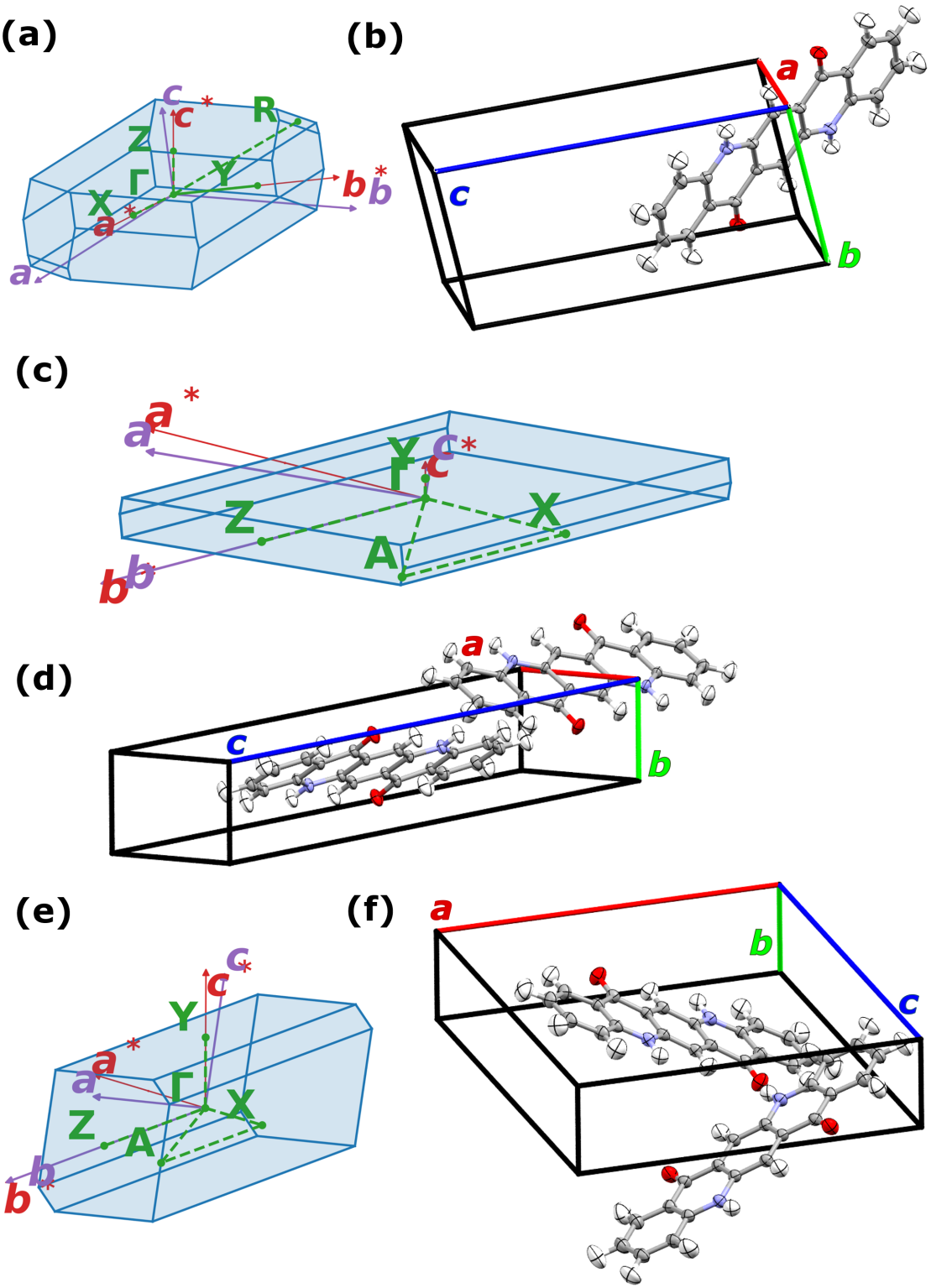

Fig. 5.23.: (a,c,e) First Brillouin zones including the high symmetry points used in the band structure diagrams and (b,d,f) real-space unit-cell of the α-, β-, and γ-phase of crystalline quinacridone, respectively (αQ, βQ, γQ). The atoms are drawn in terms of the thermal ellipsoids for a probability level of 50 % and a temperature of 0°C.

the anisotropy of the unit-cell, also the interactions are supposed to be relatively anisotropic [150]: within the layers, the dominant interaction is caused by the π-stacking of the relatively closely packing molecules in one direction (close to lattice vector **a**) and hydrogen bonds due to the polar oxygens in the molecule in the other direction. Conversely, the layers are loosely coupled by van der Waals interactions.
In γQ, the molecules pack in a "hunter fence" fashion (see Appendix A.7), which can most easily be seen by looking at the crystal along lattice vector **c**. This perspective reveals that the molecules mimic the typical rhombic pattern of a hunter fence. Again, this crystal structure can be considered layered, although the polar moieties in the quinacridone molecules are directed towards the layer boundaries. Thus, one expects the layers to be coupled to a significant extent also by hydrogen bridges.
A first interesting difference between the three phases can be seen in the DOS in the very low frequency region. In contrast to the DOS in αQ, which shows a typical parabolic onset up to ~1 THz, the DOSs of the other two systems rather reminds of a linear increase - especially in the β-phase. It can be shown easily that in three dimensions, a dispersion relation like $\omega(q) \propto q^{3/2}$ would result in a linear DOS. This unusual q-dependence (linear for acoustic bands, quadratic for entirely free phonons) might be explained by the fact that many acoustic bands (in particular in βQ) show a nearly quadratic dispersion near Γ such as the TA bands along ΓZ, as it is often observed for two-dimensional systems such as graphene [151]. The observed dispersion of those bands is, thus, supposed to be related to the layered structure of βQ, since within the layers, parallel planes can be discerned, in which entire molecules lie and couple to each other by means of hydrogen bonds forming (quasi-)two-dimensional sheets (see Appendix A.6).
This precise alignment of molecules in certain planes is not exactly fulfilled in γQ. That circumstance is most probably also the reason why the band dispersion of the acoustic bands is rather linear than quadratic for most of the bands except for the lowest TA band along ΓY. Here, the linear behaviour of the DOS near zero frequency might rather be a coincidence determined by the relatively broad variation in band widths of the acoustic bands: nearly every band hits the boundary of the first Brillouin zone at a different frequency such that the increase in the DOS due to the flattening of the band near the boundary of the first Brillouin zone happens at many frequencies. These individual contributions add up to this more linear shape of the DOS. In other words, the anisotropic shape of the crystal structure leads to notable deviations from the (isotropic) Debye-like behaviour of the acoustic bands.
In general, the band widths of the acoustic bands are relatively small in γQ compared to the other phases, where they sometimes amount to more than 3 THz. However, this might also be a consequence of the relatively densely lying bands in the low-frequency region causing several avoided crossings and, thus, diminishing the band widths.
For all three systems, the first notable band gap is found slightly above ~4 THz. However, this frequency range cannot be unambiguously identified as being the intermolecular regime. In particular, there are only three (rotational) intermolecular modes for the α-phase as there is only one molecule per unit-cell. This means that at Γ, all molecules in the crystal oscillate equivalently, and such RIMMs as for the other systems with more molecules per unit-cells cannot be observed. In both the other phases, one can find

bands with particularly high PR below ~4 THz. The discrimination between inter- and intramolecular modes is, however, much more involved than in any of the previously discussed systems. Intermolecular modes are often found at very low frequencies, significantly overlapping in spectral regimes with other intermolecular motions. For example, the high-PR band found at 1.07 THz at Γ in the β-phase corresponds to the rigid oscillation of the two layers with respect to each other. The two bands directly above are already two low-PR intramolecular bands (at 1.46 and 1.52 THz at Γ), which are related to first- and second-order bending of the molecules. A further complication regarding the strict separation of inter- and intramolecular regimes is the fact that most of the modes below ~3 THz show an extraordinarily high degree of dispersion. Therefore, bands belonging to one regime or the other cross, and, thus, blur the spectral boundaries significantly.
Also in γQ, the separation according to the nature of the observed phonon modes is complicated by relatively low-lying intramolecular modes such as a (first-order) bending mode at 1.84 THz at Γ or even torsions around the long molecular axes at 2.44 THz. In contrast to βQ, the band dispersion is, however, considerably decreased. One can even identify a pronounced region of flat bands near 1 THz, which happen to coincide with the frequency at which several acoustic bands hit the boundary of the first Brillouin zone. This can be seen as a peak in the DOS at that region.

Since already in the low-frequency region, a detailed discussion of the optical bands would go beyond the scope of this thesis, it should be briefly commented on the anisotropy of the acoustic band dispersion in the following paragraph. In αQ, the slope of the LA band near Γ is relatively similar in all (shown) high-symmetry directions, although the LA band in ΓZ-direction is slightly steeper than in the other directions, in spite of the band width being strongly reduced due to the shorter corresponding length in reciprocal space. The reason for this slight increase in band dispersion in that direction might be ascribed to the fact that this direction is closer to the long molecular axis than the other high-symmetry directions. Therefore, to make compression waves propagate in this direction, many strong covalent bonds have to be stretched and compressed, which is, of course, energetically more unfavourable than displacing the molecule in directions which are dominated by non-bonding interactions. Conversely, the ΓX direction is close to being perpendicular to the planes in which the molecules lie. Thus, the intermolecular interactions are supposed to be dominated by non-bonding interactions such as van der Waals interactions and the interactions between the π-clouds of the molecules. Both the LA and the TA band higher in frequency contain intermolecular motion in which the molecules approach each other close to the plane normal, while the lower TA band involves a slipping motion roughly in the plane of the molecules along the molecular axis. The latter shows a notably reduced band dispersion suggesting that it is more favourable to only slip the molecules (with large parts of the π-interactions remaining the same) instead of effectively reducing/increasing the distance in the π-stacking direction. For the same reason, the higher TA band in ΓY-direction shows a similar dispersion as the lower TA band along ΓX, since the corresponding motion contains such a slipping displacement. The LA bands in this direction involve periodic compressions of the crystal nearly along the short molecular axis, in which the sum of non-bonding interactions

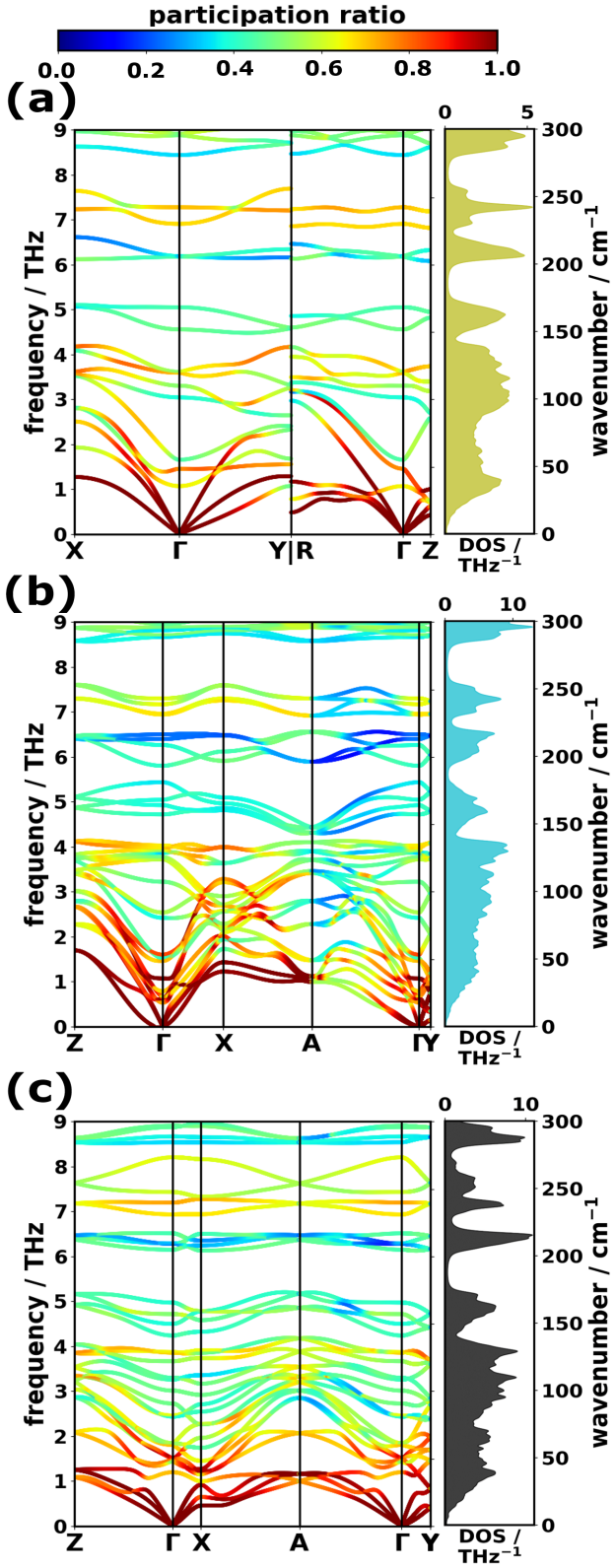

Fig. 5.24.: PBE/D3-BJ-calculated phonon band structure (coloured according to the mode participation ratio) and DOS of (a) α- (αQ), (b) β- (βQ), and (c) γ-quinacridone (γQ).

(H-bonds, van der Waals) result in an effective stiffness similar to the one governed by the π-interactions in ΓX. Finally, the low-dispersion TA band along ΓY again involves molecular slipping, which does not happen in the direction of the H-bonds and is, thus, only determined by the van der Waals interactions. Hence, the effective stiffness is much lower, consistent with the smaller band dispersion.
A very similar type of motion is also responsible for the unusual band dispersion of the lowest TA band in βQ along ΓZ. The effective interactions are basically only determined by the weak van der Waals forces of only a small number of atoms. Thus, the aforementioned layers consisting of periodic replica of one of the two molecules per unit-cell, can slip with respect to each other with hardly any hindrance (similar for the TA bands in ΓY). Besides the typically low band dispersion of the TA bands near Γ, the LA bands are extraordinarily steep in all high-symmetry directions suggesting a high resistance against compressive deformation.
Also for γQ, the slopes of the acoustic bands seem to be relatively similar, with the LA bands being slightly steeper in ΓY, which is close to the direction perpendicular to the "hunter fence" and, thus, the short molecular axes. The reason for this additional degree of dispersion might be the extra intermolecular interactions determined by the H-bonds in that direction. One can also observe a small difference in band slope of the LA bands in ΓX- and ΓZ-direction, with the latter being somewhat decreased compared to the former. This is most probably again a consequence of the fact that along ΓX (roughly parallel to **a**), more covalent bonds in the molecules can be found, which have to be compressed for the propagation of acoustic waves with $\mathbf{q} \neq 0$. In contrast, the stacking in ΓZ direction (corresponding exactly to the direction of **b**) is dominated by van der Waals and π-interaction and less by the covalent bonds.
The example of the three phases of quinacridone emphasises how important the molecular packing in an organic crystal is for determining its phonon properties. The resulting properties derived from the phonon band structures are quantitatively discussed in the next section.

5.2. Properties Derived from the Phonon Spectrum

5.2.1. Group Velocities

Prior to the discussion of thermodynamic phonon properties depending also on the higher-lying intramolecular phonons, the band dispersion shall be briefly discussed in terms of the associated group velocities as a measure for the speed at which phonon wave packages transport heat in the crystal. Since every phonon mode (characterised by two quantum numbers: band index n and wave vector $\mathbf{q}$) can be assigned a group velocity, which is a three-component vector, a detailed discussion of the Cartesian components is considered too complicated. Thus, the group velocities have been analysed in terms of their (vector-)norms. Additionally, it is useful to relate the group velocities to the frequency of the corresponding phonon modes to assess how relevant they are (lower frequencies are thermally occupied already at lower temperatures). The group velocities of the discussed organic semiconductors as a function of frequency are shown

in Fig. 5.25 for the oligoacenes and in Fig. 5.26 for the remaining systems. Unfortunately, these scatter plots fail to convey a quantitative picture of the density of phonons with certain group velocities. Therefore, an averaged group velocity according to the following equation is plotted as well:

$$\langle v_g \rangle_p (\omega) = \frac{\sum\limits_{\lambda=(n,\mathbf{q})} p(\omega_\lambda|\omega) v_{g,\lambda}}{\sum\limits_{\lambda=(n,\mathbf{q})} p(\omega_\lambda|\omega)} \tag{5.4}$$

In Eq. (5.4), the function $p(\omega_\lambda|\omega)$ is a weighting function (with a parameter (vector) ω) that can be chosen arbitrarily. Here, it has been chosen to be (i) a step function with $p(\omega_\lambda|\omega) = 1$ if ω_λ is below a given cutoff frequency ω and $p(\omega_\lambda) = 0$ above, and (ii) a window function ($p = 1$ for frequencies between two cutoff frequencies $\omega_{1/2}$, $p = 0$ everywhere else). While case (i) corresponds to a quantity that can be referred to as "running mean", case (ii) represents the average group velocity in a small frequency window with a width of 0.1 THz ("window mean").
One notices that the group velocities near 0 THz (corresponding to the acoustic bands near Γ) are typically the largest. They correspond to the (anisotropic) speed of sound in the respective materials and range from ~33 THzÅ (=3300 ms^{-1}) in 1c_m to ~40 THzÅ (=4000 ms^{-1}) in 5c. Additionally, Fig. 5.25 shows that for 1c_m, 1c_o and 2c, the running mean of group velocities starts at about 20 THzÅ and drops below 10 THzÅ considering all modes in the low-frequency region. For 3c, 4c, and 5c, this is insofar slightly different as the running v_g mean increases from a notably smaller value at small frequencies to peak values at ~0.5 THz which are somewhat higher (lower) in 4c and 5c (3c) than for the smaller oligoacenes. Considering the entire low-frequency regime (i.e. looking at the running mean at the upper limit of the shown frequency range), all systems show comparable values of the average group velocity of ~8 THzÅ, suggesting that, on average, phonon transport is comparably fast in all oligoacenes. Conversely, the most notable differences between the systems occur in the very low-frequency region (below 2 THz). Interestingly, anthracene seems to represent some kind of minimum in terms of the (average) group velocities amongst the studied oligoacenes in this very limited region which is dominated by intermolecular interactions. This could possibly be rationalised with the following argument based on the simple expression for the group velocity in a one-dimensional linear chains of atoms with mass m, coupled by springs with force constant k, separated by the lattice constant a [134]:

$$v_g = \pm a \sqrt{\frac{k}{m}} \cos\left(\frac{qa}{2}\right) \tag{5.5}$$

Although, strictly speaking, Eq. (5.5) is only valid for the acoustic band of a one-dimensional chain, it still helps to emphasise the basic concept that for group velocities, an additional length scale is necessary to obtain the correct units: in general, the group velocities are the $\mathbf{q}$-gradients of the frequencies ($v_{g_i} = \partial\omega/\partial q_i$). Since the dimension of v_g is length/time, while it is 1/time for ω, a proportionality between ω and v_g must include

the lattice parameter(s) as the length scale. In other words, the group velocities must include products of length-quantities (lattice vectors) and frequencies (or band widths). As it has already been discussed in Sec. 5.1, the frequency scales for the intermolecular modes show the tendency to rather decrease with increasing molecular size of the oligoacenes: the increasing interaction strength is typically outweighed by the increasing mass (see Fig. 5.17). Therefore, the frequency factor in this general consideration of the group velocity decreases, while the lattice parameters (length scales) increase with the size of the oligoacene. Thus, a minimum at a certain molecular size might appear, which could be (close to) anthracene.
Interestingly, the window v_g mean shows some distinct regions above ~2 THz for 4c, 4c and 5c which exhibit increased (average) group velocities suggesting that also low-frequency optical bands could be promising pathways for transporting thermal energy through the crystal.

In the same way, the group velocities for the phonons sampled on discrete meshes, the running and the window means of group velocities are shown for fluorene, pyrene, α-, β-, and γ-quinacridone in Fig. 5.26. The overall situation for fluorene is relatively similar to that for the oligoacenes: the highest group velocities are found below ~1 THz (up to 39 THzÅ), with the running mean dropping to roughly 7 THzÅ at the right end of the shown spectral region. The optical bands present in this low-frequency regime do not show high group velocities. In pyrene, however, the latter statement does not apply. In this system, one observes large group velocities for the optical bands between ~4.5 and 5.5 THz. As discussed before, these modes correspond to intramolecular torsions of the aromatic molecules (see Fig. 5.22(b)), and they can be clearly seen in a peak of the window mean in this frequency range. In contrast to the peak of similar height at ~2.2 THz, the group velocities are much less spread suggesting that all the bands in that region show a high dispersion. Although the running mean converges to about the same value as in fluorene at 10 THz, the optical bands show much more features than the more monotonically decreasing behaviour of the group velocities with the frequency in fluorene.
In terms of their group velocities, the three polymorphs of quinacridone cold not be more diverse. While in αQ, the group velocities at low-frequency start already at a moderate level, some modes at slightly elevated frequency show group velocities higher than in all previously discussed organic crystals for a comparable frequency (> 50 THzÅ). The window v_g mean shows, however, that the average group velocity per frequency interval is much lower, although both the running and the window v_g mean stay approximately constant (amounting to roughly 20 THzÅ) up to frequencies greater than 2 THz. This observation is really astonishing because both averages typically tend to decay relatively rapidly with increasing frequency. Here, the extraordinarily large band widths of the acoustic bands (and those parts of them after potential avoided crossings) retain a constant high level of group velocities over a relatively large frequency range. In total, the average group velocity considering all modes is slightly higher (> 10 THzÅ) than in all other systems.
Consistent with the band structures, βQ shows extremely high group velocities at low

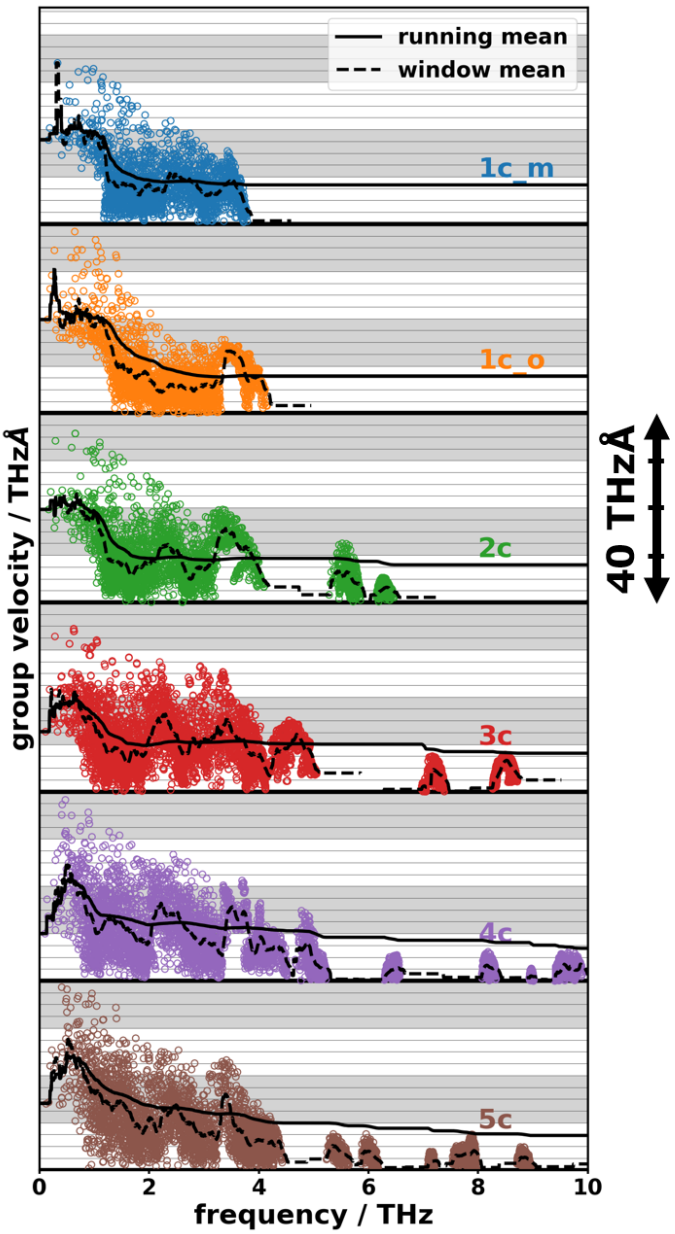

Fig. 5.25.: Group velocities of the phonon modes sampled on the discrete **q**-meshes in Tab. 3.3 for monoclinic (1c_m) and orthorhombic benzene (1c_o), naphthalene (2c), anthracene (3c), tetracene (4c) and pentacene (5). Each dataset has its own zero-line (horizontal, thick black lines), while the alternating grey-white shading serves as guide to the eyes indicating a group velocity magnitude of 10 THzÅ each, which is also shown by the scale bar on the right hand side. The solid and dashed curves represent the running mean considering all modes up to the shown (cutoff) frequency and the mean in a certain moving frequency window (0.1 THz width), respectively. For details see main text.

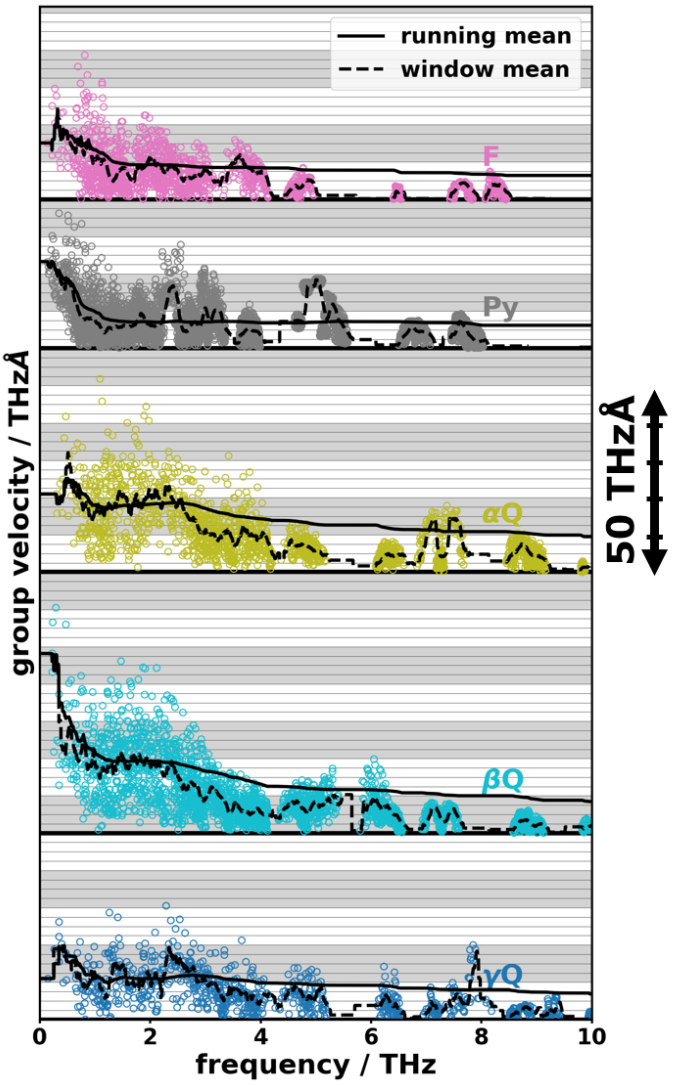

Fig. 5.26.: Group velocities of the phonon modes sampled on the discrete **q**-meshes in Tab. 3.3 for the fluorene (F), pyrene (Py), and the quinacridone polymorphs (α-, β-, and γQ). Each dataset has its own zero-line (horizontal, thick black lines), while the alternating grey-white shading serves as guide to the eyes indicating a group velocity magnitude of 10 THzÅ each, which is also shown by the scale bar on the right hand side. The solid and dashed curves represent the running mean considering all modes up to the shown (cutoff) frequency and the mean in a certain moving frequency window (0.1 THz width), respectively. For details see main text.

frequencies (> 60 THzÅ) - even higher than in αQ. These initial extremes drop, however relatively fast to moderate level, with only a few high-v_g modes being present up to frequencies beyond ~2 THz. The strong anisotropy and the spectral overlap of inter- and intramolecular modes results in a relatively large spread around the window and the running v_g mean, which - after the initial drop - remains at a level comparable to αQ in that frequency range. In spite of the unprecedented magnitude of the group velocities in the very low-frequency region, the group velocities are notably smaller for the optical bands above ~7 THz than in the α-polymorph. This is probably the reason, why the final value of the running v_g mean is somewhat lower than in αQ.
The γ-polymorph shows consistently smaller values of the group velocities than the other two for frequencies up to ~5.5 THz (max. ~30 THzÅ). Also the spread around the (window) mean is notably reduced compared to α- and βQ. Except for the first peak below 1 THz due to the acoustic bands, the running v_g mean essentially stays constant throughout the entire low-frequency regime, and reaches a value of ~8 THzÅ in the end. The overall notion of the group velocities is that they are (constantly) rather low, which also applies to the optical bands - with some exceptions such as the pronounced peak near 8 THz.

In order to facilitate the quantitative direct comparison between the systems, the running means of group velocities are replotted in Fig. 5.27. Several conclusions can be drawn from this plot. The upper panel emphasises that (i) the orthorhombic benzene phase shows higher (average) group velocities than the monoclinic phase up to ~2.5 THz (in line with the reduced density of avoided crossings due to the higher symmetry), where the running mean of the monoclinic phases exceeds it due to the lower group velocities of the increased number of optical (intermolecular) bands. This is natural, as these bands typically show slightly smaller band widths. (ii) Pentacene shows the largest running v_g mean of all the oligoacenes up considering all modes up to ~4 THz. (iii) Anthracene displays the smallest height in the peak around 1 THz suggesting the smallest (average) low-frequency group velocities. (iv) The running means of the larger oligoacenes keep decaying with frequency, while the corresponding graphs for the crystals containing smaller molecules stay nearly constant. This observation is only a consequence of the fact that in 3c, 4c, or 5c the intramolecular modes with small group velocities are already included in the averaging to some extent, while no or few new (intramolecular) phonons enter the averaging for 1c and 2c due to the larger separation of the two regimes.
The lower panel of Fig. 5.27 stresses the extraordinarily large running v_g mean in βQ: starting above ~48 THzÅ, it relatively quickly drops (below ~1 THz) to essentially the same value as in αQ, both being larger as any of the oligoacenes. The running v_g mean of γQ is considerably lower than that of the other two polymorphs. In fact, it is more similar to 4c and 5c rather than to αQ and βQ. Finally, the running v_g mean of fluorene and pyrene are even lower, with that of Py being the smallest amongst all studied systems (except for the frequencies below ~0.6 THz) followed by fluorene with the second-smallest overall running mean. In the case of pyrene (Py), the bands show a minor degree of dispersion, with the lattice constants not being extraordinarily much larger than for 4c or 5c. Both contributions result in (on average) small group velocities so that, effectively, phonon transport is expected to be the least efficient in this system. For fluorene (F),

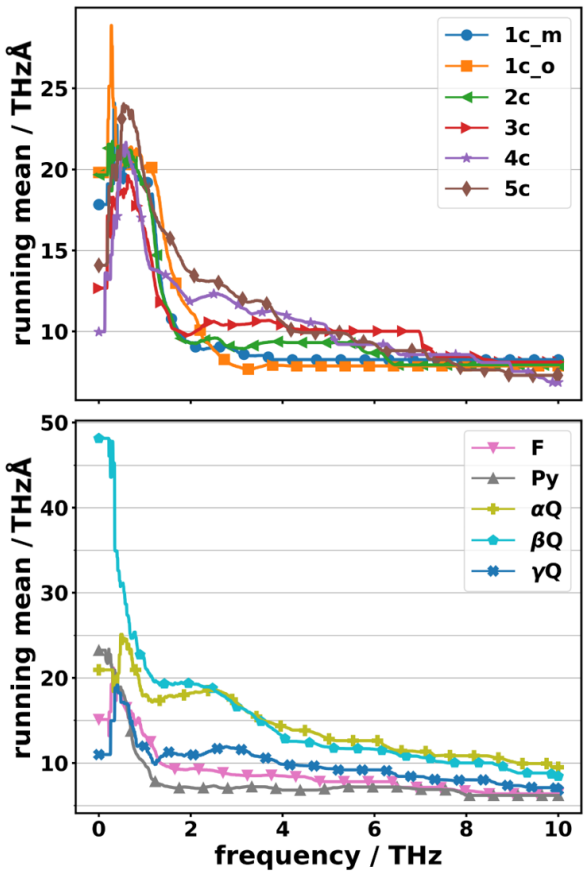

Fig. 5.27.: Direct comparison of the running means of group velocities considering all modes up to the shown (cutoff) frequency. The symbols only serve as guides to the eye and do not represent the actually calculated data points, which lie much more densely. The legend uses the consistently used abbreviations for the studied systems as introduced in Tab. 3.1.

the negligibly higher overall mean of group velocities in the low-frequency region can be ascribed to (i) relatively flat bands occurring already at low frequencies due to the layer-like packing of the molecules in the unit-cell and (ii) the early presence (=low frequencies) of flat intramolecular bands. Therefore, in terms of the averaged group velocities, Py and F promise to be bad choices when efficient transport via phonons is needed (unless the phonon lifetimes in these systems are surprisingly much higher than in all others).

5.2.2. Densities of States

In this section, the phonon densities of states (DOSs) of the systems, for which the entire band structure was computationally accessible, should be briefly discussed. Starting with 1c_m and 1c_o, one can see a clear separation (~4-12 THz) between the low-frequency intermolecular modes and the high-frequency intramolecular modes with only little dis-

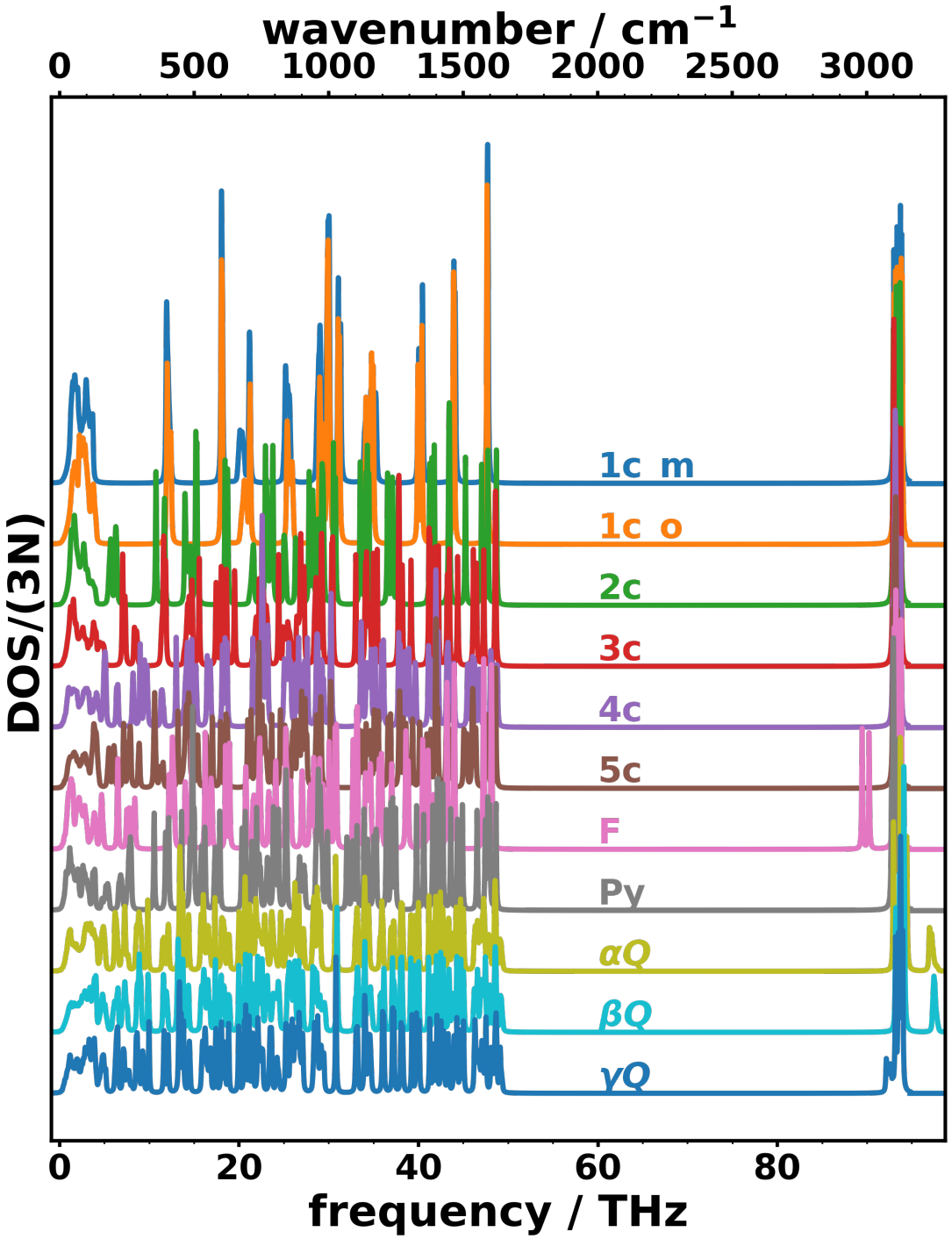

Fig. 5.28.: PBE/D3-BJ-calculated phonon densities of states (DOS) as a function of phonon frequency for the studied molecular crystals (according to the abbreviations introduced in Tab. 3.1). Every DOS has been normalised individually by the respective number of degrees of freedom per unit-cell.

persion. Thus, these modes appear as sharp peaks in the DOS. With larger molecule size, this distinct gap is increasingly filled with (intramolecular) bands. This also applies to the smaller gaps between the well-resolved intramolecular peaks in the benzene polymorphs: the more complex the molecules become, the more all gaps are filled with densely packed peaks originating from the increasing number of intramolecular modes. In fact, the high-frequency intramolecular regime grows very rapidly in peaks, whereas the low-frequency intermolecular region keeps its number of peaks for a constant number of molecules per unit-cell: while the former only consists of $6Z$ modes (with Z being the number of molecules per unit-cell) the latter encompasses $3N - 6Z = 3N(1 - 2/n_{mol})$ bands (with N being the number of atoms per unit-cell and $n_{mol} = N/Z$ the number of atoms per molecule). Thus, if Z is fixed, the number of intramolecular modes grows proportional to $3N$, while the number of intermolecular bands stays the same. Additionally, it can be shown that the number of the former outweighs the latter always, provided that the molecule in question consists of more than 4 atoms. Thus, the high-frequency phonon spectrum of pyrene and fluorene is particularly dense. However, due to the fact that both systems contain only two atomic species, the possible frequencies are limited to some extent. The nitrogen and oxygen in quinacridone, however, introduce much more variation in the detailed chemical environment within the molecule such that even a larger spread of intramolecular frequencies becomes possible.
Interestingly, the different polymorphs of a given molecule (1c_m and 1c_o or the polymorphs of quinacridone) yield nearly exactly the same high-frequency spectrum emphasising once more that these vibrations are more related to the molecules than to the exact packing in the unit-cells. The most pronounced deviation from this observations are the highest peaks in γQ (see discussion below).
For all systems, one can observe a large band gap between ~50 THz and ~92 THz (~88 THz in the case of fluorene) separating the motions involving the carbon atoms, with the highest frequencies corresponding to modes in which the molecules experience in-plane deformations, from the high-energy C-H stretching vibrations. One notices that the lower edge of this large band gap is slightly decreased for the benzene polymorphs compared to the remaining systems, whereas one observes a somewhat increased lower edge for the quinacridone polymorphs. The reason for the lower band edge in benzene is the fact that all carbons are equivalent (disregarding the crystalline environment which, for intramolecular modes, can be done as an approximation) with two carbon and one hydrogen nearest neighbour. In the larger oligoacenes, there are, however, also carbon sites which are covalently bonded with three carbon atoms and no hydrogen. As the C-C force constant is (somewhat) higher than the C-H force constant (see the discussion in Sec. 4.3.1, Fig. 4.23), participation of those carbon atoms in the vibrations lead to slightly higher frequencies. Conversely, it is the slight increase in the force constants caused by the nitrogen and, to a smaller extent, also by the oxygen in the quinacridone molecules which leads to the somewhat increased lower band edge in those three systems. There are two reasons why the C-H stretching vibrations show so high frequencies: (i) the moving atoms - i.e. the hydrogen - is very lightweight and (ii) the bonding potential is relatively strong and results in a high force constant comparable to that of a C-C bond. Because of the large number of C-H bonds in the considered molecular crystals,

there are many nearly equivalent C-H-stretching bands resulting in high, sharp peaks at 92-93 THz. In fluorene, two peaks at lower frequencies can be found. The reason for this observation is that only in fluorene there are sp^3-hybridised carbon atoms bonded to two hydrogen atoms. These two atoms undergo a symmetric (89.4 THz at Γ) and an anti-symmetric (90.2 THz at Γ) stretching motion, which are both lower in frequency than the C-H stretching found in aromatic (sp^2-hybridised) moieties.
Finally, one sees a notable difference in the high-frequency ends of the spectrum of γQ compared to the other two quinacridone polymorphs: while αQ and βQ display peaks at ~97 THz (corresponding to N-H stretching motion), these peaks seem to be missing in the γ-phase. At second glance, one recognises the smaller peaks at 92.1-92.7 THz, which, according to the animations of the corresponding vibrations, are the supposedly missing N-H stretching modes. Interestingly, they lie significantly lower in γQ than in the other polymorphs. This must be a direct consequence of the hunter-fence packing via the H-bridges: the covalent bonding distance between N and H amounts to 1.04 Å, while the hydrogen and (partially negative) oxygen from the neighbouring molecule are only 1.70 Å apart. The electrostatic interaction obviously distorts the potential energy surface of the hydrogen coordinates in such a way that its curvature (i.e. the force constants) becomes significantly smaller. More graphically speaking, the oxygen from the neighbouring molecule exerts such a strong force on the hydrogen that the effective (covalent) N-H bonding potential is reduced. This is possible due to the nearly linear alignment of the three atoms (the N-H-O angle amounts to 165.6°). Although a similar geometrical arrangement can be observed for αQ, the N-H bonding distance is slightly shorter (1.04 Å), the H-bonding distance between O and H is somewhat larger (1.81 Å), and also the angle between the three atoms is reduced by a few degrees (159.2°). These differences are obviously enough to considerably (by more than 4 THz) shift the associated N-H stretching modes. Notably, these modes offer a much more convenient way to identify the γ-polymorph by means of vibrational spectroscopy other than conducting experimentally more challenging low-frequency measurements.

5.2.3. Thermodynamic Properties

Based on the equations from statistical physics derived for a (grand) canonical ensemble (see Sec. 2.4), one is able to calculate the contributions of the phonons to various thermodynamic properties. It should be stressed again that in the (grand) canonical ensemble the volume is constant and the (Helmholtz) free energy F is the thermodynamic potential from which all other macroscopic thermodynamic quantities can be calculated by partially differentiating F. The discussion will, thus, focus on the free energy being the basic quantity from which, theoretically, all further thermodynamic properties can be computed. However, it is more instructive to start the discussion with the phonon contribution to the heat capacity (at constant volume), C_V. The reason for this is that at low temperatures only low-frequency modes enter the expression for C_V, with the relevant spectral region being extended with temperature, while for F already at 0 K the high-frequency intramolecular modes contribute in terms of the zero-point energy (ZPE) of the harmonic oscillators (which is a quantum-mechanical effect).

In contrast to the methodological benchmark for naphthalene (see Sec. 4), here, different systems (with different numbers of atoms per unit-cell, N, and different numbers of molecules per unit-cell, Z) are compared. Thus, it is necessary to not only look at the heat capacity per unit-cell normalised by $3N$ and the Boltzmann constant as before, but also to consider the heat capacity per formula unit (i.e. per molecule) - as it would be measured in an experiment. This is most conveniently done by converting the heat capacities to the unit J/mol/K.[48]

Fig. 5.29 shows the heat capacities in the two mentioned ways. In the upper panel, which displays the normalised heat capacity per unit-cell (corresponding to the heat capacity per degree of freedom), one can see that there are hardly any differences between the relatively diverse systems. The most notable difference is observed for the two benzene polymorphs, for which the temperature dependence of the heat capacity shows a distinct shoulder above all other curves for temperatures between ~50 an 150 K. The reason for this feature is essentially the small number of atoms per unit-cell. At these very low temperatures, basically only the intermolecular modes contribute to the heat capacity. In case of 1c_m (1c_o), this amounts to a fraction of 12/72=1/6 (24/144=1/6) of all modes, which is the value $C_V/(3N/k_B)$ reaches for both polymorphs at roughly 118 K. For all the other crystals with more atoms per unit-cell, the ratio of intermolecular modes to the total number of modes is much smaller, thus, leading to a notably smaller heat capacity at very low temperatures. A zoom into the temperature range up to 150 K is shown in the Appendix in Fig. A.10. For a similar reason, 2c and F show the next-highest normalised heat capacity after benzene up to ~100 K. Considering only the intermolecular modes, this would correspond to the fraction 12/108=1/9 in naphthalene and 24/276=2/23≈ 0.087 in fluorene. In the former case, this fraction roughly agrees with the normalised heat capacity at about 80 K, whereas, in the latter case, this estimation results in a slight overestimation of the heat capacity. For fluorene, the comparably rapid increase in the heat capacity is a result of the low-lying (first) intramolecular bands. Including those (eight) bands in the estimation yields $(24 + 8)/276 \approx 0.116$, which is reached by $C_V/(3Nk_B)$ at ~88 K. To sum up, the high density of states at low frequencies in fluorene is responsible for the normalised heat capacity being comparably large.

While most of the other systems (3c, 4c, 5c, and Py) show essentially the same temperature behaviour, there is one further peculiarity in the data. Interestingly, above ~200 K, the normalised heat capacity of all three polymorphs of quinacridone is larger than for all other systems. The reason for that is clearly the chemical structure of the molecules and can be rationalised as follows. Due to the fact that quinacridone contains two oxygen atoms instead of two carbons which would have needed a bond to a hydrogen atom each, effectively, in quinacridone there should be 2×3 fewer (high-frequency) C-H modes per molecule compared to e.g. pentacene, which consists of the same number of atoms (per molecule). Instead, these high-frequency modes are replaced by modes

[48] For the sake of comprehensibility, the normalised heat capacities per unit-cell, $C_V/(3Nk_B)$, are multiplied with a factor $3Nk_BN_A/Z$, with N_A being the Avogadro constant and n being the number of atoms per primitive unit-cell.

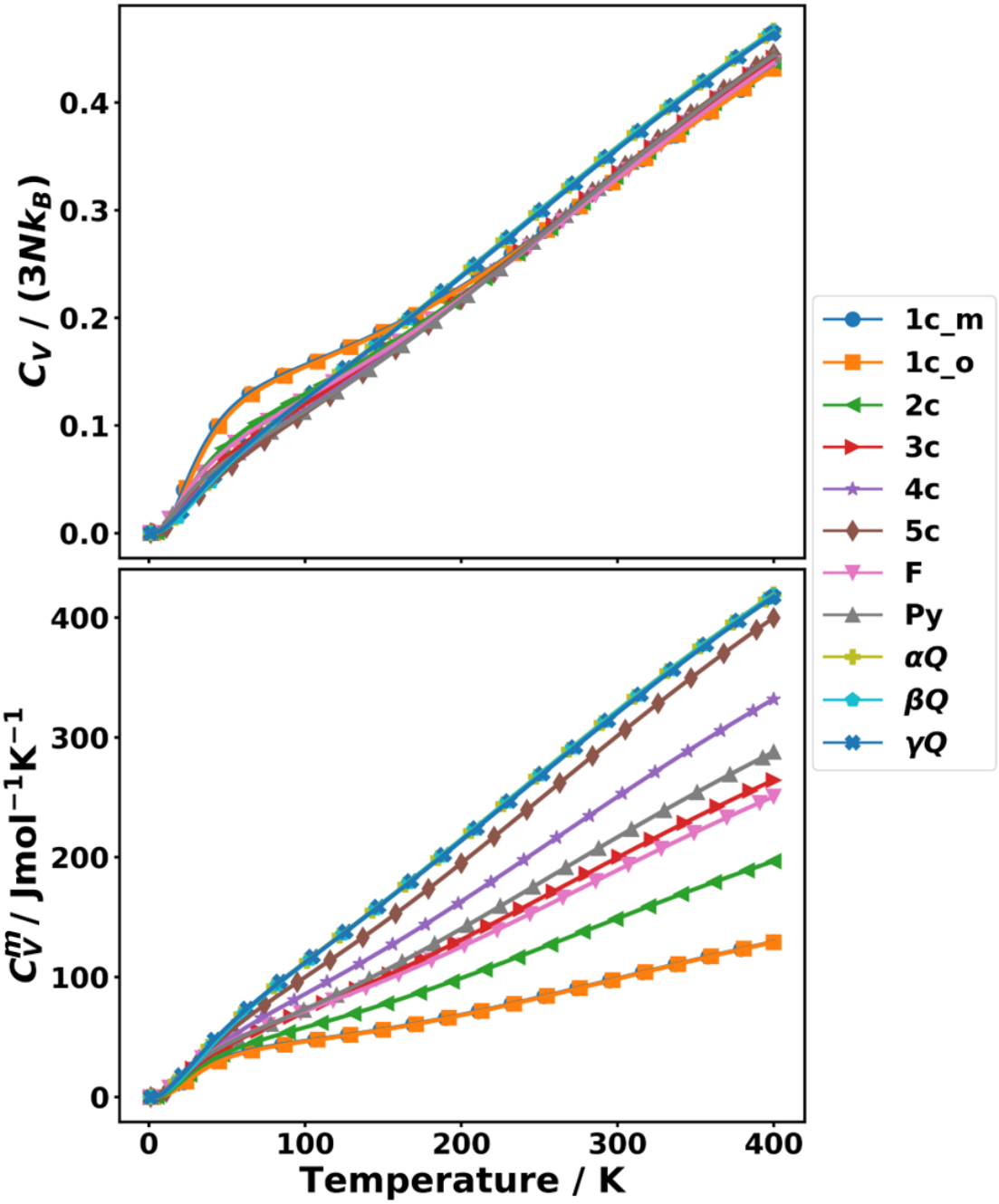

Fig. 5.29.: Phonon contributions to the heat capacities (C_V) as a function of temperature for the studied molecular crystals (according to the abbreviations introduced in Tab. 3.1). The upper panel shows the dimensionless phonon heat capacity per degree of freedom (= the heat capacity per unit-cell, C_V, normalised by the number of bands, $3N$, and the Boltzmann constant, k_B) so that $\lim_{T\to\infty} C_V/(3Nk_B) = 1$. The lower panel shows the heat capacity per mole of the molecule, C_V^m, (i.e. considering the number of molecules per unit-cell). The symbols only serve as guides to the eye and do not represent the actually calculated data points, which lie much more densely.

with moderate frequencies, which can contribute to the heat capacity already at lower temperatures. Thus, the normalised heat capacity is somewhat larger than in those (hydrocarbon-based) systems with more C-H modes.
Interestingly, one notices that at 300 K, the normalised heat capacities are basically identical for most systems and amount to ~0.33. Only for the quinacridone polymorphs, they are slightly larger because of the aforementioned reasons (~0.36). Although the normalised values are very similar, the absolute molar heat capacities are visibly different amongst the systems. This offers a simple strategy for estimating the molar heat capacity of (hydrocarbon-based) organic crystals similar to the ones investigated here at room temperature:

$$C_V^m \approx 0.33 \times \frac{3N}{Z} N_A k_B \approx \frac{N}{Z} N_a k_B \tag{5.6}$$

It turns out that this very simple approximation only relying on the number of atoms per unit-cell, N, and the number of molecules per unit-cell, Z (indeed, N/Z is simply the number of atoms per molecule), can be used to estimate the heat capacities very quickly and with an acceptable accuracy. For example, for tetracene and pentacene, Eq. (5.6) yields 249.3 and 299.2 J/mol/K, respectively. Fulem et al. measured the molar heat capacity of tetracene and pentacene by means of differential scanning calorimetry and obtained values of 260.7 and 312.6 J/mol/K [152], respectively, which is less than ~5% larger than estimated with the crude approximation above. The exact simulated values for the heat capacity per mole for tetracene and pentacene are 250.5 and 301.3 J/mol/K, respectively, which is even closer to the experiments. However, note that they measured the experimentally more easily accessible heat capacities at constant pressure, C_p, which can be shown to be always larger than C_V [7] (the derivation is shown in the Appendix). Thus, this difference is not only small, but also physically required.
The different ratios of N/Z for the studied systems explains the considerable differences in the magnitudes of the molar heat capacities as shown in the lower panel of Fig. 5.29. Therefore, the heat capacity increases linearly as a function of the number of rings in the oligoacenes, as per additional ring, the molecules contain six atoms more. Furthermore, pyrene and fluorene with two more, respectively one fewer atom per molecule than anthracene, show also slightly increased and decreased molar heat capacities. Additionally, the heat capacities of the different phases of benzene or quinacridone are too similar to be distinguished reasonably. Only at a few 10 K, one encounters (nearly negligible) differences due to the variations in the intermolecular phonons.
A final remark regarding the normalised heat capacity: note that at the highest shown temperature (400 K, at which benzene and naphthalene have already reached their melting temperatures) the normalised heat capacities are still below 0.5 - i.e. only half of the saturation value in the classical limit. If the temperature-dependence were similarly linear for the higher temperatures, this would mean that all degrees of freedom behave classically only at another 400 K. However, the slope of the normalised heat capacity decreases at higher temperatures so that it takes several thousand Kelvin to achieve an approximately classical, equipartitioned system. Such conditions are, however, never achieved in reality such that, in principle, one should always consider

quantum-mechanical thermal occupation of vibrational states in those systems.

As a final quantity to be compared among the systems, the discussion shall focus on the vibrational free energy F, which is the phonon contribution to the thermodynamic potential of the canonical ensemble - i.e. at constant volume and temperature[49]. As shown in Sec. 2.4, this thermodynamic property can be decomposed into a temperature-dependent contribution, $A(T)$, and the zero-point energy, ZPE. If one additionally normalises the free energy by the number of phonon bands, $3N$, the normalised ZPE directly corresponds to (half) the average phonon frequency in the crystal (with $\hbar$ being the proportionality constant; see Eq. (4.7)). The upper panel of Fig. 5.30 shows the normalised vibrational free energy for all the systems calculated from their entire phonon band structure. Focussing on the ZPE ($= F(T = 0\ \mathrm{K})$), one can see that among the oligoacenes, the average frequency obviously decreases with the number of rings. This can easily be rationalised by the fact that with growing molecular size, the number of carbon atoms increases more than the number of hydrogen atoms. Thus, one expects more moderate-frequency modes related to motion of the heavier carbon atoms than the high-frequency modes involving the hydrogens.
Regarding the molecular systems which do not consist of oligoacenes, both pyrene and fluorene have the same number of hydrogen atoms per molecule as anthracene. However, the pyrene (fluorene) molecule has two carbon atoms more (one fewer) than anthracene, so that the average frequency is obviously shifted to lower (higher) frequencies compared to anthracene. In fact, the ratio of carbon to hydrogen atoms in fluorene is only slightly higher than even in naphthalene so that one would expect even a better agreement with the (normalised) vibrational free energy of naphthalene. However, one must keep in mind that in the phonon spectrum of fluorene a few high-frequency C-H stretching modes are shifted to lower frequencies due to the different hybridisation of one carbon atom in the molecule.
Consistently with the above-discussed reasons for the slightly increased heat capacities in the polymorphs of quinacridone (less hydrogen, but oxygen and nitrogen instead), the ZPEs and, thus, the average frequency in the crystals are notably smaller than in the other systems.
With higher temperature, the total free energy is increasingly reduced due to the negative contribution from the temperature-dependent term $A(T)$, which favours the low-frequency modes (see mathematical form derived in Sec. 2.4). Thus, one expects a stronger decrease in F for those systems with comparably many low-frequency modes - such as the benzene polymorphs. It can indeed be seen in the temperature dependence of the (normalised) vibrational free energies, that $F/(3N)$ drops more rapidly for 1c_m and 1c_o than for the other systems, which show a comparable, similar temperature-dependence, although the spread between the values at 400 K is slightly smaller than the spread of ZPEs at 0 K. This suggests that among those systems, the ones with a higher ZPE also show a (slightly) more pronounced temperature-dependence. As the

[49] Or, equivalently, for the grand-canonical potential if the chemical potential - as for the case of phonons - vanishes.

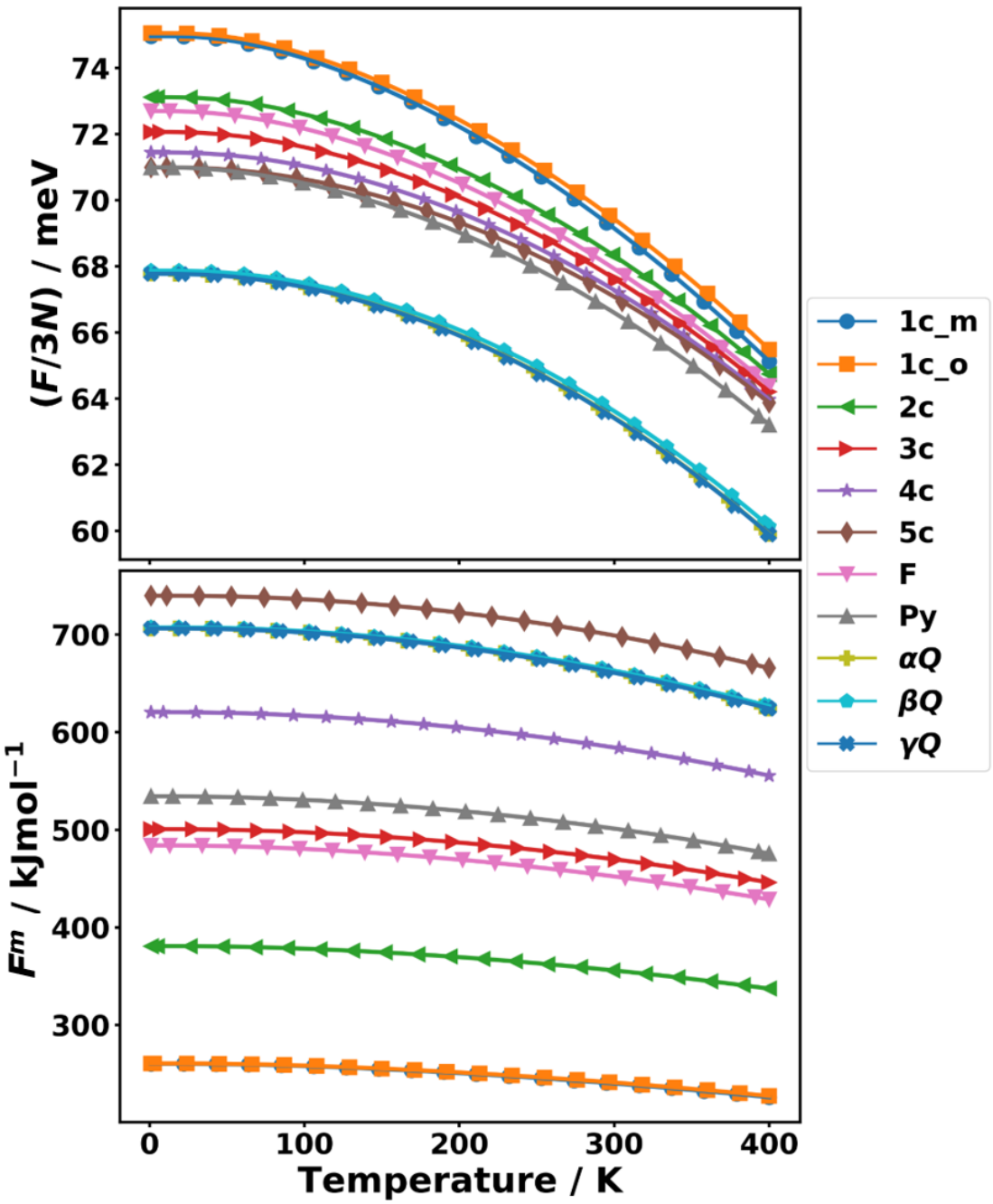

Fig. 5.30.: Phonon contributions to the Helmholtz free energy (F) as a function of temperature for the studied molecular crystals (according to the abbreviations introduced in Tab. 3.1). The upper panel shows the phonon free energy per unit-cell normalised by the number of bands ($3N$). The lower panel shows the free energy per mole of the molecule, F^m (i.e. considering the number of molecules per unit-cell). The symbols only serve as guides to the eye and do not represent the actually calculated data points, which lie much more densely.

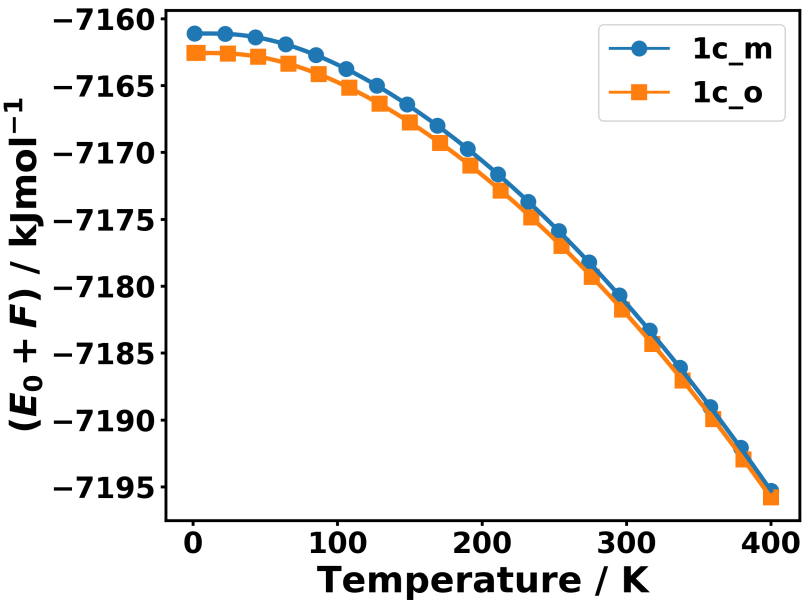

Fig. 5.31.: Total free energy (sum of the electronic energy E_0 obtained from the equation of state and the vibrational free energy F) per mole of the two phases of benzene (1c_m: monoclinic, 1c_o: orthorhombic). The symbols only serve as guides to the eye and do not represent the actually calculated data points, which lie much more densely.

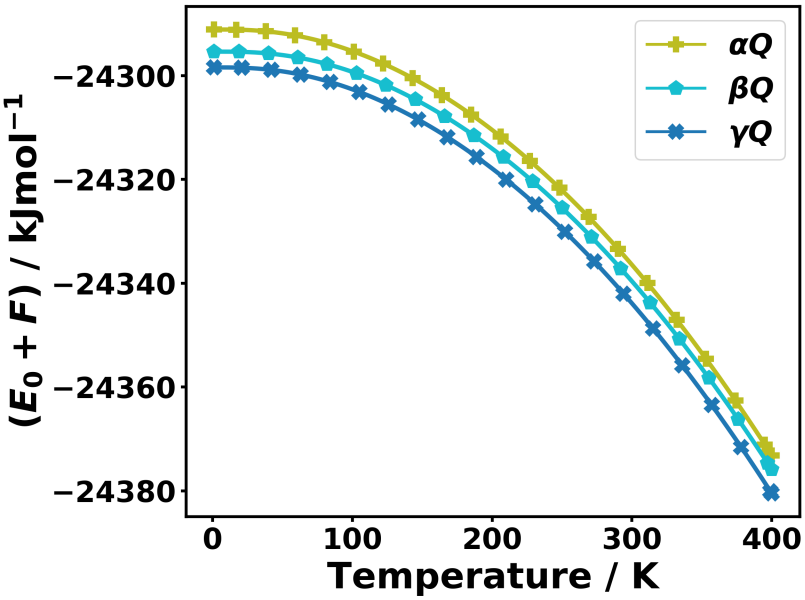

Fig. 5.32.: Total free energy (sum of the electronic energy E_0 obtained from the equation of state and the vibrational free energy F) per mole of the three phases of quinacridone. The symbols only serve as guides to the eye and do not represent the actually calculated data points, which lie much more densely.

(negative) partial derivative of the vibrational free energy with respect to temperature corresponds to the entropy, one can indeed see a slightly increased entropy for naphthalene and fluorene as well as a notably higher (normalised) entropy for the benzene polymorphs as shown in Fig. A.12 in the Appendix.
In terms of absolute scales, the vibrational free energies do not vary more than a few tens of kJ/mol in the entire shown temperature range also showing no large differences within the polymorphic systems. In the normalised vibrational energies one can only vaguely recognise that the vibrational free energy would actually favour the monoclinic phase of benzene over the orthorhombic one. The energetic advantage becomes even more pronounced at higher temperatures. However, when considering also the electronic energy (in terms of the fitted energy E_0 from the equation of state; see Tab. 5.2), the orthorhombic polymorph turns out to be the thermodynamically stable one over the entire shown temperature range (see Fig. 5.31). Since solid benzene melts at ~278.65 K [137], the monoclinic phase should be thermodynamically only accessible under variation of the pressure - i.e. if the volume is allowed to change, which is not the case in the (grand) canonical ensemble. This is in agreement with what has been found in literature [139, 140]. Hypothetically, one would expect a phase transition beyond 400 K, as there, the free energy of the phonons reverses the relative energetic stability of the two phases. At this point it should be emphasised once more that these considerations are only valid for the (grand) canonical ensemble - i.e. for fixed volume rather than fixed pressure. This means one neglects the effect of thermal expansion of the lattice on the phonon frequencies. In order to include these effects (and pressure) as well, one must perform lattice dynamics simulations within the quasi-harmonic approximation (QHA), which, however, still neglects certain anharmonic effects [26].
Similarly, the vibrational free energy alone would predict the following relative stability of the polymorphs of quinacridone (in order of increasing F) over the entire shown temperature range: γQ, αQ, and βQ, with αQ and γQ showing essentially the same values, while the vibrational free energy of βQ is somewhat higher. Including also the electronic contribution into the thermodynamic considerations results in the situation shown in Fig. 5.32. According to the total free energy, the γ-phase should be the thermodynamically most stably polymorph, followed by βQ and αQ, which is in agreement with experimental observations [118]. Here, the order of αQ and βQ are switched depending on whether the total or only the vibrational free energy is considered, leading to αQ becoming thermodynamically more stable (within the canonical ensemble, neglecting thermal expansion) than the β-phase. Since the γ-phase shows both, the smallest vibrational free energy and the smallest electronic energy, this phases will never be overtaken in terms of thermodynamic stability by means of a variation of temperature only. The influence of pressure could, again, be studied within the QHA.

6. Summary

Organic semiconductors (OSCs) are a fascinating class of materials. They have not only already become industrially important, but they also remain an interesting scientific topic in many fields of science and engineering. Today a lot of effort has been spent to understand and design their electronic properties, which enabled their application in real-live devices such as organic light-emitting diodes, organic thin film transistors, or organic solar cells. However, other also practically relevant properties in OSCs are less well understood. Many of those properties in crystalline OSCs are primarily determined by the quanta of lattice vibrations (phonons). The importance of phonons in OSCs is obvious from the number of relevant quantities, which rely on lattice vibrations: heat capacities, the entropy, thermal expansion, the free energy of a crystal relevant for the relative thermodynamic stability of a polymorph, phonon (heat) transport, thermal atomic motion, vibrational spectra for fast experimental structure identification, and even for electronic (charge) transport and thermoelectricity, where the electron-phonon coupling is often seen to be one of the main obstacles for the charge carrier mobility [10]. The basic ingredient for all phonon-related properties - the phonon band structure - of OSCs turns out to pose significant challenges on both, experiments and simulations. Nevertheless, it is more convenient to rely on the latter rather than on the former, since many aspects regarding the sample preparation and the measurement itself require much more effort than in other (inorganic) materials.
As OSCs typically contain large numbers of atoms per unit-cell, the widely used supercell-based approach to compute phonon bands soon becomes rather expensive using state-of-the-art quantum-mechanical methods such as dispersion-corrected density functional theory (DFT) [65, 66]. To efficiently handle periodic quantum-mechanical systems, one desires to have an alternative (less expensive) method to successfully and reliably produce phonon band structures with no or little loss of accuracy. Several alternative methodologies with varying level of sophistication are available, which could, in principle, be utilised to compute the phonon band structure of a given crystal structure. However, here one must precisely know which approximations are made and why. One of such approximate methods is density functional tight binding (DFTB), which is based on the DFT formalism, but approximates the Hamiltonian as a Taylor series in the charge density up to second or third order [32, 79]. Additionally, only a special shape of the variation in charge density in comparison to the free atom charge density is allowed in this formalism, and all necessary integrals occurring in the Schrödinger equations are read from tabulated parameter files. Classical force fields (FFs) go even a step further and do not consider quantum-mechanical effects (and, thus, the electrons) explicitly. Instead, they aim at directly describing the potential energy surface - i.e. the interatomic interactions - by means of fixed energy terms for bond distances, angles, dihedrals etc., and combinations of those [81].
At this point the questions arise whether and to which extent dispersion-corrected DFT or even such an approximate methodology is capable of yielding reliable phonon band structures and the derived properties. Quantitatively answering these questions has been the first goal of this thesis. To this end, (deuterated) naphthalene was chosen as

a benchmarking system, which is still the only OSC for which the phonon band structure was also obtained experimentally [24]. These experimental results were used as an integral part of the quantitative comparisons of the simulations: the phonon band structure and selected derived properties were calculated with various levels of theory - comprising DFT, DFTB, and FFs - and compared to the experiments. By the time of writing, the majority of the results of this study has already been published in the *Journal of Chemical Theory and Computation* [1].
The employed strategic approach in this benchmark was the following: as a first step, a suitable "high-level" reference methodology (DFT with different dispersion corrections) had to be found, which most closely reproduces experimental observables such as the lattice constants, vibrational (Raman) spectra, and, most importantly, the low-frequency phonon band structure. Judging based only on the former two criteria, the PBE functional [68] in combination with the two *a posteriori* van der Waals corrections - the D3-BJ [73, 74] or the many-body dispersion (MBD) van der Waals correction [76, 77] as implemented in the *Vienna Ab-Initio Simulation Package* (*VASP* [38, 39, 40, 87]) - turned out to be the most promising candidates to reproduce the experiments. However, the latter, which is computationally much more expensive than the former, was found incapable of handling the large number of atoms present in the supercells. Therefore, only the D3-BJ method remained as a potential reference methodology. In fact, the agreement between the PBE/D3-BJ-simulated phonon band structure and the experimental data is more than satisfying (with a root-mean-square deviation of frequencies of ~0.13 THz). Beyond the low-frequency regime dominated by intermolecular modes, also excellent agreement regarding the high-frequency intramolecular modes is observed. This is evident by comparing the simulated Raman spectra with an experimentally obtained one [128]. Since the PBE/D3-BJ approach shows an extra-ordinarily good agreement in both spectral regimes (inter- and intramolecular phonon modes), it was chosen as the reference method, to whose results those of potential approximate methodologies should be compared [1].
However, the DFTB approach did not yield a good agreement with this reference method: the optimised unit-cells were too closely packed resulting in distorted phonon bands with prevailingly overestimated frequencies. Also the approach suggested in literature (see Ref. [131]) to use DFTB with the DFT-optimised unit-cell could not achieve a satisfying improvement, although the qualitative agreement with the low-frequency DFT bands was notably increased compared to the situation with the DFTB-optimised lattice vectors. Since with this approach, the majority of the frequencies were observed to be too low, a logical but physically little motivated trick was applied: starting from the DFT-optimised unit-cell, the volume was isotropically reduced to create slightly more densely packed unit-cells as input for the DFTB calculations. The volume was reduced such that the root-mean-square deviation of frequencies compared to the reference data was minimised. In the case of naphthalene, this volume scaling factor was found to amount to 95 %. Although this approach is, of course, not a general applicable one, and one must carry out careful tests to find the optimal value for such a scaling, similar improvements to the phonon bands within DFTB were also found for anthracene and fluorene with similar volume scaling factors (96 and 97 %, respectively) in both cases.

As the next step of simplification, the interatomic interactions were modelled with three classical force fields of varying sophistication. The simplest of the tested FFs was the GAFF [81], which describes the bonded interactions only via harmonic terms without any cross terms and the van der Waals interactions via a commonly used 12-6-Lennard-Jones potential. The next level of complexity was brought about by the so-called COMPASS FF [83], which already contains anharmonic terms and couplings between the bonded interaction, while the van der Waals interactions are described via a softer 9-6-Lennard-Jones potential. While these two FFs belong to the class of transferable FFs - i.e. they could, in principle, be used for other systems without the need for a reparametrisation - also an intransferable FF, especially parametrised for naphthalene was included in the benchmark. To this end, our own parametrisation of the MOF-FF [84] (parametrised with molecular naphthalene), a second-generation FF containing anharmonic terms and cross terms for the bonded interaction, and utilising a (damped) Buckingham potential for the dispersion forces, has been tested [1].
Because of the fundamental differences of the physical origin of the low- and the high-frequency phonons due to intermolecular (dominated by van der Waals interaction) and intramolecular motion (dominated by covalent bonding), respectively, the evaluation of the observed discrepancies was split into these two separate regimes, partly by means of statistical analysis. Thus, the tested methodologies were quantitatively compared in the following categories: the deviations in frequencies in the low-frequency region and in the entire spectrum, the group velocities of the low-frequency modes, the mean-squared thermal displacements (MSTDs), the vibrational free energy at 0 K (zero-point energy) and at 300 K, and the (phonon contribution to the) heat capacity. In the low-frequency regime, MOF-FF and the DFTB approach based on the slightly shrunk DFT-optimised unit-cell ("DFTB@95%DFT") show the best agreement with the reference phonon band structures. Overall, considering all tested categories, the clear winner among the tested approaches is the system-specifically parametrised MOF-FF. Besides its only slightly higher frequency error in the low-frequency band structure compared to the lowest observed value (DFTB@95%DFT), it is only outperformed in terms of its suitability to reproduce MSTDs (here, all methodologies except for the pure DFTB approach fare better). Interestingly, the best agreement when it comes to reproducing the MSTDs is exerted by GAFF and COMPASS, whose strength obviously lies in an accurate description of the low-frequency acoustic phonon band dispersion. While GAFF very often finds itself at the bottom of the ranking lists in the above-mentioned categories, COMPASS often yields results of acceptable accuracy for properties involving a summation over frequencies. This is, however, rather a coincidence than an indicator for high accuracy, since many frequencies are equally over- and underestimated. As it was shown, a case like this results in a cancellation of errors when computing sums over phonon frequencies as they appear in the free energy or the heat capacity, for instance.
The origin of intramolecular modes being over- or underestimated in frequency can typically be found through a detailed analysis of the relevant harmonic force constants. It turns out that in all DFTB approaches, the C-H force constants are drastically too small, resulting in too low C-H stretching frequencies. This fact, in turn, significantly reduces the zero-point energy (ZPE) calculated with DFTB. In general, the C-H interac-

tions seem to pose quite a challenge to all approximate approaches except for MOF-FF, which, as a result, shows the best agreement in terms of ZPE with the reference. The difference in free energy between an approximate methodology and the reference was found to decrease with temperature if the average (signed) frequency deviation in the low-frequency region is positive. In contrast to the more involved case of the free energy, the heat capacity is a more robust quantity and, regardless of the method, only shows relative deviations of up to 0.5 % at room temperature.
The only category in which all the tested methodologies should be considered as having dramatically failed is the description of group velocities. Here, none of the tested methodologies yields a good agreement with the PBE/D3-BJ reference, with errors comparable to the actual magnitudes of the group velocities.

The only methodology to most reliably reproduce the majority of aspects of the reference data is the MOF-FF (which is intransferable and would have been required to be parametrised for every studied system separately). Because of that and its few remaining weaknesses (group velocities and mean-squared thermal displacements), the reference methodology PBE/D3-BJ was employed to study further, systematically chosen crystalline OSCs. These include various oligoacenes, oligophenylenes, rubrene, fluorene, pyrene and (polymorphs of) quinacridone. Unfortunately, technical reasons (inconsistencies in the crystal structures or the too large system sizes) prevented obtaining phonon frequencies beyond Γ for the oligophenylenes and rubrene. Nevertheless, interesting insights into structure-to-property relations in the remaining eleven systems could be established.
An analysis based on the mode participation ratios (PRs) revealing those phonon modes with a large degree of atomic motion was utilised to identify acoustic modes beyond possible avoided crossings with other, symmetry-equivalent bands. Moreover, the PRs show special intermolecular modes, in which the inequivalent molecules per unit-cell rigidly undergo translational motions, which are referred to as RIMMs ("rigid intermolecular modes") in the following. By monitoring the frequencies of the RIMMS as a function of the molecule size in the studied oligoacenes, one can see that the intermolecular force constant responsible for rigid molecular displacements perpendicular to the long molecular axes - i.e. along the short molecular axis or in those directions increasing/decreasing the herringbone packing distance - increases in strength with the number of rings in the molecule. This can be rationalised by stronger variation of the van der Waals interaction for these two types of displacements: in this way, a part of every ring contributes to the gain/loss in interaction leading to an enhanced curvature of this special section of the potential energy surface. In contrast, the intermolecular force constant for displacements along the long molecular axis was found to stay approximately constant throughout the oligoacenes. Based on the arguments above, this is to be expected, since for all oligoacenes, the absolute gain/loss in van der Waals interaction is always the same (roughly only determined by the "first" and "last" ring) for this type of displacement. Thus, for translational modes along the long molecular axis, the frequency dependence can be ascribed only to the increased mass of the larger oligoacenes. For the modes corresponding to displacements perpendicular to the long molecular axes, the higher mass is (partly) compensated by the stronger interaction. If similar relations can be verified

also for further systems, this insight is supposed to be promising to quickly estimate the frequency of modes which have been found to be rather unbeneficial for charge transport in literature (*killer phonon mode* [10]).
Based on the studied band structures, the group velocities were evaluated in a statistical way. The running mean of group velocity (vector) norms is typically found to be higher for larger oligoacenes up to a certain threshold frequency, at which more and more dispersionless low-lying bands reduce the average value again. Thus, pentacene shows the largest values for modes up to ~4 THz. This frequency approximately corresponds to the upper limit of the intermolecular regime observed in all oligoacenes. Compared to the oligoacenes, pyrene and fluorene display slightly reduced (running means of) group velocities due to a weaker intermolecular interaction and the special layer-like packing, respectively. Concerning the polymorphs of quinacridone, the β- and α-phases show extra-ordinarily large regions with increased band dispersion due to the gigantic band widths of the acoustic bands (with the former displaying the highest group velocities among all studied systems). Conversely, the thermodynamically most stable γ-phase is more similar to the oligoacenes. Because of the pronounced differences in the band structures of the three studied phases, a phase transition is supposed to tremendously impact the phonon properties of the material.
Another important finding concerns the group velocities in different polymorphs of the same organic molecule. In crystals with reduced symmetry, the phonon bands are more likely to experience hybridisation effects (avoided crossings) with other bands such that, effectively, the band dispersion in the region of the hybridisation is decreased. This effect can be seen very clearly when comparing the average group velocities in orthorhombic benzene with that of the monoclinic polymorph. In the latter, the average group velocity is notably reduced due to the higher amount of avoided crossings. The higher average group velocity in the orthorhombic phase can, however, only be observed up to that point at which the larger number of (nearly dispersionless) higher-lying bands are considered, which decrease the average value again. This means that - in analogy to the observations in Refs. [147, 148, 149] - one could use/functionalise molecules in such a way that the space group of the crystal is reduced, thus, leading to more avoided crossings and decreased group velocities, when less efficient phonon transport in the OSC is desired.
Regarding thermodynamic quantities in the canonical ensemble, the phonon heat capacities calculated in the context of this thesis are found to be in excellent agreement with experimental data for the oligoacenes. An interesting aspect in this context is that the heat capacity was shown to be roughly 33 % of the respective classical limiting value (hypothetically approached for $T \to \infty$) throughout all hydrocarbon-based systems. Only in the polymorphs of quinacridone it amounts to a slightly higher value (~36%) due to the reduced number of high-frequency C-H stretching modes. Thus, for the systems consisting of carbon and hydrogen only, the fact that the heat capacity per unit-cell relative to its saturation value is (approximately) constant can be exploited to conveniently estimate the molar heat capacity at room temperature by only knowing the number of atoms per molecule.
As a last aspect, the phonon contribution to the free energy is discussed for all sys-

tems. For the oligoacenes it can be observed that the ZPE normalised by the number of bands (being proportional to the average phonon frequency in the system) decreases with the molecule size (approximately from 75 to 71 meV per unit-cell). This can be rationalised by the fact that the larger the oligoacene, the more the ratio of carbon atoms to hydrogen atoms increases. Thus, more intermediate frequencies are added to the system rather than new high-frequency modes involving hydrogen. For the same reason, the normalised ZPE of the quinacridone polymorphs is notably reduced (~68 meV per unit-cell) compared to the pure hydrocarbon-based systems. Considering the sum of the electronic energy and the vibrational free energy, the correct, experimentally observed relative order of the thermodynamic stability of the studied polymorphs of benzene and quinacridone could be reproduced, further verifying the quality of the simulated data. Eventually, a temperature-induced phase transition from the second-most stable β-polymorph to the least stable α-polymorph is predicted at temperatures beyond 400 K - disregarding thermal expansion, pressure and anharmonic effects in the (grand) canonical ensemble.

References

[1] Tomas Kamencek, Sandro Wieser, Hirotaka Kojima, Natalia Bedoya-Martínez, Johannes P. Dürholt, Rochus Schmid, and Egbert Zojer. Evaluating Computational Shortcuts in Supercell-Based Phonon Calculations of Molecular Crystals: The Instructive Case of Naphthalene. *Journal of Chemical Theory and Computation*, 16(4):2716–2735, 2020.

[2] Chengliang Wang, Huanli Dong, Lang Jiang, and Wenping Hu. Organic semiconductor crystals. *Chem. Soc. Rev.*, 47:422–500, 2018.

[3] Amin Salehi, Xiangyu Fu, Dong-Hun Shin, and Franky So. Recent advances in oled optical design. *Advanced Functional Materials*, 29(15):1808803, 2019.

[4] Brijesh Kumar, Brajesh Kumar Kaushik, and Yuvraj Singh Negi. Organic thin film transistors: Structures, models, materials, fabrication, and applications: A review. *Polymer Reviews*, 54(1):33–111, 2014.

[5] G.A. Chamberlain. Organic solar cells: A review. *Solar Cells*, 8(1):47 – 83, 1983.

[6] Hugo Bronstein, Christian B Nielsen, Bob C Schroeder, and Iain McCulloch. The role of chemical design in the performance of organic semiconductors. *Nature Reviews Chemistry*, 4(2):66–77, 2020.

[7] R Gross and A Marx. *Festkörperphysik*. Oldenbourg Wissenschaftsverlag, 2012.

[8] Veaceslav Coropceanu, Jérôme Cornil, Demetrio A da Silva Filho, Yoann Olivier, Robert Silbey, and Jean-Luc Brédas. Charge Transport in Organic Semiconductors. *Chemical Reviews*, 107(4):926–952, apr 2007.

[9] N Karl. Charge carrier transport in organic semiconductors. *Synthetic Metals*, 134:1–9, 2003.

[10] Guillaume Schweicher, Gabriele D'Avino, Michael T Ruggiero, David J Harkin, Katharina Broch, Deepak Venkateshvaran, Guoming Liu, Audrey Richard, Christian Ruzie, Jeff Armstrong, Alan R Kennedy, Kenneth Shankland, Kazuo Takimiya, Yves H Geerts, J Axel Zeitler, Simone Fratini, and Henning Sirringhaus. Chasing the 'killer' phonon mode for the rational design of low disorder, high mobility molecular semiconductors. *Advanced Materials*, 31, 2019.

[11] Nir Tessler, Yevgeni Preezant, Noam Rappaport, and Yohai Roichman. Charge transport in disordered organic materials and its relevance to thin-film devices: A tutorial review. *Advanced Materials*, 21(27):2741–2761, 2009.

[12] Simone Fratini, Didier Mayou, and Sergio Ciuchi. The transient localization scenario for charge transport in crystalline organic materials. *Advanced Functional Materials*, 26(14):2292–2315, 2016.

[13] Harald Oberhofer, Karsten Reuter, and Jochen Blumberger. Charge Transport in Molecular Materials: An Assessment of Computational Methods. *Chemical Reviews*, 117(15):10319–10357, 2017.

[14] Dong Wang, Ling Tang, Mengqiu Long, and Zhigang Shuai. Anisotropic thermal transport in organic molecular crystals from nonequilibrium molecular dynamics simulations. *Journal of Physical Chemistry C*, 115(13):5940–5946, 2011.

[15] Yinhang Zhang, Young Jung Heo, Mira Park, and Soo Jin Park. Recent advances in organic thermoelectric materials: Principle mechanisms and emerging carbon-based green energy materials. *Polymers*, 11(1), 2019.

[16] Boris Russ, Anne Glaudell, Jeffrey J. Urban, Michael L. Chabinyc, and Rachel A. Segalman. Organic thermoelectric materials for energy harvesting and temperature control. *Nature Reviews Materials*, 1(10), 2016.

[17] Bouke P van Eijck. Ab initio crystal structure predictions for flexible hydrogen-bonded molecules. Part III. Effect of lattice vibrations. *Journal of Computational Chemistry*, 22(8):816–826, 2001.

[18] Aurora J. Cruz-Cabeza, Susan M. Reutzel-Edens, and Joel Bernstein. Facts and fictions about polymorphism. *Chemical Society Reviews*, 44(23):8619–8635, 2015.

[19] Jonas Nyman and Graeme M. Day. Static and lattice vibrational energy differences between polymorphs. *CrystEngComm*, 17(28):5154–5165, 2015.

[20] Keith T. Butler, Katrine Svane, Gregor Kieslich, Anthony K. Cheetham, and Aron Walsh. Microscopic origin of entropy-driven polymorphism in hybrid organic-inorganic perovskite materials. *Physical Review B*, 94(18):1–5, 2016.

[21] Varley F. Sears. Neutron scattering lengths and cross sections. *Neutron News*, 3(3):26–37, 1992.

[22] S. J. Fisher, M. P. Blakeley, E. I. Howard, I. Petit-Haertlein, M. Haertlein, A. Mitschler, A. Cousido-Siah, A. G. Salvay, A. Popov, C. Muller-Dieckmann, T. Petrova, and A. Podjarny. Perdeuteration: Improved visualization of solvent structure in neutron macromolecular crystallography. *Acta Crystallographica Section D: Biological Crystallography*, 70(12):3266–3272, 2014.

[23] Ai Woon Yee, Matthew P. Blakeley, Martine Moulin, Michael Haertlein, Edward Mitchell, and V. Trevor Forsyth. Back-exchange of deuterium in neutron crystallography: Characterization by IR spectroscopy. *Journal of Applied Crystallography*, 50:660–664, 2017.

[24] I. Natkaniec, E. L. Bokhenkov, B. Dorner, J. Kalus, G. A. MacKenzie, G. S. Pawley, U. Schmelzer, and E. F. Sheka. Phonon dispersion in d8-naphthalene crystal at 6K. *Journal of Physics C: Solid State Physics*, 13(23):4265–4283, 1980.

[25] Xavier Gonze and Changyol Lee. Dynamical matrices, Born effective charges, dielectric permittivity tensors, and interatomic force constants from density-functional perturbation theory. *Physical Review B - Condensed Matter and Materials Physics*, 55(16):10355–10368, apr 1997.

[26] Stefano Baroni, Stefano de Gironcoli, Andrea Dal Corso, and Paolo Giannozzi. Phonons and related crystal properties from density-functional perturbation theory. *Rev. Mod. Phys.*, 73(2):515–562, jul 2001.

[27] Atsushi Togo and Isao Tanaka. First principles phonon calculations in materials science. *Scripta Materialia*, 108:1–5, 2015.

[28] Anthony M. Reilly and Alexandre Tkatchenko. Role of dispersion interactions in the polymorphism and entropic stabilization of the aspirin crystal. *Physical Review Letters*, 113(5):1–5, 2014.

[29] Anna Y. Likhacheva, Sergey V. Rashchenko, Artem D. Chanyshev, Talgat M. Inerbaev, Konstantin D. Litasov, and Dmitry S. Kilin. Thermal equation of state of solid naphthalene to 13 GPa and 773 K: In situ X-ray diffraction study and first principles calculations. *Journal of Chemical Physics*, 140(16), 2014.

[30] Florian Brown-Altvater, Tonatiuh Rangel, and Jeffrey B. Neaton. Ab initio phonon dispersion in crystalline naphthalene using van der Waals density functionals. *Physical Review B*, 93(19):60–63, 2016.

[31] G Seifert, D Porezag, and Th. Frauenheim. Calculations of molecules, clusters, and solids with a simplified LCAO-DFT-LDA scheme. *International Journal of Quantum Chemistry*, 58(2):185–192, jan 1996.

[32] Augusto F Oliveira, Gotthard Seifert, Thomas Heine, and Hélio A Duarte. Density-functional based tight-binding: an approximate DFT method , 2009.

[33] D Porezag, Th. Frauenheim, Th. Köhler, G Seifert, and R Kaschner. Construction of tight-binding-like potentials on the basis of density-functional theory: Application to carbon. *Physical Review B*, 51(19):12947–12957, may 1995.

[34] Th. Frauenheim, G Seifert, M Elsterner, Z Hajnal, G Jungnickel, D Porezag, S Suhai, and R Scholz. A Self-Consistent Charge Density-Functional Based Tight-Binding Method for Predictive Materials Simulations in Physics, Chemistry and Biology. *physica status solidi (b)*, 217(1):41–62, jan 2000.

[35] H. Haken and H.C. Wolf. *Molekülphysik und Quantenchemie: Einführung in die experimentellen und theoretischen Grundlagen*. Springer-Lehrbuch. Springer Berlin Heidelberg New York, 5 edition, 2006.

[36] Duane C. Wallace and Herbert Callen. Thermodynamics of Crystals, 2005.

[37] Wolfgang Nolting. *Grundkurs Theoretische Physik 6: Statistische Physik*. Springer-Lehrbuch. Springer Berlin Heidelberg, 7 edition, 2014.

[38] G Kresse and J Hafner. Ab initio molecular dynamics for liquid metals. *Physical Review B*, 47(1):558–561, jan 1993.

[39] G Kresse and J Hafner. Ab initio molecular-dynamics simulation of the liquid-metal–amorphous-semiconductor transition in germanium. *Physical Review B*, 49(20):14251–14269, may 1994.

[40] G Kresse and J Furthmüller. Efficiency of ab-initio total energy calculations for metals and semiconductors using a plane-wave basis set. *Computational Materials Science*, 6(1):15–50, 1996.

[41] G Kresse and D Joubert. From ultrasoft pseudopotentials to the projector augmented-wave method. *Physical Review B*, 59(3):1758–1775, jan 1999.

[42] Atsushi Togo. Formulations - commensurate q-points, phonopy v.2.8.1. http://phonopy.github.io/phonopy/formulation.html16:03 13.01.2021. accessed on 04 January 2021.

[43] Paolo Giannozzi, Stefano Baroni, Nicola Bonini, Matteo Calandra, Roberto Car, Carlo Cavazzoni, Davide Ceresoli, Guido L Chiarotti, Matteo Cococcioni, Ismaila Dabo, Andrea Dal Corso, Stefano de Gironcoli, Stefano Fabris, Guido Fratesi, Ralph Gebauer, Uwe Gerstmann, Christos Gougoussis, Anton Kokalj, Michele Lazzeri, Layla Martin-Samos, Nicola Marzari, Francesco Mauri, Riccardo Mazzarello, Stefano Paolini, Alfredo Pasquarello, Lorenzo Paulatto, Carlo Sbraccia, Sandro Scandolo, Gabriele Sclauzero, Ari P Seitsonen, Alexander Smogunov, Paolo Umari, and Renata M Wentzcovitch. Quantum espresso: a modular and open-source software project for quantum simulations of materials. *Journal of Physics: Condensed Matter*, 21(39):395502 (19pp), 2009.

[44] P Giannozzi, O Andreussi, T Brumme, O Bunau, M Buongiorno Nardelli, M Calandra, R Car, C Cavazzoni, D Ceresoli, M Cococcioni, N Colonna, I Carnimeo, A Dal Corso, S de Gironcoli, P Delugas, R A DiStasio Jr, A Ferretti, A Floris, G Fratesi, G Fugallo, R Gebauer, U Gerstmann, F Giustino, T Gorni, J Jia, M Kawamura, H-Y Ko, A Kokalj, E Küçükbenli, M Lazzeri, M Marsili, N Marzari, F Mauri, N L Nguyen, H-V Nguyen, A Otero de-la Roza, L Paulatto, S Poncé, D Rocca, R Sabatini, B Santra, M Schlipf, A P Seitsonen, A Smogunov, I Timrov, T Thonhauser, P Umari, N Vast, X Wu, and S Baroni. Advanced capabilities for materials modelling with quantum espresso. *Journal of Physics: Condensed Matter*, 29(46):465901, 2017.

[45] Paolo Giannozzi, Oscar Baseggio, Pietro Bonfà, Davide Brunato, Roberto Car, Ivan Carnimeo, Carlo Cavazzoni, Stefano de Gironcoli, Pietro Delugas, Fabrizio Ferrari Ruffino, Andrea Ferretti, Nicola Marzari, Iurii Timrov, Andrea Urru, and

Stefano Baroni. Quantum espresso toward the exascale. *The Journal of Chemical Physics*, 152(15):154105, 2020.

[46] X Gonze, J.-M. Beuken, R Caracas, F Detraux, M Fuchs, G.-M. Rignanese, L Sindic, M Verstraete, G Zerah, F Jollet, M Torrent, A Roy, M Mikami, Ph. Ghosez, J.-Y. Raty, and D C Allan. First-principles computation of material properties: {The} {ABINIT} software project. *Computational Materials Science*, 25(3):478–492, nov 2002.

[47] Xavier Gonze, Bernard Amadon, Gabriel Antonius, Frédéric Arnardi, Lucas Baguet, Jean-Michel Beuken, Jordan Bieder, François Bottin, Johann Bouchet, Eric Bousquet, Nils Brouwer, Fabien Bruneval, Guillaume Brunin, Théo Cavignac, Jean-Baptiste Charraud, Wei Chen, Michel Côté, Stefaan Cottenier, Jules Denier, Grégory Geneste, Philippe Ghosez, Matteo Giantomassi, Yannick Gillet, Olivier Gingras, Donald R. Hamann, Geoffroy Hautier, Xu He, Nicole Helbig, Natalie Holzwarth, Yongchao Jia, François Jollet, William Lafargue-Dit-Hauret, Kurt Lejaeghere, Miguel A. L. Marques, Alexandre Martin, Cyril Martins, Henrique P. C. Miranda, Francesco Naccarato, Kristin Persson, Guido Petretto, Valentin Planes, Yann Pouillon, Sergei Prokhorenko, Fabio Ricci, Gian-Marco Rignanese, Aldo H. Romero, Michael Marcus Schmitt, Marc Torrent, Michiel J. van Setten, Benoit Van Troeye, Matthieu J. Verstraete, Gilles Zérah, and Josef W. Zwanziger. The abinit project: Impact, environment and recent developments. *Comput. Phys. Commun.*, 248:107042, 2020.

[48] Aldo H. Romero, Douglas C. Allan, Bernard Amadon, Gabriel Antonius, Thomas Applencourt, Lucas Baguet, Jordan Bieder, François Bottin, Johann Bouchet, Eric Bousquet, Fabien Bruneval, Guillaume Brunin, Damien Caliste, Michel Côté, Jules Denier, Cyrus Dreyer, Philippe Ghosez, Matteo Giantomassi, Yannick Gillet, Olivier Gingras, Donald R. Hamann, Geoffroy Hautier, François Jollet, Gérald Jomard, Alexandre Martin, Henrique P. C. Miranda, Francesco Naccarato, Guido Petretto, Nicholas A. Pike, Valentin Planes, Sergei Prokhorenko, Tonatiuh Rangel, Fabio Ricci, Gian-Marco Rignanese, Miquel Royo, Massimiliano Stengel, Marc Torrent, Michiel J. van Setten, Benoit Van Troeye, Matthieu J. Verstraete, Julia Wiktor, Josef W. Zwanziger, and Xavier Gonze. Abinit: Overview, and focus on selected capabilities. *J. Chem. Phys.*, 152:124102, 2020.

[49] Dirk Werner. *Funktionalanalysis*. Springer-Lehrbuch. Springer Berlin Heidelberg, 7 edition, 2011.

[50] M.T. Dove. Introduction to the theory of lattice dynamics. *École thématique de la Société Française de la Neutronique*, 12:123–159, 2011.

[51] Etienne Balan, Michele Lazzeri, Simon Delattre, Merlin Méheut, Keith Refson, and Bjoern Winkler. Anharmonicity of inner-OH stretching modes in hydrous phyllosilicates: Assessment from first-principles frozen-phonon calculations. *Physics and Chemistry of Minerals*, 34(9):621–625, 2007.

[52] R J Bell, P Dean, and D C Hibbins-Butler. Localization of normal modes in vitreous silica, germania and beryllium fluoride. *Journal of Physics C: Solid State Physics*, 3(10):2111–2118, 1970.

[53] J T Edwards and D J Thouless. Numerical studies of localization in disordered systems. *Journal of Physics C: Solid State Physics*, 5(8):807–820, 1972.

[54] J Canisius and J L van Hemmen. Localisation of phonons. *Journal of Physics C: Solid State Physics*, 18(25):4873–4884, 1985.

[55] Atsushi Togo, Laurent Chaput, and Isao Tanaka. Distributions of phonon lifetimes in Brillouin zones. *Physical Review B - Condensed Matter and Materials Physics*, 91(9), 2015.

[56] A. A. MARADUDIN and FEIN A. E. Scattering of Neutrons by an Anharmonic Crystal. *Physical Review*, 128(6), 1962.

[57] Joseph P. Heremans. The anharmonicity blacksmith. *Nature Physics*, 11(12):990–991, 2015.

[58] Tomas Kamencek, Natalia Bedoya-Mart\'\inez, and Egbert Zojer. Understanding phonon properties in isoreticular metal-organic frameworks from first principles. *Phys. Rev. Materials*, 3(11):116003, nov 2019.

[59] Lei Wang, Cong Wang, Ying Sun, Kewen Shi, Sihao Deng, and Huiqing Lu. Large negative thermal expansion provided by metal-organic framework MOF-5: A first-principles study. *Materials Chemistry and Physics*, 175:138–145, 2016.

[60] W. Zhou, H. Wu, T. Yildirim, J. R. Simpson, and A. R.Hight Walker. Origin of the exceptional negative thermal expansion in metal-organic framework-5 Zn4 O (1,4-benzenedicarboxylate)3. *Physical Review B - Condensed Matter and Materials Physics*, 78(5):1–5, 2008.

[61] Ethan T. Ritz, Sabrina J. Li, and Nicole A. Benedek. Thermal expansion in insulating solids from first principles. *Journal of Applied Physics*, 126(17), 2019.

[62] K N Trueblood, H.-B. Bürgi, H Burzlaff, J D Dunitz, C M Gramaccioli, H H Schulz, U Shmueli, and S C Abrahams. Atomic Dispacement Parameter Nomenclature. Report of a Subcommittee on Atomic Displacement Parameter Nomenclature. *Acta Crystallographica Section A*, 52(5):770–781, sep 1996.

[63] R W Grosse-Kunstleve and P D Adams. On the handling of atomic anisotropic displacement parameters. *Journal of Applied Crystallography*, 35(4):477–480, aug 2002.

[64] G.P. Srivastava. *The Physics of Phonons*. Taylor & Francis, 1990.

[65] P Hohenberg and W Kohn. Inhomogeneous Electron Gas. *Physical Review*, 136(3B):B864–B871, nov 1964.

[66] W Kohn and L J Sham. Self-Consistent Equations Including Exchange and Correlation Effects. *Physical Review*, 140(4A):A1133–A1138, nov 1965.

[67] D. M. Ceperley and B. J. Alder. Ground state of the electron gas by a stochastic method. *Phys. Rev. Lett.*, 45:566–569, Aug 1980.

[68] John P Perdew, Kieron Burke, and Matthias Ernzerhof. Generalized Gradient Approximation Made Simple. *Physical Review Letters*, 77(18):3865–3868, oct 1996.

[69] Martin Stöhr, Troy Van Voorhis, and Alexandre Tkatchenko. Theory and practice of modeling van der waals interactions in electronic-structure calculations. *Chem. Soc. Rev.*, 48:4118–4154, 2019.

[70] Kristian Berland, Valentino R Cooper, Kyuho Lee, Elsebeth Schröder, T Thonhauser, Per Hyldgaard, and Bengt I Lundqvist. van der waals forces in density functional theory: a review of the vdW-DF method. *Reports on Progress in Physics*, 78(6):066501, may 2015.

[71] M. Dion, H. Rydberg, E. Schröder, D. C. Langreth, and B. I. Lundqvist. Van der waals density functional for general geometries. *Phys. Rev. Lett.*, 92:246401, Jun 2004.

[72] Stefan Grimme. Semiempirical GGA-type density functional constructed with a long-range dispersion correction. *Journal of Computational Chemistry*, 27(15):1787–1799, nov 2006.

[73] Stefan Grimme, Jens Antony, Stephan Ehrlich, and Helge Krieg. A consistent and accurate ab initio parametrization of density functional dispersion correction (DFT-D) for the 94 elements H-Pu. *The Journal of Chemical Physics*, 132(15):154104, apr 2010.

[74] Stefan Grimme, Stephan Ehrlich, and Lars Goerigk. Effect of the damping function in dispersion corrected density functional theory. *Journal of Computational Chemistry*, 32(7):1456–1465, may 2011.

[75] Alexandre Tkatchenko and Matthias Scheffler. Accurate molecular van der Waals interactions from ground-state electron density and free-atom reference data. *Physical Review Letters*, 102(7):6–9, 2009.

[76] Alexandre Tkatchenko, Robert A. Distasio, Roberto Car, and Matthias Scheffler. Accurate and efficient method for many-body van der Waals interactions. *Physical Review Letters*, 108(23):1–5, 2012.

[77] Alberto Ambrosetti, Anthony M. Reilly, Robert A. Distasio, and Alexandre Tkatchenko. Long-range correlation energy calculated from coupled atomic response functions. *Journal of Chemical Physics*, 140(18), 2014.

[78] Pekka Koskinen and Ville Mäkinen. Density-functional tight-binding for beginners. *Computational Materials Science*, 47(1):237 – 253, 2009.

[79] Michael Gaus, Qiang Cui, and Marcus Elstner. DFTB3: Extension of the Self-Consistent-Charge Density-Functional Tight-Binding Method (SCC-DFTB). *Journal of Chemical Theory and Computation*, 7(4):931–948, apr 2011.

[80] Martin Stöhr, Leonardo Medrano Sandonas, and Alexandre Tkatchenko. Accurate Many-Body Repulsive Potentials for Density-Functional Tight-Binding from Deep Tensor Neural Networks. (2), 2020.

[81] David A. Case, Thomas E. Cheatham, Tom Darden, Holger Gohlke, Ray Luo, Kenneth M. Merz, Alexey Onufriev, Carlos Simmerling, Bing Wang, and Robert J. Woods. The Amber biomolecular simulation programs. *Journal of Computational Chemistry*, 26(16):1668–1688, 2005.

[82] David Dubbeldam, Krista S. Walton, Thijs J. H. Vlugt, and Sofia Calero. Design, parameterization, and implementation of atomic force fields for adsorption in nanoporous materials. *Advanced Theory and Simulations*, 2(11):1900135, 2019.

[83] H. Sun. COMPASS: An ab Initio Force-Field Optimized for Condensed-Phase ApplicationsOverview with Details on Alkane and Benzene Compounds. *The Journal of Physical Chemistry B*, 102(38):7338–7364, 1998.

[84] Sareeya Bureekaew, Saeed Amirjalayer, Maxim Tafipolsky, Christian Spickermann, Tapta Kanchan Roy, and Rochus Schmid. MOF-FF - A flexible first-principles derived force field for metal-organic frameworks. *Physica Status Solidi (B) Basic Research*, 250(6):1128–1141, 2013.

[85] R. A. Buckingham and John Edward Lennard-Jones. The classical equation of state of gaseous helium, neon and argon. *Proceedings of the Royal Society of London. Series A. Mathematical and Physical Sciences*, 168(933):264–283, 1938.

[86] Ph. Ghosez, J.-P. Michenaud, and X. Gonze. Dynamical atomic charges: The case of ABo_3 compounds. *Phys. Rev. B*, 58:6224–6240, Sep 1998.

[87] G Kresse and J Furthmüller. Efficient iterative schemes for ab initio total-energy calculations using a plane-wave basis set. *Physical Review B*, 54(16):11169–11186, oct 1996.

[88] P E Blöchl. Projector augmented-wave method. *Physical Review B*, 50(24):17953–17979, dec 1994.

[89] Pascal Vinet, John R Smith, John Ferrante, and James H Rose. Temperature effects on the universal equation of state of solids. *Physical Review B*, 35(4):1945–1953, feb 1987.

[90] Péter Pulay. Convergence acceleration of iterative sequences. the case of scf iteration. *Chemical Physics Letters*, 73(2):393–398, jul 1980.

[91] Georg Kresse, Martijn Marsman, and Jürgen Furthmüller. VASP the Guide, 2018.

[92] M J Frisch, G W Trucks, H B Schlegel, G E Scuseria, M A Robb, J R Cheeseman, G Scalmani, V Barone, G A Petersson, H Nakatsuji, X Li, M Caricato, A V Marenich, J Bloino, B G Janesko, R Gomperts, B Mennucci, H P Hratchian, J V Ortiz, A F Izmaylov, J L Sonnenberg, D Williams-Young, F Ding, F Lipparini, F Egidi, J Goings, B Peng, A Petrone, T Henderson, D Ranasinghe, V G Zakrzewski, J Gao, N Rega, G Zheng, W Liang, M Hada, M Ehara, K Toyota, R Fukuda, J Hasegawa, M Ishida, T Nakajima, Y Honda, O Kitao, H Nakai, T Vreven, K Throssell, J A Montgomery Jr., J E Peralta, F Ogliaro, M J Bearpark, J J Heyd, E N Brothers, K N Kudin, V N Staroverov, T A Keith, R Kobayashi, J Normand, K Raghavachari, A P Rendell, J C Burant, S S Iyengar, J Tomasi, M Cossi, J M Millam, M Klene, C Adamo, R Cammi, J W Ochterski, R L Martin, K Morokuma, O Farkas, J B Foresman, and D J Fox. Gaussian 16 Revision 16.A.03 Inc., Wallingford CT, 2016.

[93] B Aradi, B Hourahine, and Th. Frauenheim. DFTB+, a Sparse Matrix-Based Implementation of the DFTB Method. *The Journal of Physical Chemistry A*, 111(26):5678–5684, jul 2007.

[94] Michael Gaus, Albrecht Goez, and Marcus Elstner. Parametrization and Benchmark of DFTB3 for Organic Molecules. *Journal of Chemical Theory and Computation*, 9(1):338–354, jan 2013.

[95] DFTB Consortium.

[96] Xinyu Wang, Jingchao Zhang, Yue Chen, and Paddy K.L. Chan. Molecular dynamics study of thermal transport in a dinaphtho[2,3-b:2′,3′-f]thieno[3,2-b]thiophene (DNTT) organic semiconductor. *Nanoscale*, 9(6):2262–2271, 2017.

[97] Xiaoyan Zheng, Hua Geng, Yuanping Yi, Qikai Li, Yuqian Jiang, Dong Wang, and Zhigang Shuai. Understanding lattice strain-controlled charge transport in organic semiconductors: A computational study. *Advanced Functional Materials*, 24(35):5531–5540, 2014.

[98] S. Leitherer, C. M. Jäger, A. Krause, M. Halik, T. Clark, and M. Thoss. Simulation of charge transport in organic semiconductors: A time-dependent multiscale method based on nonequilibrium Green's functions. *Physical Review Materials*, 1(6):1–6, 2017.

[99] Carlos Campañá, Bastien Mussard, and Tom K. Woo. Electrostatic potential derived atomic charges for periodic systems using a modified error functional. *Journal of Chemical Theory and Computation*, 5(10):2866–2878, 2009.

[100] Zhigang Shuai, Hua Geng, Wei Xu, Yi Liao, and Jean Marie André. From charge transport parameters to charge mobility in organic semiconductors through multiscale simulation. *Chemical Society Reviews*, 43(8):2662–2679, 2014.

[101] Linjun Wang, Qikai Li, Zhigang Shuai, Liping Chen, and Qiang Shi. Multiscale study of charge mobility of organic semiconductor with dynamic disorders. *Physical Chemistry Chemical Physics*, 12(13):3309–3314, 2010.

[102] Nicolas G. Martinelli, Yoann Olivier, Stavros Athanasopoulos, Maricarmen Ruiz Delgado, Kathryn R. Pigg, Demétrio A. Da Silva Filho, Roei S. Sánchezcarrera, Elisabetta Venuti, Raffaele G. Delia Valle, Jean Luc Brédas, David Beljonne, and Jérôme Cornil. Influence of intermolecular vibrations on the electronic coupling in organic semiconductors: the case of anthracene and perfluoropentacene. *ChemPhysChem*, 10(13):2265–2273, 2009.

[103] Hua Geng, Qian Peng, Linjun Wang, Haijiao Li, Yi Liao, Zhiying Ma, and Zhigang Shuai. Toward quantitative prediction of charge mobility in organic semiconductors: Tunneling enabled hopping model. *Advanced Materials*, 24(26):3568–3572, 2012.

[104] Hiroyasu Furukawa, Kyle E Cordova, Michael O'Keeffe, and Omar M Yaghi. The Chemistry and Applications of Metal-Organic Frameworks. *Science*, 341(6149), 2013.

[105] Johannes P. Dürholt, Guillaume Fraux, François Xavier Coudert, and Rochus Schmid. Ab Initio Derived Force Fields for Zeolitic Imidazolate Frameworks: MOF-FF for ZIFs. *Journal of Chemical Theory and Computation*, 15(4):2420–2432, 2019.

[106] Norman L. Allinger, Young H. Yuh, and Jenn Huei Lii. Molecular mechanics. the mm3 force field for hydrocarbons. 1. *Journal of the American Chemical Society*, 111(23):8551–8566, 1989.

[107] Steve Plimpton. Fast Parallel Algorithms for Short-Range Molecular Dynamics. *Journal of Computational Physics*, 117(1):1–19, mar 1995.

[108] Christopher J. Fennell and J. Daniel Gezelter. Is the Ewald summation still necessary? Pairwise alternatives to the accepted standard for long-range electrostatics. *Journal of Chemical Physics*, 124(23), 2006.

[109] H W Kuhn. The Hungarian method for the assignment problem. *Naval Research Logistics Quarterly*, 2(1-2):83–97, mar 1955.

[110] G. J. Piermarini, A. D. Mighell, C. E. Weir, and S. Block. Crystal structure of benzene ii at 25 kilobars. *Science*, 165(3899):1250–1255, 1969.

[111] G. E. Bacon, N. A. Curry, S. A. Wilson, and Robert Spence. A crystallographic study of solid benzene by neutron diffraction. *Proceedings of the Royal Society of London. Series A. Mathematical and Physical Sciences*, 279(1376):98–110, 1964.

[112] Silvia C. Capelli, Alberto Albinati, Sax A. Mason, and Bertram T.M. Willis. Molecular motion in crystalline naphthalene: Analysis of multi-temperature X-ray and neutron diffraction data. *Journal of Physical Chemistry A*, 110(41):11695–11703, 2006.

[113] C. P. Brock and J. D. Dunitz. Temperature dependence of thermal motion in crystalline anthracene. *Acta Crystallographica Section B*, 46(6):795–806, Dec 1990.

[114] Daniel Holmes, Sriram Kumaraswamy, Adam J. Matzger, and K. Peter C. Vollhardt. On the nature of nonplanarity in the [n]phenylenes. *Chemistry – A European Journal*, 5(11):3399–3412, 1999.

[115] Christine C. Mattheus, Anne B. Dros, Jacob Baas, Auke Meetsma, Jan L. de Boer, and Thomas T. M. Palstra. Polymorphism in pentacene. *Acta Crystallographica Section C*, 57(8):939–941, Aug 2001.

[116] V. K. Belsky, V. E. Zavodnik, and V. M. Vozzhennikov. Fluorene, C_13H_10. *Acta Crystallographica Section C*, 40(7):1210–1211, Jul 1984.

[117] Akinobu Matsumoto, Mitsuharu Suzuki, Hironobu Hayashi, Daiki Kuzuhara, Junpei Yuasa, Tsuyoshi Kawai, Naoki Aratani, and Hiroko Yamada. Aromaticity relocation in perylene derivatives upon two-electron oxidation to form anthracene and phenanthrene. *Chemistry – A European Journal*, 22(41):14462–14466, 2016.

[118] Erich F. Paulus, Frank J. J. Leusen, and Martin U. Schmidt. Crystal structures of quinacridones. *CrystEngComm*, 9:131–143, 2007.

[119] Liwei Huang, Qing Liao, Qiang Shi, Hongbing Fu, Jinshi Ma, and Jiannian Yao. Rubrene micro-crystals from solution routes: their crystallography, morphology and optical properties. *J. Mater. Chem.*, 20:159–166, 2010.

[120] Malte Fugel, Dylan Jayatilaka, Emanuel Hupf, Jacob Overgaard, Venkatesha R. Hathwar, Piero Macchi, Michael J. Turner, Judith A. K. Howard, Oleg V. Dolomanov, Horst Puschmann, Bo B. Iversen, Hans-Beat Bürgi, and Simon Grabowsky. Probing the accuracy and precision of Hirshfeld atom refinement with HARt interfaced with Olex2. *IUCrJ*, 5(1):32–44, Jan 2018.

[121] J. Trotter. The crystal and molecular structure of biphenyl. *Acta Crystallographica*, 14(11):1135–1140, Nov 1961.

[122] H. Cailleau, J. L. Baudour, and C. M. E. Zeyen. Structural phase transition in polyphenyls. VII. A neutron diffraction study of the structural phase transition in biphenyl-d10. *Acta Crystallographica Section B*, 35(2):426–432, Feb 1979.

[123] H. M. Rietveld, E. N. Maslen, and C. J. B. Clews. An X-ray and neutron diffraction refinement of the structure of p-terphenyl. *Acta Crystallographica Section B*, 26(6):693–706, Jun 1970.

[124] Kenneth N. Baker, Albert V. Fratini, Timothy Resch, Howard C. Knachel, W.W. Adams, E.P. Socci, and B.L. Farmer. Crystal structures, phase transitions and energy calculations of poly(p-phenylene) oligomers. *Polymer*, 34(8):1571 – 1587, 1993.

[125] Natalia Bedoya-Martínez, Andrea Giunchi, Tommaso Salzillo, Elisabetta Venuti, Raffaele Guido Della Valle, and Egbert Zojer. Toward a Reliable Description of the Lattice Vibrations in Organic Molecular Crystals: The Impact of van der Waals Interactions. *Journal of Chemical Theory and Computation*, 14(8):4380–4390, aug 2018.

[126] K. P. Meletov. Phonon spectrum of a naphthalene crystal at a high pressure: Influence of shortened distances on the lattice and intramolecular vibrations. *Physics of the Solid State*, 55(3):581–588, 2013.

[127] R Bhandari and V K Jindal. Calculation of thermal expansion and implicit phonon frequency shift in deuterated anthracene. *Journal of Physics: Condensed Matter*, 3(8):899–907, 1991.

[128] Jun Zhao and Richard Mccreery. Multichannel FT-Raman Spectroscopy: Noise Analysis and Performance Assessment. *Applied Spectroscopy - APPL SPECTROSC*, 51:1687–1697, 1997.

[129] Axel D Becke. Density-functional thermochemistry. iii. the role of exact exchange. *The Journal of Chemical Physics*, 98(7):5648–5652, apr 1993.

[130] P J Stephens, F J Devlin, C F Chabalowski, and M J Frisch. Ab Initio Calculation of Vibrational Absorption and Circular Dichroism Spectra Using Density Functional Force Fields. *The Journal of Physical Chemistry*, 98(45):11623–11627, nov 1994.

[131] Jan Gerit Brandenburg and Stefan Grimme. Accurate modeling of organic molecular crystals by dispersion-corrected density functional tight binding (DFTB). *Journal of Physical Chemistry Letters*, 5(11):1785–1789, 2014.

[132] Wolfgang von der Linden, Volker Dose, and Udo von Toussaint. *Bayesian Probability Theory: Applications in the Physical Sciences*. Cambridge University Press, 2014.

[133] Janine George, Ruimin Wang, Ulli Englert, and Richard Dronskowski. Lattice thermal expansion and anisotropic displacements in urea, bromomalonic aldehyde, pentachloropyridine, and naphthalene. *Journal of Chemical Physics*, 147(7), 2017.

[134] C Kittel. *Introduction to Solid State Physics*. Wiley, New York, 2004.

[135] Clare F Macrae, Ioana Sovago, Simon J Cottrell, Peter T A Galek, Patrick McCabe, Elna Pidcock, Michael Platings, Greg P Shields, Joanna S Stevens, Matthew Towler, and Peter A Wood. Mercury 4.0: from visualization to analysis, design and prediction. *Journal of Applied Crystallography*, 53(1), feb 2020.

[136] Edward Prince. *Mathematical Techniques in Crystallography and Materials Science*. Springer Berlin Heidelberg, 1994.

[137] D R Lide. *CRC Handbook of Chemistry and Physics, 90th Edition*. Taylor & Francis, Boca Raton, Florida, 2009.

[138] Jonas Nyman, Orla Sheehan Pundyke, and Graeme M. Day. Accurate force fields and methods for modelling organic molecular crystals at finite temperatures. *Physical Chemistry Chemical Physics*, 18(23):15828–15837, 2016.

[139] Raffaele Guido Della Valle, Elisabetta Venuti, and Aldo Brillante. Quasi harmonic lattice dynamics: The phase diagram of benzene. *Chemical Physics*, 202(2-3):231–241, 1996.

[140] Sam Azadi and R. E. Cohen. Low-pressure phase diagram of crystalline benzene from quantum Monte Carlo. *Journal of Chemical Physics*, 145(6), 2016.

[141] P. Puschnig, C. Ambrosch-Draxl, G. Heimel, E. Zojer, R. Resel, G. Leising, M. Kriechbaum, and W. Graupner. Pressure studies on the intermolecular interactions in biphenyl. *Synthetic Metals*, 116(1-3):327–331, 2001.

[142] J. L. Baudour. Structural phase transition in polyphenyls. X. Potential barrier heights in crystalline polyphenyls and in gaseous biphenyl determined uniquely from diffraction data. *Acta Crystallographica Section B*, 47(6):935–949, 1991.

[143] Peter S. Friedman, Raoul Kopelman, and Paras N. Prasad. Spectroscopic evidence for a continuous change in molecular and crystal structure: deformation of biphenyl in the low temperature solid. *Chemical Physics Letters*, 24(1):15–17, 1974.

[144] Arnaud Marmier, Zoe A.D. Lethbridge, Richard I. Walton, Christopher W. Smith, Stephen C. Parker, and Kenneth E. Evans. ElAM: A computer program for the analysis and representation of anisotropic elastic properties. *Computer Physics Communications*, 181(12):2102–2115, 2010.

[145] Tommaso Salzillo, Arianna Rivalta, Nicola Castagnetti, Simone D'Agostino, Matteo Masino, Fabrizia Grepioni, Elisabetta Venuti, Aldo Brillante, and Alberto Girlando. Spectroscopic identification of quinacridone polymorphs for organic electronics. *CrystEngComm*, 21:3702–3708, 2019.

[146] H Kuzmany. *Festkörperspektroskopie: eine Einführung*. Springer, 1990.

[147] Mogens Christensen, Asger B. Abrahamsen, Niels B. Christensen, Fanni Juranyi, Niels H. Andersen, Kim Lefmann, Jakob Andreasson, Christian R.H. Bahl, and Bo B. Iversen. Avoided crossing of rattler modes in thermoelectric materials. *Nature Materials*, 7(10):811–815, 2008.

[148] Taishan Zhu, Krishnan Swaminathan-Gopalan, Kevin J. Cruse, Kelly Stephani, and Elif Ertekin. Vibrational Energy Transport in Hybrid Ordered/Disordered Nanocomposites: Hybridization and Avoided Crossings of Localized and Delocalized Modes. *Advanced Functional Materials*, 28(17):1–8, 2018.

[149] Wu Li, Jesús Carrete, Georg K.H. Madsen, and Natalio Mingo. Influence of the optical-acoustic phonon hybridization on phonon scattering and thermal conductivity. *Physical Review B*, 93(20):1–5, 2016.

[150] Christian Winkler, Andreas Jeindl, Florian Mayer, Oliver T. Hofmann, Ralf Tonner, and Egbert Zojer. Understanding the correlation between electronic coupling and energetic stability of molecular crystal polymorphs: The instructive case of quinacridone. *Chemistry of Materials*, 31(17):7054–7069, 2019.

[151] Giorgia Fugallo, Andrea Cepellotti, Lorenzo Paulatto, Michele Lazzeri, Nicola Marzari, and Francesco Mauri. Thermal conductivity of graphene and graphite: Collective excitations and mean free paths. *Nano Letters*, 14(11):6109–6114, 2014.

[152] Michal Fulem, Václav Laštovka, Martin Straka, Květoslav Růžička, and John M. Shaw. Heat capacities of tetracene and pentacene. *Journal of Chemical and Engineering Data*, 53(9):2175–2181, 2008.

[153] Alexander Stukowski. Visualization and analysis of atomistic simulation data with OVITO-the Open Visualization Tool. *MODELLING AND SIMULATION IN MATERIALS SCIENCE AND ENGINEERING*, 18(1), 2010.

A. Appendices

A.1. Mathematical Details for the Derivation of the Bose-Einstein Distribution

$$\sum_{n=0}^{\infty} nq^n \tag{A.1}$$

$$\sum_{n=0}^{\infty} q^n = \frac{1}{1-q} \qquad |\frac{d}{dq} \tag{A.2}$$

$$\sum_{n=0}^{\infty} nq^{n-1} = \frac{1}{(1-q)^2} \tag{A.3}$$

$$\sum_{n=0}^{\infty} nq^{n-1} = \frac{1}{q}\sum_{n=0}^{\infty} nq^n \tag{A.4}$$

$$\sum_{n=0}^{\infty} nq^n = \frac{q}{(1-q)^2} \tag{A.5}$$

A.2. Commutation Rules for Phonon Ladder Operators

The important commutation relations should be briefly listed here [36]:

$$\left[a_\lambda, a_{\lambda'}^\dagger\right] = \delta_{\lambda,\lambda'} \tag{A.6}$$

Here, again, λ has been used as a condensed quantum number labelling the band n and the wave vector $\mathbf{q}$.

$$\delta_{\lambda,\lambda'} = \delta_{n,n'}\delta\left(\mathbf{q}-\mathbf{q}'\right) \tag{A.7}$$

$$[a_\lambda, a_{\lambda'}] = \left[a_\lambda^\dagger, a_{\lambda'}^\dagger\right] = 0 \tag{A.8}$$

A.3. Some More Details on the One-Dimensional Phonon Model System

The one-dimensional model system used to illustrate the quantum effects on the average kinetic energy consists of three atoms per unit-cell (lattice parameter a). One of the three atoms is heavier with mass M, while the others have a reduced mass $m < M$. Here, $M/m = 5$ has been chosen. The atoms are coupled by linear springs which only connect the nearest neighbours. There is one force constant which describes the interaction between the two lighter atom (γ) and one ($k = \gamma/2$) quantifying the force constant between the heavy and one of the light atoms. A sketch of the one-dimensional crystal is shown in the following figure.

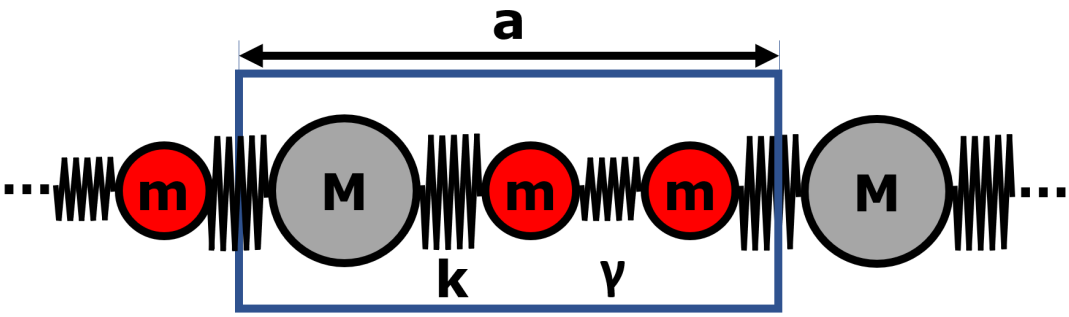

Fig. A.1.: One-dimensional model system consisting of three atoms per unit-cell (blue box) with lattice parameter a. One of the three atoms (large ball) has a larger mass than the others $M > m$. Furthermore, the force constant between the heavy and the light atoms (k) is smaller than the force constant coupling the two light atoms (γ).

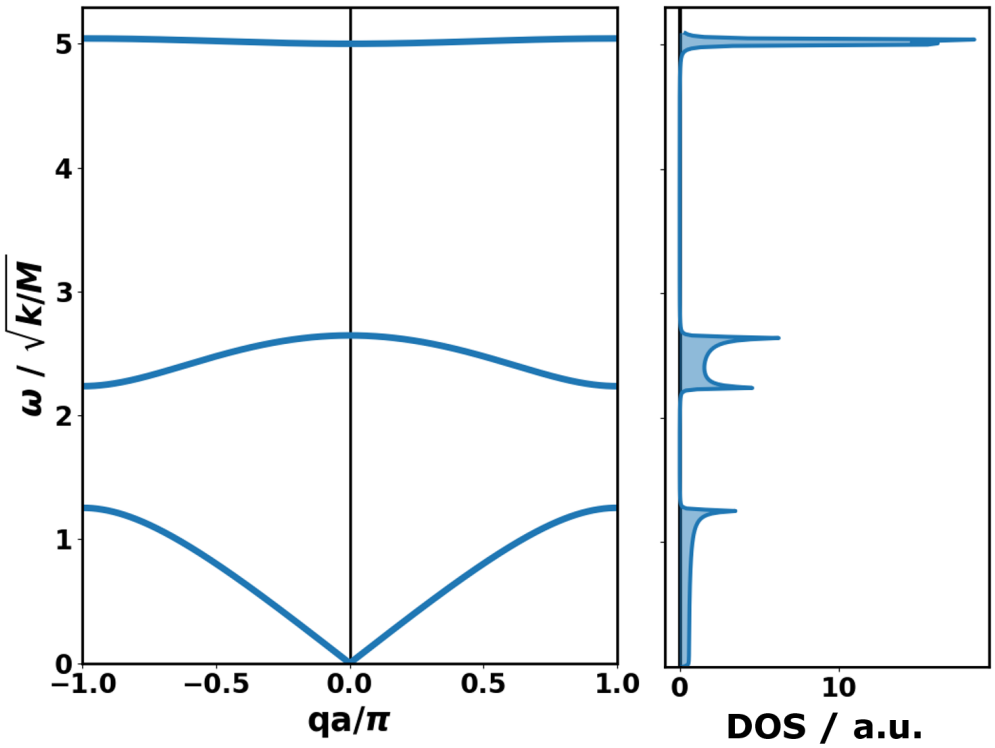

Fig. A.2.: Phonon band structure of the descibed three-atomic model system. The (angular) frequency ω is given in units of the force constant k and the heavy mass M (see the text in Sec. A.3). The right panel shows the associated density of states (DOS) as a function of frequency. The DOS has been calculated according to Eq. (2.81), replacing the delta-distributions by Lorentzian function with a full-width at half maximum of 0.01 (angular) frequency units.

The relatively large difference in mass and bonding strength leads to the phonon band structure and DOS shown in Fig. A.2. A relatively large band gap opens between the acoustic and the first optical band similar to the case of two atoms per unit-cell. Due to the third atom (and the considerably stiffer bond), there is a third band at higher frequencies corresponding to modes, in which the light atoms move out of phase so that the much stiffer bond is constantly stretched and compressed resulting in the high energy of this vibration. This band results in a very sharp peak in the DOS due to the absence of a relevant band dispersion. The first optical band has only a relatively small band width so that the part of the DOS corresponding to this band is limited to a narrow spectral window with two peaks (van Hove singularity) typical for one-dimensional DOSs. In contrast to the three-dimensional case, in which the linear band dispersion of the acoustic modes results in a quadratically increasing DOS near zero frequency, in one-dimensional space, the DOS is constant for a linear band dispersion as is reproduced correctly in the shown DOS.

A.4. Convergence of the DOSs with respect to the wave vector sampling

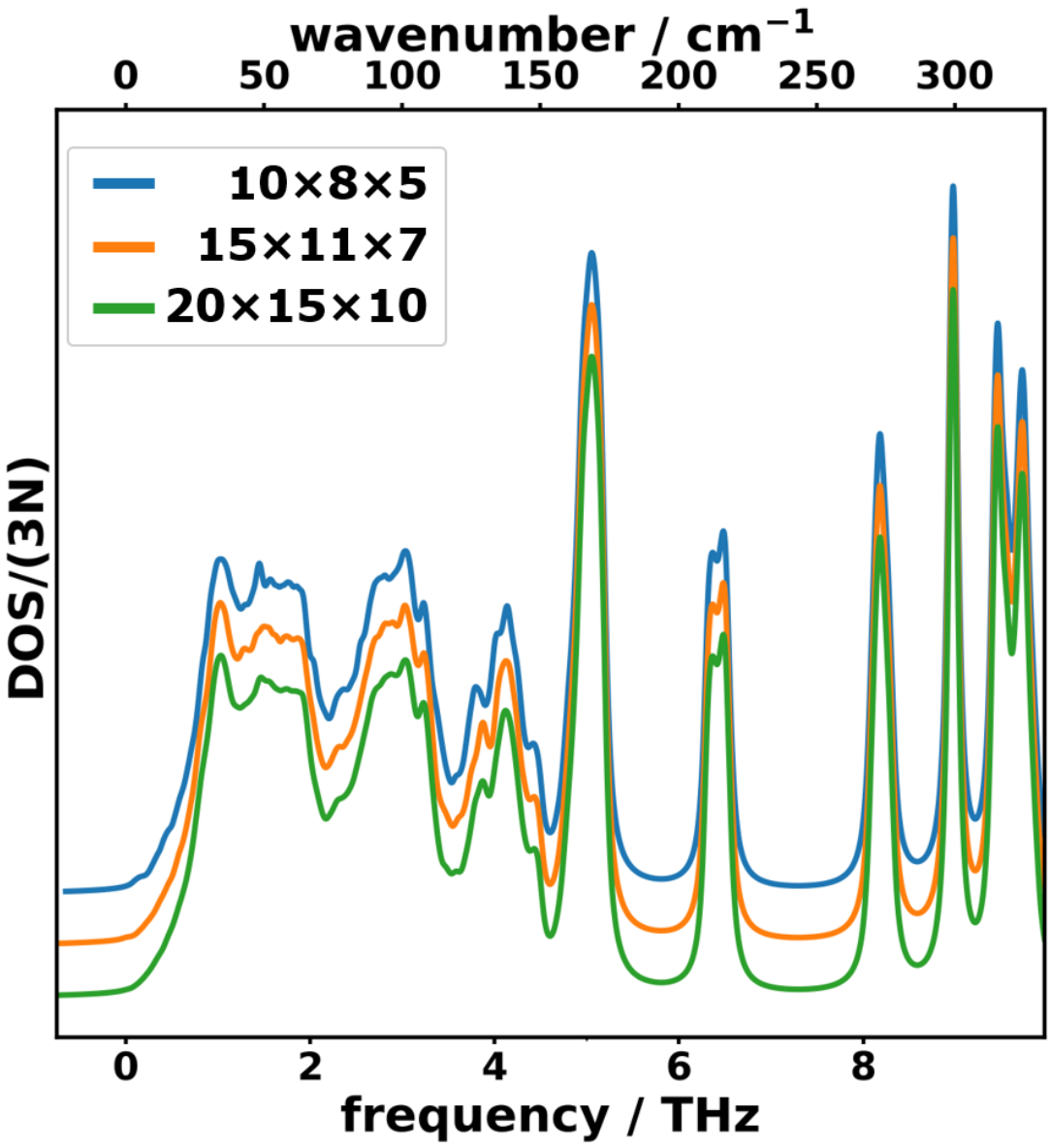

Fig. A.3.: Convergence of the PE/D3-BJ-calculated phonon DOSs of tetracene with respect to the **q**-mesh sampling (see legend). The curves have been slightly shifted vertically to improve the visibility.

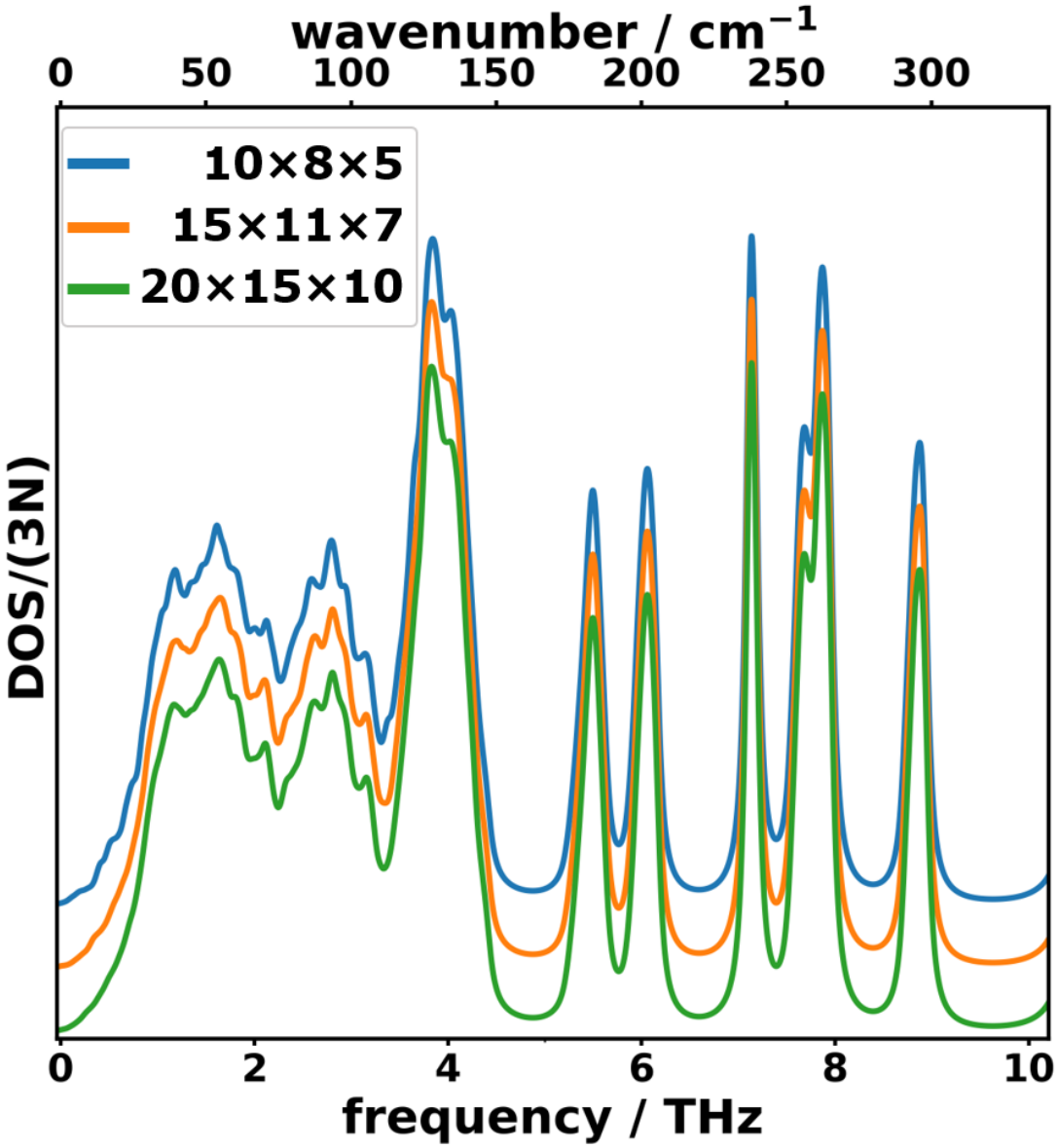

Fig. A.4.: Convergence of the PE/D3-BJ-calculated phonon DOSs of tetracene with respect to the **q**-mesh sampling (see legend). The curves have been slightly shifted vertically to improve the visibility.

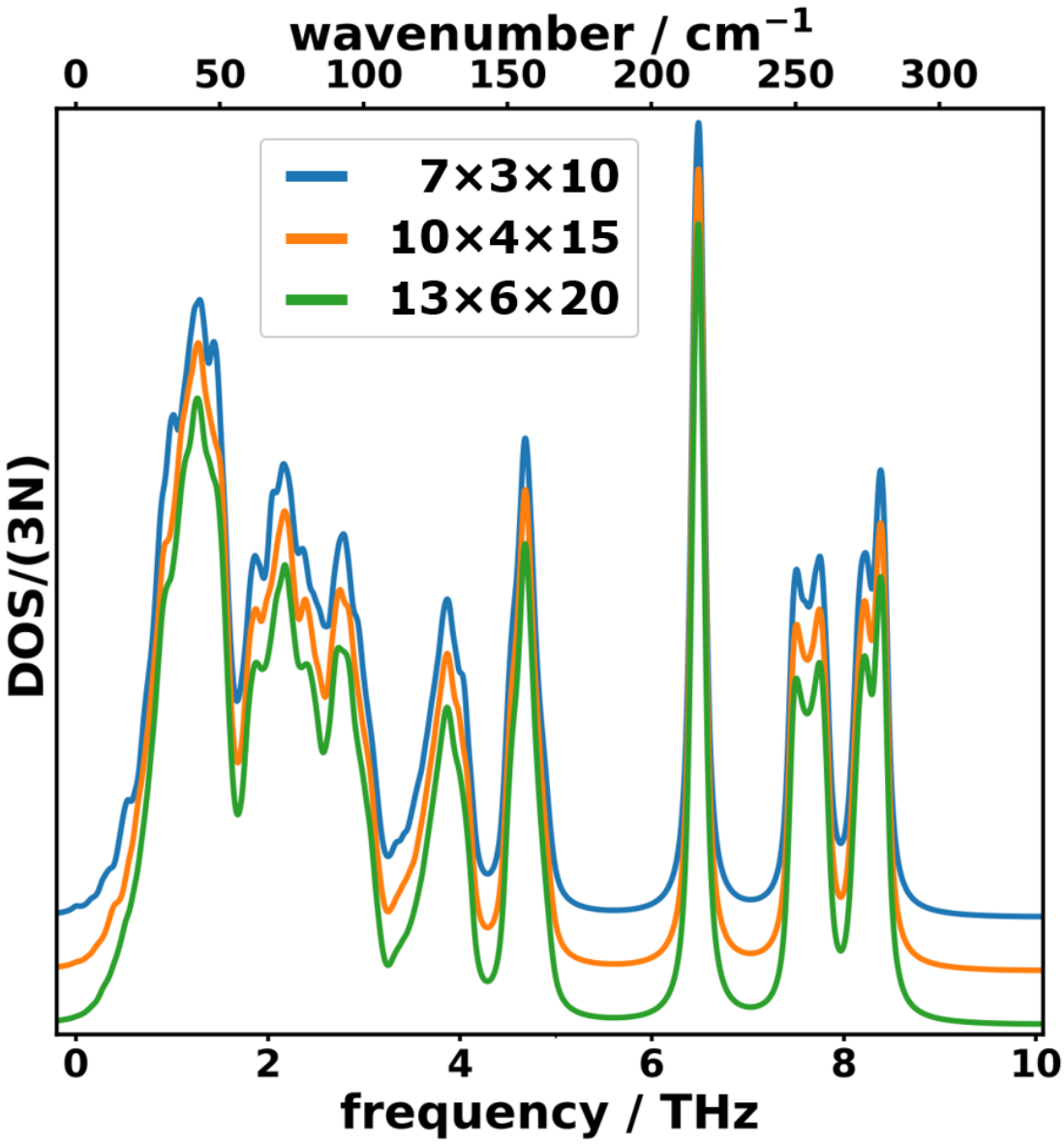

Fig. A.5.: Convergence of the PE/D3-BJ-calculated phonon DOSs of tetracene with respect to the **q**-mesh sampling (see legend). The curves have been slightly shifted vertically to improve the visibility.

A.5. Lowest-frequency Intramolecular Modes in Naphthalene

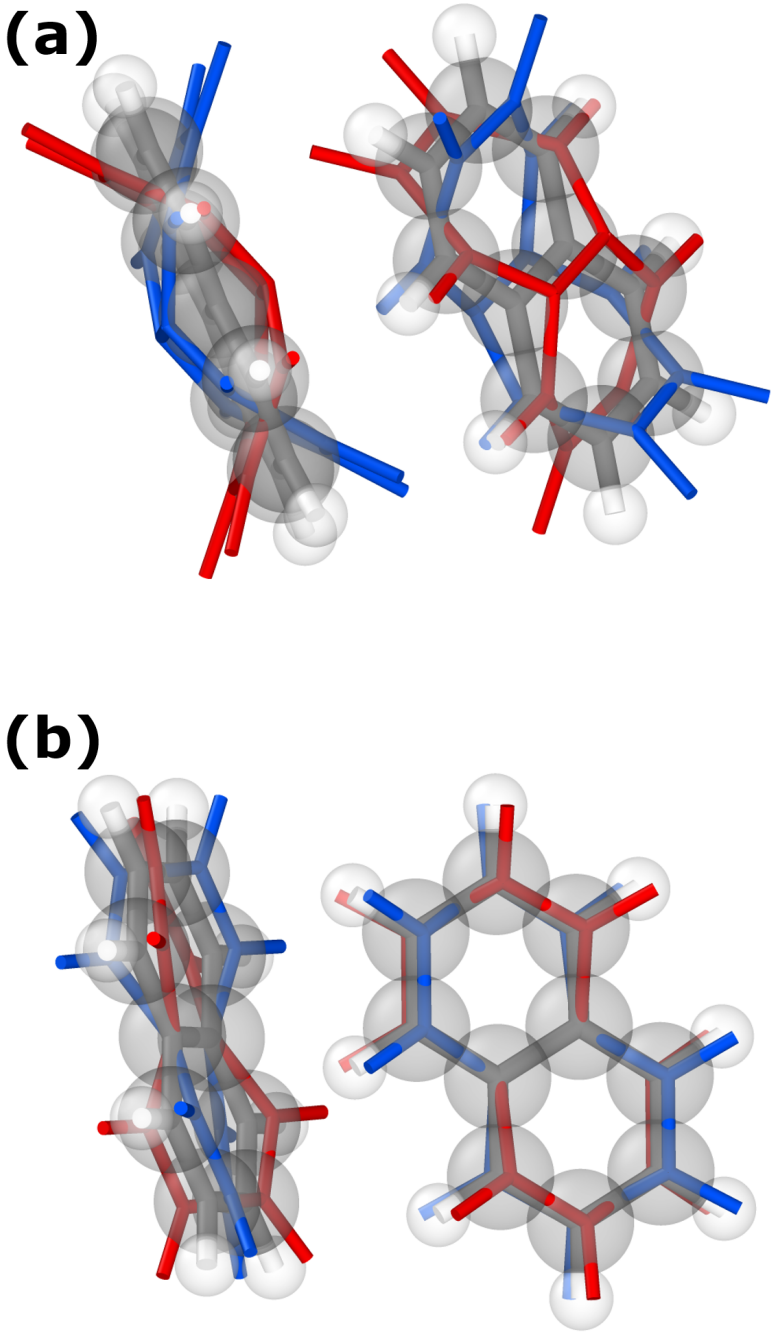

Fig. A.6.: Γ-point displacement patterns of the lowest intramolecular bands: (a) bending modes (in-phase at 5.3 THz and anti-phase at 5.8 THz at Γ) (b) intramolecular torsions (anti-phase at 6.37 THz and in-phase at 6.41 THz at Γ) in naphthalene. The red and blue wireframe structures correspond to the positive and negative amplitudes of the vibration, respectively.

A.6. More Views of the Crystal Structure of β-Quinacridone

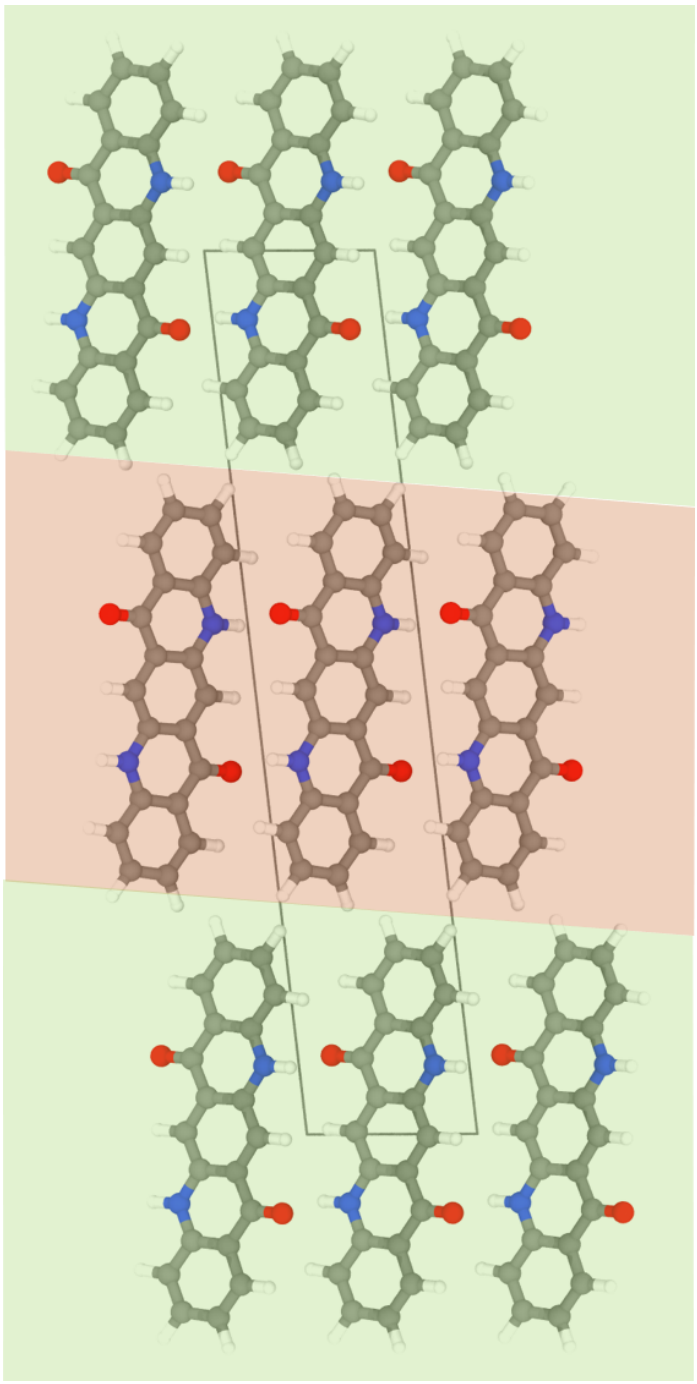

Fig. A.7.: Crystal structure of β-quinacridone (visualised with *Ovito* [153]) seen in the direction along the lattice vector **b** (colour coding: C...grey, H...white, N...blue, O...red). The two well separated layers consisting of only one of the two inequivalent molecules per unit-cell and its periodic replica are indicated by the green and orange background, respectively.

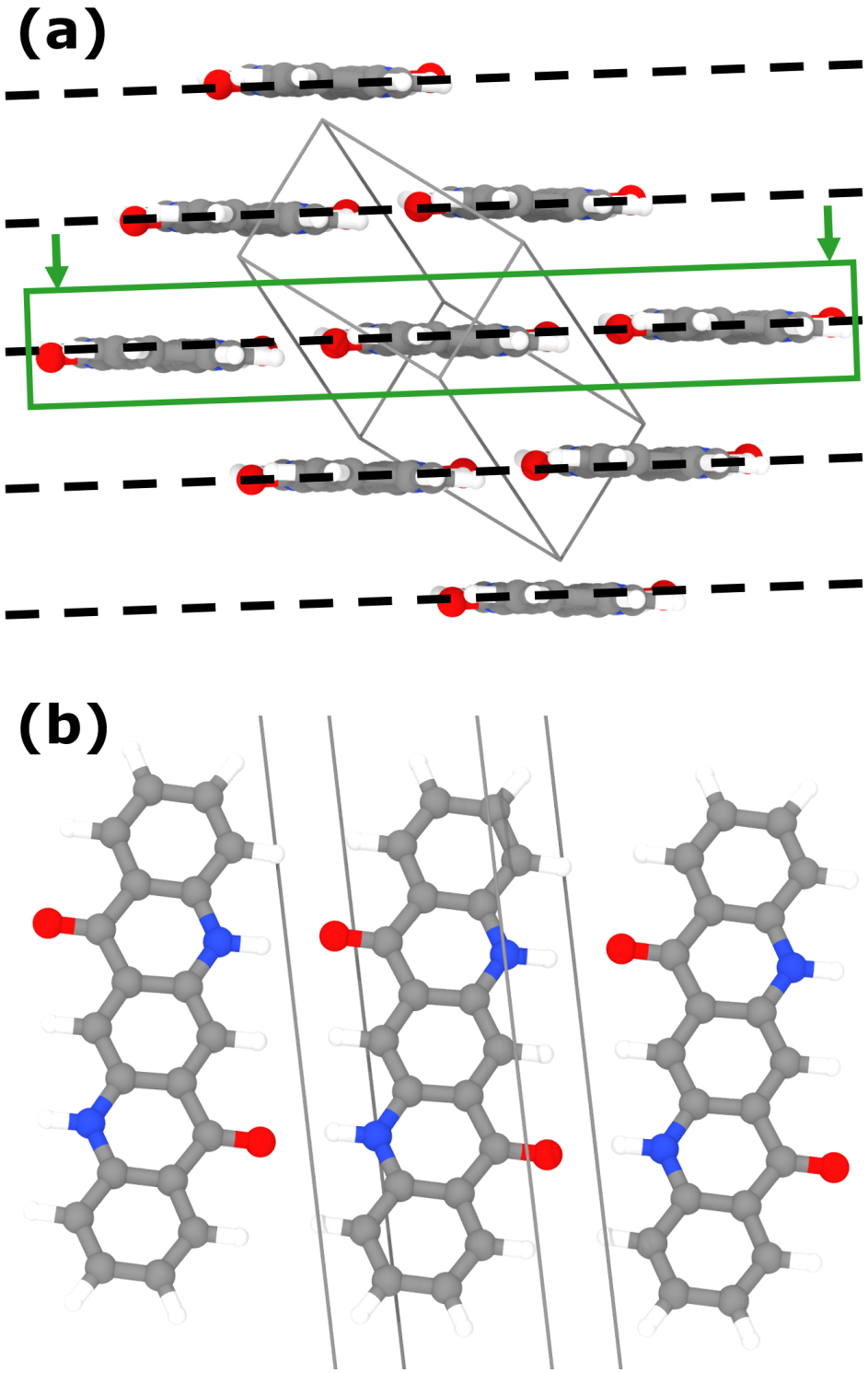

Fig. A.8.: Detailed view of one of the layers shown in Fig. A.7. (a) Within the layers, the molecules arrange in such a way that they nearly perfectly lie in (parallel) planes, which are indicated by the black dashed lines. (b) Top view of one such a plane (green box in (a)) showing the similarity of the planes to two-dimensional graphene, for instance (colour coding: C...grey, H...white, N...blue, O...red). The crystal structure was visualised with *Ovito* [153].

A.7. More Views of the Crystal Structure of γ-Quinacridone

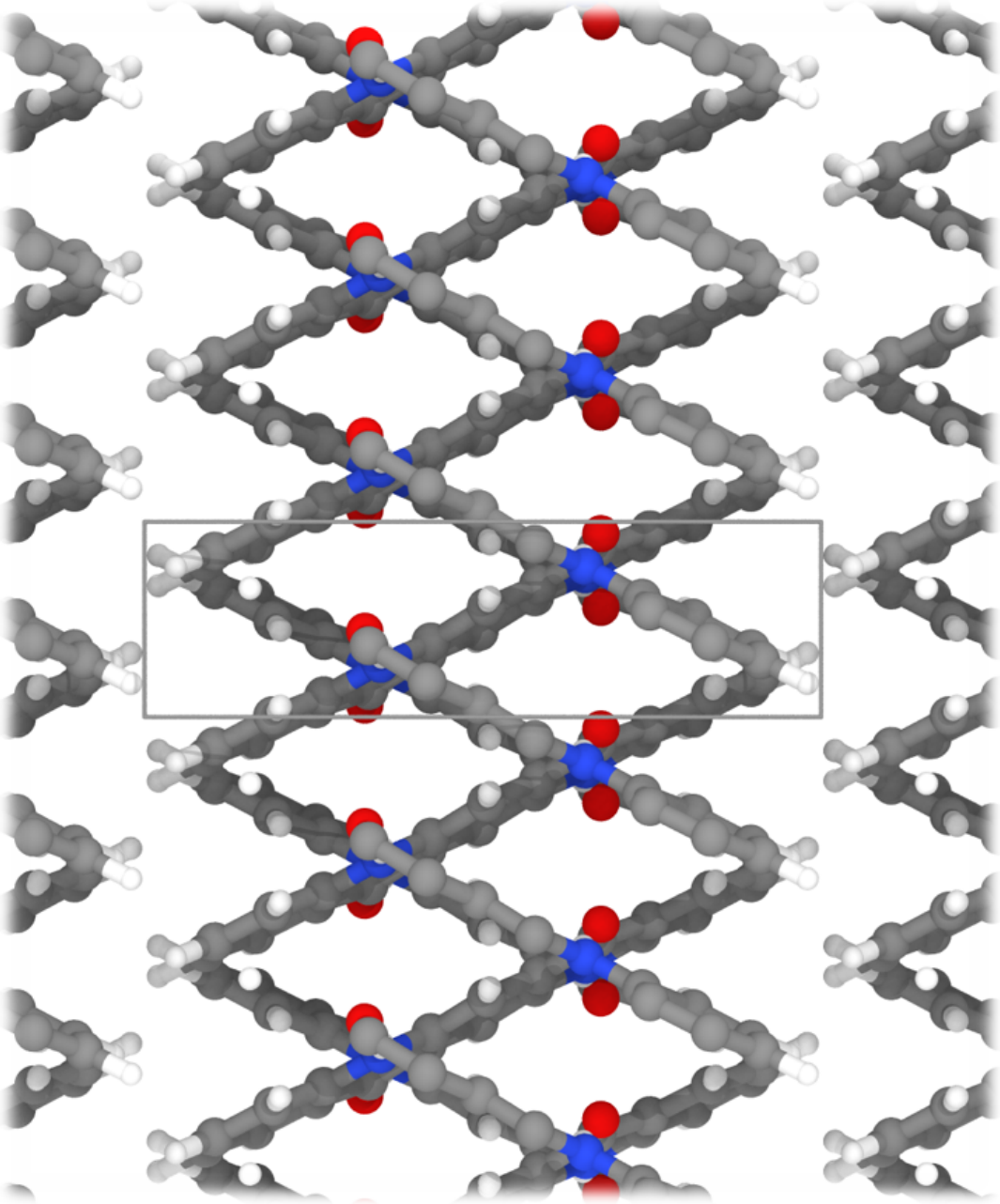

Fig. A.9.: Crystal structure of γ-quinacridone (visualised with *Ovito* [153]) seen in the direction along the lattice vector **c** (colour coding: C...grey, H...white, N...blue, O...red). The two molecules per unit-cell arrange in a so-called "hunter fence" pattern.

A.8. Further Thermodynamic Properties

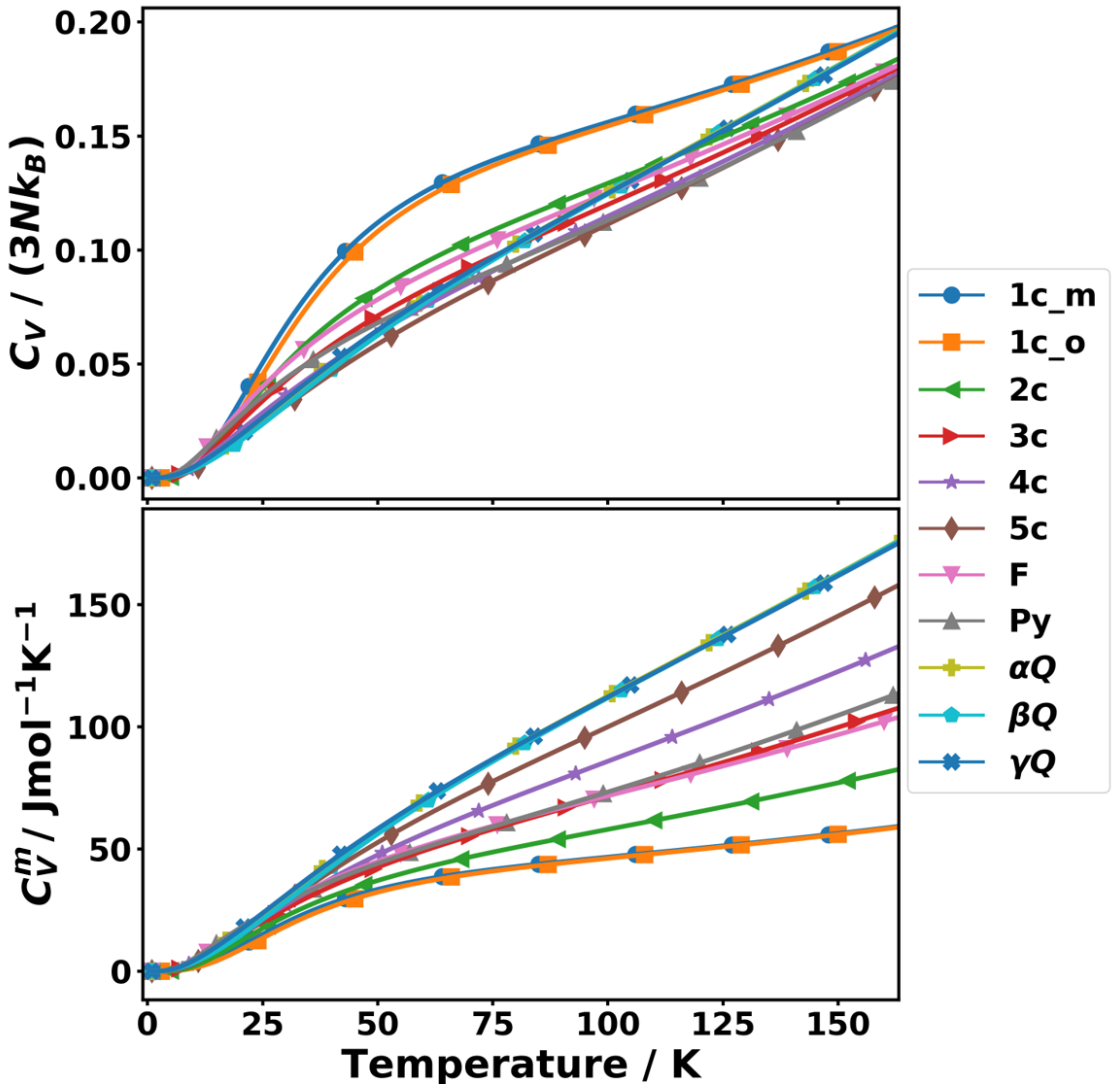

Fig. A.10.: Phonon contributions to the heat capacities (C_V) as a function of temperature for the shown molecular crystals (according to the abbreviations introduced in Tab. 3.1) for a smaller temperature range. The upper panel shows the phonon heat capacity per unit-cell normalised by the number of bands ($3N$) and the Boltzmann constant (k_B) so that $\lim_{T\to\infty} C_V/(3Nk_B) = 1$. The lower panel shows the heat capacity per mole of the molecule, C_V^m, (i.e. considering the number of molecules per unit-cell). The symbols only serve as guides to the eye and do not represent the actually calculated data points, which lie much more densely.

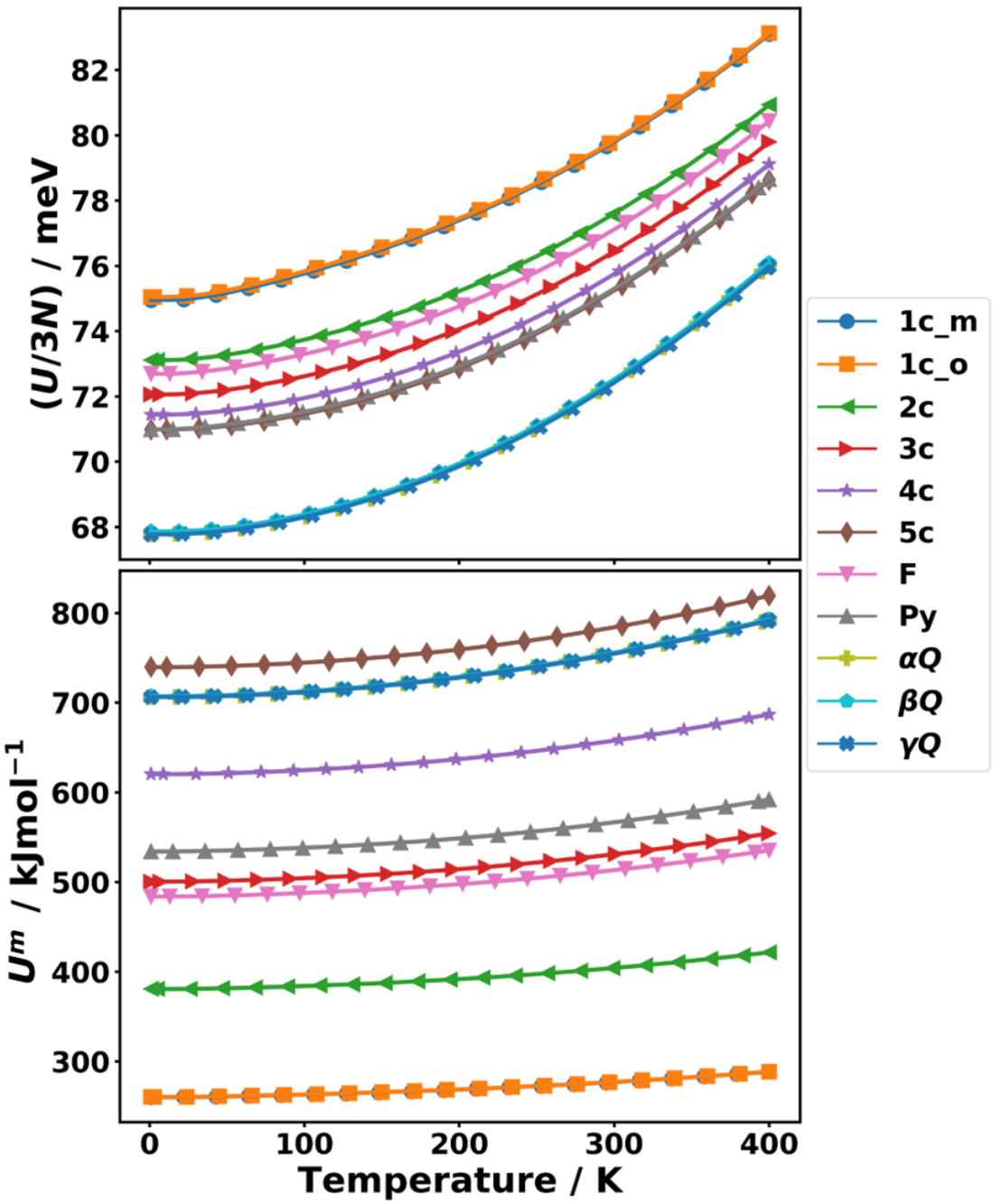

Fig. A.11.: Phonon contributions to the internal energy (U) as a function of temperature for the shown molecular crystals (according to the abbreviations introduced in Tab. 3.1). The upper panel shows the phonon internal energy per unit-cell normalised by the number of bands ($3N$). The lower panel shows the internal energy per mole of the molecule, U^m, (i.e. considering the number of molecules per unit-cell). The symbols only serve as guides to the eye and do not represent the actually calculated data points, which lie much more densely.

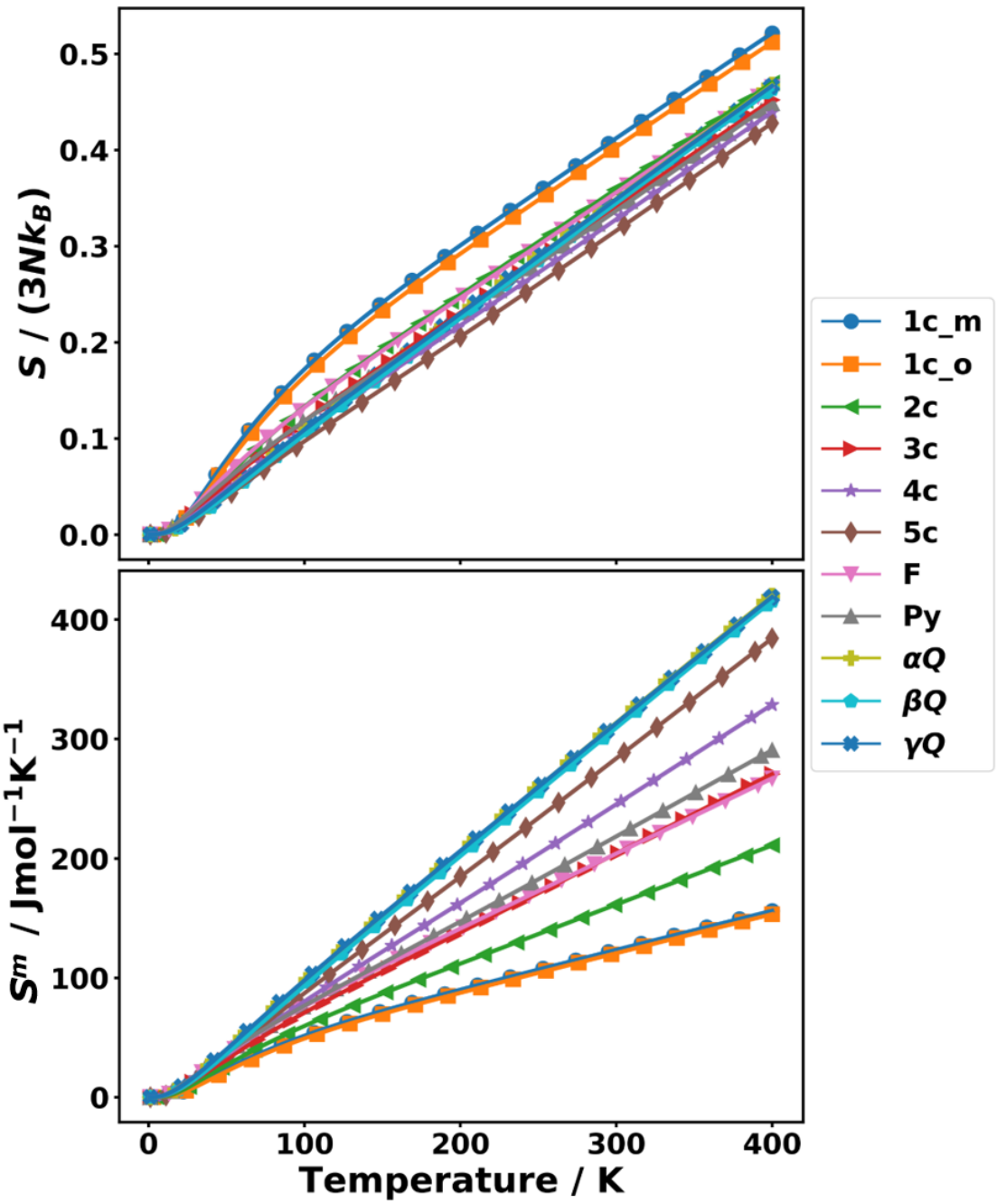

Fig. A.12.: Phonon contributions to the entropy (S) as a function of temperature for the shown molecular crystals (according to the abbreviations introduced in Tab. 3.1). The upper panel shows the phonon entropy per unit-cell normalised by the number of bands ($3N$) and the Boltzmann constant (k_B). The lower panel shows the entropy per mole of the molecule, S^m (i.e. considering the number of molecules per unit-cell). The symbols only serve as guides to the eye and do not represent the actually calculated data points, which lie much more densely.

A.9. General relation between the heat capacities at constant pressure and at constant volume

The derivation can, in principle, be found in Ref. [7], although some additional steps are included here. The notation $\frac{\partial x}{\partial y}\Big|_z$ is used here to describe the partial derivative of x with respect to the variable y with z being kept constant. Analogously to Ref. [7], one starts with expressing the entropy as its partial derivative with respect to experimentally easily accessible variables temperature T and pressure p:

$$dS = \frac{\partial S}{\partial T}\bigg|_p dT + \frac{\partial S}{\partial p}\bigg|_T dp \tag{A.9}$$

This equation can be partially differentiated with respect to T, which yields:

$$\frac{\partial S}{\partial T}\bigg|_V = \frac{\partial S}{\partial T}\bigg|_p + \frac{\partial S}{\partial p}\bigg|_T \frac{\partial p}{\partial T}\bigg|_V \tag{A.10}$$

The resulting partial derivatives of the entropy with respect to temperature at constant volume/pressure in this equation can be most easily evaluated by using the relation between entropy and the internal energy U:

$$dS = \frac{dU}{T} \Rightarrow \frac{\partial S}{\partial T}\bigg|_{V/P} = \frac{1}{T}\frac{\partial U}{\partial T}\bigg|_{V/p} = \frac{C_{V/p}}{T} \tag{A.11}$$

The second term on the right hand side in Eq. A.10 can be evaluated by (i) recalling the proper Maxwell relation stemming from the differential expression of the Gibbs free enthalpy G, which is the thermodynamic potential in (N, p, T) space:

$$dG = dU - SdT + Vdp(+\mu dN) \tag{A.12}$$

The last term in brackets being the (differential) contribution from the chemical potential μ of the involved particles, which is not relevant in this derivation. One can, however, write the entropy as partial derivative of G:

$$S = -\frac{\partial G}{\partial T}\bigg|_p \Rightarrow \frac{\partial S}{\partial p}\bigg|_T = -\frac{\partial^2 G}{\partial T \partial p} = -\frac{\partial V}{\partial T}\bigg|_p = -\alpha_V V \tag{A.13}$$

Here, it has been used that one can switch the order of differentiation so that $\partial G/\partial p = V$ can be used. The temperature-derivative of the volume at constant pressure, can equivalently be written as the volumetric thermal expansion coefficient α_V multiplied with the volume V.
Finally, the last required term is the derivative of the pressure with respect to the temperature at constant volume. To this end, the total derivative of the volume (in the Gibbs ensemble) can be written as:

$$dV = \frac{\partial V}{\partial T}\bigg|_p dT + \frac{\partial V}{\partial p}\bigg|_T dp \tag{A.14}$$

For the condition of constant volume, one requires $dV = 0$ so that one can rewrite the above equation:

$$\left.\frac{\partial p}{\partial T}\right|_V = -\left.\frac{\partial V}{\partial T}\right|_p \left.\frac{\partial p}{\partial V}\right|_T \tag{A.15}$$

The first derivative in this equation can again be rewritten using the volumetric thermal expansion coefficient ($= \alpha_V V$), while the second factor is proportional to the bulk modulus B ($\left.\frac{\partial p}{\partial V}\right|_T = -B/V$). Both factors together yield:

$$\left.\frac{\partial p}{\partial T}\right|_V = +\alpha_V B \tag{A.16}$$

Putting together the results from Eqs. (A.10), (A.11), and (A.16), one finally arrives at the relation between C_p and C_V:

$$C_p - C_V = T\alpha_V^2 V B \tag{A.17}$$